

This pdf file contains all figure pages in the dissertation:

The geology, geochronology, structure and geochemistry of the
Wild Rogue Wilderness remnant of the Coast Range ophiolite, southwest Oregon:
implications for the magmatic and tectonic evolution of the Coast Range ophiolite

by

Stefan B. Kosanke

A Dissertation

Submitted to the University at Albany, State University of New York

in Partial Fulfillment of

the Requirements for the Degree of

Doctor of Philosophy

College of Arts & Sciences

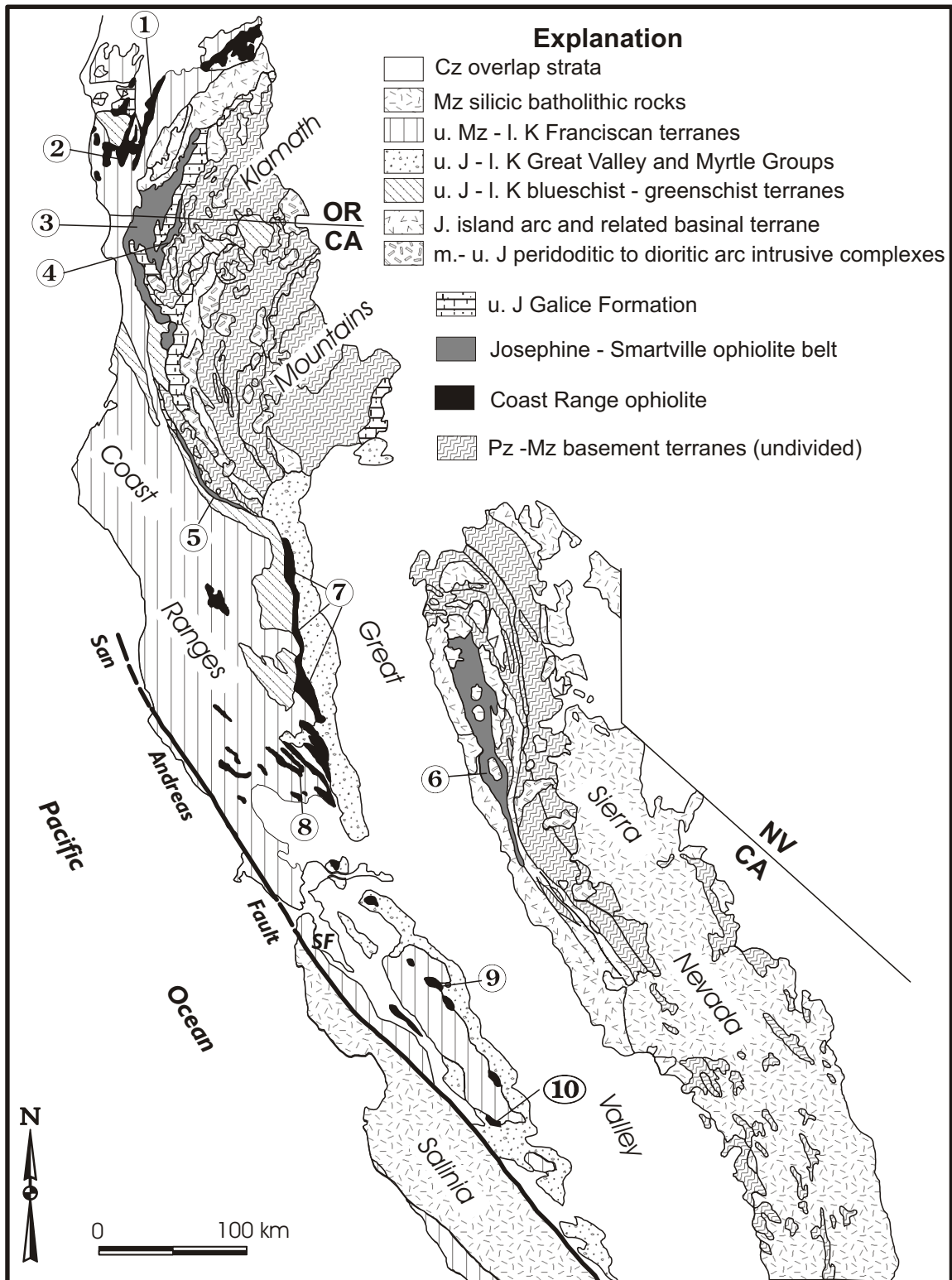
Department of Earth and Atmospheric Sciences

2000

Figure 1.1

Generalized map showing major accretionary terranes but also mid- to late Jurassic ophiolitic and related rocks of California and SW Oregon. Map modified from Harper et al. (1985). Two belts of mid- to late Jurassic ophiolites include the Coast Range ophiolite (western belt), and the Josephine - Smartville ophiolites (eastern belt). Numbers refer to the localities listed below.

1. Wild Rogue Wilderness: 164 Ma (Saleeby, 1984)
2. Snow Camp Mountain: 169 Ma (Saleeby et al., 1984).
3. Josephine ophiolite: 162 Ma (Harper et al., 1994)
4. Preston Peak 'ophiolite' (Saleeby and Harper, 1993)
5. Devils Elbow remnant of the JO: 164 Ma (Wyld and Wright, 1988)
6. Smartville ophiolite: 160-164 Ma (Edelman et al, 1989; Saleeby et al, 1989).
7. Northern Coast Range ophiolite remnants (e.g., Elder Creek, Paskenta, Stonyford)
8. Black Mountain
9. Del Puerto: 155-157 Ma (Hopson et al., 1981; Evarts et al., 1992)
10. Llanada: 164 Ma (Hopson et al., 1981)



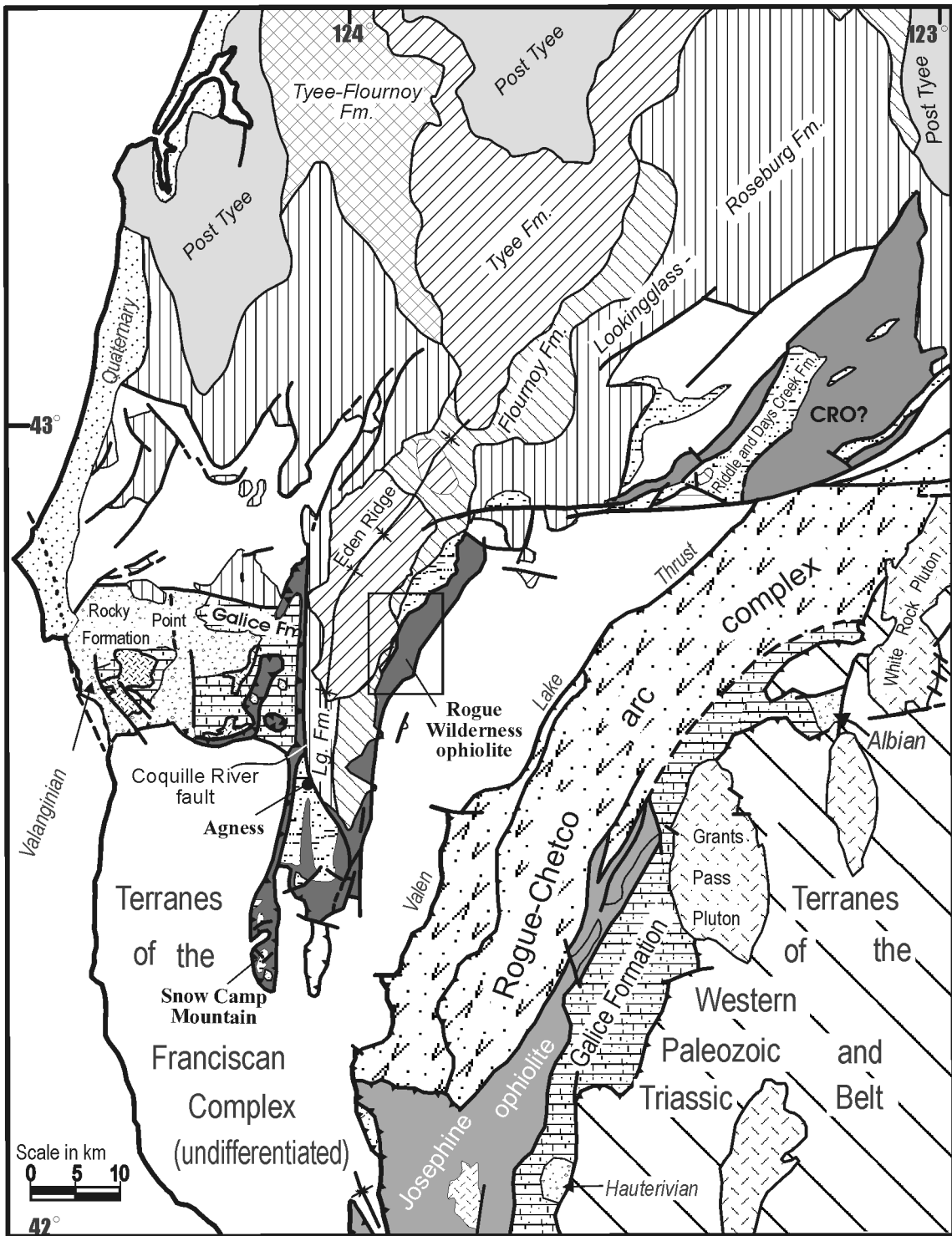


Figure 1.2

Simplified geological map of SW Oregon. The area of the field map is outlined (box).

See figure 1.3 for explanation.

Figure 1.3

Tectonostratigraphic diagram comparing Coast Range ophiolite (CRO) - basal Great Valley Group (volcanopelagic sequence) succession with the Josephine ophiolite - Galice succession. Minimum and estimated maximum possible ages of the Coast Range ophiolite remnant at Cuesta Ridge and Llanada are based on U/Pb and Pb/Pb isotopic ages, respectively (Hopson et al., in Dickinson et al., 1996). Terrigenous sedimentation on Coast Range ophiolite - volcanopelagic sequence began with basal strata of the Great Valley Group in the latest Jurassic. Ages for the Josephine ophiolite are from Harper et al. (1994), for the Rogue Chetco island arc complex from Yule (1996), for the Coast Range ophiolite remnant at Cuesta Ridge and Llanada from Hopson et al. (in Dickinson et al., 1996). The data for the Snow Camp mountain area and the Wild Rogue Wilderness are from Saleeby et al. (1984) and Saleeby (1984), respectively. Additionally, the $^{40}\text{Ar}/^{39}\text{Ar}$ and U/Pb data obtained for this study for the Half Moon Bar gabbro and the Mule Mountain volcanics are used. The cherts within and above pillows near Snow Camp Mountain contain radiolarians of Callovian to mid Oxfordian age (Pessagno written communication, 1996).

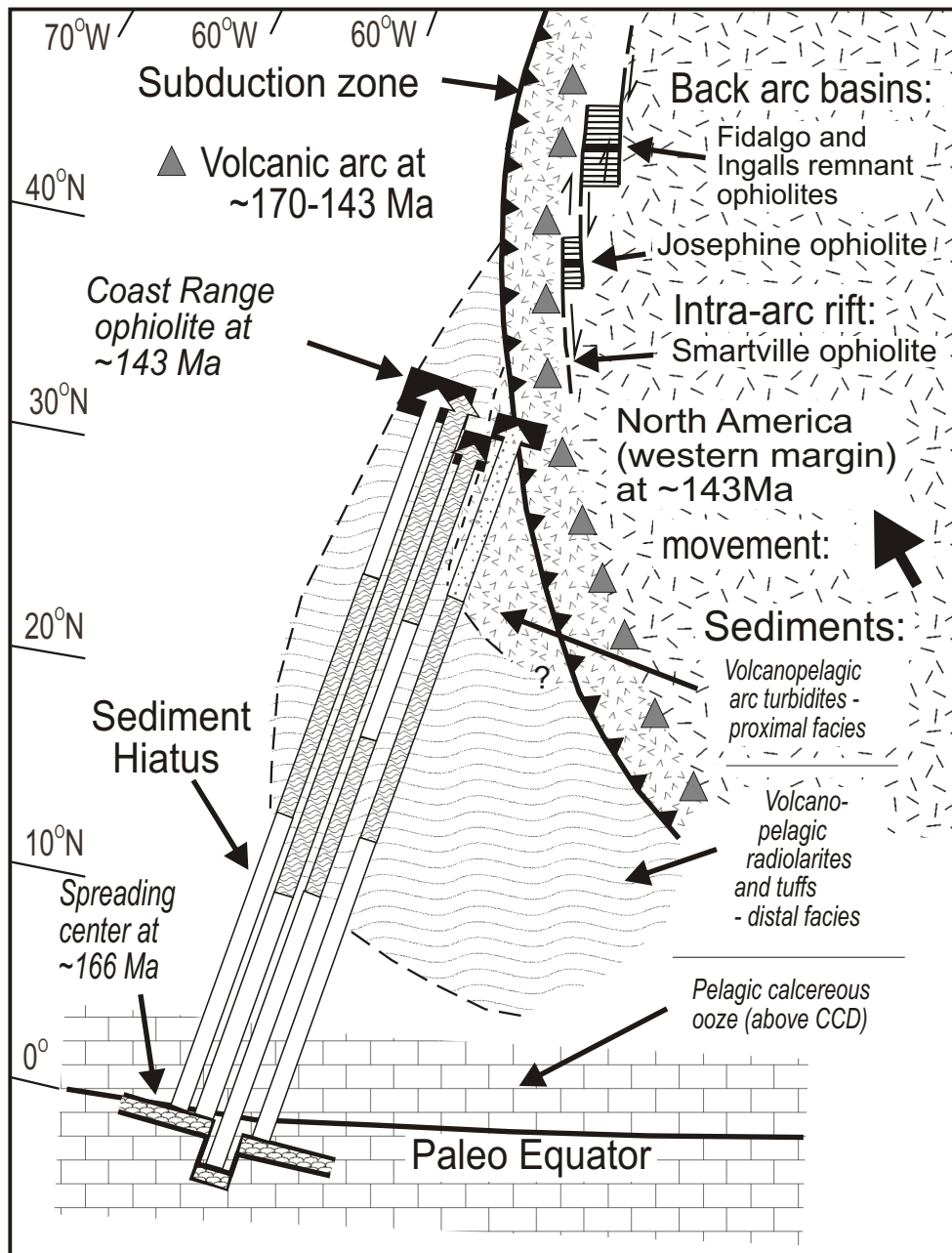


Figure 1.4

Tectonic model for the Coast Range ophiolite after Hopson et al. (in Dickinson et al.; 1996).

This model involves seafloor spreading at a mid-ocean ridge followed by accretion to

N. America by latest Jurassic time.

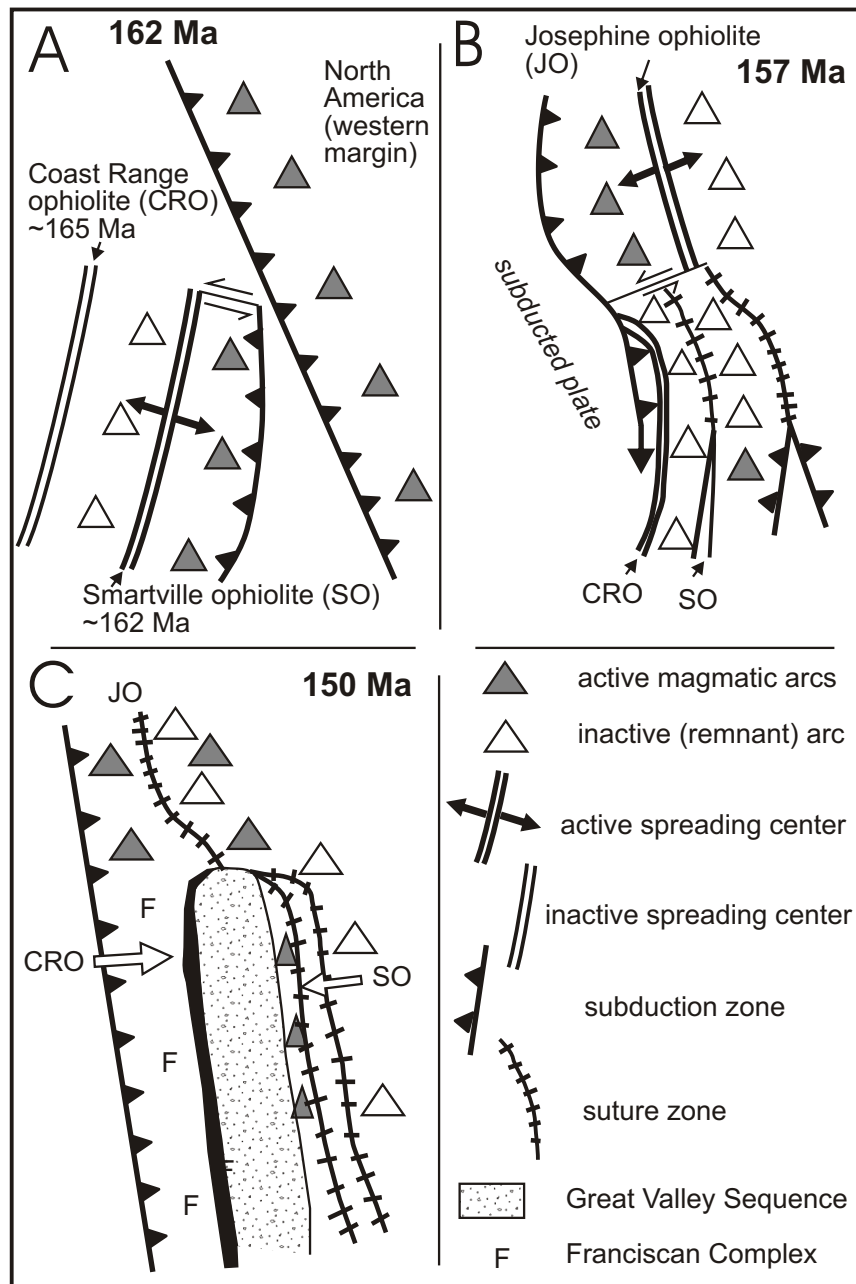


Figure 1.5

Tectonic model for the Coast Range ophiolite after Ingersoll and Schweikert (1986)

This model involves back-arc spreading in an intra-oceanic arc that collided with N. America during the late Jurassic Nevadan orogeny.

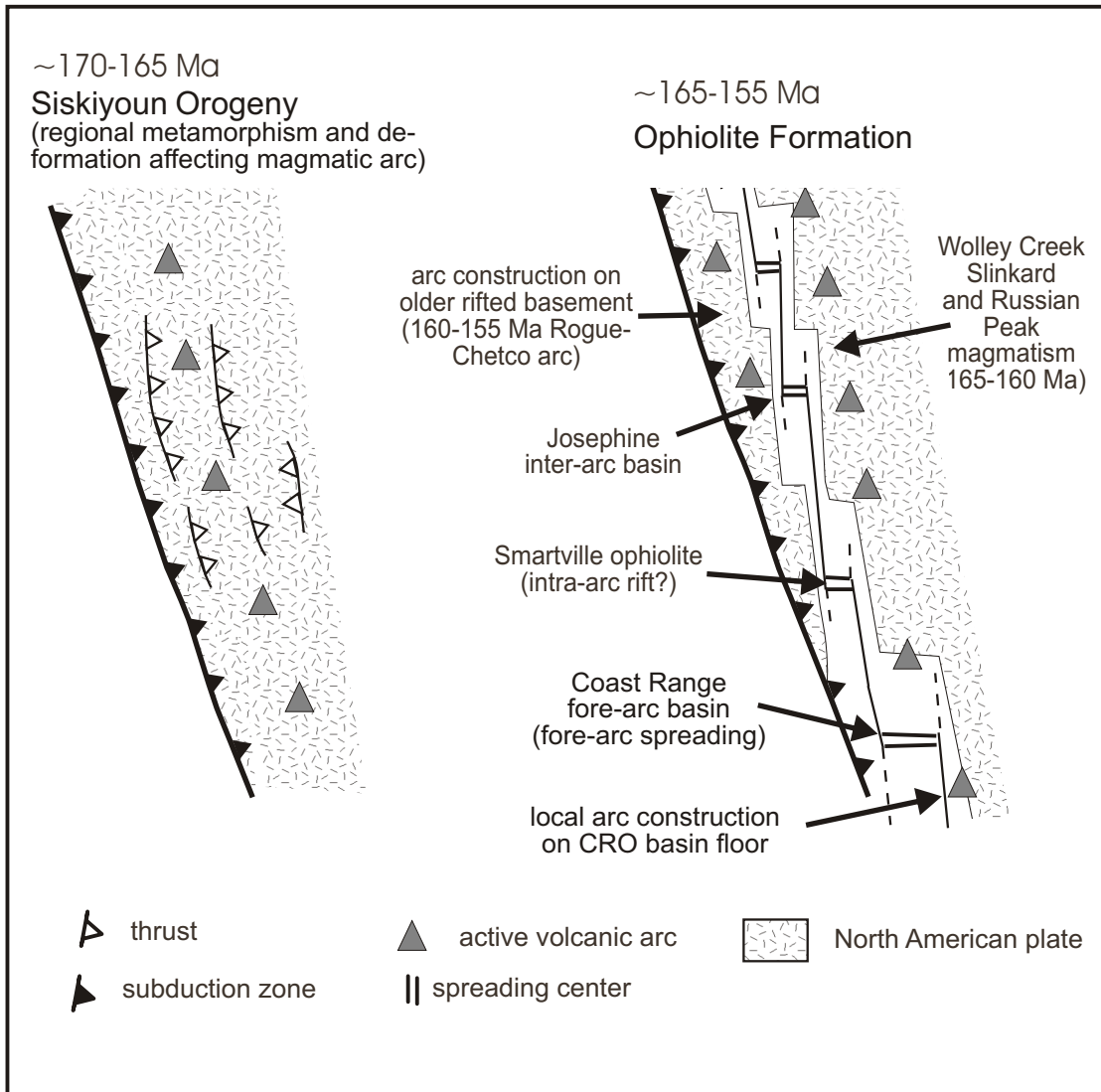


Figure 1.6

Tectonic model for the generation of the Josephine ophiolite and Coast Range ophiolite (CRO) after Harper and Wright (1984), Wyld and Wright (1988), Saleeby and Harper (1993), Saleeby et al. (1992), and Harper et al. (1985, 1994). This model involves spreading within the fore-arc of the Mid-Jurassic Sierran-Klamath arc during oblique subduction and trench rollback (see also figure 1.7).

Model 3 (see figure 1.6)

Model 4 (Stern and Bloomer, 1992)

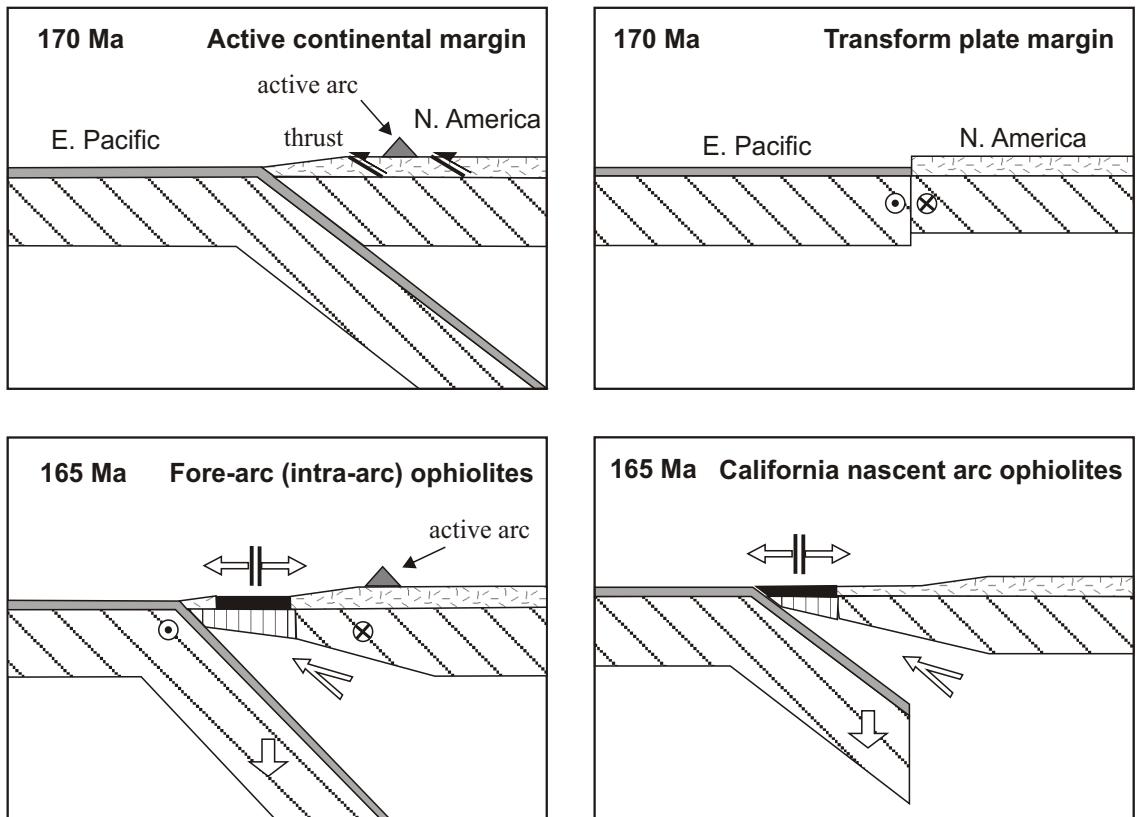


Figure 1.7

Tectonic model for the Coast Range ophiolite after Stern and Bloomer (1992) compared to the model shown in figure 6 (after Harper and Wright, 1984; Wyld and Wright, 1988; Saleeby and Harper 1993; and Harper et al., 1985, 1994). The model invokes extension of the North American plate into the 'gap' that resulted from the sinking and subduction of the Pacific plate.

Thus, the CRO represents 'infant arc crust' formed by seafloor spreading.

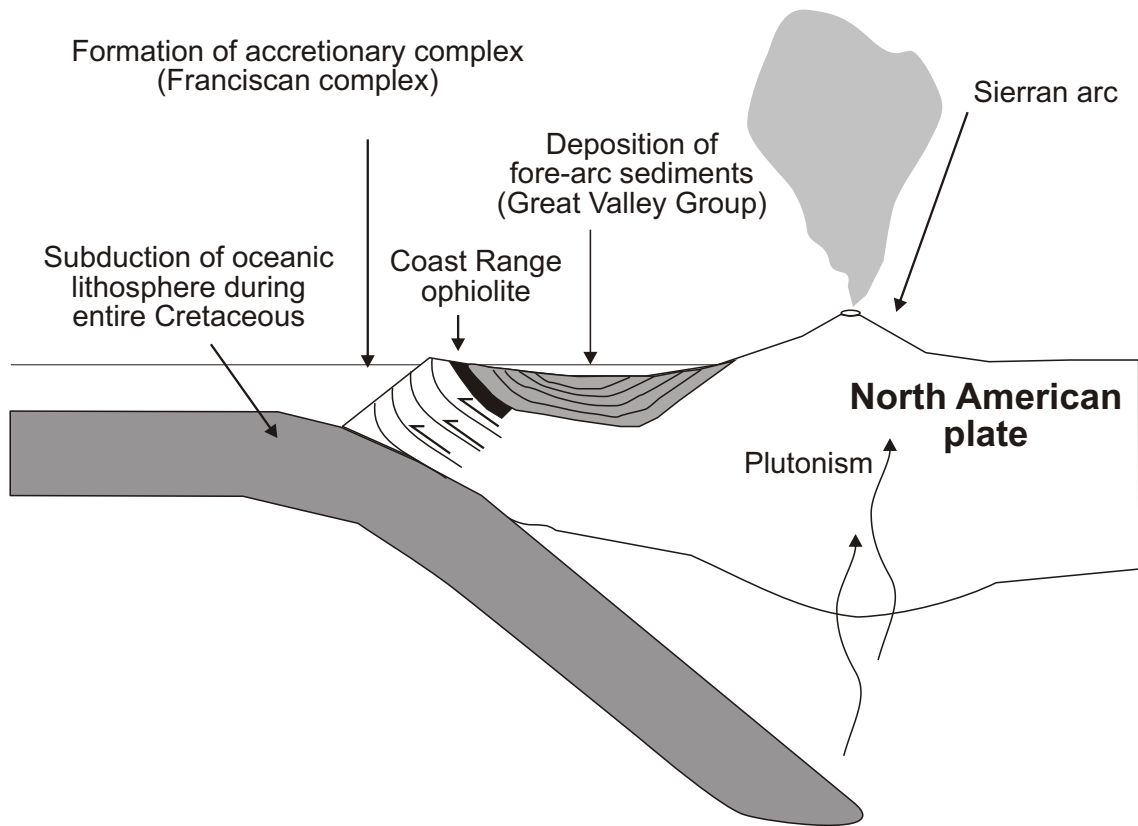
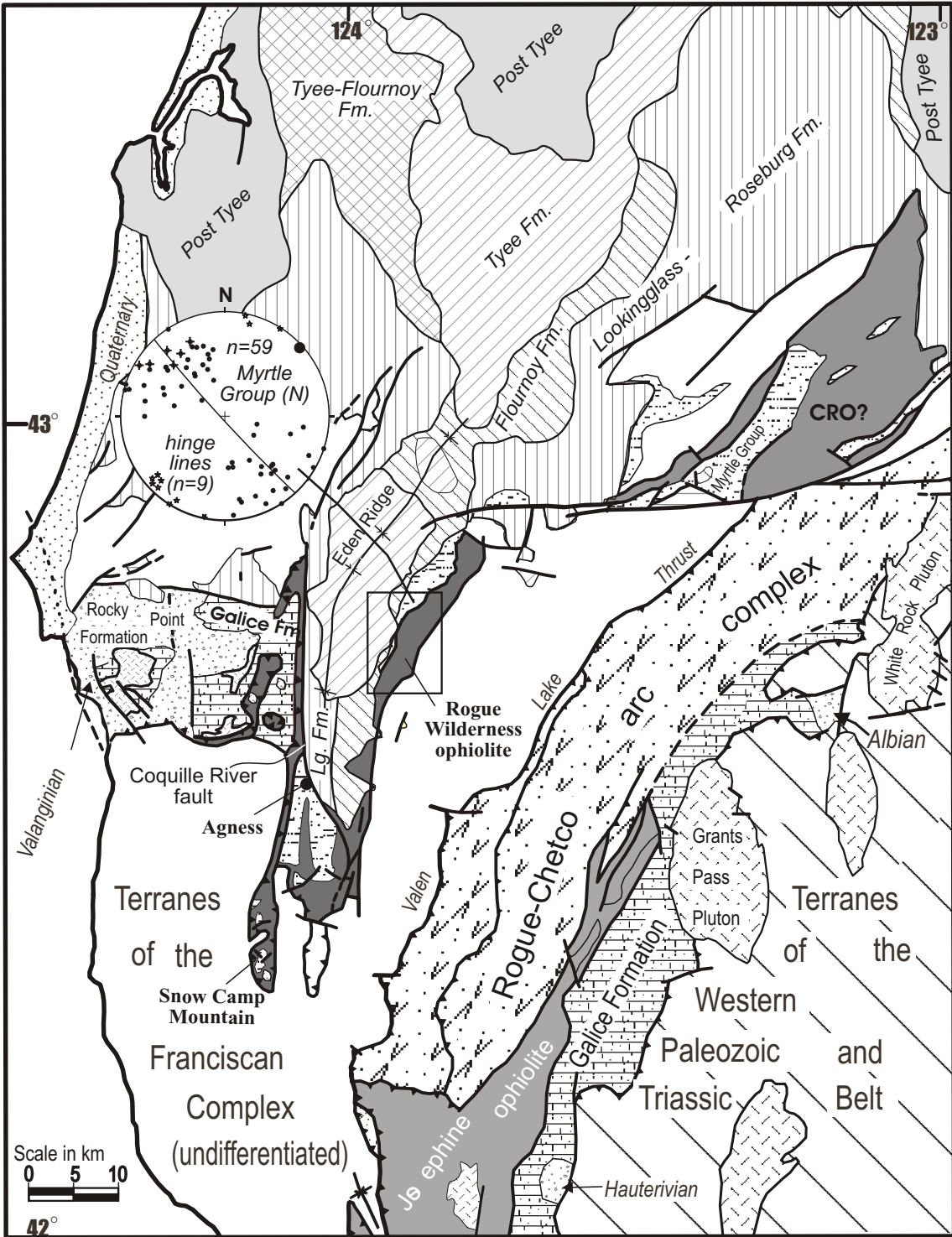


Figure 1.8

Model modified after Page (1972) showing subduction of oceanic lithosphere beneath western North America during the Cretaceous.

Figure 2.1

- A. Simplified geologic map of SW Oregon. The geologic map of Tertiary strata in Oregon is modified from Chan and Dott (1983) and Niem and Niem (1990), and the geologic map of pre-Tertiary rocks is modified from Walker and MacLeod (1991) and Blake et al. (1985a). The structural data suggest that the Rogue Wilderness ophiolite occurs on the east-limb of a large Cretaceous syncline (folded thrust sheet).
- B. Interpretative cross section along line AA' (figure 2.1a). The Snow Camp terrane, consisting of an ophiolitic basement and late Jurassic to early Cretaceous fore-arc sediments (Myrtle Group), is interpreted as the remnant of a folded thrust sheet that is thrust over the terranes of the Franciscan complex (Yolla Bolly terrane and Sixes River terrane) (Blake et al., 1985a). This remnant appears to be preserved in a graben and is largely covered by Tertiary strata with great unconformity.



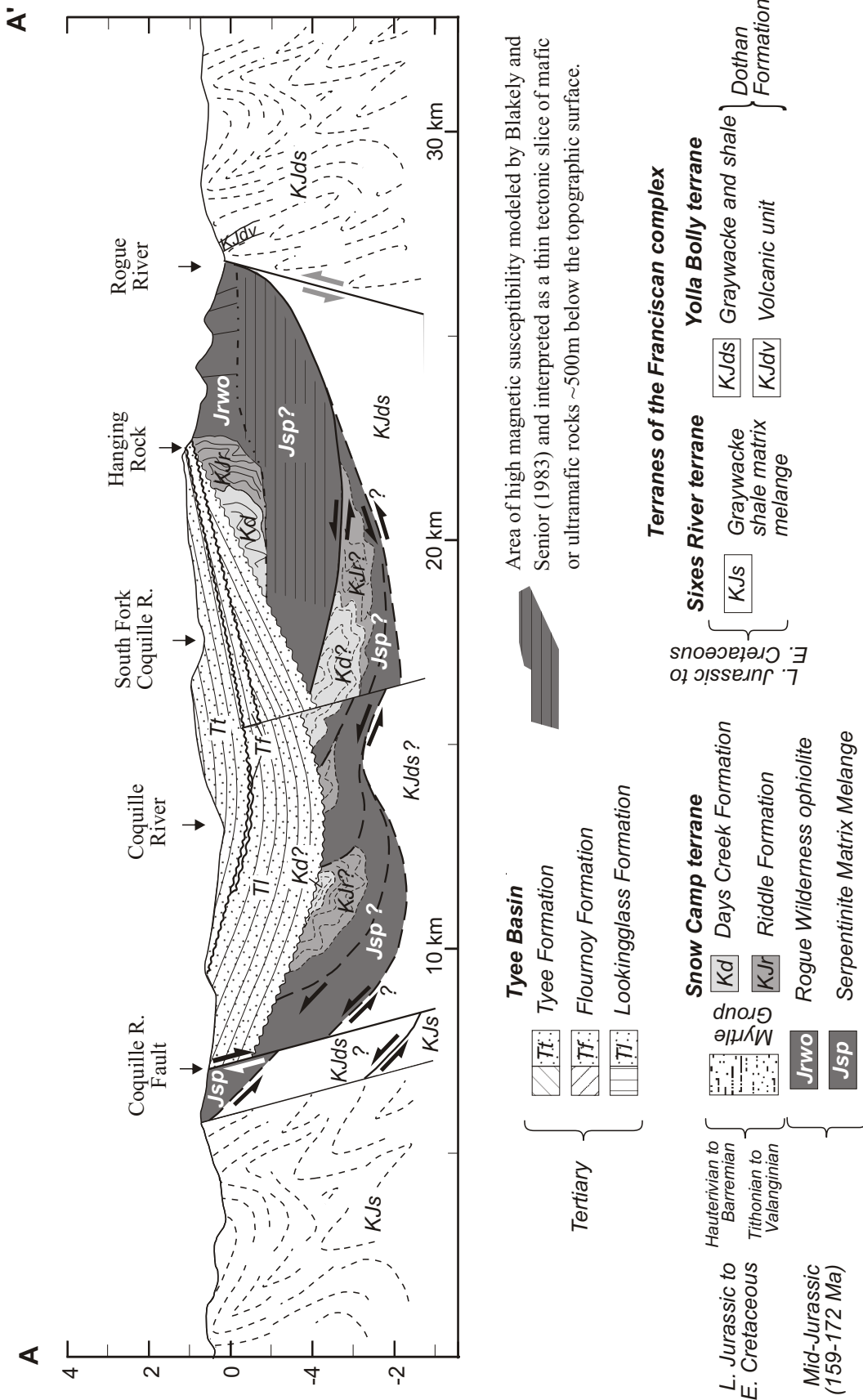
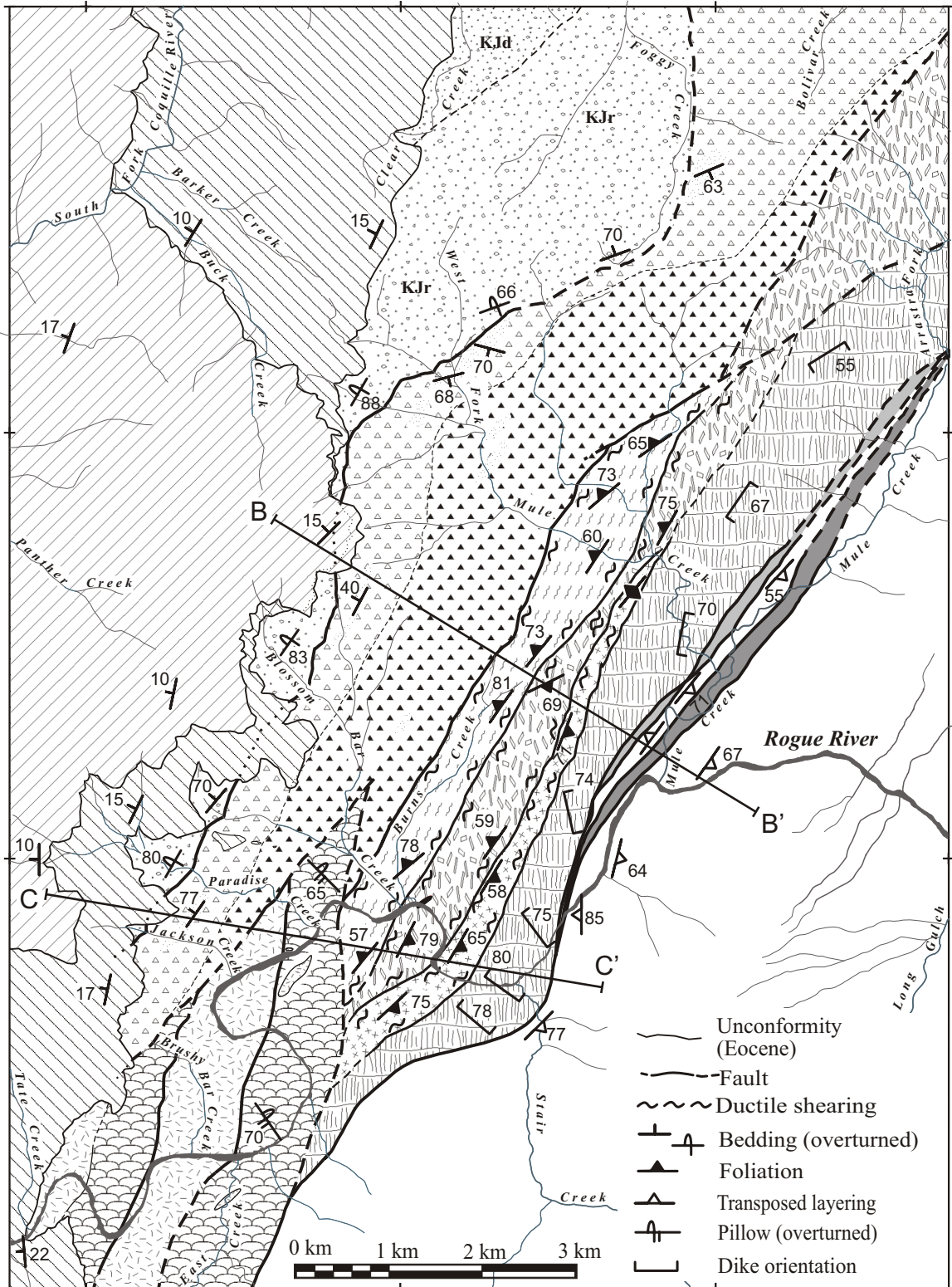


Figure 2.1b Cross section along line AA' (figure 2.1a)

Figure 2.2

- A. Simplified geologic map of the Wild Rogue Wilderness (see plate 1) showing mapped units and structural data. The Myrtle Group and its igneous basement are part of the Snow Camp terrane in SW Oregon. The Dothan Formation (Yolla Bolly terrane) is part of the Franciscan complex.
- B. Cross sections along lines BB' and CC' (figure 2.2a). Isotopic and fossil ages are given. Line BB' is subparallel to line AA' in figure 2.1a.



Tertiary	{		Tye and Flournoy Fms.	(Myrtle Group)
Late Jurassic - early Cretaceous	{		Days Creek & Riddle Fms.	
			Dothan Formation	
Late Jurassic	{		Blossom Bar shear zone	
			Half Moon Bar diorite	

Middle Jurassic - Late Jurassic	{		Mule Mountain volcanics
			Pillows
			Sheeted dikes
			Metatonalite
			Metagabbro

Figure 2.3

**Reconstruction of the
Rogue Wilderness ophiolite**

Columnar section showing likely reconstruction of ophiolitic units identified in the Wild Rogue Wilderness compared to a typical pseudostratigraphy (e.g., Penrose conference, 1972) of ophiolites shows only the middle and upper crustal section is preserved. The metagabbro unit may not be part of the ophiolite

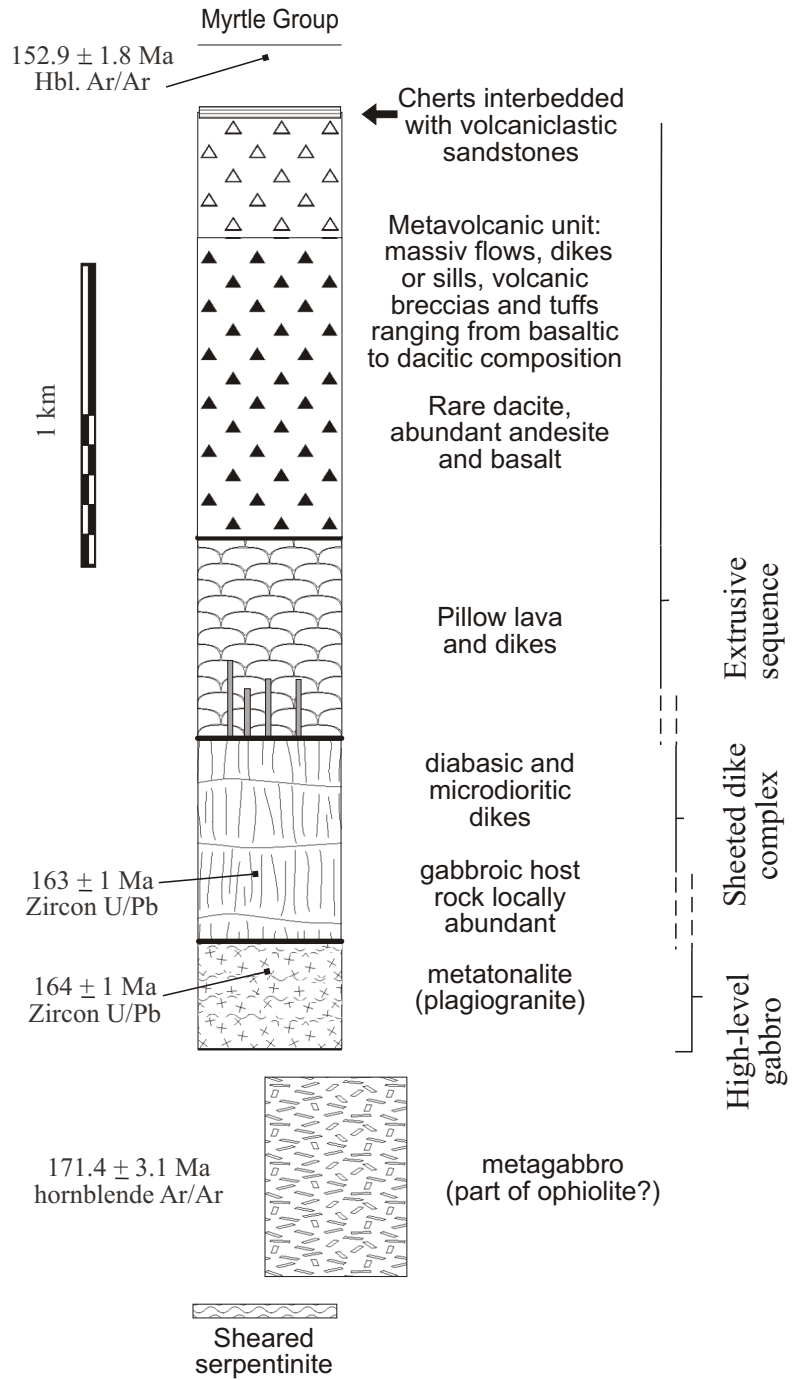




Figure 2.4

Photograph of typical medium grained gabbro of the metagabbro unit (O/C-385.1) containing abundant fine grained mafic enclaves. The enclaves and the host gabbro are very similar in composition and contain hornblende, calcic plagioclase, and accessory magnetite and apatite. The enclaves are elongate and aligned parallel to the magmatic flow foliation of the host gabbro. Two mineralized faults (cataclastic) cut the gabbro at moderate angles to the flow foliation (lower half of the photograph). The upper of the two faults developed within a 2 cm wide ductile shear band indicating a change from ductile to brittle deformation with decreasing temperature. The lens cap is 5.5 cm in diameter.

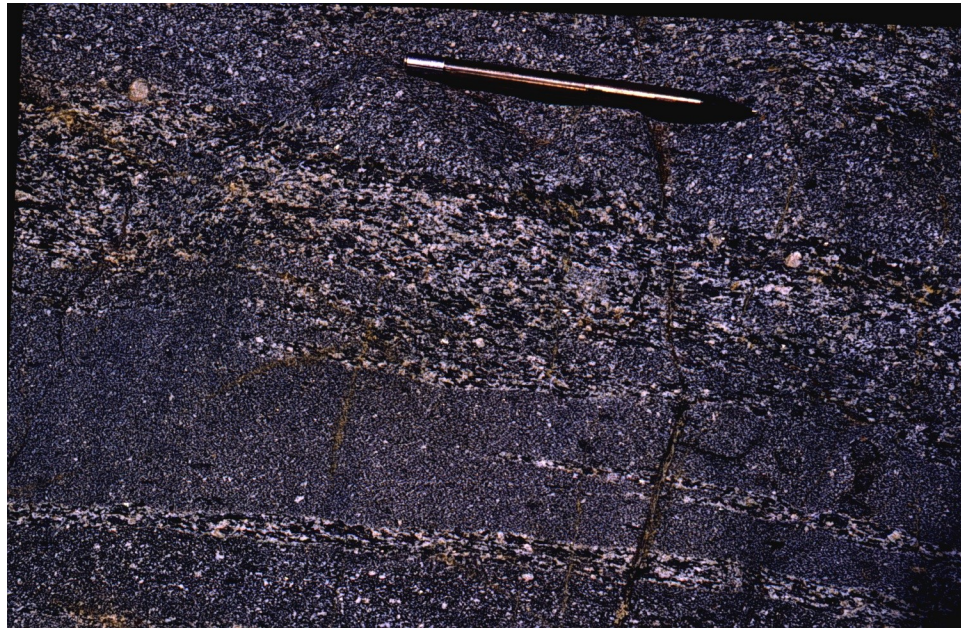


Figure 2.5

Close-up photograph of outcrop in metagabbro unit consisting mainly of mafic enclaves (O/C-385.2). The flow foliation in the fine grained enclaves is subparallel to that in the medium grained host gabbro. The terminations of the enclaves are pointed or wispy, and small selvages (~ 1 cm) occur within the medium grained gabbro. Overall, a continuum in shape of gabbroic enclaves exists ranging from deformed, dike-like intrusions to round and ellipsoidal enclaves (figure 2.4) and ultimately to thin, tabular or ellipsoidal selvages and schlieren (this photograph and figure 2.6). Note pen for scale.

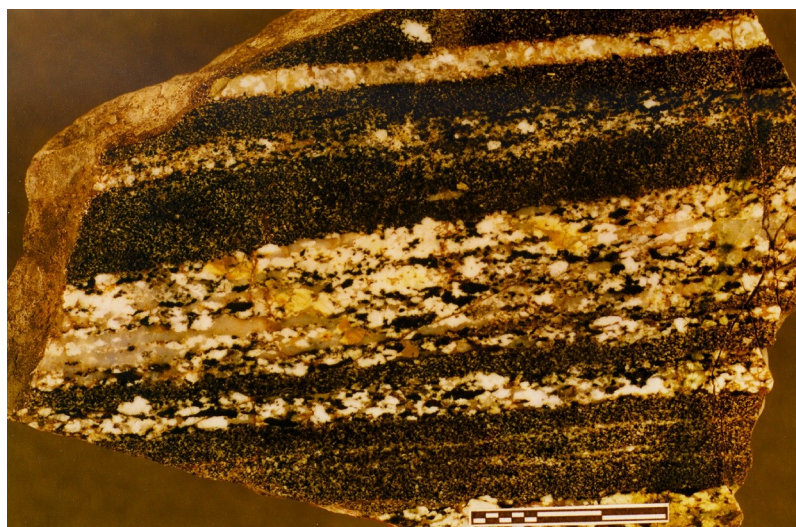


Figure 2.6

Photograph of compositionally layered metagabbro (GH-97-16b) characterized by laminae and lenses of fine-grained gabbro in medium-grained leucocratic quartz-gabbro and tonalite. The fine grained mafic metagabbro probably intruded the felsic fractionates of a plutonic suite ranging in composition from hornblende gabbro to tonalite-trondhjemite. Schlieren, thin tabular selvages and single crystals (arrow) of the felsic rock occur in the fine grained mafic layers. Tiny selvages (red outline) of mafic rock, occasionally consisting of only a few crystals, occur within the felsic laminae as well. Thus, mechanical mixing of felsic and mafic magma is inferred. Note also that the quartz grains are stretched, and dynamic recrystallization of quartz is evident in thin section. The magmatic flow foliation is clearly overprinted by solid-state deformation. The structures are interpreted as follows: the mafic magma intruded a crystal rich felsic magma as dikes, which was followed by attenuation and mixing due to magmatic flow resulting in a thinly banded rock. Later ductile shearing overprinted the magmatic foliation. The scale bar is 3 cm long.

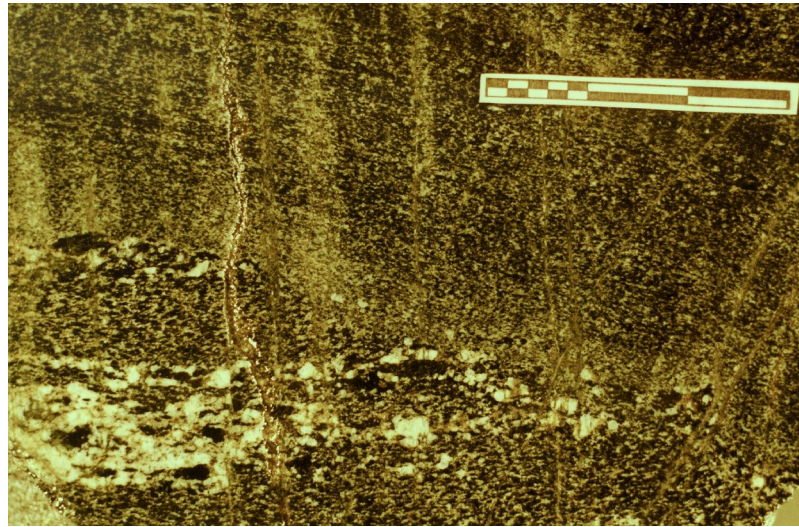


Figure 2.7

Photograph showing the relationship between three different phases of gabbro (O/C-374b) easily distinguishable by their grain size. The two oldest phases are the medium grained leuco-gabbro (largest grain size) and the mafic metagabbro (second largest grain size). Mixing of these two magmatic phases and magmatic flow produced the schlieren-type layering. Note that clusters of grains (red outline) or single grains of one phase can be found within the other. The gabbro with the schlieren-type layering was subsequently cut by a late mafic dike (smallest grain size) which has no chilled margins and a magmatic flow foliation subparallel to the host rock and. The alignment of the minerals in the late dike is likely due to continued magmatic deformation after dike intrusion. Single, coarse-grained crystals from the leuco-gabbro occur as xenocrysts in the mafic dike (arrow). The scale bar is 3 cm long.

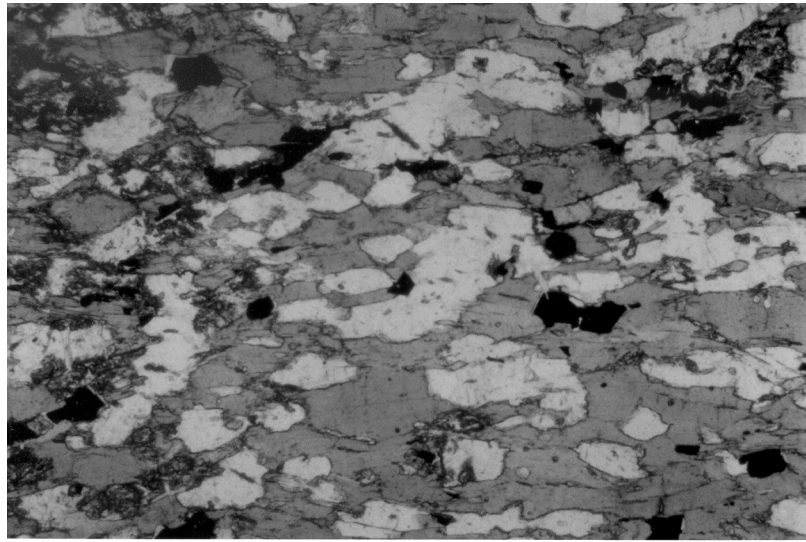


Figure 2.8

Photomicrograph of fine grained mafic dike in metagabbro (O/C-374b) showing typical texture and composition of gabbroic rocks in the metagabbro unit. Plagioclase is white, hornblende gray and magnetite black. Plagioclase and hornblende are aligned (crystal shape fabric) defining the foliation and range from anhedral to subhedral in shape. The width of the photograph is 2.14 mm.

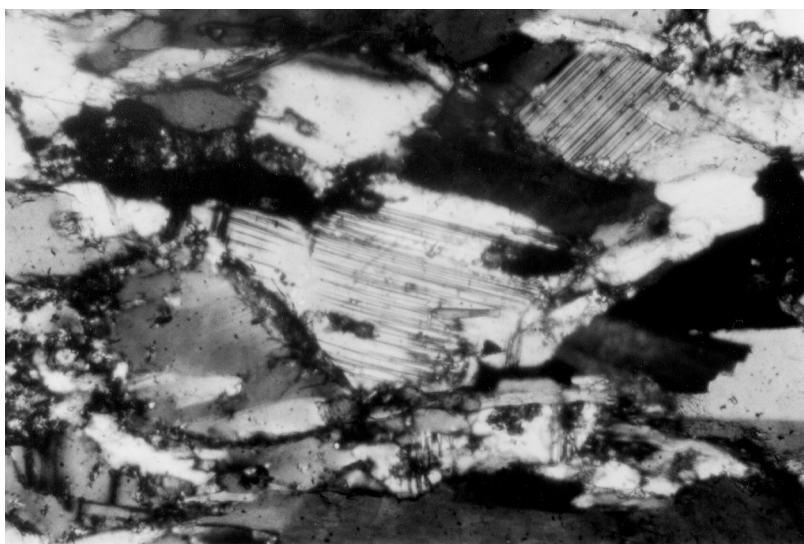


Figure 2.9

Photomicrograph of plagioclase in weakly foliated mafic dike in metagabbro (O/C-374b). Typically, plagioclase grains in most samples have tapering deformation twins. The wedge-shaped twins are thought to indicate temperatures of deformation between 300°C and 400°C (Passchier and Trouw, 1996, p.49). The width of the photograph is 0.54 mm.

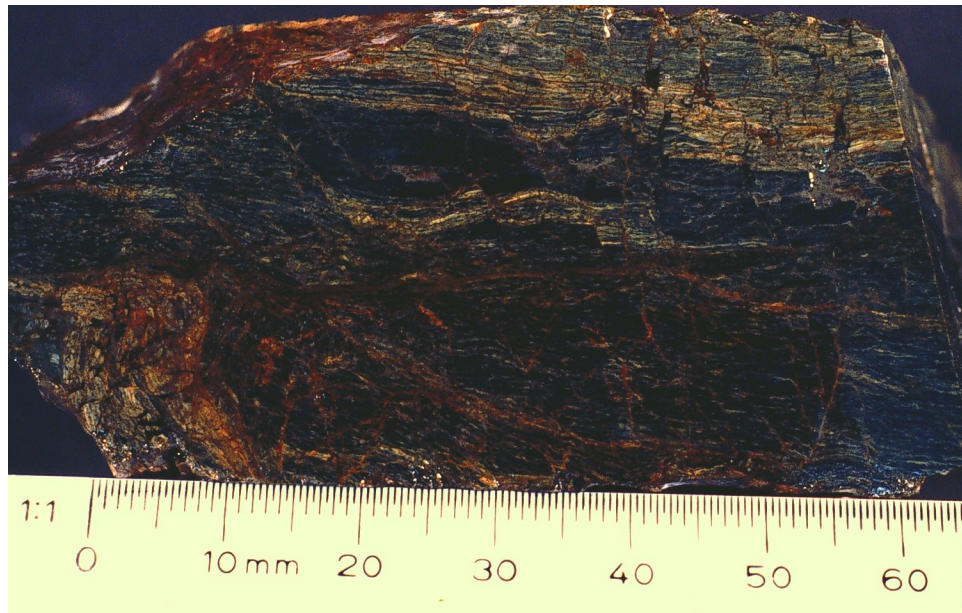


Figure 2.10

Photograph of slabbed and polished sample from a narrow (13cm) mylonite zone (O/C-13-S22.1) which is paralleled by a prominent mineralized fault in the metagabbro unit. Fracturing and cataclastic overprint of mylonites in the metagabbro unit is common. The sample is strongly foliated, and the extremely fine grain size compared to other gabbroic rocks indicates intense grain size reduction during solid-state deformation.



Figure 2.11

Photomicrograph of typical mylonitic metagabbro (from figure 2.10, O/C-13-S22.2) showing plagioclase and hornblende porphyroclasts in a fine grained matrix. Porphyroclasts are ovoid or augen-shaped and occasionally have tails. The matrix consists of fine hornblende and a range of greenschist facies minerals such as actinolite, chlorite, epidote, clinozoisite, and albite. The width of the photomicrograph is 2.14 mm.

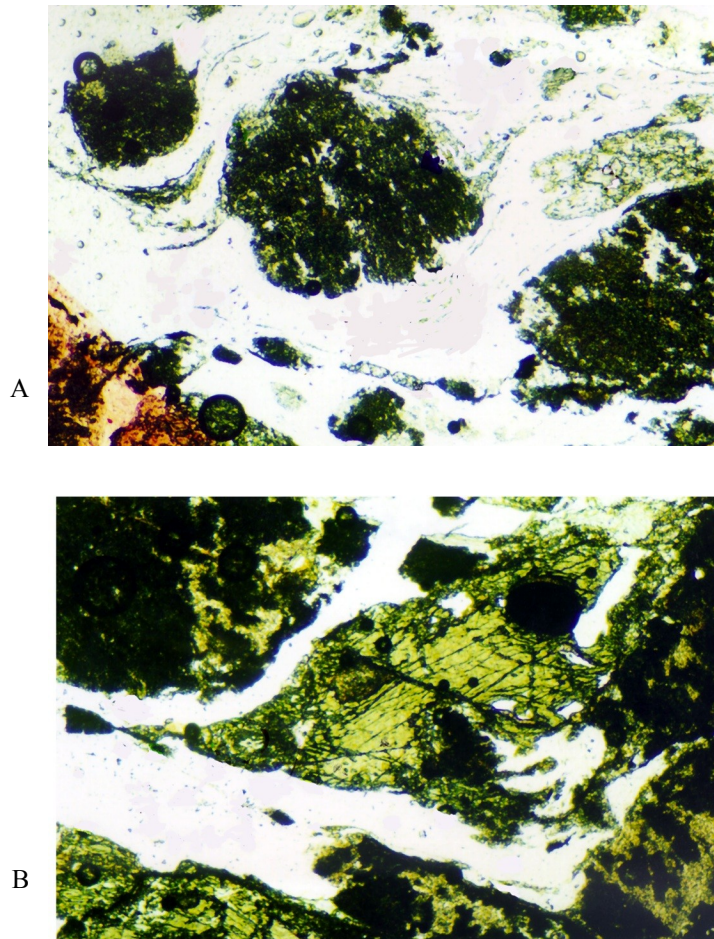


Figure 2.12

- A. Photomicrograph showing typical plagioclase porphyroclasts in quartz bearing rocks (O/C-13-S28) in the metagabbro unit. Plagioclase is completely replaced by a dark cloudy mass consisting of epidote or clinozoisite, chlorite and possibly albite. The matrix consists of very fine-grained, strongly recrystallized quartz. Grain size reduction of what used to be plagioclase probably occurred by abrasion during deformation. The height of the photograph is 2.14 mm. The sense of shear is dextral.
- B. Photomicrograph showing typical augen-shaped hornblende porphyroclast in quartz bearing rocks (O/C-13-S28) in the metagabbro unit. Hornblende is uniformly colored and the wings of these porphyroclasts consist of same-color hornblende as well as of epidote and chlorite. Epidote and chlorite occur also as alteration in fractures and cracks in hornblende. The height of the photograph is 2.14 mm. The sense of shear is dextral.

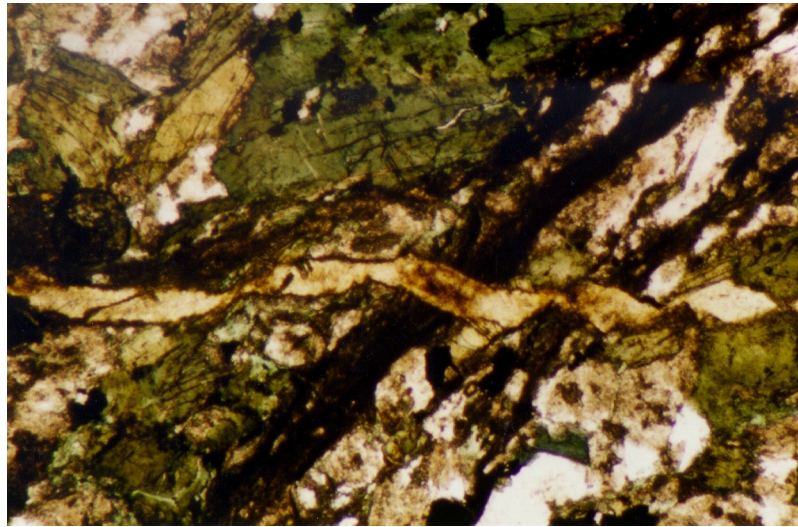


Figure 2.13

Photomicrograph showing a shear band cut by an epidote vein (ep). The dark cloudy mass in the shear band consists of very fine-grained chlorite and epidote. This sample (O/C-229) is from a section of hornblende-quartz diorite within the metatonalite unit and consists of variably colored hornblende (hbl), plagioclase (pl) and quartz (qz). The width of the photomicrograph is 2.14 mm.

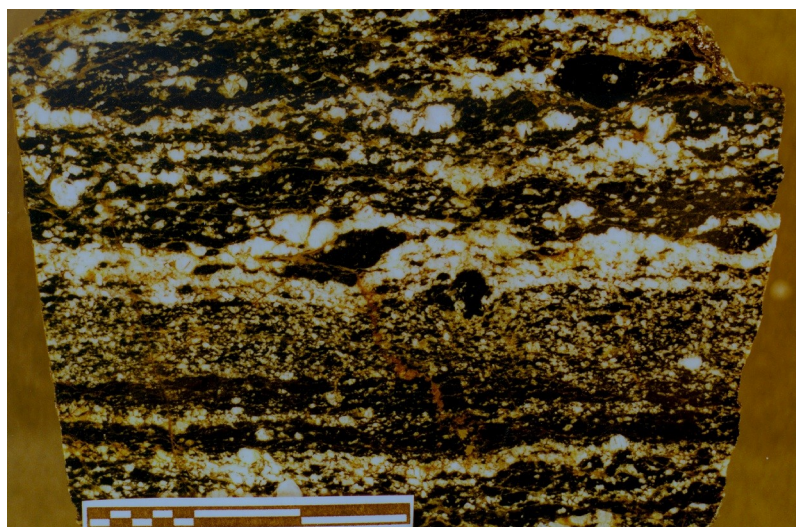


Figure 2.14

Slabbed and polished metagabbro protomylonite (O/C-371) from the shear zone between the metatonalite and metagabbro units (figures 2.2a and 2.2b). This photograph shows a typical, strongly foliated metagabbro having compositional banding. The lamination is similar to that of less deformed metagabbro and reflects the compositional variations in the metagabbro unit and is probably a primary igneous feature (i.e. magmatic flow) that was later overprinted by a tectonic foliation. Augen-shaped hornblende are common in rocks from this contact zone as well as stretched and fractured plagioclase crystals. The sense of shear is dextral. The scale bar is 3 cm long.



Figure 2.15

Photograph of prominent brittle fault with shear zone exposed at mile 46 at the Rogue River. The photograph is taken looking due north. The sharp contact is the brittle fault (the cliff is about 8 m high). Foliated metagabbro occurs to the left of the fault (northwest), and a 50 m wide ductile-brittle shear zone between the metagabbro unit and the metatonalite unit occurs to the right of the fault (southeast). The fault is subparallel to the shear foliation in the metagabbro to the left and the shear zone to the right of the fault. The 50 m wide shear zone to the right of the fault consists of strongly foliated and banded mylonitic rocks similar to the metagabbro unit (figure 2.14) and metatonalite unit (section 2.6.3). Epidosite mylonites become more abundant towards the metatonalite unit., and about 50 m southeast of this fault, only epidosite-mylonites typical of the metatonalite unit occur.

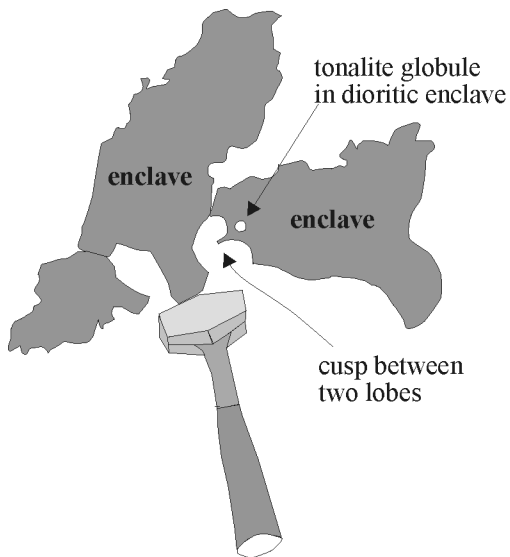
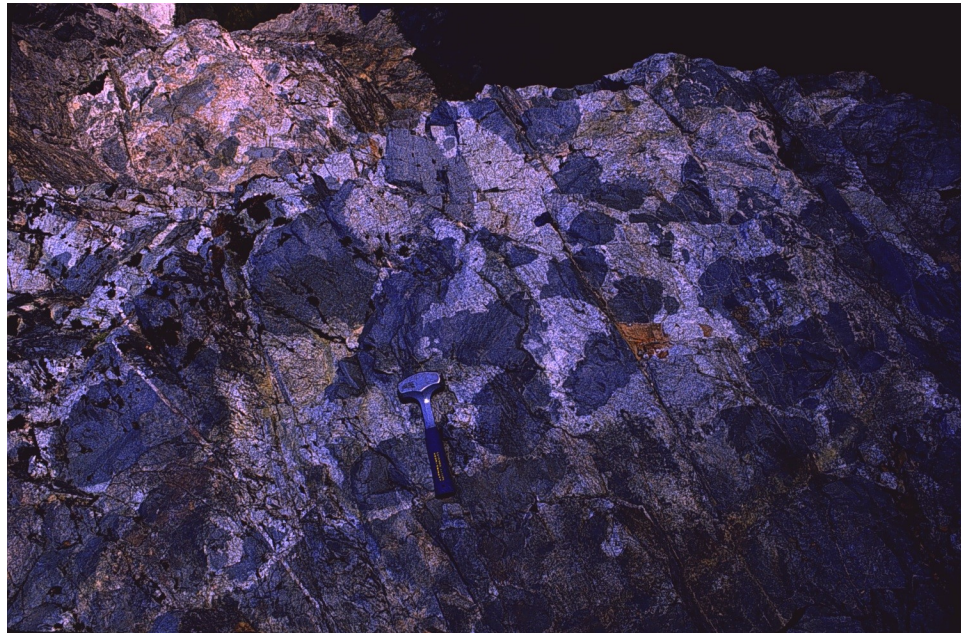


Figure 2.16

Photograph of metatonalite (light colored) and dioritic enclaves (dark) in O/C-10 at the Rogue River. Diorite enclaves in this outcrop become less abundant from bottom to top. Most of the enclaves in this outcrop appear to be angular. However, the enclaves are angular because of the cusped shapes of the enclave margins. Note the cusp between two concave lobes of the enclave margin. A small inclusion of tonalite occurs in the dioritic enclave. Other enclaves are globular and have lobate margins (figure 2.17). These features are interpreted as due to magma mingling.

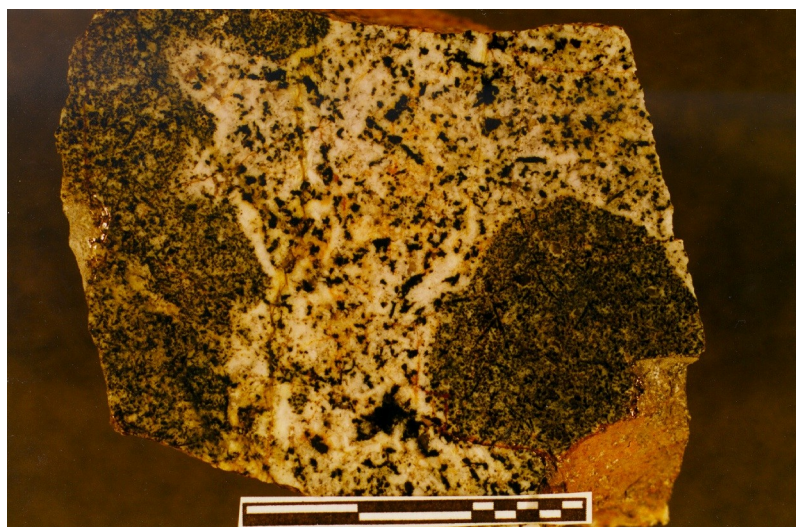


Figure 2.17

Slabbed and polished hand sample from the metatonalite unit (O/C-11) showing two globular fine-grained dioritic enclaves in medium-grained hornblende tonalite. Acicular hornblende similar to that of the hornblende tonalite occurs in the fine-grained diorite. Note that the enclave to the left has a lobate margin. Scale bar is 3 cm.

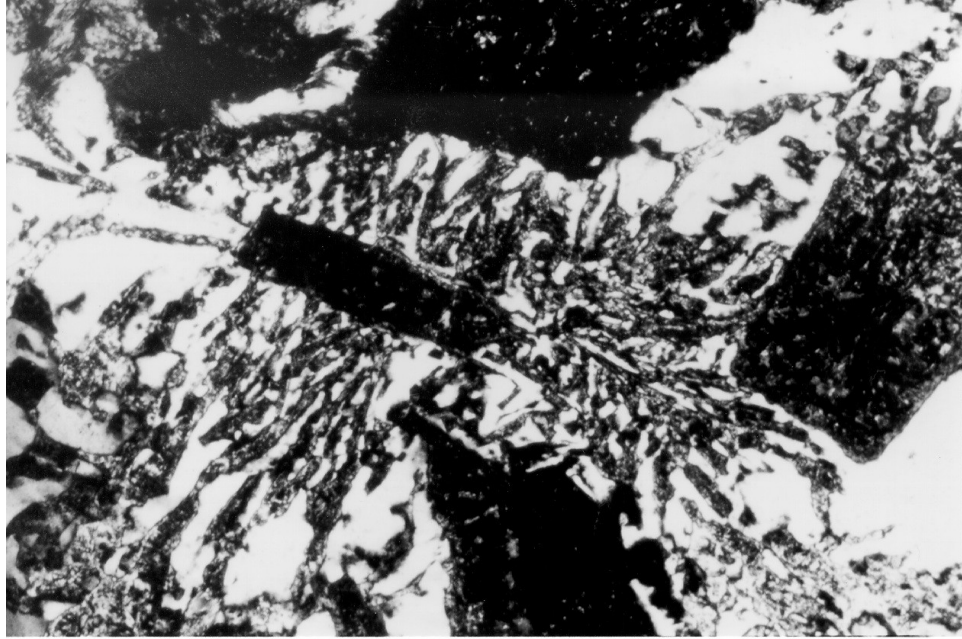


Figure 2.18

Plane light microphotograph of granophyric texture in metatonalite (O/C-368G). Plagioclase in this microphotograph is dark gray to black (cloudy masses of cz or ep + ab \pm chl \pm musc) and quartz is white. Radiate intergrowths of quartz and feldspar arranged about euhedral plagioclase crystals is common. The width of the microphotograph is 2.14 mm.



Figure 2.19

Photograph of a zone of strongly foliated rock within the metatonalite unit. These rocks are characterized by extremely fine grain sizes, tightly spaced foliation and compositional (color) banding. The color of the mylonites is highly variable; they are bright white, beige, pistachios green, bluish-green, dark-green, gray-green, and rust-brown, depending on strain, composition of protolith, and weathering. The lens cap is 5.5 cm in diameter.



Figure 2.20

Photomicrograph showing fabric of typical mylonite (type 1) in the metatonalite unit. Porphyroclasts are epidote and saussuritized plagioclase. Only few large quartz grains are preserved in quartz-rich layers. Typically, quartz porphyroclasts are stretched, contain subgrains and/or show undulatory extinction and laterally grade into strongly recrystallized quartz. The foliation is characterized by quartz ± albite ribbons (clear) that alternate with laminae consisting of fine grained mineral aggregates (dark-green layers) which include mainly ep or cz, but may also include ac, chl, pr, musc, pu(?). The foliation wraps around porphyroclasts. The width of the photograph is 6 mm.

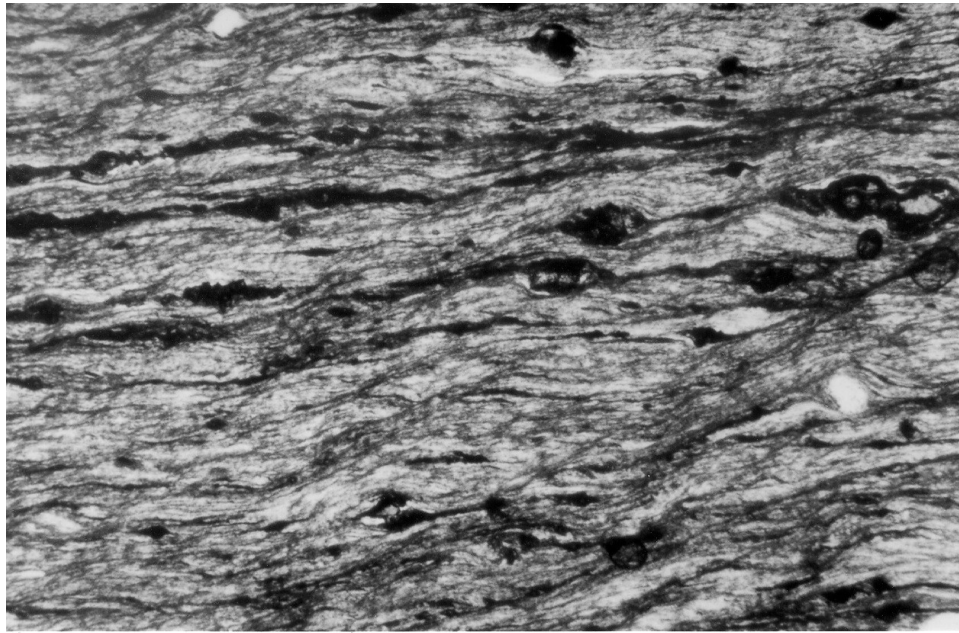


Figure 2.21

Photomicrograph showing fabric of typical mylonite (type 2) in the metatonalite unit. Porphyroclasts consists of saussuritized plagioclase, epidote and quartz. The foliation is characterized by cleavage domains rich in chlorite (dark gray) separating microlithons rich in recrystallized quartz (light gray/cloudy). Elongate microlithons define the foliation (C). Asymmetrical extensional shear bands (C') consisting mainly of chlorite typically form in type-2 mylonites. Grain size reduction of epidote porphyroclasts results in planar, discontinuous layers consisting of epidote fragments (black, discontinuous layers). The cloudy appearance of microlithons in thin section is due to abundant disseminated alteration phases. The width of the photograph is 2.14 mm.



Figure 2.22

Photomicrograph of porphyroblast of albite (center) occurring in a matrix of recrystallized quartz (metatonalite unit, O/C-9-S12). The largest albite fragment shows a Carlsbad twin as well as undulatory and patchy extinction. It seems as if albite consists of several subgrains. The large, twinned fragment is surrounded by numerous smaller albite fragments in a matrix of recrystallized quartz. Possibly, a fine grained albite-quartz mixture forms with progressive deformation. Although the undulatory extinction and formation of subgrains could be due to dislocation glide, abundant microscopic cracks and fractures in albite are consistent with predominantly cataclastic deformation of albite in a matrix of quartz, indicating relatively low temperatures of deformation (<450C). The width of the photograph is 0.6 mm.

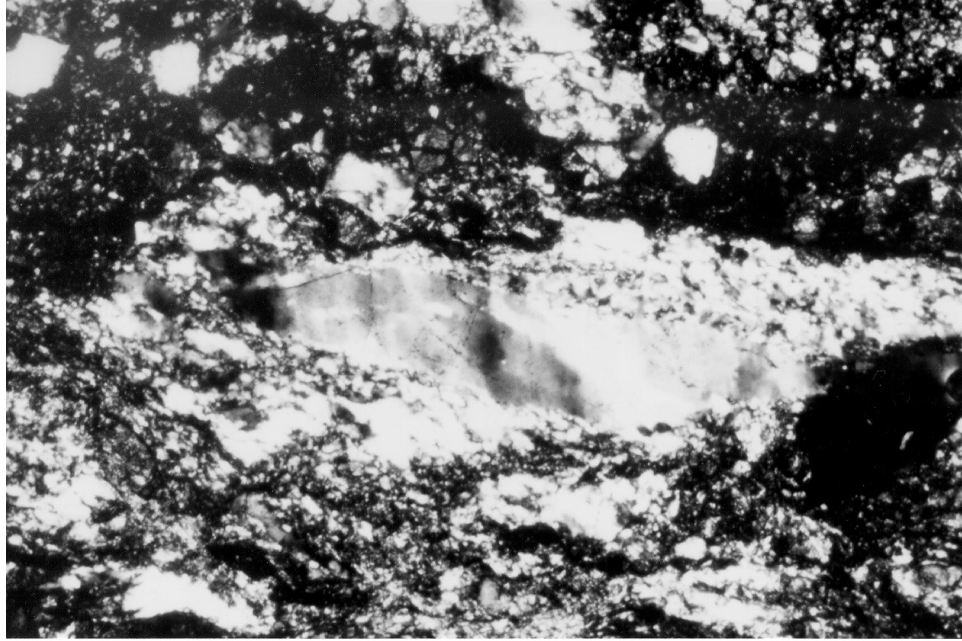


Figure 2.23

Photomicrograph of large, relic quartz grain in a monomineralic layer of quartz showing several subgrains and undulose extinction. Note that the relic quartz grain passes laterally into domains of small, dynamically recrystallized grains. This indicates that the temperature of deformation was high enough for climb assisted dislocation glide allowing subgrain rotation recrystallization. The width of the photograph is 2.14 mm.



Figure 2.24

Photograph of outcrop (facing north) showing the brittle fault contact (in steep shadow) between the metatonalite unit (west) and the sheeted dike complex (east). The metatonalite has a mylonitic foliation subparallel to the fault, whereas the sheeted dike complex within 15 m of the fault is heavily fractured and brecciated. The fault breccia is cemented by epidote and quartz. Also, this fault breccia is cut by prehnite veins. Other secondary minerals include chlorite and sulfide.

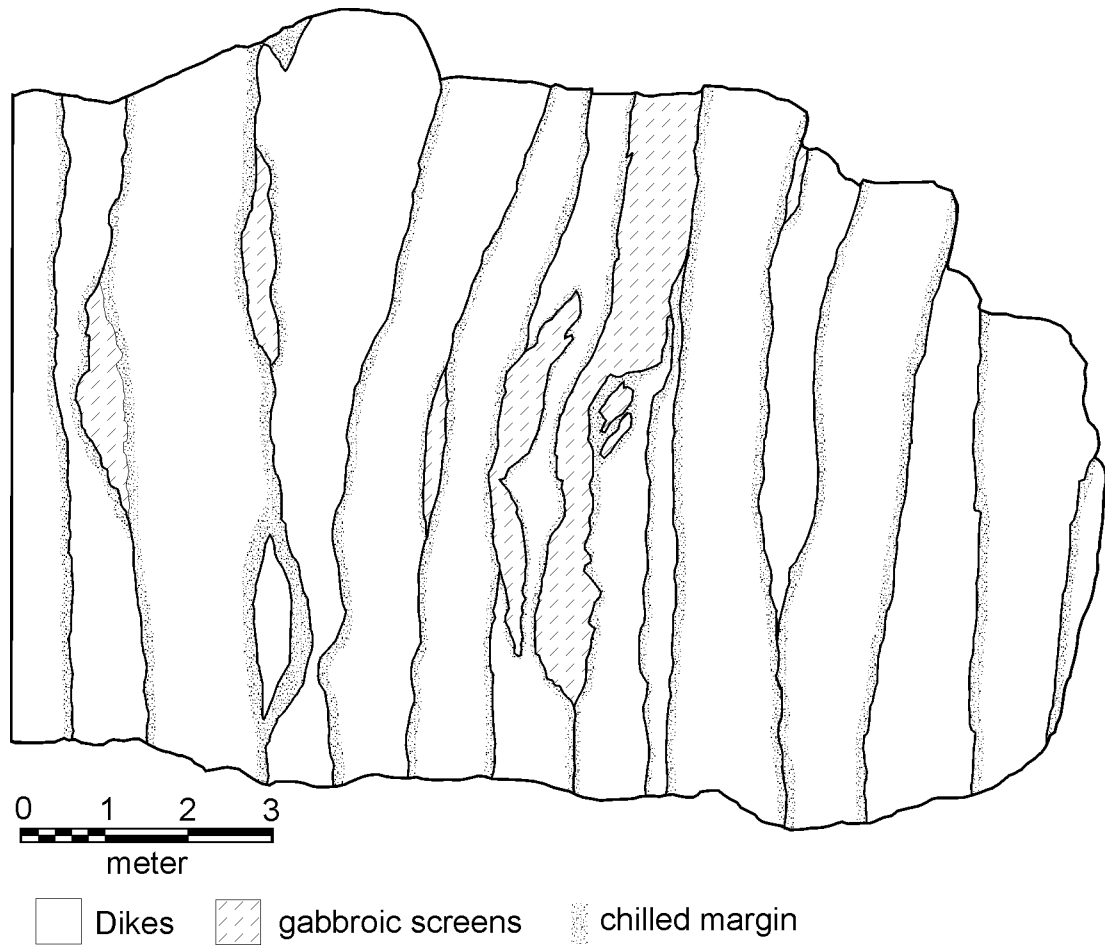


Figure 2.25

Outcrop map of sheeted dikes in the Rogue River canyon near Stair Creek falls shows the typical relationships between dikes and gabbroic screens. This map is traced from a photograph taken from opposite canyon wall. The vertical cliff faces NW perpendicular to the strike of the dikes. In this randomly selected section of sheeted dikes, nine chilled margins face NE whereas only six face SW. Ramp and Gray (1981) also reported that the number of chilled margins is greater on the northeast side.

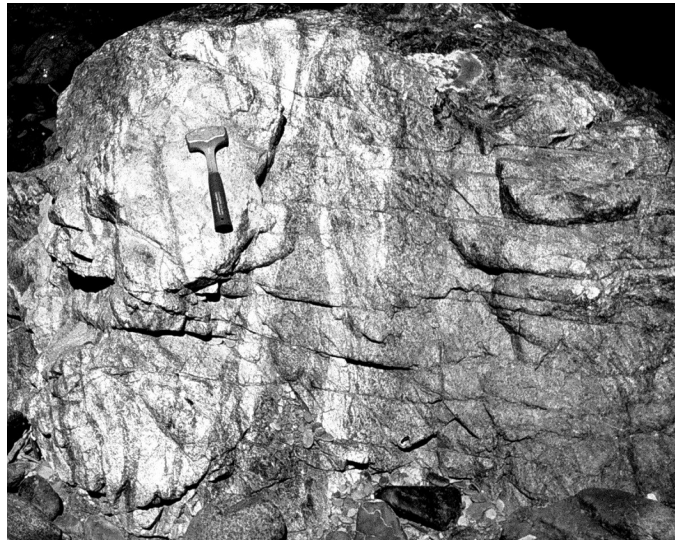


Figure 2.26

Photograph of layered cumulate gabbro seen in the sheeted dike complex on the Rogue River near Stair Creek Falls. This photograph shows irregular leucocratic (anorthosite) layers and laminae in a fine grained plag-cpx cumulate gabbro. Many screens contain irregular layers and lenses of anorthosite with occasional ultramafic rims. Note hammer for scale.



Figure 2.27

Layered cumulate gabbro in sheeted dike complex near the Coffee Pot (whirlpool on the Rogue River above Stair Creek falls). This photograph was taken looking northwest and shows wispy leucocratic layers and laminae in a fine grained plag-cpx cumulate gabbro cut by a chilled dike. The mafic dike to the right cuts the layering at a high angle. Note that the epidote vein having an amphibole alteration halo (2cm right of the knife) is truncated by the dike. All structures are cut and offset by a epidote + quartz vein (fault) located 4 cm above the knife. The length of the knife is 10 cm.

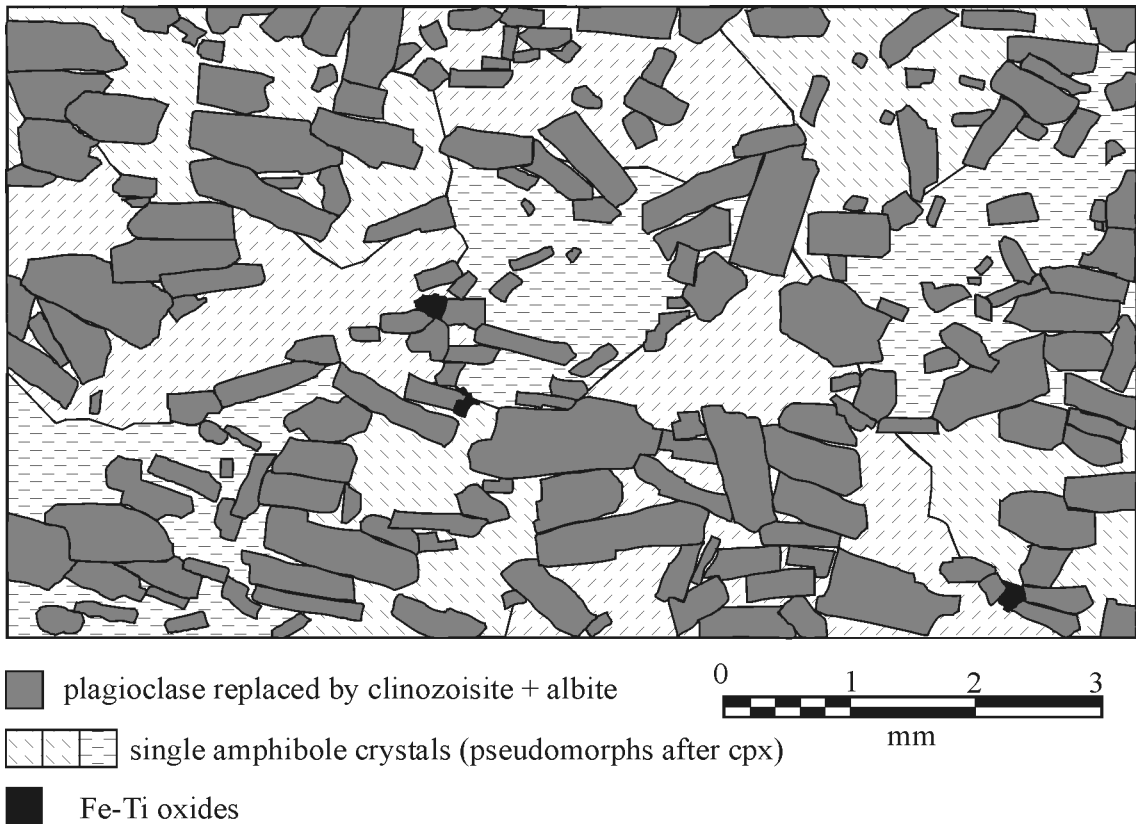


Figure 2.28

Part of thin section was traced to show relict igneous texture of cumulate gabbro (O/C-360). Subhedral plagioclase is poikilitically enclosed in much larger pyroxene oikocrysts, the latter are replaced by patchy and pale green amphibole often containing small specks of opaque minerals. The plagioclase displays a weak preferred orientation defining the planar lamination of the cumulate gabbro.

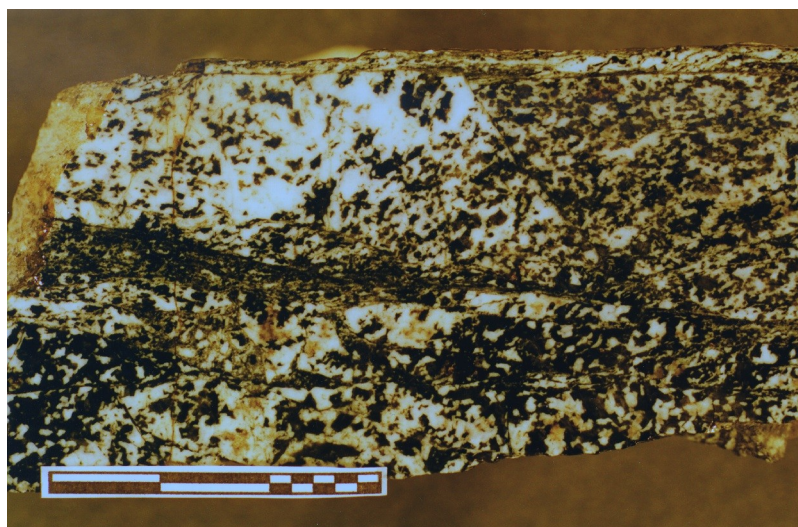


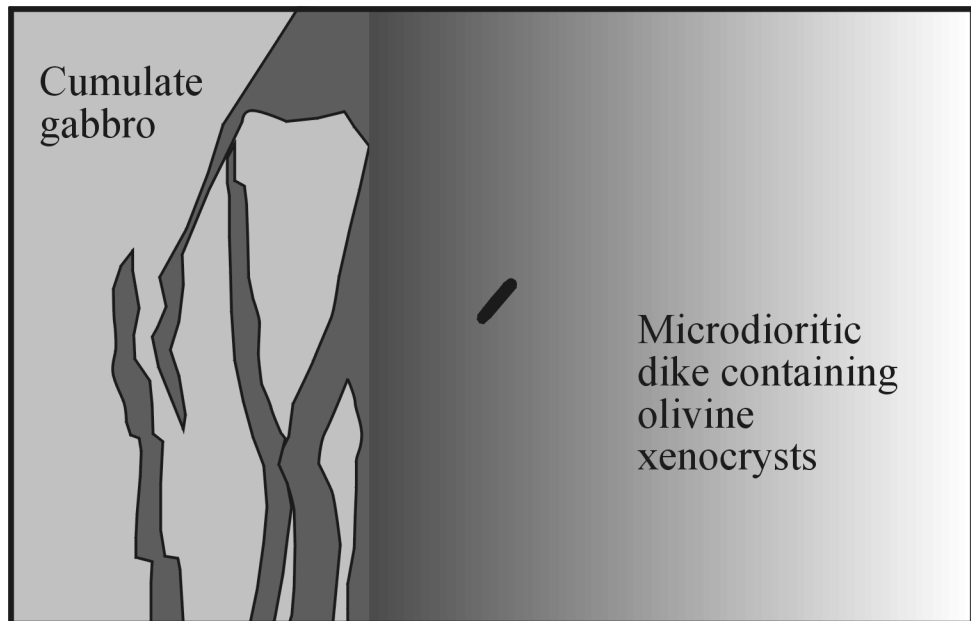
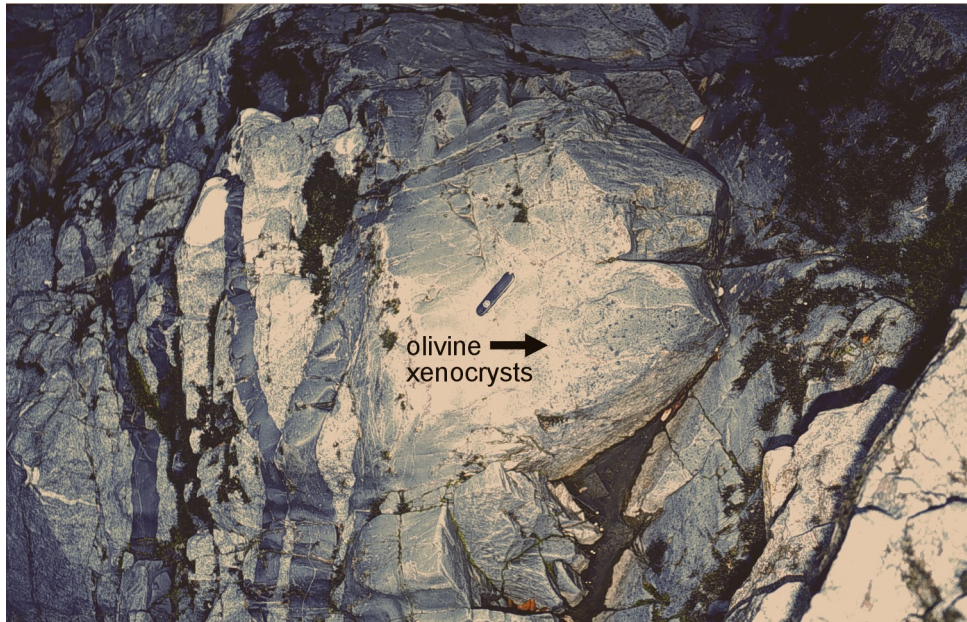
Figure 2.29

Photograph of polished hand sample showing a narrow shear band in cumulate gabbro. The shear bands probably formed at high temperature as indicated by deformed amphibole forming in the shear bands. They occur at high angles with respect to the layering in cumulate gabbro. Also, the shear bands are only found in gabbroic screens and are cut by dikes. Scale bar is 3 cm.

Figure 2.30

Photograph of a quartz-bearing dike of group two intruding a gabbroic host rock (O/C-4-S3). The main dike contains a small domain rich in olivine xenocrysts (right and above knife) whereas the remainder of the dike is almost devoid of olivine xenocrysts. The small dikes fed by the main intrusion are actually completely free of olivine xenocrysts. Unfortunately, such narrow, xenocryst-free dikes of group 2 can rarely be traced to a large dike intrusion with clearly identifiable interstitial quartz and/or olivine xenocrysts. Most of the time, they are indistinguishable in the field from phenocryst-free dikes of group 1. The chaotic distribution of olivine xenocrysts in quartz-bearing microdioritic dikes may indicate turbulent flow and/or magma mixing. The microdioritic dike shown in this photograph intrudes dikes of group 1 about 6 m above this outcrop.

The knife is 10 cm long.



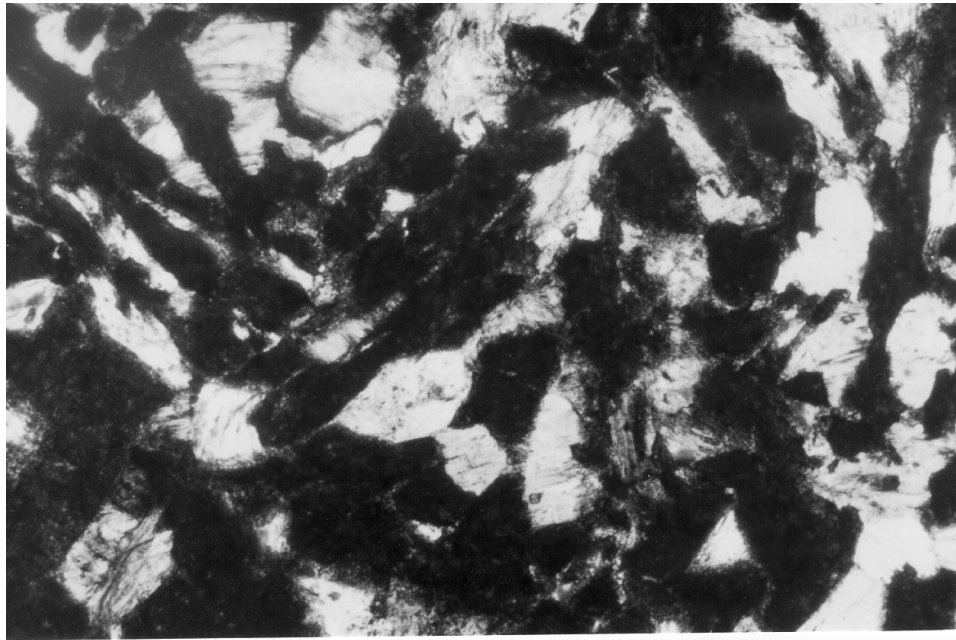


Figure 2.31

Photomicrograph showing texture typical of aphyric diabasic dikes (O/C-58) in the sheeted dike complex of the Rogue Wilderness remnant of the CRO. Clinopyroxene replaced by pale to light green amphibole (white in b/w photograph) is subophitically intergrown with laths of plagioclase pseudomorphed by a cloudy, dark mass consisting of clinozoisite + albite \pm chlorite \pm mica (almost black in b/w photograph). The width of the photograph is 2.16 mm.

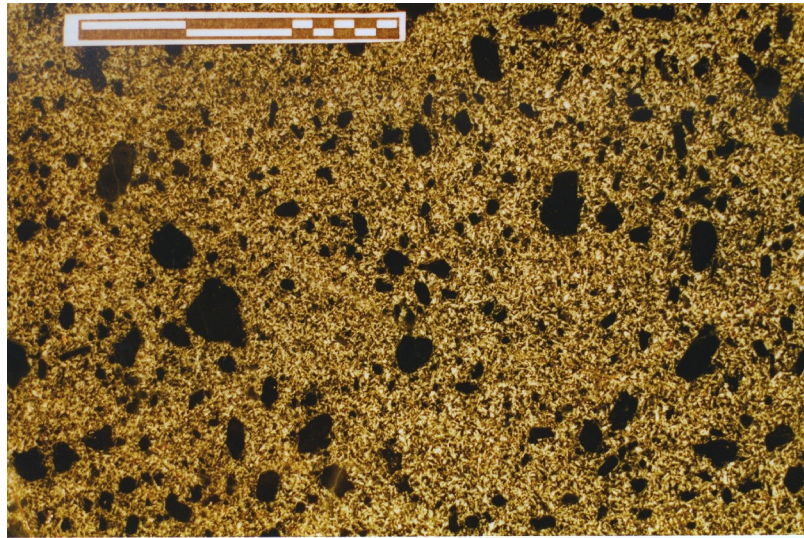


Figure 2.32

Slabbed and polished sample (O/C-4-S3) of a microdioritic dike having abundant olivine xenocrysts (pseudomorphed). The sampled dike consists of several irregular domains (figure 2.30): xenocryst rich parts within the dike contain no or little quartz and have subophitic texture whereas areas without xenocrysts have up to 12% interstitial quartz and hypidiomorphic granular texture. The irregular and heterogeneous distribution of the xenocrysts in a compositionally and texturally variable dike suggests mixing of magmas. The scale bar is 3 cm long.

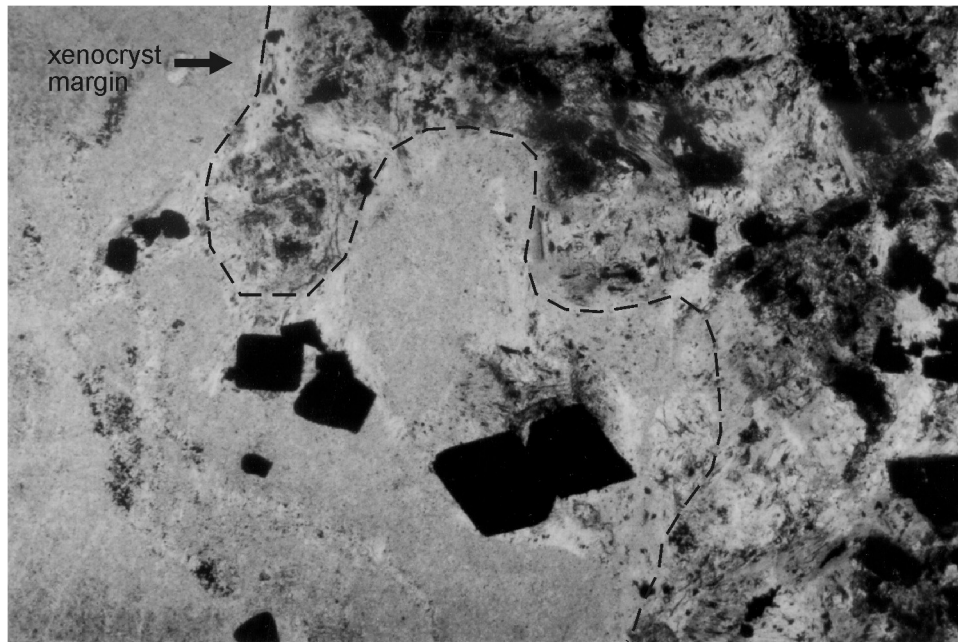


Figure 2.33

Photomicrograph showing translucent brown Cr-spinel (large black diamonds in b/w photograph) in partially resorbed olivine xenocryst (O/C-4-S3b). The resorption of the olivine xenocrysts may result in Cr-spinel crystals occurring in the ground mass (Cr-Spinel in matrix not shown). The ground mass consists of pyroxene and plagioclase; pyroxene is replaced by pale, fibrous amphibole (light gray, cloudy) whereas the dark-gray to black, cloudy masses represent plagioclase replaced by clinozoisite + albite ± chlorite ± mica. In this thin section, interstitial quartz is not present. Few percent of Fe-Ti oxides are present as well (small black minerals in the matrix). The width of the photograph is 2.16 mm.



Figure 2.34

Photograph of an exposed fault surface with patches of pistachio green ep+qtz mineralization. Recent abrasion by cobbles along the bank of the Rogue River left these small patches of epidote on the fault surface. White prehnite + quartz veins cut the fault at high angles suggesting retrograde conditions during deformation. The pen is 14 cm long.



Figure 2.35

Photograph of one of several faults across which an abrupt change in dike orientations was observed at the Rogue River section of the sheeted dike complex. The distinctly different orientation of dikes across a large fault zone suggests rotation of fault blocks during deformation. This fault is cemented by quartz and sulfide. The weathering color of the fault is rust brown.



Figure 2.36

Photograph of water polished outcrop near Paradise Bar on the Rogue River just above the summer water-level. Interpillow material is eroded out, and the round and subspherical shapes of the pillows are exceptionally well-exposed. Just few meters above this outcrop (above winter water-level), the pillow-shapes are not identifiable because of poor exposure and strong weathering.



Figure 2.37

Photograph of pillow exposed in Huggins Canyon (O/C-228). The interpillow material in this outcrop is completely recrystallized and consists of epidote+quartz±chlorite (epidosite). The veins, possibly representing cooling fractures, contain epidote and quartz. Vesicles in this pillow occur in the dark rim (originally glassy) and are filled with prehnite+quartz or quartz±chlorite (white amygdules). Only a few meters downstream of this outcrop, chert occurs in the interpillow matrix suggesting abyssal conditions of eruption. Vesicles occurring in glassy rims of pillows that erupted at considerable water depth indicate high volatile content of the magma (e.g. Harper, 1982).

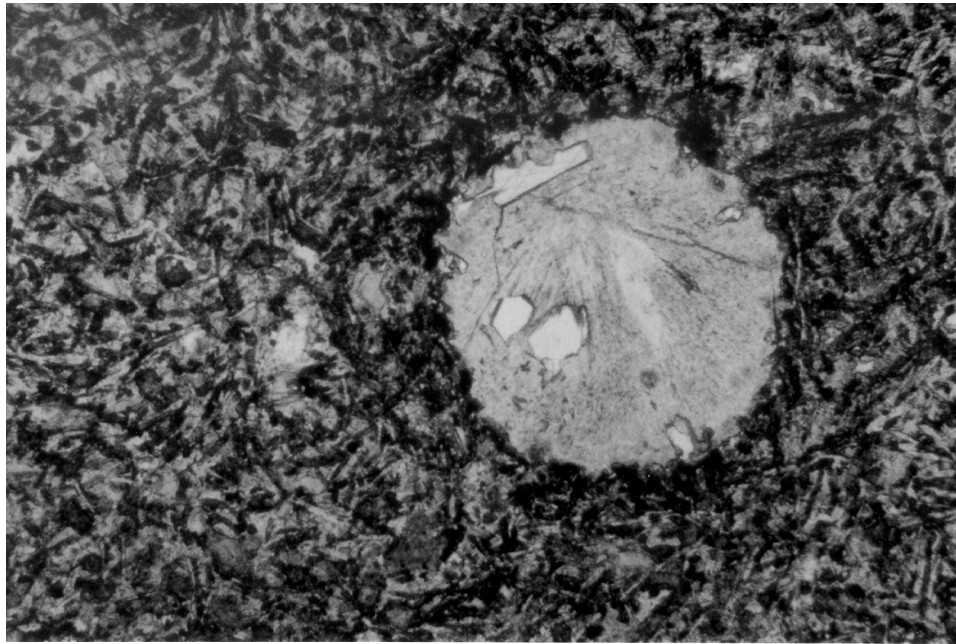


Figure 2.38

Photomicrograph of center of pillow (O/C-227A) showing typical intergranular (intersertal?) texture of pillows away from chilled margins. Laths of plagioclase and clinopyroxene as well as the interstitial matrix are partially to completely replaced obscuring much of the original texture. The metamorphic assemblage in the pillows includes albite + chlorite + epidote + titanite + quartz \pm actinolite \pm pumpellyite \pm prehnite \pm muscovite \pm calcite. Few vesicles occur in the centers of most pillows. The vesicle is filled with radiating epidote, quartz and disseminated flakes of chlorite. The width of the photomicrograph is 2.14 mm.



Figure 2.39

Photomicrograph of granophyric texture in dikes intruding pillows (O/C-226a). These dikes are indistinguishable in color from the pillows and appear to be mafic at first glance. However, they contain up to 10% primary quartz which is either intergrown with plagioclase and/or occurs as late, interstitial phase between laths of plagioclase and clinopyroxene. Similar to the granophyric texture in samples from the metatonalite unit (figure 2.18), radiate intergrowth of quartz and plagioclase are arranged about euhedral, equant plagioclase crystals. The width of the photomicrograph is 2.14 mm.



Figure 2.40

Photograph of leucocratic dike in the pillow unit near Brushy Bar (O/C-231). These light colored dikes consist essentially of plagioclase and quartz, are porphyritic (15-20% plag, 5-10% qtz and $\ll 1\%$ cpx phenocrysts) and contain a similar metamorphic assemblage as the pillows (ab, ep, chl, pr, pu). The width of the dikes is highly variable ranging from few centimeters to 2 meters. Note hammer for scale.

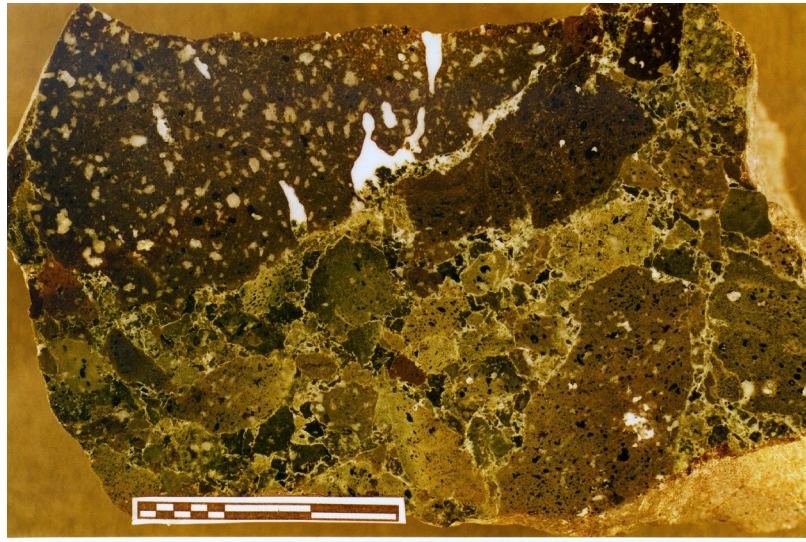


Figure 2.41

Photograph of slabbed and polished hand sample of typical breccia in the Mule Mountain volcanic unit. Volcanic flow rocks of basaltic to andesitic composition are intercalated with these volcanic breccias. The fragments are angular to subangular in shape and consist of volcanic rocks of various composition as well as broken phenocrysts. The color of the volcanic rocks is primarily determined by the secondary mineral assemblage. Reddish or purplish brown colors indicate abundant disseminated hematite whereas green colors correlate with abundant chlorite and epidote. The fragments with different colors in this breccia suggest that they were derived from a volcanic source characterized by heterogeneous alteration. Transport and redeposition of fragments must have occurred after the heterogeneous alteration of the volcanic rocks. The scale bar is 3 cm long.

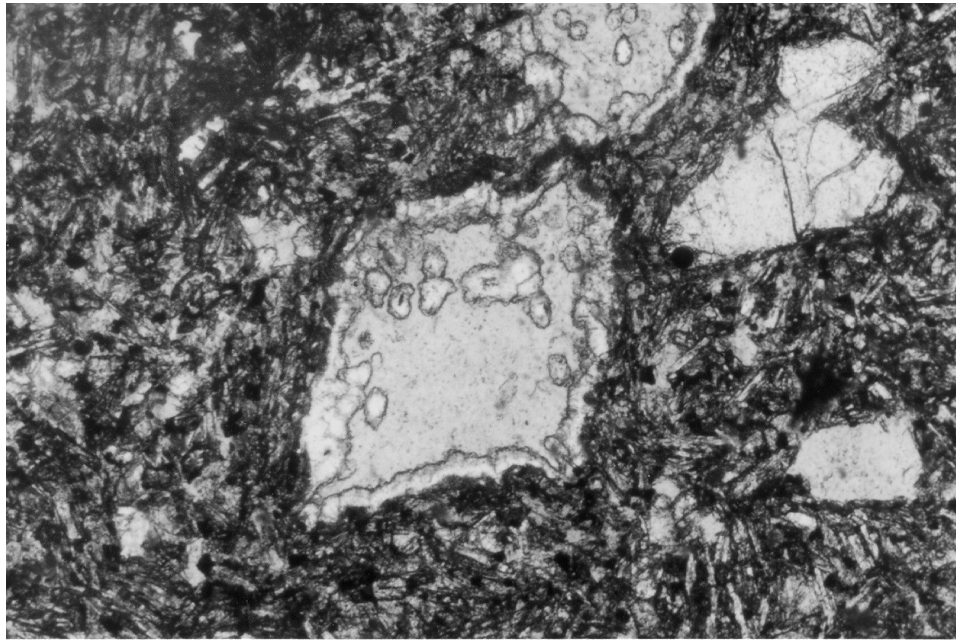


Figure 2.42

Photomicrograph of the intergranular texture of the basalt sample O/C-81a. The matrix is composed of lath-shaped, euhedral plagioclase, subhedral to anhedral augite and Fe-Ti oxides. Two phenocrysts of unaltered clinopyroxene (augite) are shown to the right and two larger olivine pseudomorphs consisting of quartz and chlorite in the center. Alteration and replacement of igneous phases by a wide range of secondary minerals is common. Clinopyroxene is relatively well-preserved. The width of the photomicrograph is 2.14 mm.

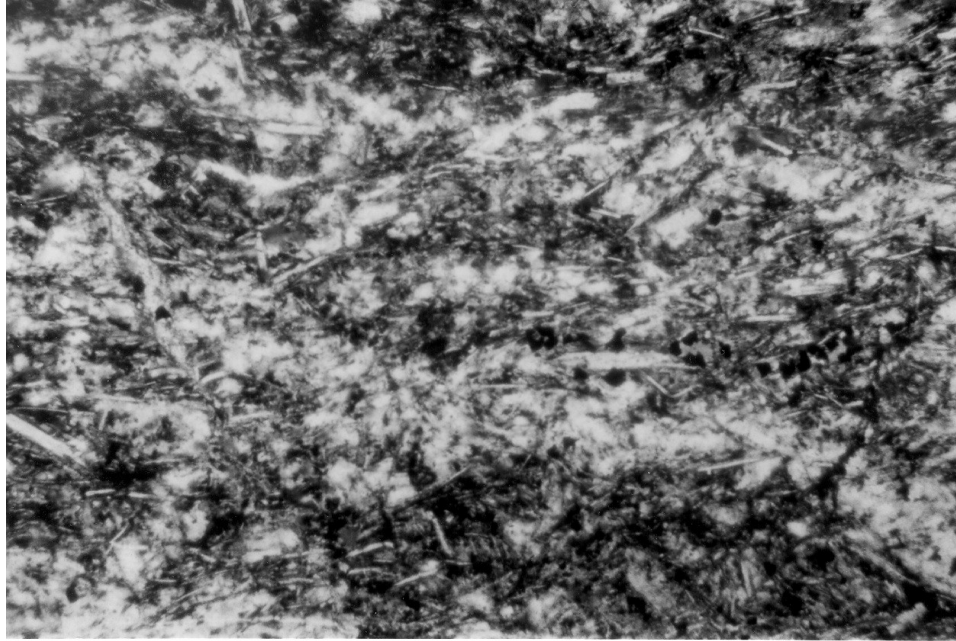


Figure 2.43

Photomicrograph of the trachytic texture of an aphyric andesitic sample in the Mule Mountain volcanics (O/C-186). Acicular and lath-shaped plagioclase are aligned and have the tendency to be arranged in bands. Note the two lighter colored bands stretching from left to right. Other matrix components include granular pyroxene, Fe-Ti oxides and a wide range of secondary minerals such as chlorite (replacing glass), albite, epidote, quartz, prehnite, and hematite. The width of the photomicrograph is 0.6 mm.

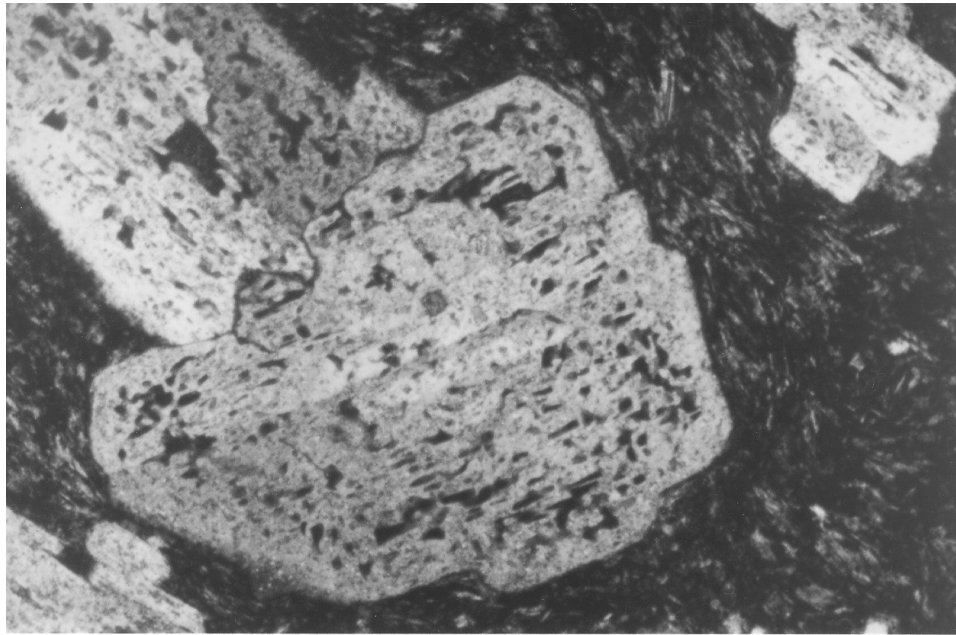


Figure 2.44

Photomicrograph of plagioclase phenocryst in dacitic sample from the Mule Mountain volcanics (GDH-2b). The twinned plagioclase phenocrysts contain abundant inclusions of chlorite probably replacing glass (crossed Nicols). The width of the photograph is 2.14 mm.



Figure 2.45

Photograph of sedimentary rocks exposed on the 4WD road leading to the Golden Bullet (Old Red) Mine in the Wild Rogue Wilderness. Layers range from about 1 cm to 20 cm in thickness and are thinly laminated. The clastic component is extremely fine grained (mud), and can be up to 0.8 mm in size (sand) and is probably of volcanogenic origin. Occasionally, the thin laminae contain radiolarians in an extremely fine grained matrix suggesting deep ocean deposition. A polished hand sample from this outcrop shows graded bedding.

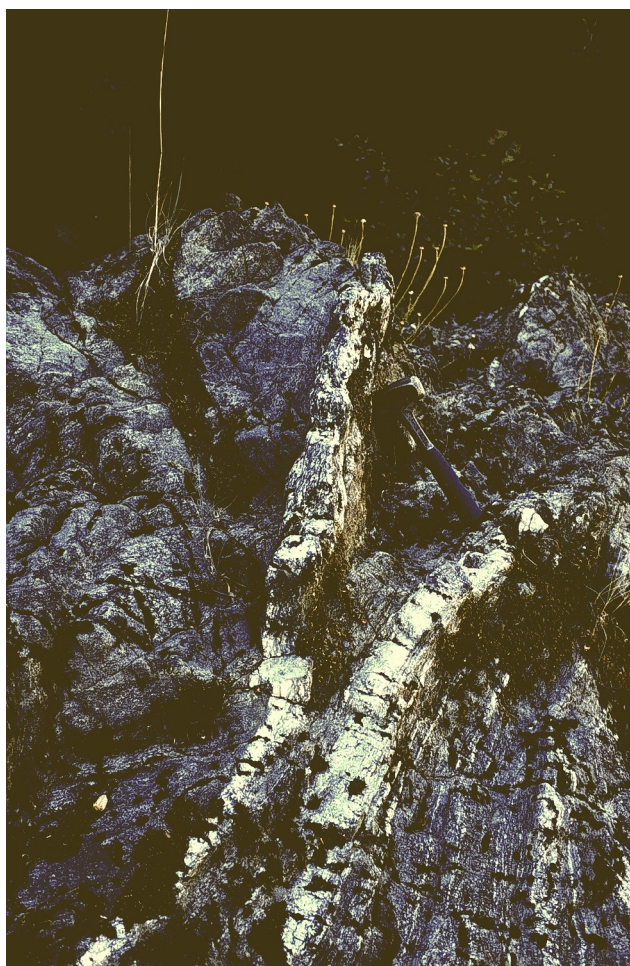


Figure 2.46

Photograph showing outcrop of late tonalitic dikes in the metagabbro unit (O/C-372b). The tonalite occurs parallel magmatic layering as well as dike like intrusions cutting layering at low to medium angles. The tonalite contains plagioclase, quartz, muscovite and garnet and is typically very coarse grained. The composition and texture is unlike all other quartzo-feldspathic rocks in the metagabbro unit. See hammer for scale.

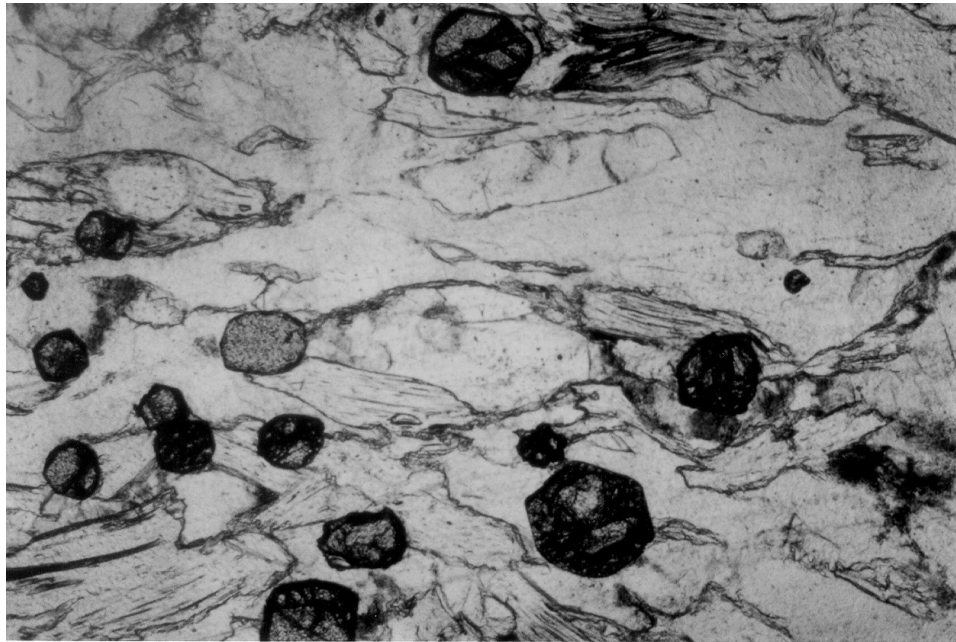


Figure 2.47

Photomicrograph showing the texture of a foliated tonalite dike (GH-97-20). The tonalite consists of weakly recrystallized quartz (clear, low relief), plagioclase (grayish, medium relief), muscovite (cleavage, high relief) and euhedral garnet (dark, high relief). The garnet-muscovite tonalites are compositionally distinct from all other quartzo-feldspathic rocks in the metagabbro unit. Muscovite separates of this samples yielded a $^{40}\text{Ar}/^{39}\text{Ar}$ cooling (below 350°C) age of 147.99 ± 0.45 Ma. The width of the photomicrograph is 2.14 mm.

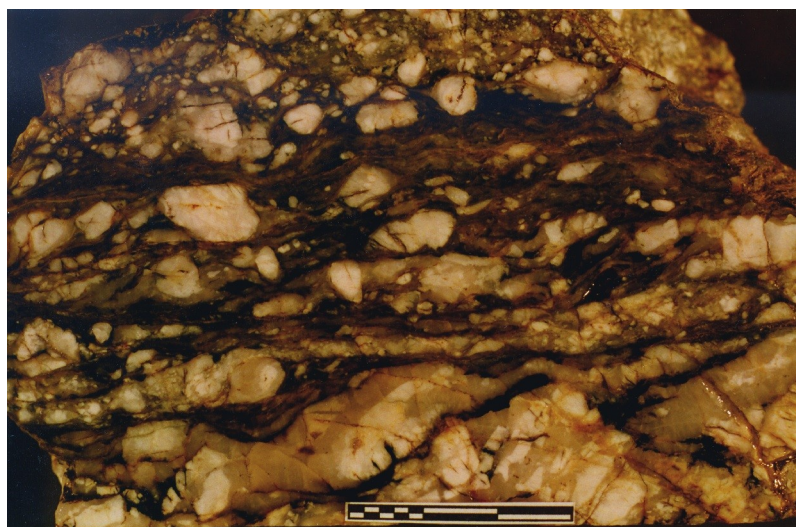


Figure 2.48

Slabbed and polished sample of muscovite-garnet tonalite intrusion having S/C-type fabric (GH-97-6). The rock consists of plagioclase (white), quartz (clear), muscovite (often altered to chlorite and appears dark green to black) and garnet (similar to figure 2.47). Plagioclase is heavily fractured, and muscovite-poor portions of the tonalite (arrow) look similar to cataclasites. Muscovite and chlorite occur in C-type shears (subhorizontal). S-planes trend from upper right to lower left. Sense of shear is dextral. Muscovite separates of a sample from the same dike (O/C-372b) yielded a $^{40}\text{Ar}/^{39}\text{Ar}$ cooling age of 148.52 ± 0.17 Ma. The scale bar is 3 cm long.



Figure 2.49

Photograph of a net-vein breccia about 200 m west of the fault exposed at Brushy Bar. The zone containing the net-vein breccias and intrusive breccias probably represents the wall or roof zone of the HMB diorite. The tonalite in the net-vein breccia is very similar to the tonalite dikes scattered throughout the pillow unit (figure 2.40) suggesting that the silicic dikes in the pillow unit could be related to the HMB diorite. Zircon separates of a sample (SC-13) from about this locality yielded a concordant U/Pb age of 159 Ma.



Figure 2.50

Photograph of medium-grained Half Moon Bar diorite intruded by a porphyritic dike (O/C-177). This dike is about 3 cm wide. Dikes in the HMB diorite are as wide as 30 cm and contain phenocrysts of plagioclase, clinopyroxene (pseudomorphs) and magnetite. Clinopyroxene phenocrysts in the porphyritic dikes are typically replaced by uniformly colored brownish-green amphibole.

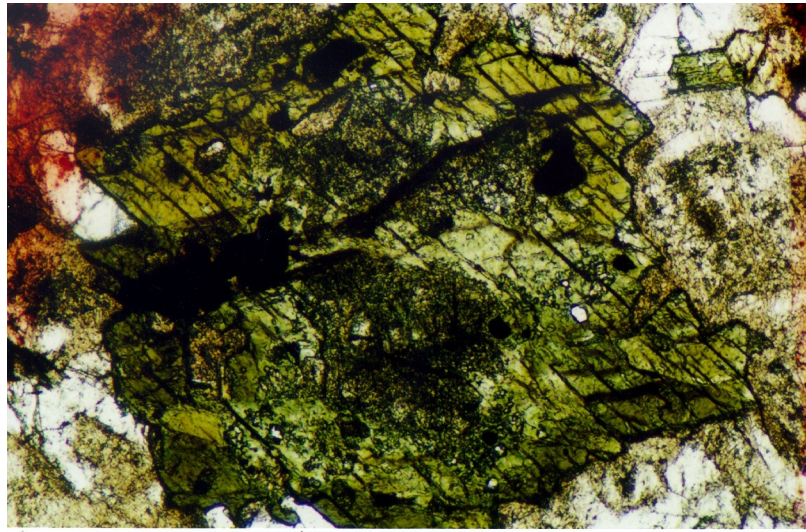


Figure 2.51

Photomicrograph of amphibole in sample O/C-377 from the HMB diorite. Dark brown-green hornblende occurs as a poorly defined rim around lighter colored, pale-green amphibole and dark, cloudy mineral aggregates. The assemblage in the cloudy aggregates includes actinolite, magnetite, chlorite, epidote. Occasionally, relic igneous cpx is preserved. The dark colored rim consists of calcic Mg-hornblende and is interpreted as a corona that formed by the incomplete reaction between cpx and melt or late stage magmatic fluids. Metamorphism (deuteric or hydrothermal alteration) followed upon crystallization of the diorite and the remaining cpx may have been replaced by cloudy mineral aggregates and pale colored amphibole. Plagioclase, especially the calcic cores are replaced as well. The width of the photomicrograph is 2.14 mm.

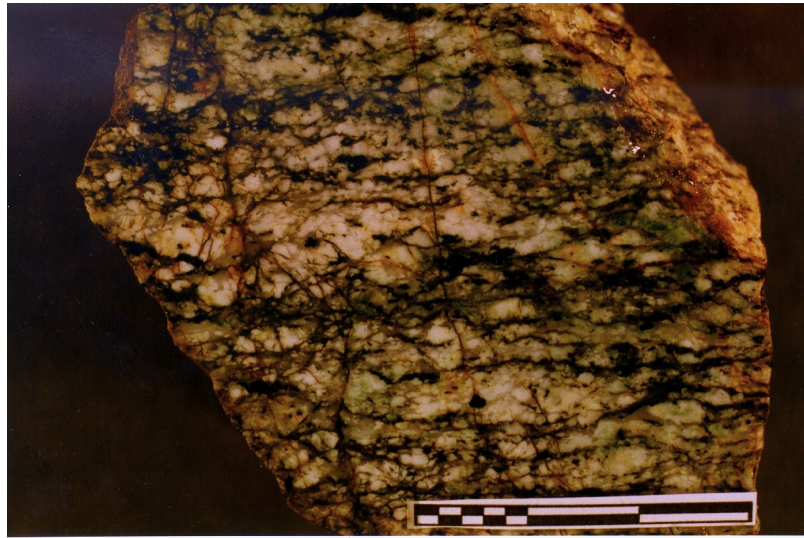


Figure 2.52

Photograph of polished hand sample (O/C-417) of S/C-type mylonite from the Blossom Bar shear zone. The rock consists of strongly recrystallized quartz, saussuritized plagioclase, biotite, muscovite and hornblende. The porphyroclasts of plagioclase and hornblende are heavily fractured. C-planes are horizontal and S-planes trend upper right to lower left. The shear sense is dextral. The scale bar is 3 cm.

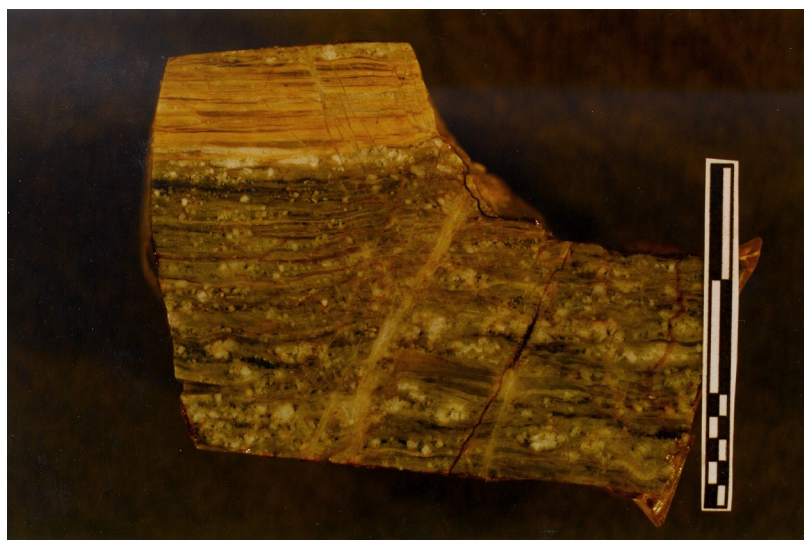


Figure 2.53

Photograph of a polished hand sample (O/C-230-S61) of mylonite (gray-green) and ultramylonite (pistachio green) sampled in a quartzo-feldspathic block at Blossom Bar on the Rogue River. The contact between mylonite and ultramylonite is sharp. The foliation of the mylonite is defined by discontinuous layers or lozenge-shaped domains of recrystallized quartz containing various porphyroclasts. The discontinuous layers or domains are separated by < 1 mm bands (C-type shears?) consisting of a fine grained mineral aggregate of mostly epidote or clinozoisite. Plagioclase porphyroclasts are heavily fractured and fragments are completely replaced. The ultramylonite consists of quartz ribbons occurring in a fine grained, pistachio green matrix. In thin section, the matrix appears dark cloudy to almost opaque, and consists probably mostly of epidote. Other minerals in the cloudy matrix may include clinozoisite, albite, chlorite, and mica. The scale bar is 3 cm.

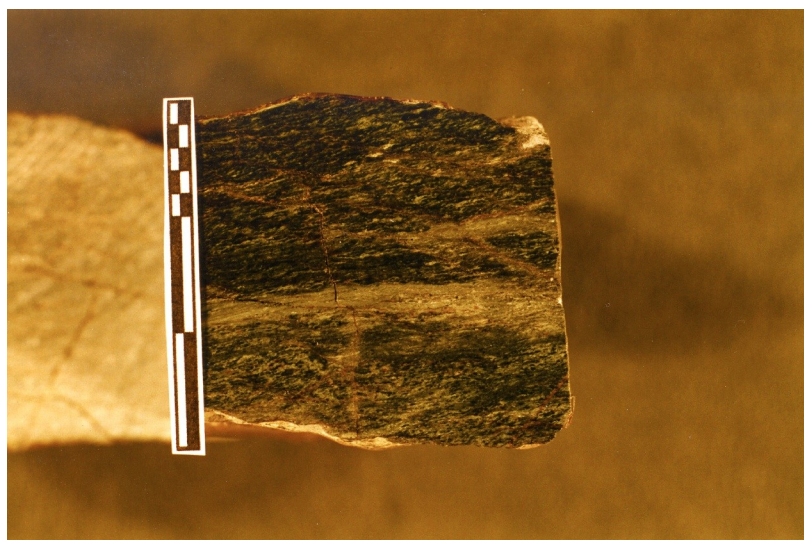


Figure 2.54

Photograph of a polished hand sample of a strongly foliated, mafic rock (O/C-45-S41) showing the characteristic fabric of foliated mafic rocks in the Blossom Bar shear zone. This sample is relatively coarse-grained possibly representing a deformed, phenocryst-free, shallow intrusive rock. Pistachio green 'epidosite-mylonite' zones (2-3 mm wide) occur parallel foliation. Igneous minerals are completely replaced and are arranged at low angles to foliation (long axis trend upper right to lower left). Amphibole (pale green in thin section) is augen-shaped and possibly replaces cpx. Plagioclase is replaced by a fine grained, cloudy mineral aggregate (cz+ep+ab±chl±mica), and secondary(?) quartz is strongly recrystallized. The extensional shear bands trend upper left to lower right. In places, chlorite is altered and the extensional shear bands may show up as rust brown, oblique bands. The scale bar is 3 cm.

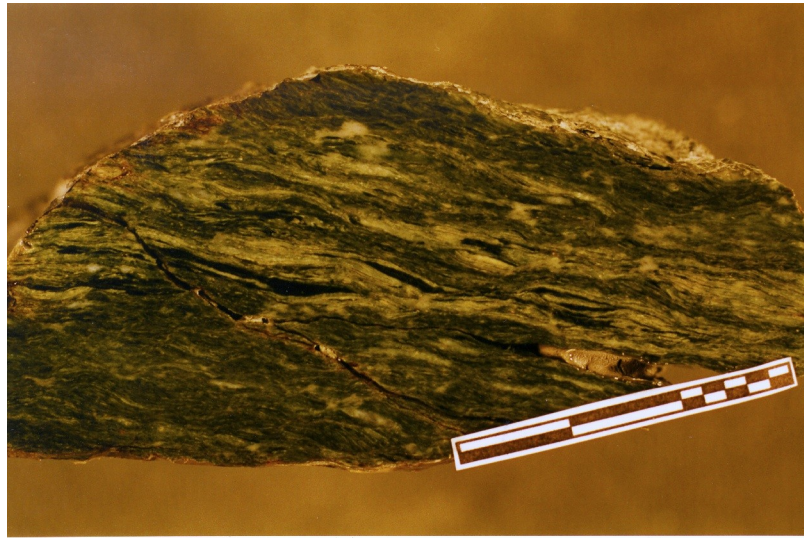


Figure 2.55

Photograph of a polished hand sample (O/C-238) of a strongly foliated rock consisting primarily of chlorite, actinolite and calcite. The foliation ranges from spaced to continuous. The microlithons or discontinuous layers (white to pale green) consist primarily of calcite, minor quartz and some disseminated chlorite, actinolite and epidote. The cleavage domains (dark green) consist primarily of chlorite and minor actinolite. The black lenses in this hand sample consist of actinolite. The scale bar is 3 cm.

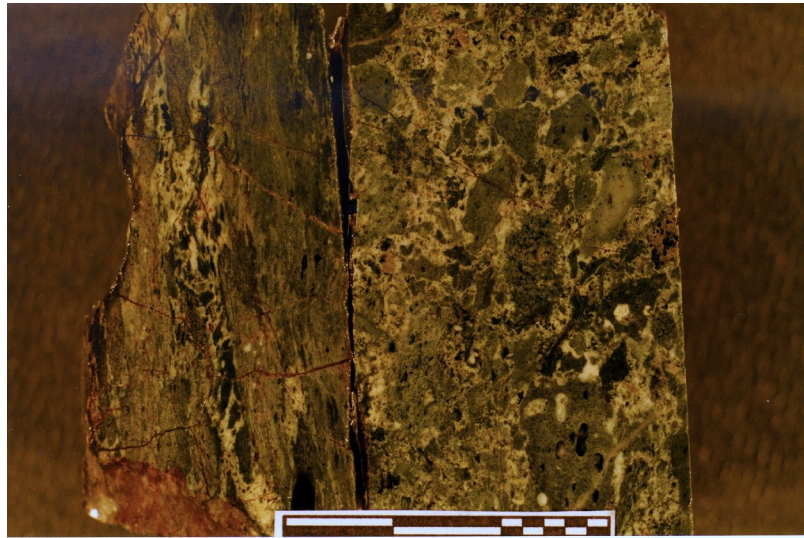


Figure 2.56

Photograph of two polished thin section chips showing an undeformed (O/C-201c) and a foliated volcanic breccia (O/C-419) from the Blossom Bar shear zone. The fragments in the deformed breccia (left) are elongate and aligned subparallel foliation. The undeformed breccia (right) is very similar to the volcanic breccias in the Mule Mountain volcanic unit. The clasts are of variable composition, texture and color indicating sedimentary transport and deposition (see figure 2.41). The scale bar is 3 cm.

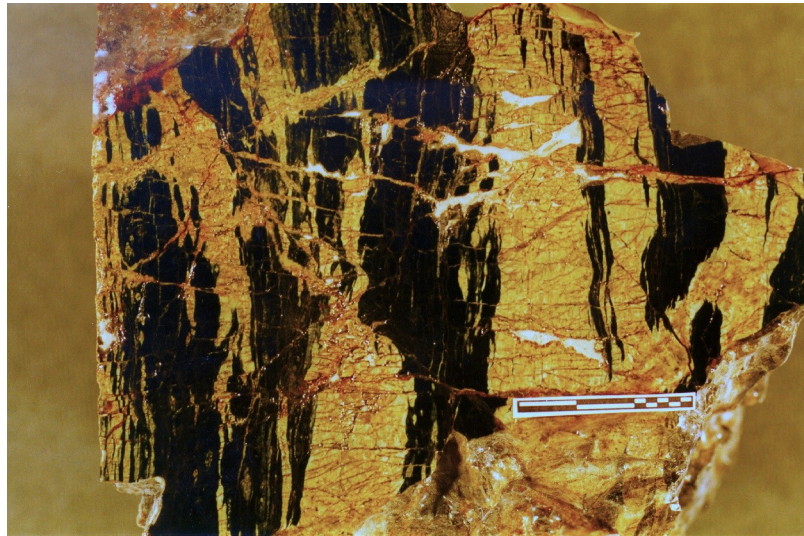


Figure 2.57

Photograph of polished hand sample of 1.5 m wide epidote+actinolite zone (O/C-382) occurring in the Blossom Bar shear zone. The sample consists of granoblastic epidote (pistachios green to yellow) and acicular actinolite (greenish black). Fibrous veins cut foliation (defined by the color banding) at high angles. The scale bar is 3 cm.

Figure 3.1

**Reconstruction of the
Rogue Wilderness ophiolite**

Columnar section showing likely reconstruction of ophiolitic units identified in the Wild Rogue Wilderness compared to a typical pseudostratigraphy (e.g., Penrose conference, 1972) of ophiolites shows only the middle and upper crustal section is preserved. The metagabbro unit may not be part of the ophiolite. A small intrusion of hornblende quartz diorite (HQ diorite) occurs in the metagabbro unit. The Half Moon Bar diorite (HMB diorite) intruded the pillows.

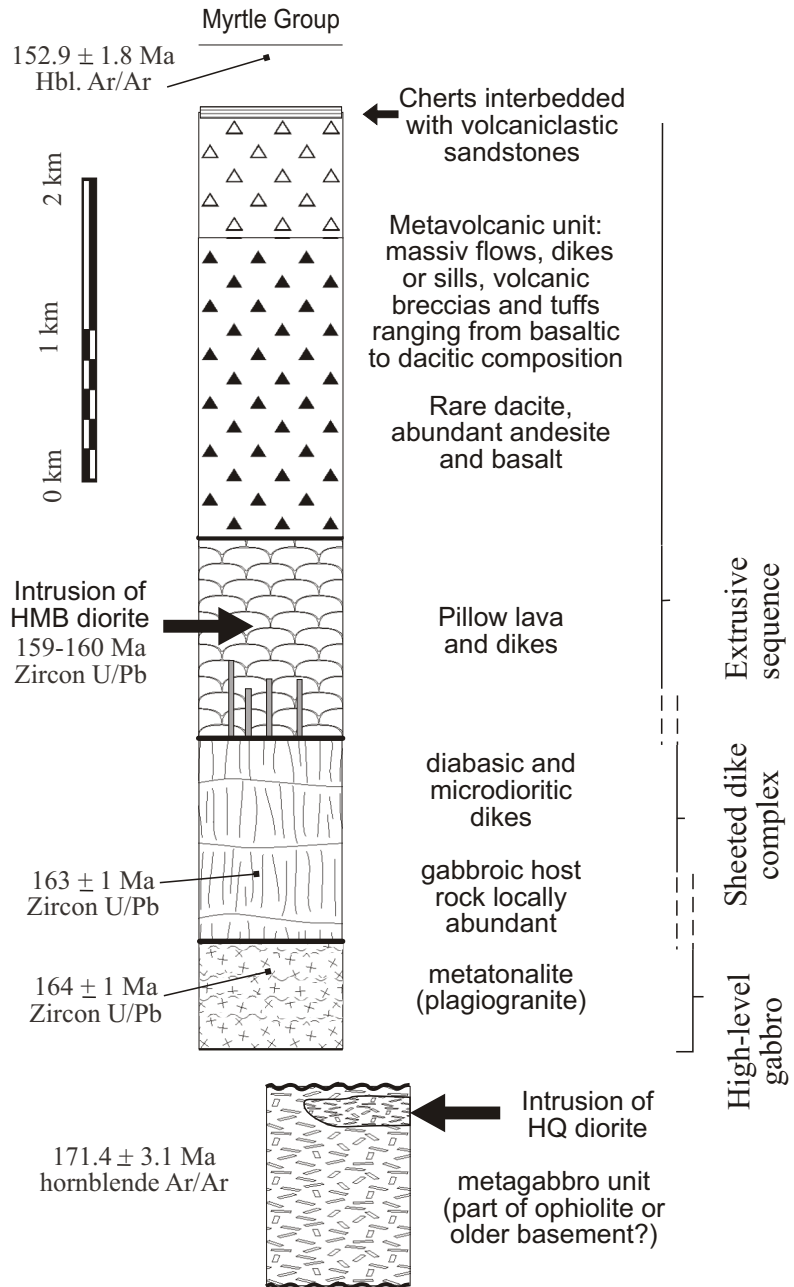


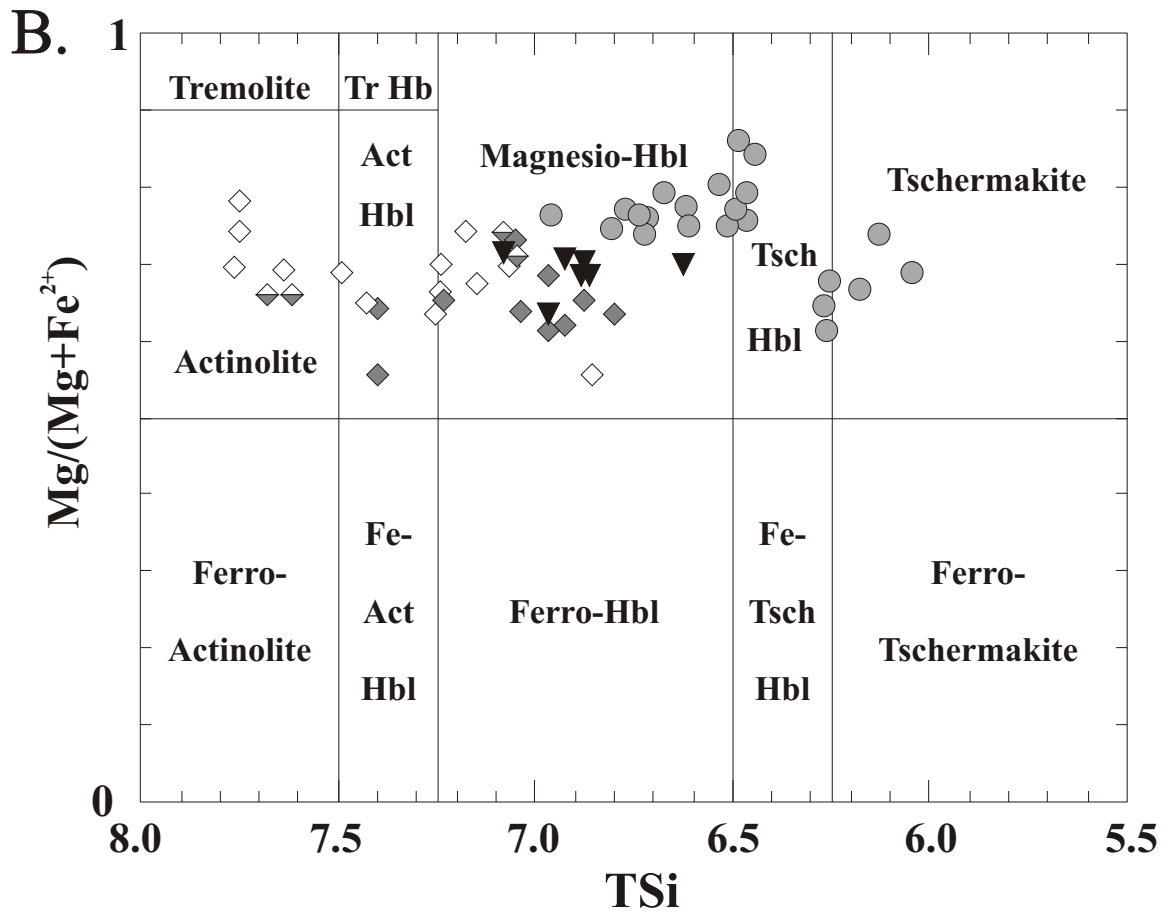
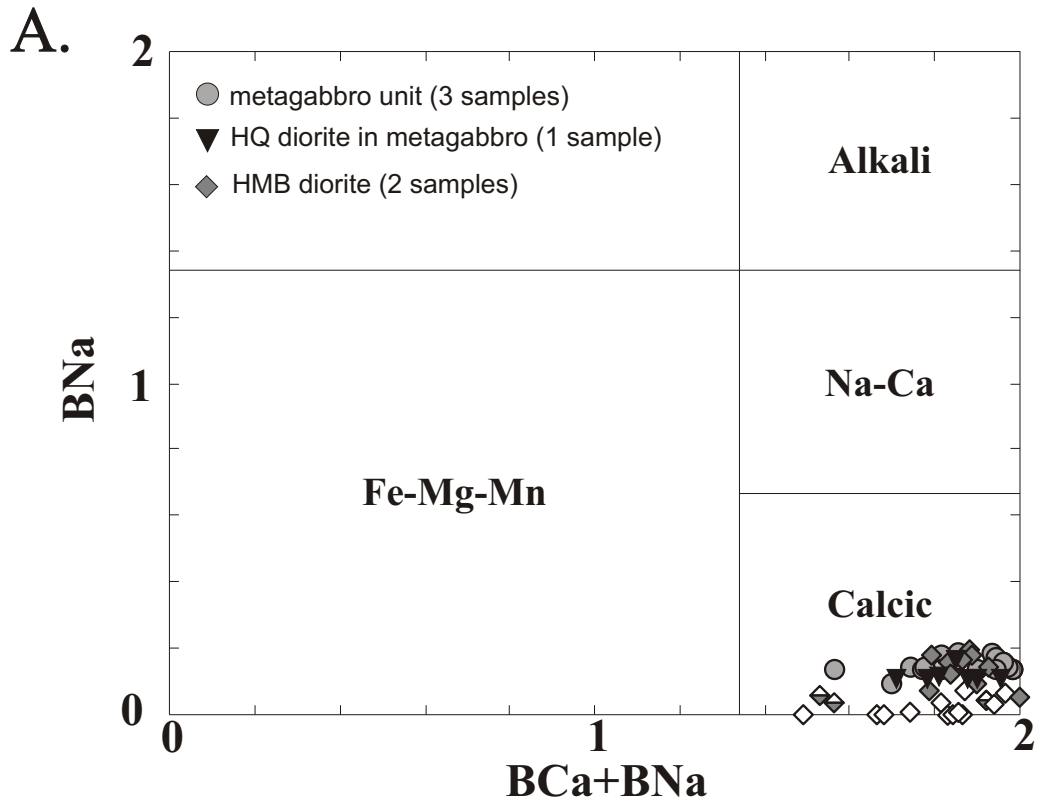


Figure 3.2

Photomicrograph of HMB diorite sample O/C-376 showing typical, strongly zoned plagioclase coexisting with quartz (yellow, upper right) and hornblende (dark blue, lower left). Plagioclase is saussuritized, has calcic cores (dark center, An₇₃₋₈₂) and normal igneous zoning ranging from labradorite to oligoclase. Patchy albitization is inferred from variable replacement of grains combined with analysis by electron microprobe. Relict carlsbad-albite twinning is visible. Overall, hornblende in the HMB diorite is in contact with plagioclase ranging in composition from andesine to oligoclase, whereas actinolite is predominantly in contact with albite. The width of the photograph is 2.14 mm, and polarizers are crossed. The selected thin section is somewhat thick (50µm), but shows twinning and zoning better in the altered samples.

Figure 3.3

- A. Classification of amphiboles determining the principle group. The samples from the metagabbro unit (n = 3), the intrusion of HQ diorite (n = 1) in the metagabbro unit, and the HMB diorite (n = 2) contain exclusively calcic amphiboles. Many amphibole compositions are not suitable for the application of the thermometers A and B (empty symbols), mainly because they contain not enough Na in the B- (or M4-) site. Few amphibole were suitable for the application of thermometer A, but not thermometer B (half filled symbols).
- B. Further subdivision of calcic amphiboles based on tetrahedral Si and Mg-# (also: $ANa + AK < 0.5$ and $Ti < 0.5$). The amphiboles are relatively magnesian and range in composition from tschermakite to actinolite.



Half Moon Bar diorite

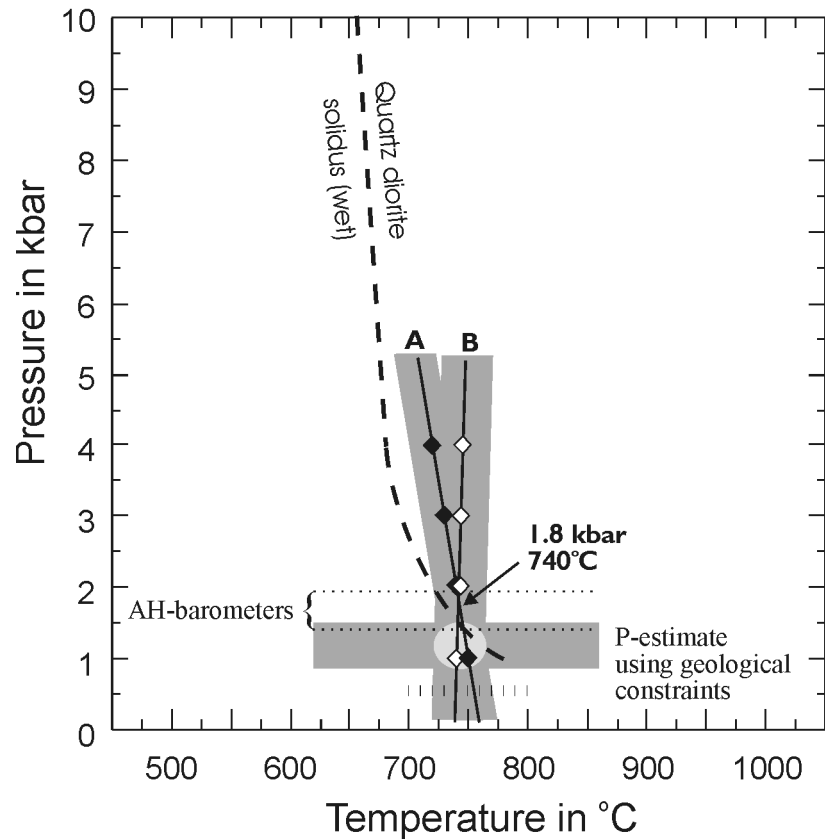


Figure 3.4

P-T diagram showing the range of inferred pressures and temperatures of equilibration of hornblende-plagioclase pairs in two samples from the Half Moon Bar (HMB) diorite. Pressure estimates using geological constraints range between 0.85 and 1.5 kbar. Al^{Tot} -in-hornblende geobarometers indicate maximum pressures of 1.4 - 1.9 kbar. These independent pressure estimates coincide with the point of interception of thermometers A and B. At pressures between 0.85 and 1.5 kbar, the average temperature of equilibration calculated using thermometers A and B is $745 \pm 25^\circ\text{C}$. For reference, the wet quartz-diorite solidus (Piwinski, 1973) is shown. Evidently, the HMB diorite equilibrated at solidus conditions.

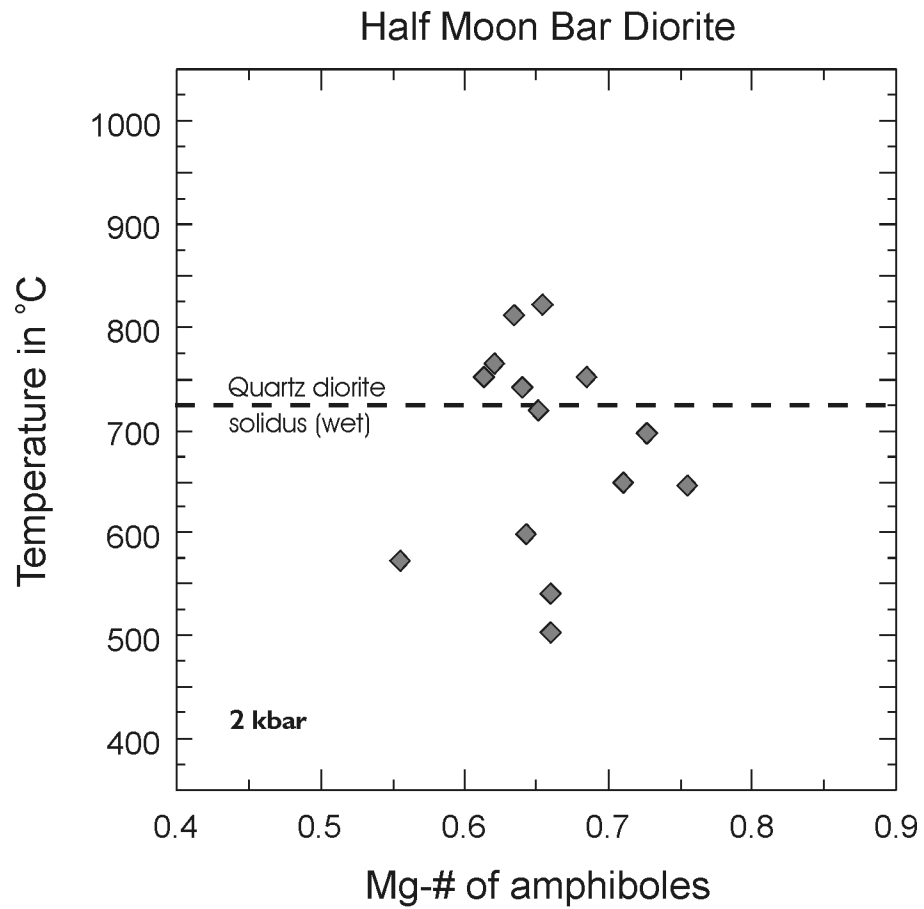


Figure 3.5

Temperature variations versus Mg-# in samples O/C-118a and O/C-376. Temperatures are calculated using thermometer A at 2 kbar (table 3.1). For reference, the wet quartz-diorite solidus at 2 kbar is shown (Piwinskii, 1973). Oxidation at near solidus conditions is indicated by the increase in Mg-# with cooling.

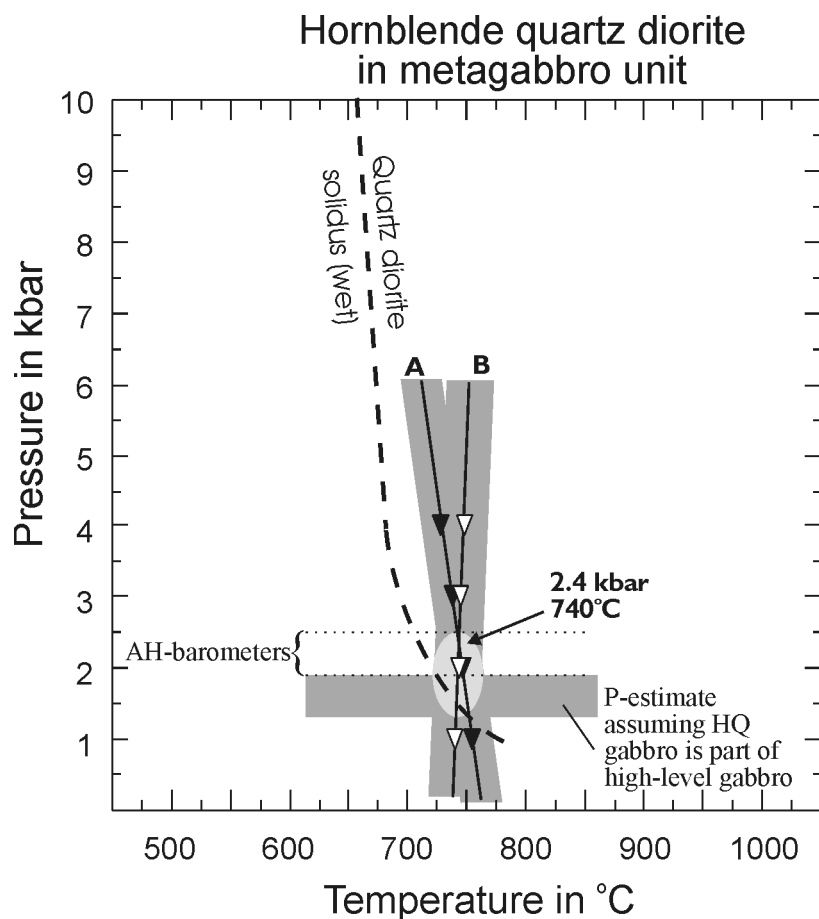


Figure 3.6

P-T diagram showing the range of inferred pressures and temperatures of equilibration of hornblende-plagioclase pairs in a samples from the hornblende quartz (HQ) diorite in the metagabbro unit. Pressure estimates assuming the HQ diorite intruded high-level gabbro range between 1.3 and 1.9 kbar. However, this is highly speculative, because the metagabbro unit is a fault-bounded unit. Al^{Tot} -in-hornblende geobarometers indicate maximum pressures of 1.9 - 2.5 kbar. These independent pressure estimates coincide with the point of interception of thermometers A and B. At pressures between 1.3 and 1.9 kbar, the average temperature of equilibration calculated using thermometers A and B is $745 \pm 25^\circ C$. For reference, the wet quartz-diorite solidus (Piwinskii, 1973) is shown. Evidently, the HMB diorite equilibrated at solidus conditions.

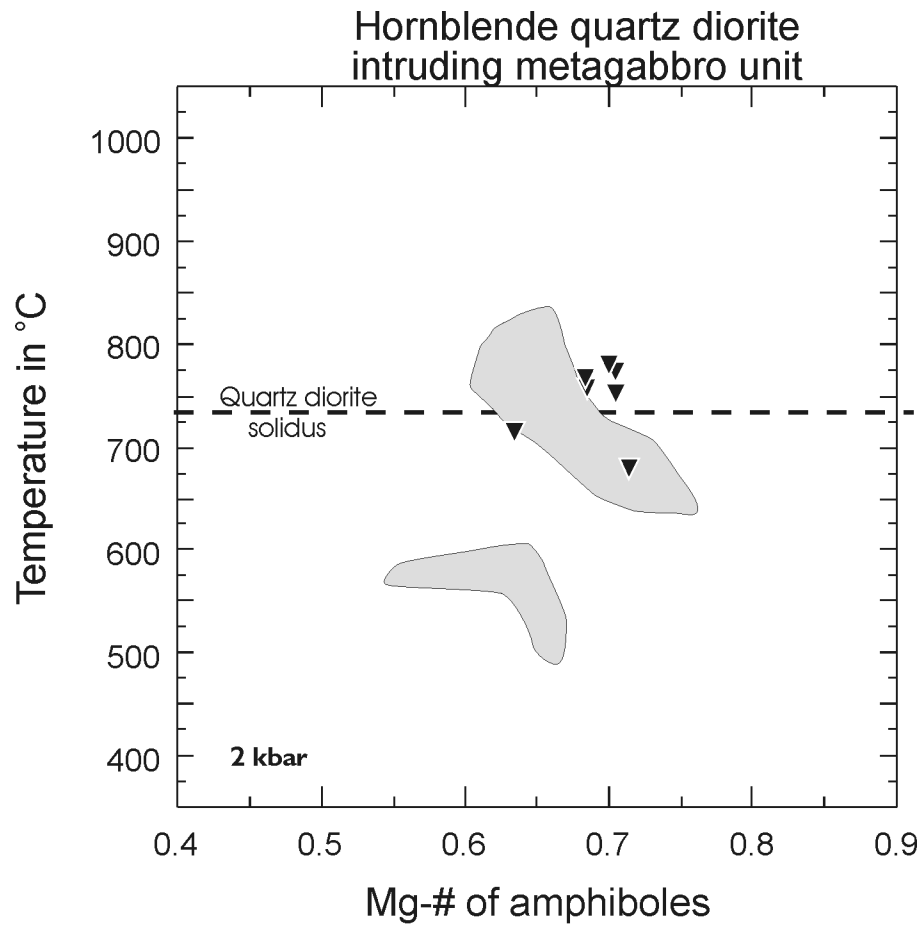


Figure 3.7

Temperature variations versus Mg-# in sample O/C-229. Temperatures are calculated using Thermometer A at 2 kbar (table 3.2). For comparison, the results from figure 3.5 (HMB diorite) are shown as well (shaded fields). The horizontal line indicates the water saturated solidus of quartz diorite at 2 kbar (Piwinski, 1973). Similar to the HMB diorite, the HQ diorite equilibrated at near solidus conditions. The Mg-# of hornblendes in the HQ gabbro increases only slightly over a temperature range of $\sim 100^{\circ}\text{C}$ ($800^{\circ}\text{C} \rightarrow 700^{\circ}\text{C}$) suggesting that oxidation during cooling was not an important process in the HQ diorite.

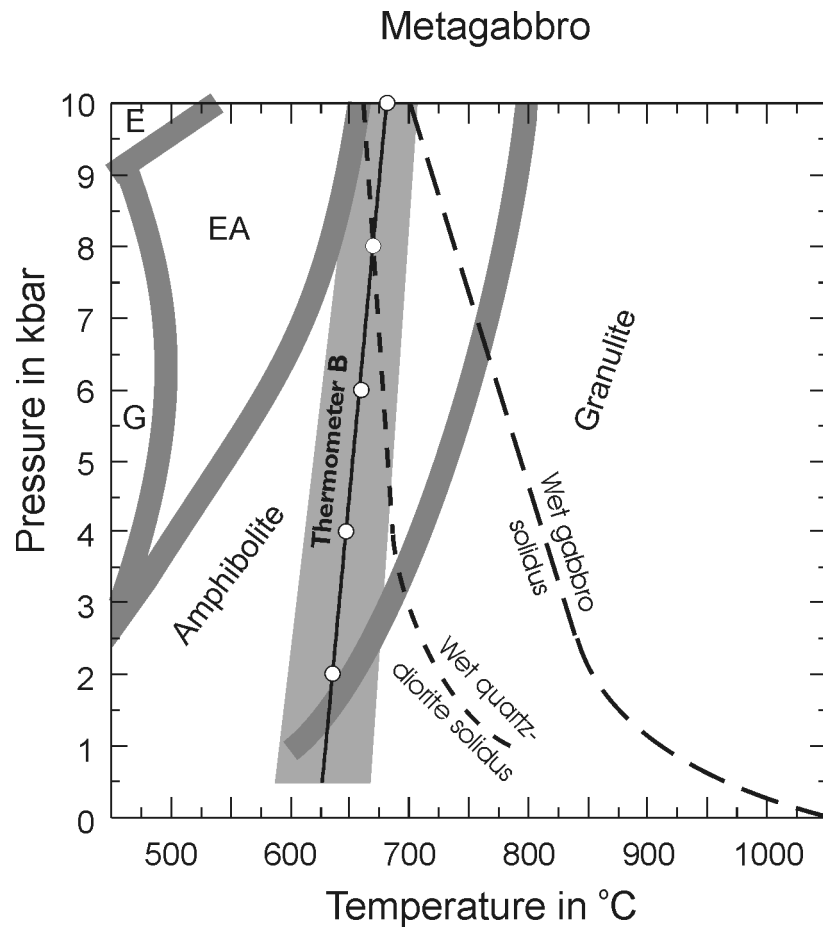


Figure 3.8

P-T diagram showing the principle metamorphic facies (after Spear, 1993; p.17). **E** denotes eclogite facies, **EA** epidote-amphibolite facies, and **G** greenschist facies. For reference, the water saturated solidi of gabbro and quartz diorite are plotted as well. Thermometer B of Holland and Blundy (1994) was used to calculate the temperatures at 2, 4, 6, 8 and 10 kbar (table 3.3). Evidently, the metagabbro (samples MRH-78/1, MRH-78/2 and O/C-373) equilibrated at conditions significantly below the water saturated solidus of gabbro (after Holloway and Burnham, 1972). Metamorphism occurred at amphibolite facies conditions. The intersection of curve B with the solidus of quartz diorite (Piwinski, 1973) at 8 kbar may be considered as an upper limit on the pressure of metamorphism. Evidence of re-melting of quartz-bearing/ quartz-rich phases in the metagabbro unit was not observed.

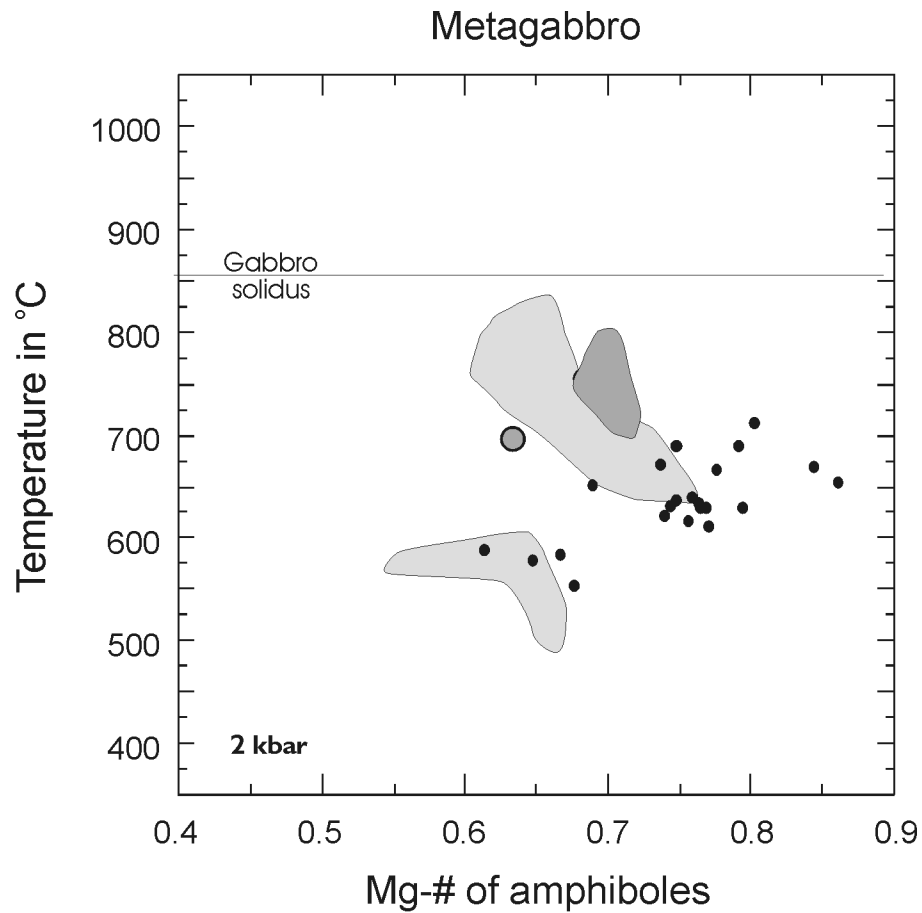


Figure 3.9

Temperature variations versus Mg-# in samples MRH-78/1, MRH-78/2 and O/C-373 from the metagabbro unit. Temperatures are calculated using thermometer B at 2 kbar (table 3.3). For comparison, the results from figures 3.5 and 3.7 are shown as well (HMB diorite: light-shaded fields; HQ diorite: dark-shaded fields). The horizontal line indicates the water saturated solidus of gabbro at 2 kbar (Holloway and Burnham, 1972). Unlike the HMB and HQ diorites, the metagabbro equilibrated significantly below solidus conditions. It is not clear whether or not the positive correlation of Mg-# with temperature represents a cooling or heating trend. Nevertheless, the conditions of equilibration of the metagabbro were much different than for the HMB and HQ gabbro.

Figure 4.1

A. Simplified geologic map of SW Oregon. The geologic map of Tertiary strata in Oregon is modified from Chan and Dott (1983) and Niem and Niem (1990), and the geologic map of pre-Tertiary rocks is modified from Walker and MacLeod (1991). The structural data are from the following sources:

Myrtle Group (S); Coleman (1972), Ramp et al. (1977)

Myrtle Group (N); Rud (1971), Ramp et al. (1977), Gray et al. (1982), this study

Eocene strata (S); Ramp et al. (1977), Gray et al. (1982), Ramp and Moring (1986),

Niem and Niem (1990), this study

Eocene strata (N); Rud (1971), Ramp et al. (1977), Gray et al. (1982), Niem and Niem (1990),
this study

B. Interpretative cross section along line AA' (figure 4.1a). The Snow Camp terrane, consisting of an ophiolitic basement and late Jurassic to early Cretaceous fore-arc sediments (Myrtle Group), is interpreted as the remnant of a folded thrust sheet that is thrust over the terranes of the Franciscan complex (Yolla Bolly terrane and Sixes River terrane) (Blake et al., 1985a). This remnant appears to be preserved in a graben and is largely covered by Tertiary strata with great unconformity. The angular unconformities between the Tertiary formations and increase of intensity of folding with age indicate that Tertiary strata was deposited in a growing syncline. The cross section of the southern Tyee basin (i.e., tertiary strata) from Hanging Rock to the Coquille River Fault is based on the report of Niem and Niem (1990). The following data are incorporated in the construction of the cross section: (1) the steeply dipping normal fault at the eastern boundary of the Rogue Wilderness ophiolite displaced Tertiary strata (Ramp and Moring, 1986; this study); (2) an area of high magnetic susceptibility (ultramafic rocks or serpentinite) occurs ~ 500 m below the topographic surface (Blakely and Senior, 1983); (3) the ophiolitic units are subvertical and fault bounded (Gray et al., 1982; this study); (4) the beds of the Myrtle Group are subvertical near the contact with the Rogue Wilderness ophiolite, and are intensely folded (this study), and the dip of the beds decreases westwards towards younger strata (Rud, 1971); (5) the structure of the ophiolitic basement may be characterized by a succession of imbricate thrust sheets (Roure and Blanchet, 1983; Harper, unpublished field mapping, 1999).

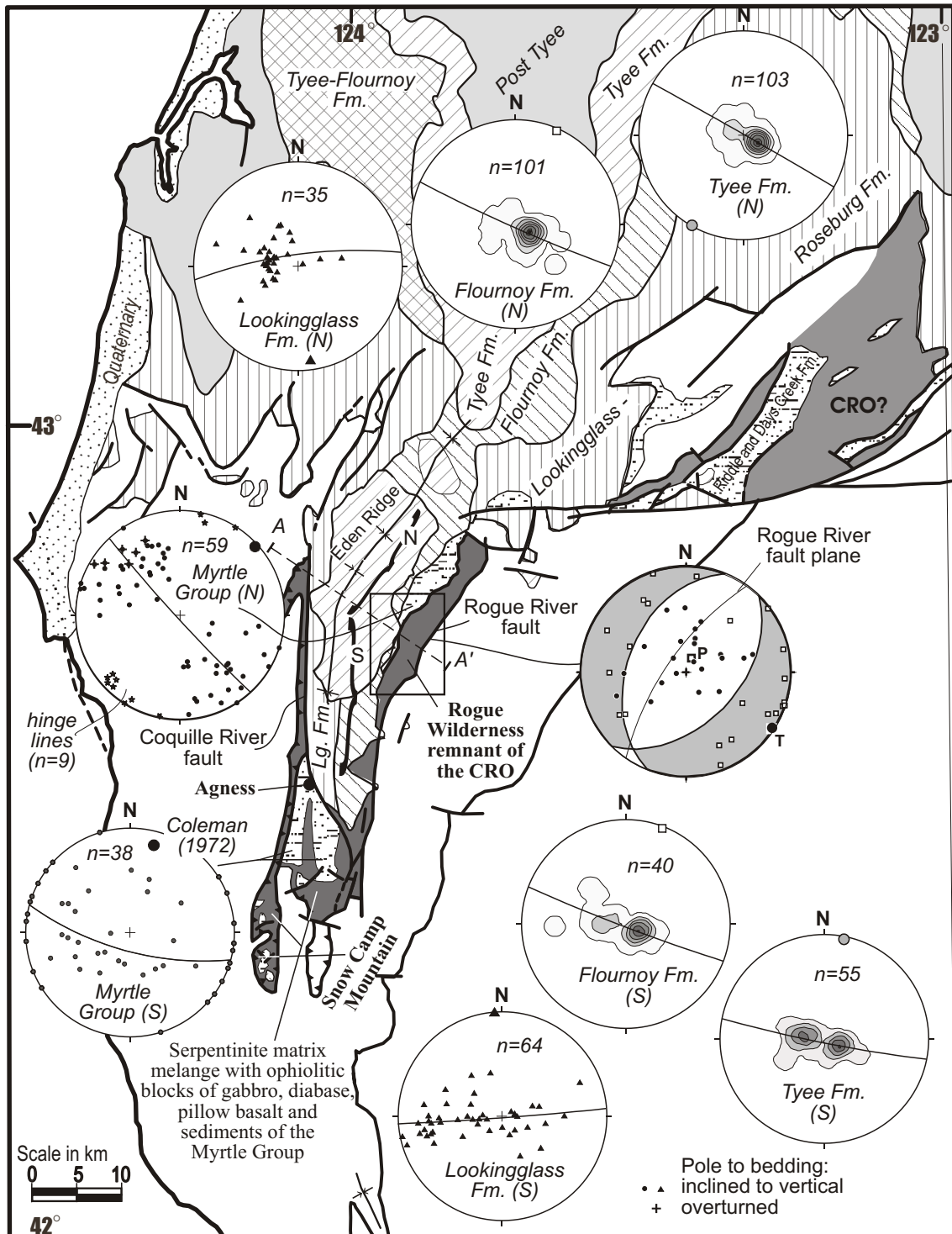
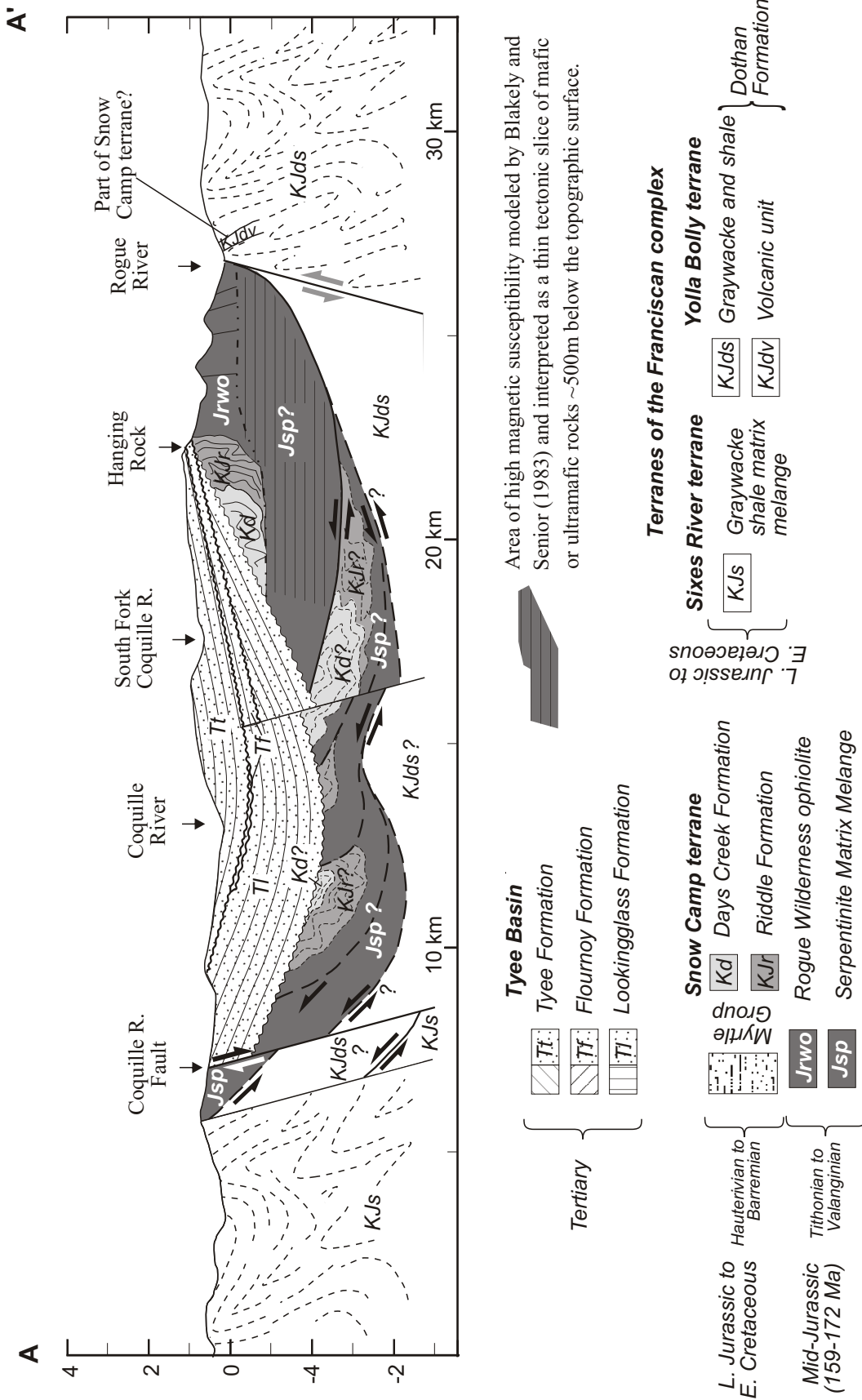


Figure 4.1a

Simplified geologic map of SW Oregon showing the area of the field map (box) and lower hemisphere stereographic projections of structural data from sedimentary units up to 50 km north (N) and south (S) of the cross section line AA'. See figure 4.1b for legend.



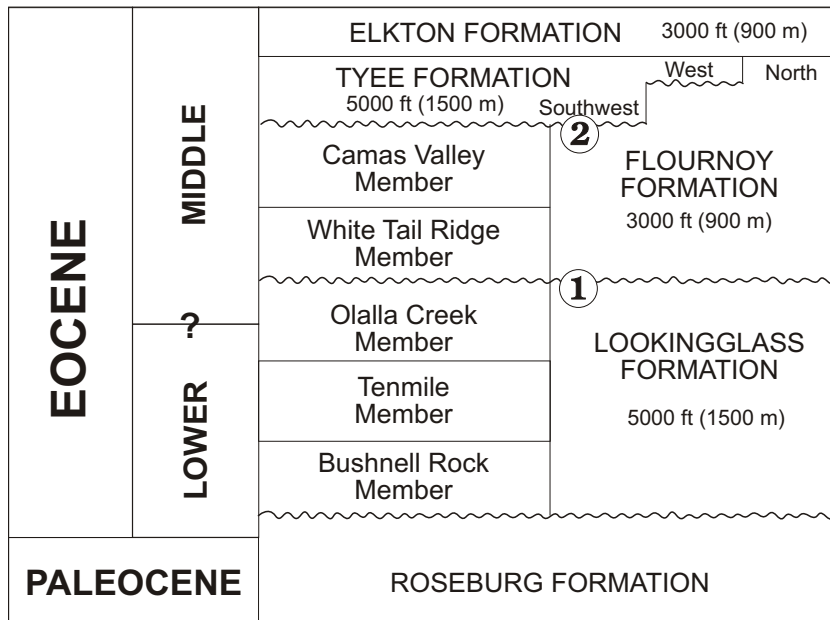


Figure 4.2

Stratigraphic nomenclature in the Tyee Basin after Baldwin (1974). An angular unconformity separates the Lookingglass and Flournoy formations in the Eden Ridge syncline (1). In the southernmost extension of the Tyee basin, the Flournoy and Tyee formations are separated by an angular unconformity (2), which appears to change to a disconformity north of line AA' (figure 4.1a).

Figure 4.3

Plots of a normal fault, reverse fault, right-lateral strike slip fault, and a left-lateral strike slip fault after the method of Hoepfner (1955). The lower hemisphere stereographic projections show the fault plane, the striation on the fault plane, and the sense and direction of movement (assumed to be parallel striation). The M-plane is defined as a plane perpendicular to the fault plane and parallel to the striation. The slip linear is defined as an arrow affixed to the pole to the fault plane and parallel to the trace of the M-plane. Normal faults have slip linears pointing towards the center, reverse faults have slip linears pointing away from the center, right-lateral and left-lateral strike slip faults have slip linears approximately parallel to the circumference of the stereographic projection. Additionally, the compressional (P) and tensional (T) axis are plotted.

To facilitate the identification of the type of fault in the Hoepfner plots, the following convention is applied throughout this chapter: if the striation on a fault has a pitch between 0° - 45° and 135° - 180° , the fault is labeled as a strike slip fault (left or right lateral), if the striation on a fault has a pitch between 45° - 135° , the fault is labeled as a dip-slip fault (normal or reverse).

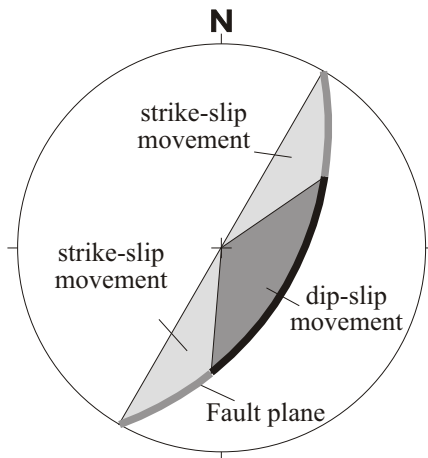
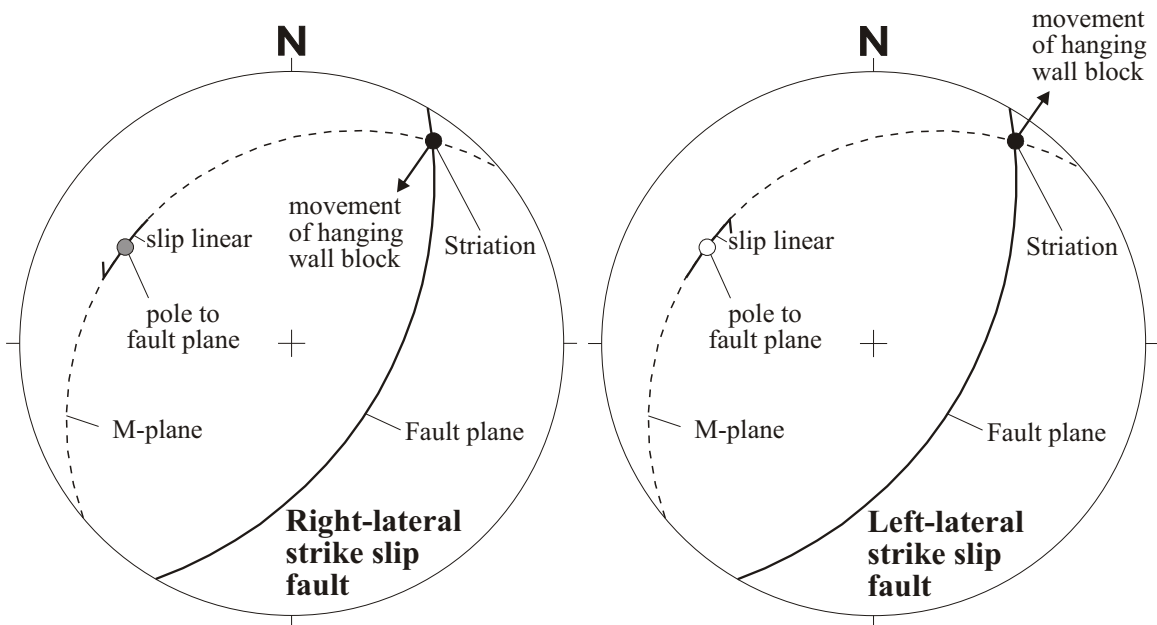
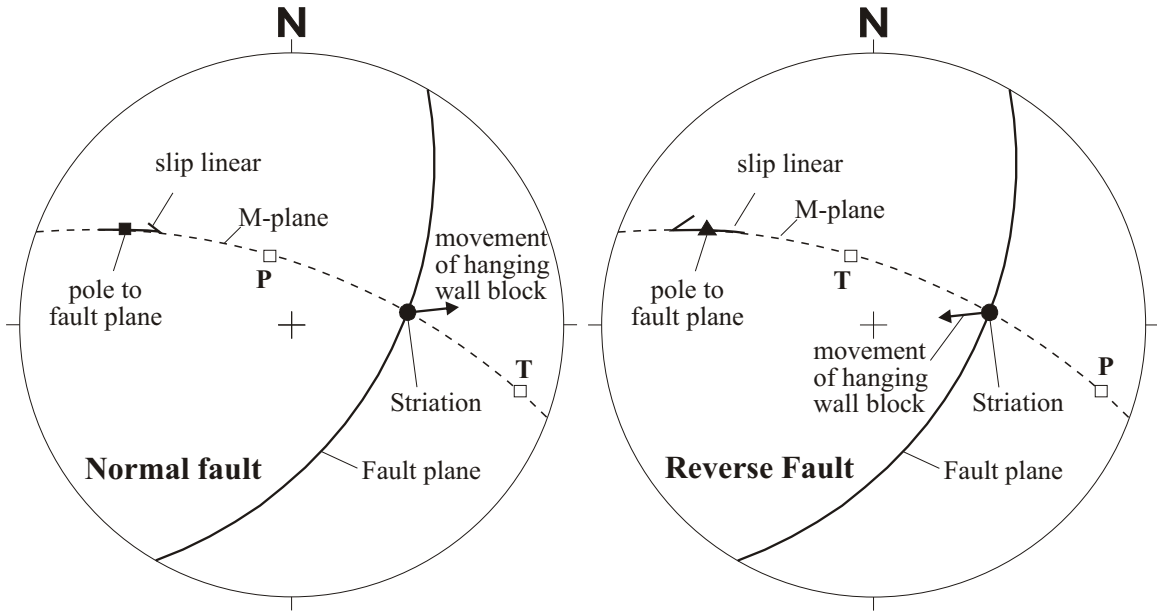
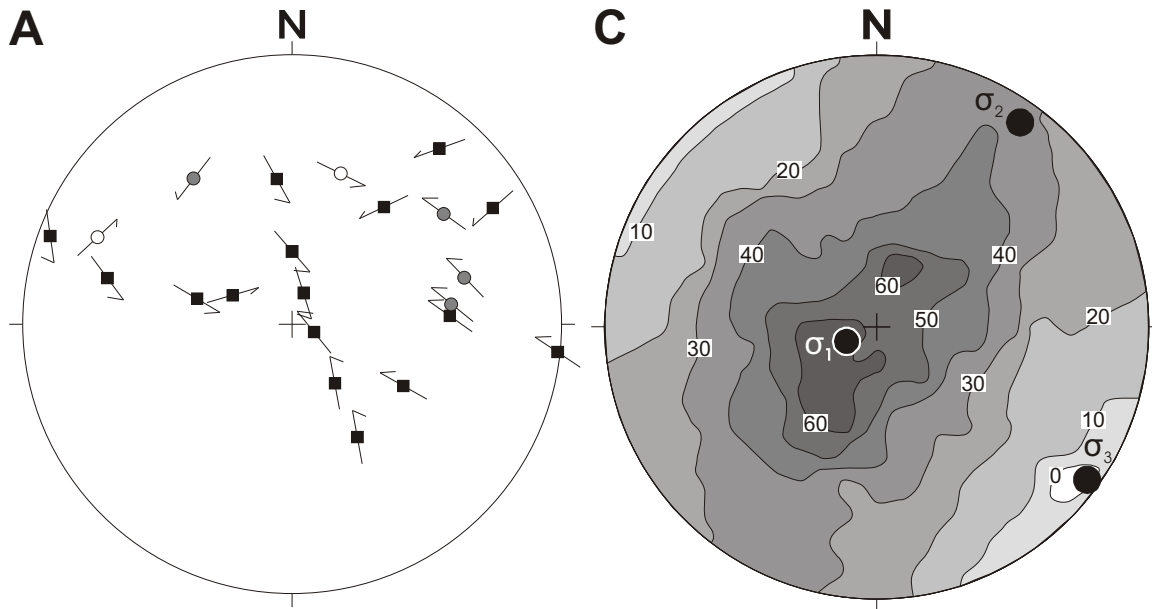


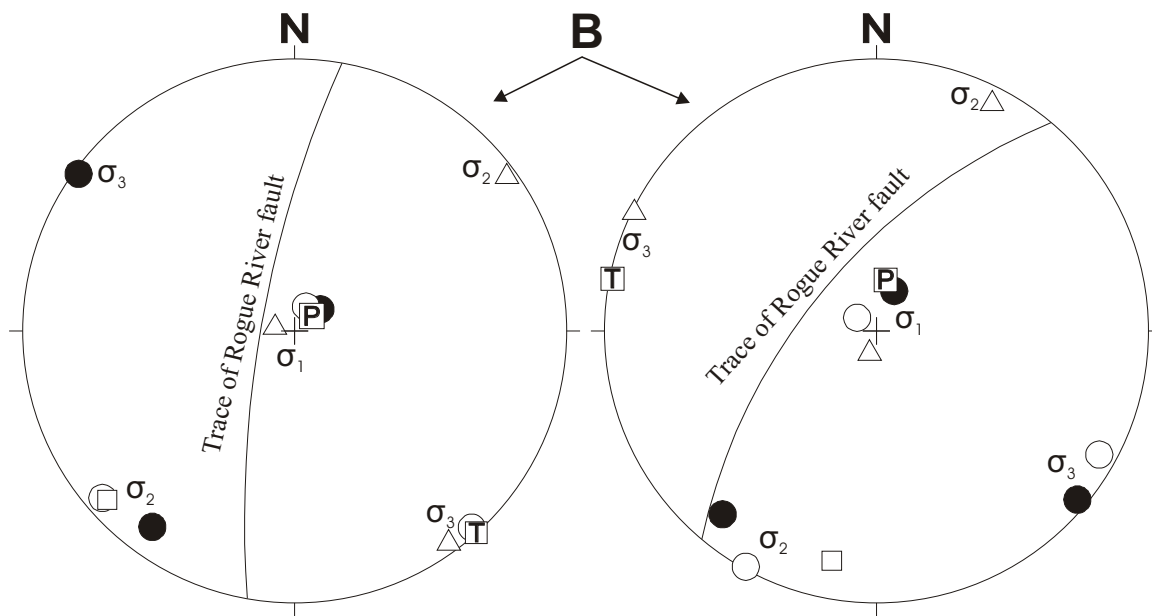
Figure 4.4

Lower hemisphere, equal area stereographic projections of poles to post-Eocene faults (4.4a) and the results of the paleostress analysis (4.4b and 4.4c) using the data shown in figure 4.4a.

- a. Poles to post-Eocene faults and their slip vectors (Hoepfner, 1955). The arrows affixed to the poles to faults indicate the direction of slip of the hanging wall block (see figure 4.3).
- b. Results of the paleostress analysis using four different programs: solid circle - ROMSA (Lisle, 1988); circle - TENSOR (Angelier, 1979); square - FAULTKIN (Allmendinger et al., 1994); triangle - STRESS (Reches, 1987). The principal stress axis σ_1 , σ_2 , and σ_3 are calculated separately for two data sets: (1) Rogue River locality (n = 8); and (2) Mule Creek locality (n = 14). The orientation of the foliation in the Rogue River fault is indicated for both localities.
- c. Solution of the analysis of the combined data sets (n = 22) using ROMSA (Lisle, 1988). The contours express the most probable orientation of σ_1 ($245^\circ / 80^\circ$). The maximum compound likelihood is $P_{\text{Total}} = 67.4\%$ (contour interval = 10%). The corresponding σ_2 and σ_3 orientations are $035^\circ / 09^\circ$ and $126^\circ / 05^\circ$, respectively.



- right-lateral strike slip fault (n = 4)
- left-lateral strike slip fault (n = 2)
- normal fault (n = 16)



Rogue River locality (8 faults)

Mule Creek locality (14 faults)

- ROMSA
- TENSOR
- △ STRESS
- FAULTKIN

Figure 4.5

Lower hemisphere, equal area stereographic projections of structural data of the Dothan Formation (a, b, and c) and simplified outcrop map (d).

- a. Poles to layering in the Dothan formation. The best-fit girdle and the pole to this girdle ($208^{\circ} / 01^{\circ}$) are shown.
- b. Hinge lines of outcrop-scale folds. Steeply plunging fold hinges are often associated with drag-folds in sheared argillite (figure 4.5d).
- c. Contoured poles to cleavage. Based on observations in outcrops, the cleavage plane probably represents the axial plane of subvertical, slightly west verging folds.
- d. Outcrop map of sheared argillite and boudinaged graywacke at China Bar. The apparent offset of bedding in this outcrop is dextral. The hinge lines plunge at almost 90° to each other.

Structural data for the Dothan Formation east of the Rogue Wilderness ophiolite

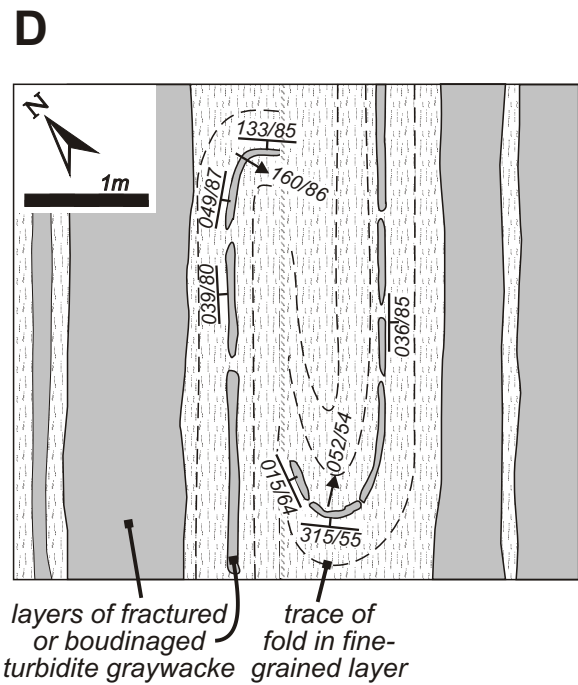
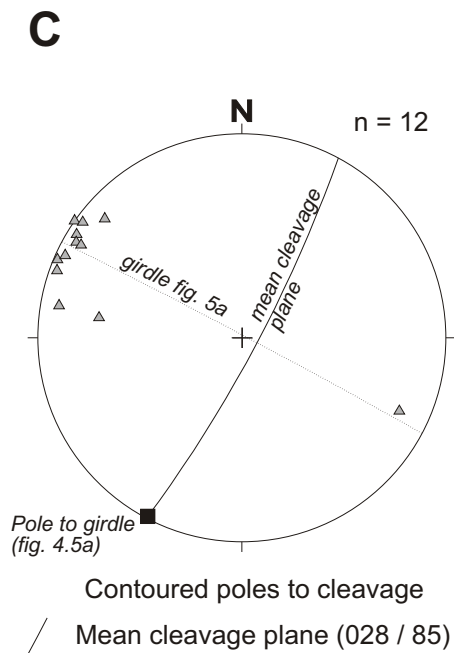
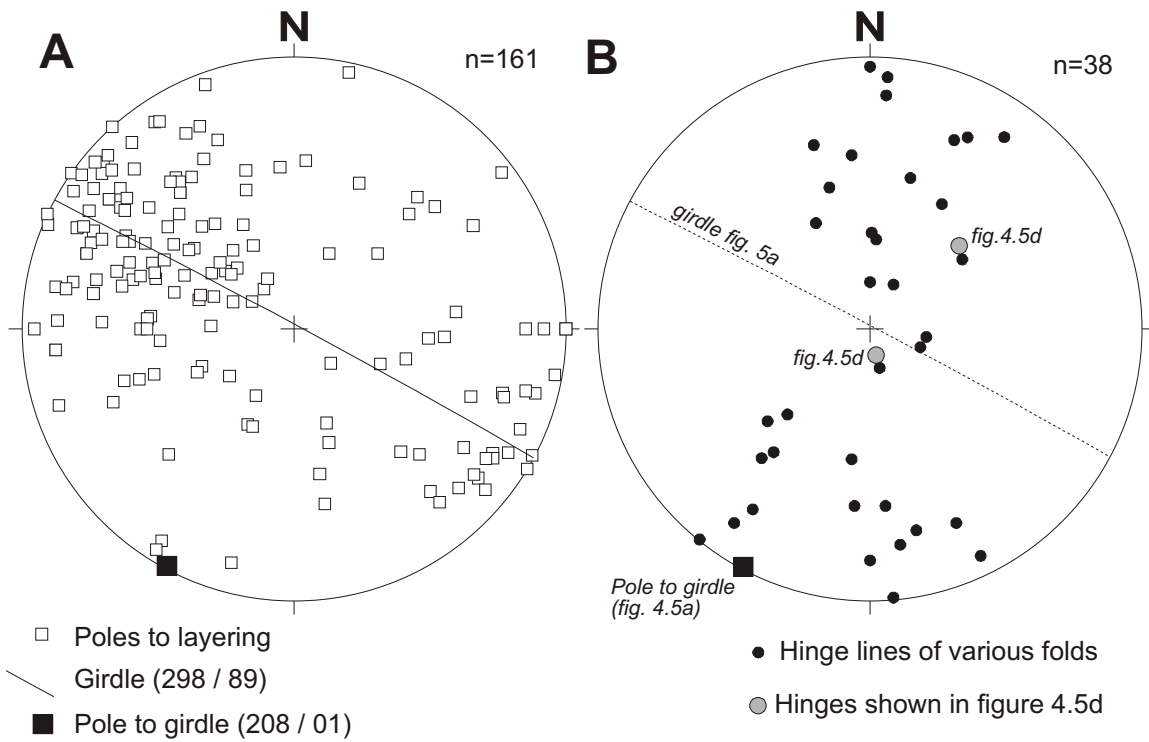


Figure 4.6

Lower hemisphere, equal area stereographic projections of poles to pillows (a), of poles to dike margins for dikes cutting pillows (b), and poles to bedding of volcanoclastic sediments (c). For comparison, the structural data for the Myrtle Group west of the Rogue Wilderness ophiolite are plotted (d).

- a. The attitude of 3-5 relatively flat pillows was measured in 10 outcrops. The submarine volcanic flows are overturned based on shape of pillows. The mean plane of the pillowed volcanic flows is shown.
- b. Dacitic and diabasic dikes intruding the pillow unit cut the pillowed flows at high angles. The acute angle between the mean plane of the pillowed volcanic flows and the mean dike is about 60° .
- c. The poles to bedding of volcanoclastic sandstones and radiolarian-bearing, tuffaceous mud- and siltstones are shown as well as the poles to sills (Mule Mountain volcanics). These poles define a broad girdle.
- d. The poles to bedding in the Myrtle Group define a broad girdle. The pole to the girdle is subparallel to most of the subhorizontal hinge lines measured in outcrop scale folds.

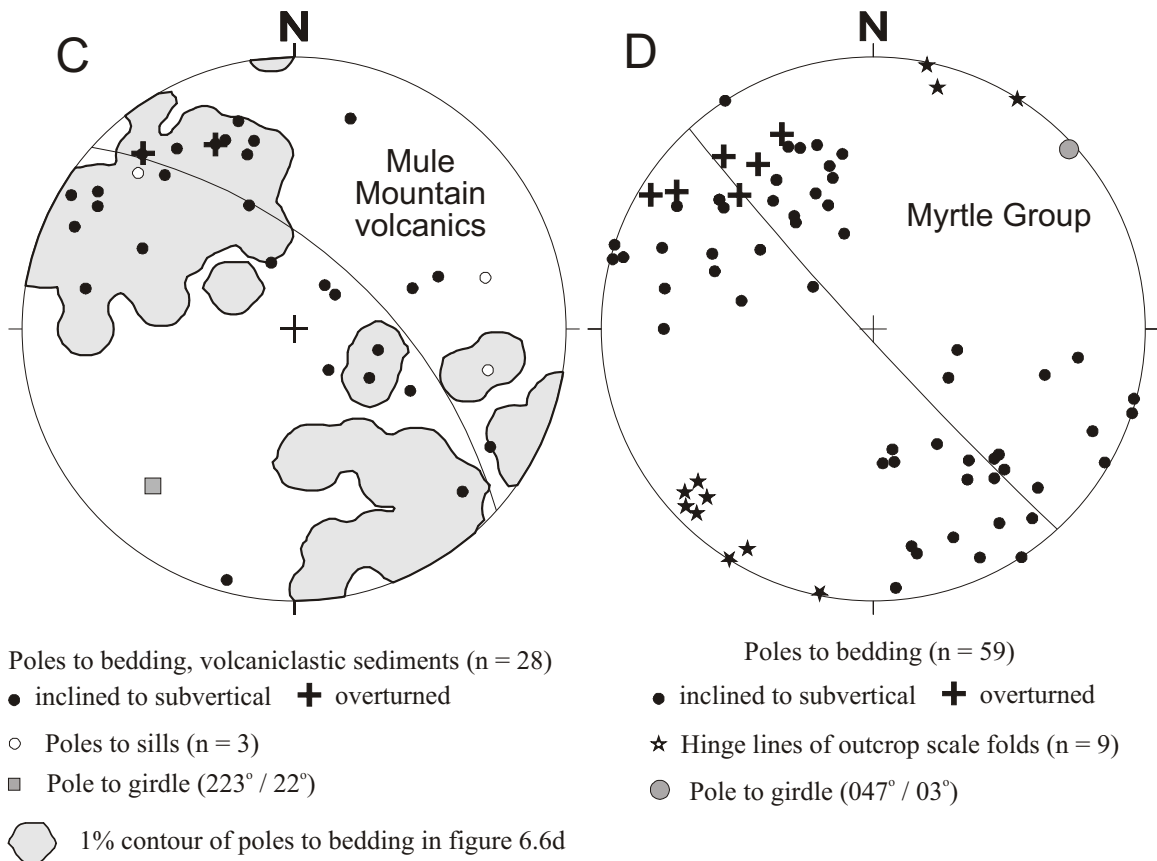
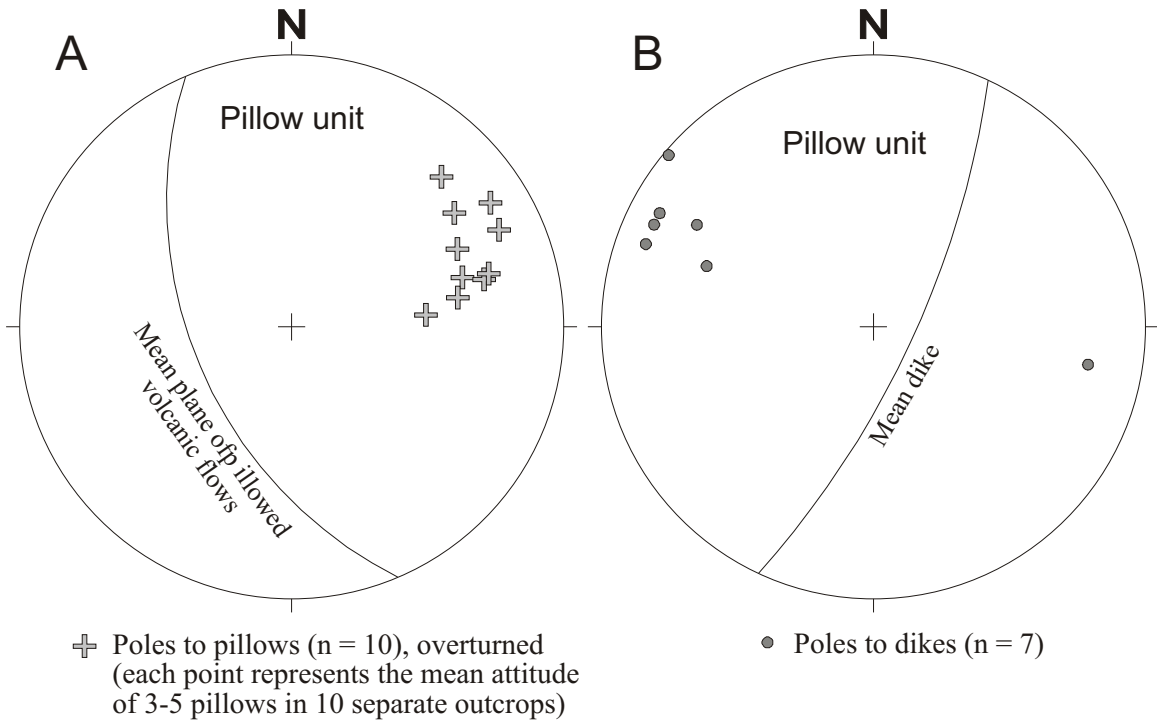
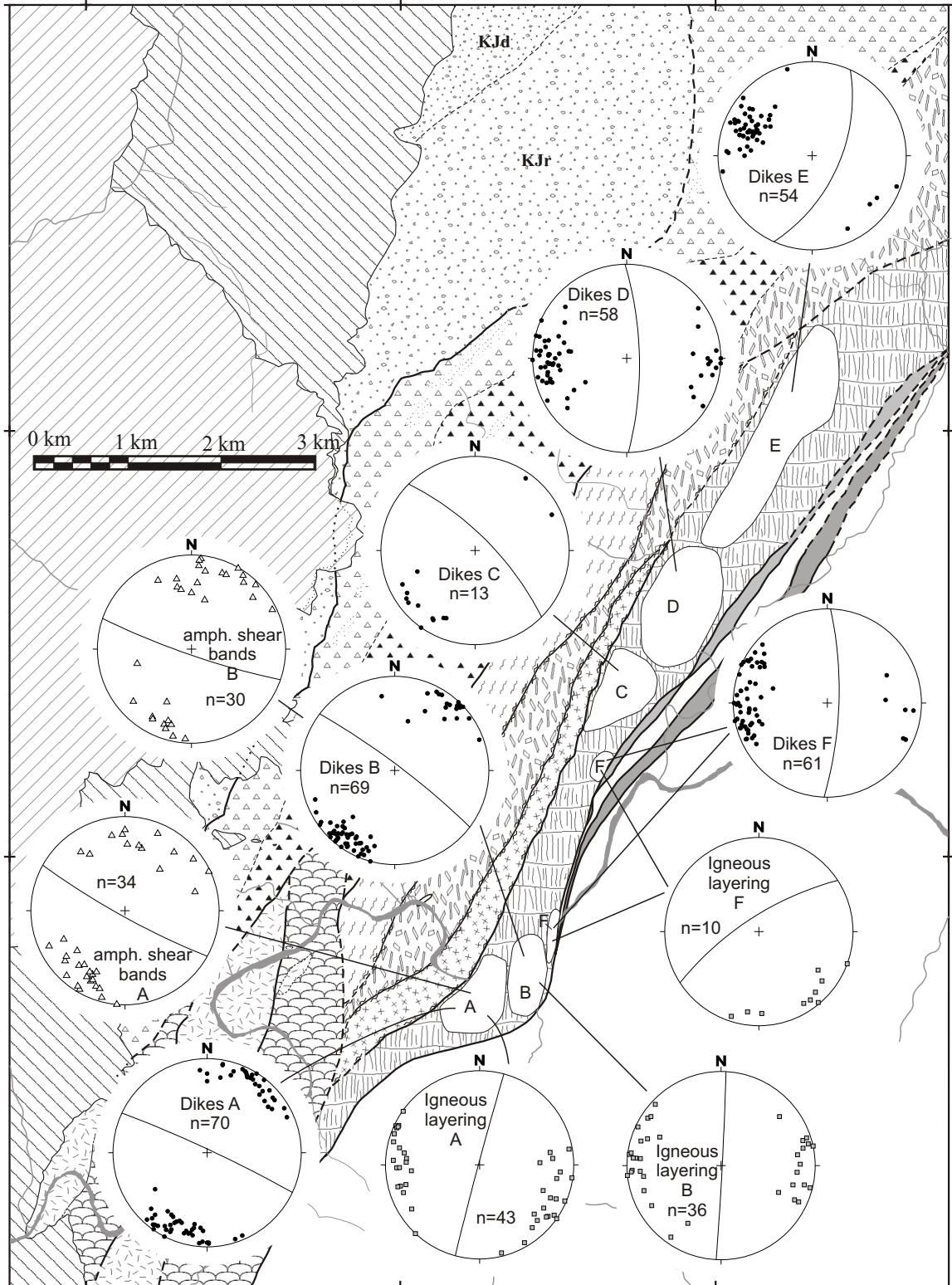
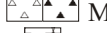
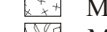
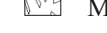


Figure 4.7

Geologic map of the Rogue Wilderness ophiolite showing the structural domains A to F in the sheeted dike complex. The structural data of each domain are presented in lower hemisphere, equal area stereographic projections. Three types of planar structures are illustrated:

1. Diabasic and microdioritic dikes; the individual measurements of the attitude of the chilled margins are plotted as poles to dike margins (solid circles; dikes A to F). The great circles indicate the mean strike and dip of the dikes in each domain (discussed in section 4.6.1).
2. Igneous layering in screens of cumulate gabbro; the data include poles to planar lamination and poles to compositional layering (squares; igneous layering A, B, and F). The mean orientations are plotted as great circles for each domain (discussed in section 4.6.2).
3. Amphibole veins and shear bands; the poles to amphibole veins and shear bands in screens of cumulate gabbro are plotted (triangles; amph. shear bands A and B). The great circles indicate the average strike and dip of these planar structures which are subparallel to the sheeted dikes in domains A and B (discussed in section 4.6.3).



- | | |
|--|---|
| <p><i>Tertiary</i> {  Tye and Flournoy Fms.</p> <p><i>Late Jurassic - early Cretaceous</i> {  Days Creek & Riddle Fms. (Myrtle Group)</p> <p> Dothan Formation</p> <p><i>Late Jurassic</i> {  Blossom Bar shear zone</p> <p> Half Moon Bar gabbro</p> | <p><i>Middle Jurassic - Late Jurassic</i> {  Mule Mountain volcanics</p> <p> Pillows</p> <p> Sheeted dikes</p> <p> Metatonalite</p> <p> Metagabbro</p> |
|--|---|

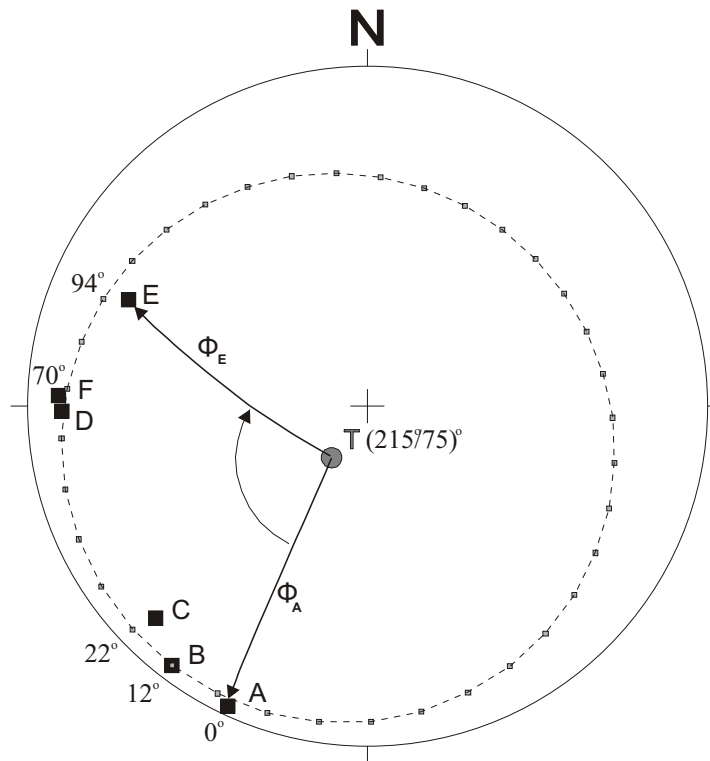


Figure 4.8

Lower hemisphere, equal area stereographic projection of pole to mean dike orientations for domains A through F (figure 4.7). The stippled, ellipse depicts the common small circle to poles A to F. The inferred rotation axis T is located in the center of the small circle. Assuming all dikes originally possessed similar attitudes prior to rotation by tilting of rigid fault blocks, it is possible to reproduce the orientation of the dikes in any one of the domains by simply rotating the dikes of anyone of the domains around T. For example, if it is assumed that the dikes in domain A remained in their original orientation since they formed, a clockwise rotation of a rigid fault block of about 94° around T would suffice to explain the orientation of the dikes in domain E. Φ_i is the angle between the tilt axis T and the poles to the mean dikes in domain i.

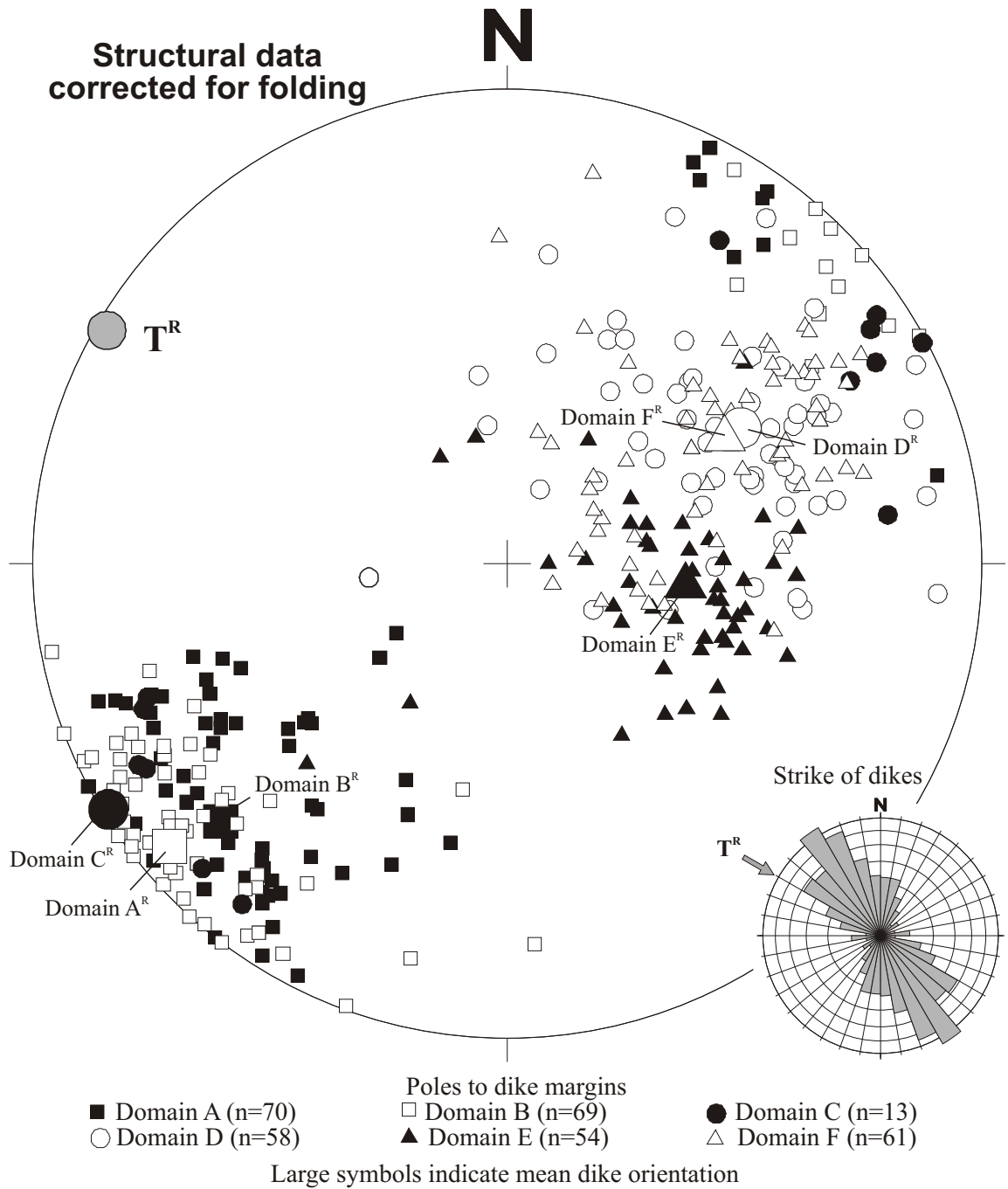


Figure 4.9

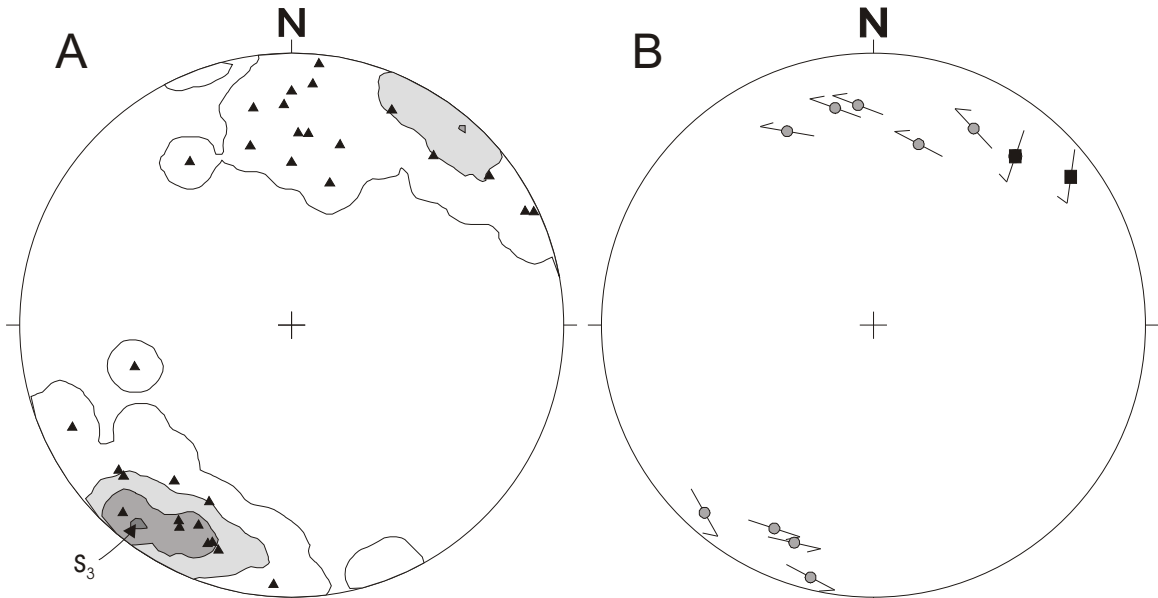
Lower hemisphere, equal area stereographic projections of poles to dikes after correcting for Tertiary and Cretaceous folding. Also, the mean dike orientations and the inferred tilt axis from figure 4.8 are shown after correcting for Tertiary and Cretaceous folding. The inset shows that 85% of the dikes strike north 010°-060° west. The restored tilt axis T^R is at an angle to the maximum of the strike of the dikes.

Figure 4.10

Analysis of structural data of domains A and B: Lower hemisphere, equal area stereographic projections of contoured poles to dikes and amphibole veins (a), of poles to shear bands (b), and the results of the paleostress analysis (c, d) using data shown in (b).

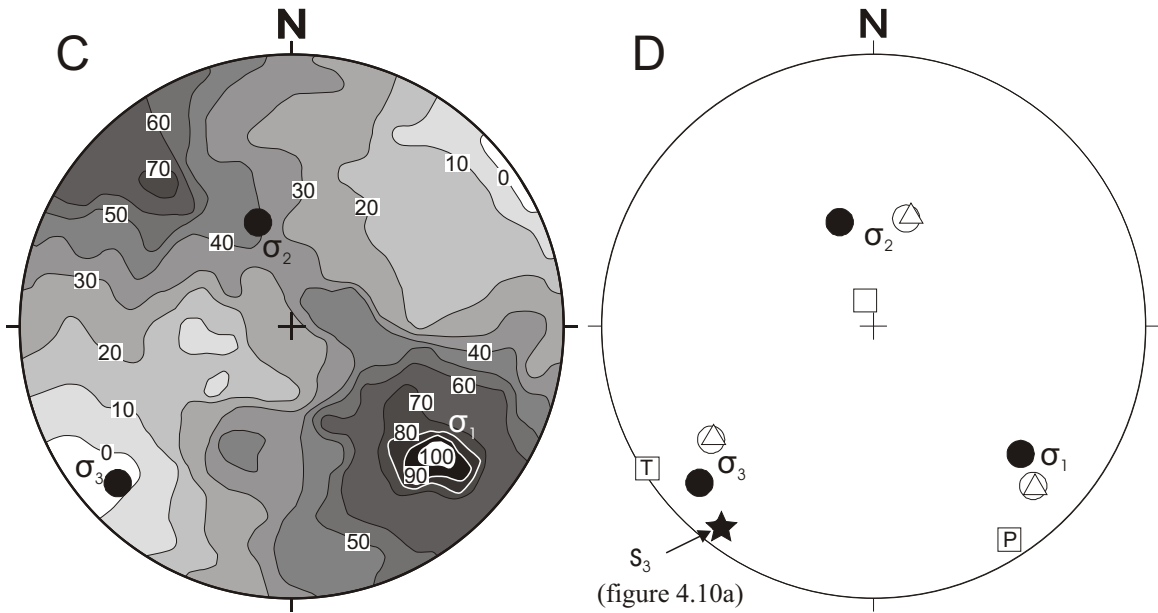
- a. The poles to dike margins ($n = 139$) and amphibole veins ($n = 31$) in domains A and B are contoured. The contour intervals are given in percent. Additionally, the poles to amphibole veins are shown. The amphibole veins shown in this diagram indicate no offsets, and the dikes and amphibole veins are interpreted to have formed by tensile fracturing (mode 1 cracks). The direction of maximum extension (minimum principal stress σ_3) is given by the maximum of the contoured poles to dike margins and amphibole veins.
- b. Poles to amphibole shear bands and their slip vectors (Hoeppener, 1955). The arrows affixed to the poles to shear bands indicate the direction of slip of the hanging wall block (see figure 4.3).
- c. Paleostress solution for the shear bands illustrated in figure 4.10b ($n = 11$) using ROMSA (Lisle, 1988). The contours express the most probable orientation of σ_1 ($131^\circ / 29^\circ$). The maximum compound likelihood is $P_{\text{Total}} = 100\%$. The corresponding σ_2 and σ_3 orientations are $341^\circ / 57^\circ$ and $228^\circ / 15^\circ$, respectively. Note that calculated σ_3 corresponds to estimate of σ_3 in figure 4.10a.
- d. Comparison of the results of the paleostress analysis for the amphibole shear bands illustrated in figure 10b using four different programs: filled circle - ROMSA (Lisle, 1988); open circle - TENSOR (Angelier, 1979); square - FAULTKIN (Allmendinger et al., 1994); triangle - STRESS (Reches, 1987). Note that the FAULTKIN returns the orientations of the compressional (P) and extensional axis (T). Small differences exist between the principal stress axis computed by the various programs. Note that the estimate for σ_3 (tensile fractures, figure 4.10a) is very close to the minimum principal stress axis computed for the shear band data.

Amphibole veins and shear bands, domain A and B



Contours include dikes ($n = 139$) and amphibole veins ($n = 31$) of domains A and B
 contour lines: 0.6, 5.3, 10.0, 15.3% / 1% area
 ▲ poles to amphibole veins

● Right-lateral strike-slip/oblique-slip faults ($n = 9$)
 ■ Normal faults ($n = 2$)



ROMSA

(figure 4.10a)

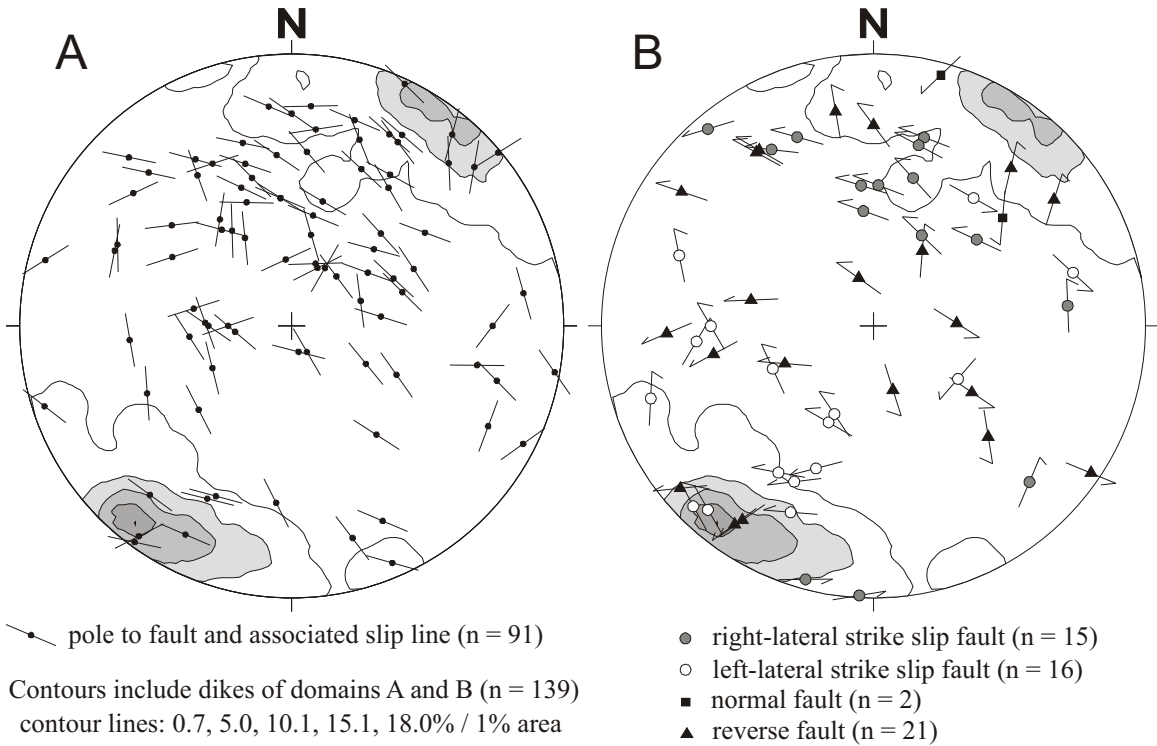
● ROMSA △ STRESS
 ○ TENSOR □ FAULTKIN

Figure 4.11

Analysis of structural data of domains A and B: Lower hemisphere, equal area stereographic projections of poles to cemented faults superimposed on contoured poles to dikes (a, b), and the results of the paleostress analysis (c, d) using data shown in (b).

- a. Poles to 91 cemented faults (filled circles) superimposed on the contoured plot of poles to dikes. The direction of slip along the fault is indicated by the line affixed to the poles similar to the Hoepfner plot in figure 4.3. The sense of slip was not determined in outcrop, therefore, only the directions, but not the sense of slip are shown.
- b. Poles to 54 cemented faults where sense of shear could be determined and their slip vectors (Hoepfner, 1955). The arrows affixed to the poles to cemented faults indicate the direction of slip of the hanging wall block (see figure 4.3).
- c. Stress inversion solution for cemented faults of figure 4.11b ($n = 54$) using ROMSA (Lisle, 1988). The contours (in %) express the most probable orientation of σ_1 ($292^\circ / 04^\circ$). The maximum compound likelihood is $P_{\text{Total}} = 56.4\%$. The calculated σ_2 and σ_3 orientations are $201^\circ / 14^\circ$ and $038^\circ / 75^\circ$, respectively.
- d. Comparison of the results of the paleostress analysis using four different programs: solid symbol - ROMSA (Lisle, 1988); circle - TENSOR (Angelier, 1979); square - FAULTKIN (Allmendinger et al., 1994); triangle - STRESS (Reches, 1987). The principal stress axes computed by the four different programs for the fault slip data shown in figure 4.11b agree well. Note that the principal stress axes σ_2 and σ_3 are switched compared to the axes shown in figure 4.10d. The σ_1 -directions in figures 4.10d and 4.11d are subparallel.

Brittle faults, domain A and B



Contours include dikes of domains A and B (n = 139)
contour lines: 0.7, 5.0, 10.1, 15.1, 18.0% / 1% area

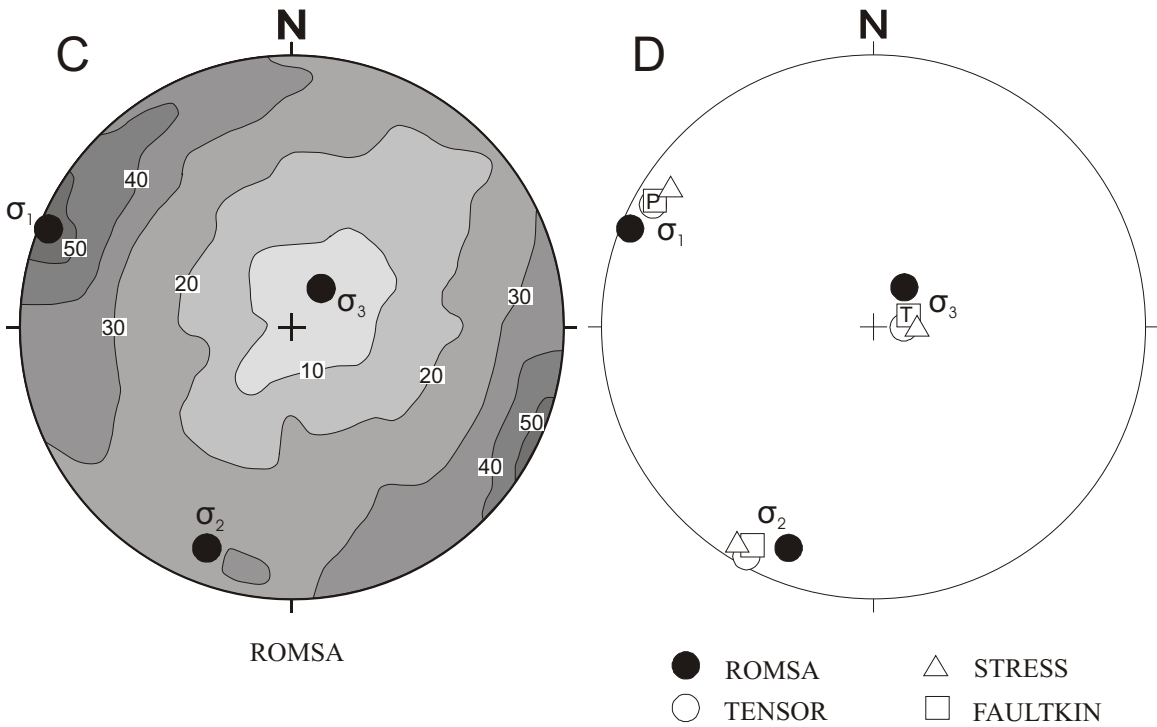
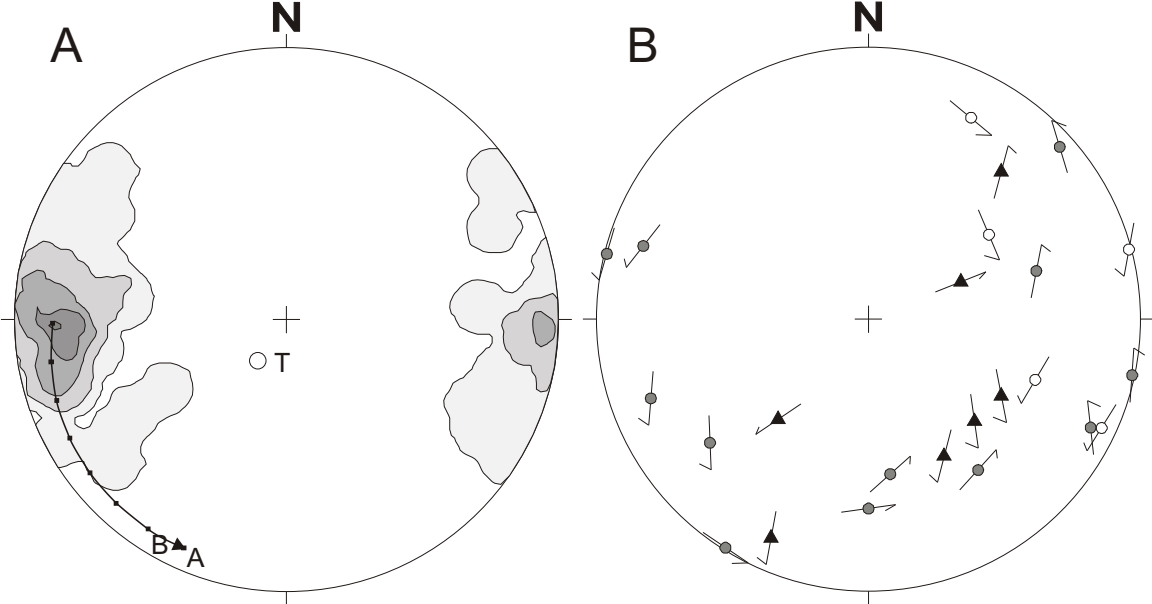


Figure 4.12

Analysis of structural data of domain D: Lower hemisphere, equal area stereographic projections of poles to dike margins (a), of poles to cemented faults (b), and the results of the paleostress analysis (c, d) using data shown in (b).

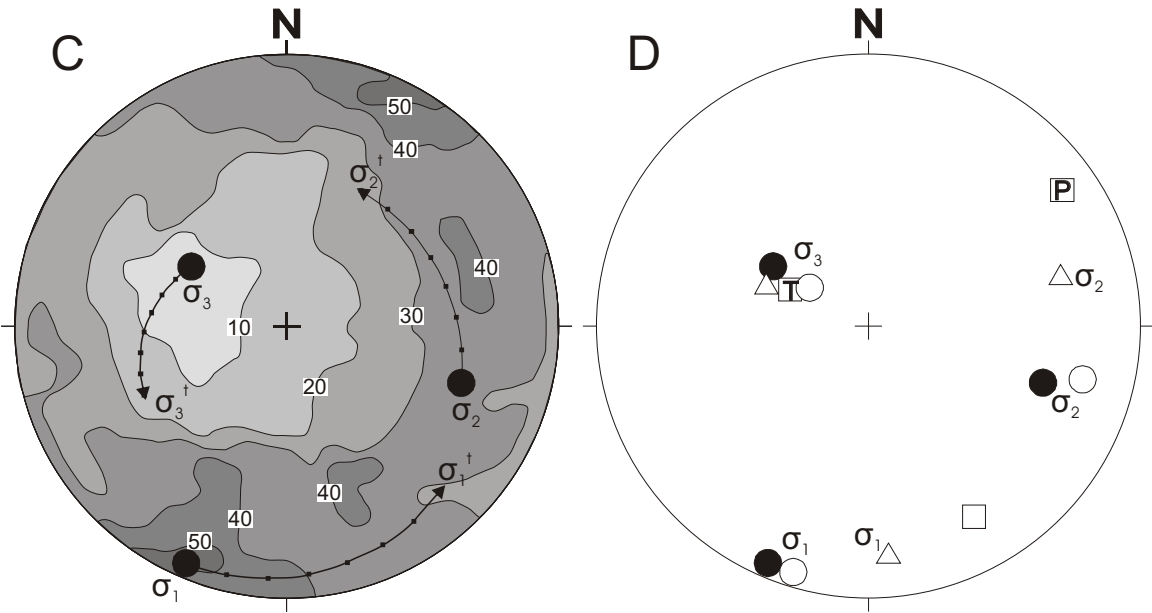
- a. Contoured plot of poles to dikes in domain D. The contour intervals are given in percent. The dikes in domain D are rotated $60^\circ - 70^\circ$ clockwise around a subvertical axis ($T = 215^\circ / 75^\circ$) with respect to the mean poles of dikes of domains A and B shown as “A” and “B” (figure 4.8, also compare figures 4.11a and 4.12a). The arrow indicates the position of the maximum contour assuming an anti-clockwise rotation of the mean dike pole to that of A by 70° around T.
- b. Poles to cemented faults and their slip vectors (Hoepfner, 1955). The arrows affixed to the poles to cemented faults indicate the direction of slip of the hanging wall block (see figure 3). Most faults suparallel to the sheeted dikes are right-lateral transfer faults.
- c. Paleostress analysis solution for cemented faults illustrated in figure 12b ($n = 24$) using ROMSA (Lisle, 1988). The contours express the most probable orientation of σ_1 ($203^\circ / 06^\circ$). The maximum compound likelihood is $P_{\text{Total}} = 56.4\%$. The corresponding σ_2 and σ_3 orientations are $108^\circ / 33^\circ$ and $302^\circ / 56^\circ$, respectively. The arrows show the position of the principal stress axes after the cemented faults are rotated 70° in an anticlockwise direction around tilt-axis T.
- d. Comparison of the results of the paleostress analysis using four different programs: filled circle - ROMSA (Lisle, 1988); open circle - TENSOR (Angelier, 1979); square - FAULTKIN (Allmendinger et al., 1994); triangle - STRESS (Reches, 1987). Significant differences exist between the principal stress axes computed by the four different programs for the data shown in figure 4.12b. Note that the principal stress axes σ_1 and σ_2 are variable whereas all programs computed similar σ_3 -directions.

Brittle faults, domain D



Contours include dikes of domain D (n = 58)
 contour lines: 1.7, 5.2, 10.3, 15.5, 19.0% / 1% area

- right-lateral strike-slip faults (n = 12)
- left-lateral strike-slip faults (n = 5)
- ▲ reverse faults (n = 7)



- ROMSA
- TENSOR
- △ STRESS
- FAULTKIN

Figure 4.13

Summary of the criteria used to infer the sense-of-shear (after Passchier and Trouw, 1996, p. 105) in mylonitic rocks from the metatonalite unit, metagabbro unit and the Blossom Bar shear zone. First, the thin sections are cut parallel to lineation and perpendicular to foliation, then the sense of shear was determined and the thin sections were reoriented to determine the shear sense in present-day coordinates. Consistent results between samples were obtained (see text).

Figure 4.13a

- Grain shape fabric

An oblique foliation, also termed oblique grain shape fabric (GSF), occurs in samples containing monomineralic layers of recrystallized quartz. During non-coaxial progressive deformation, the fabric forming elements developing in the monomineralic layers do not track the rotating principal directions of finite strain (Means, 1981). Thus, the angular relationship between the mylonitic foliation and the elongate shape of most of the grains allow to deduce the shear sense if the oblique GSF developed during the formation of the mylonite. The geometric relationship between C and the elongate shape of the grains developing in sinistral shear is shown.

- S/C and C/C'

Hanmer and Passchier (1991) interpret S-planes ('schistosity') and C-planes ('cisaillement') as follows: S-planes represent a strain-sensitive flattening (*sensu lato*) fabric which attempts to track the XY plane of the finite strain ellipsoid during progressive deformation, while C-planes are discrete narrow shear zones which are taken to lie parallel to the flow plane of the progressive deformation. In a S/C fabric, C is a pervasive foliation and S is (ideally) deflected or cut by C-foliation. C'-planes are called asymmetric extensional shear bands because they lie at an angle with respect to the flow plane of the progressive deformation.

Figure 4.13a continued

- Microfaults in porphyroclasts

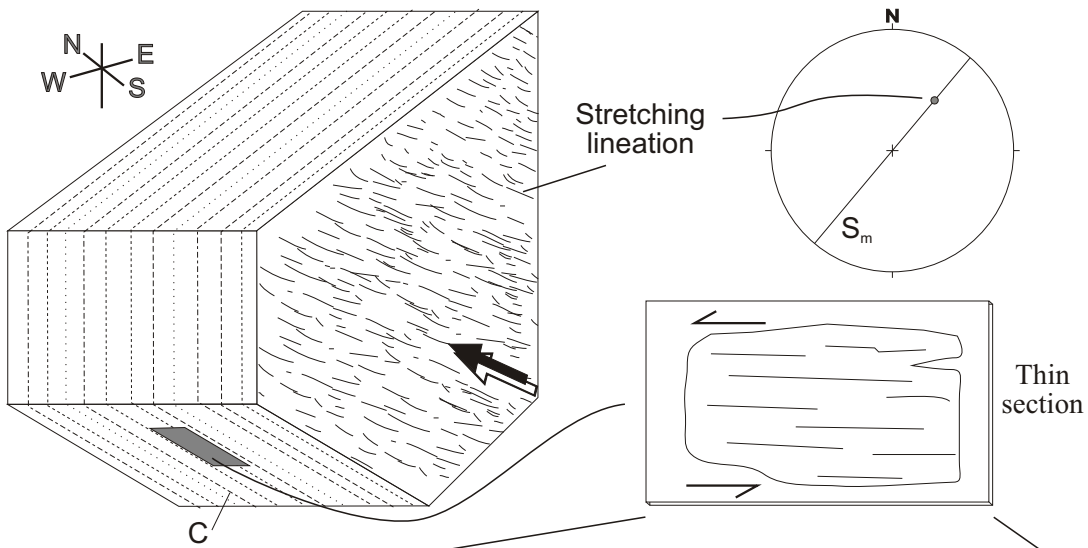
Rigid minerals occurring in a soft, plastically deforming matrix, often show cracks along weak planes, such as cleavage planes, apparently because they cannot accommodate large strains by crystal plastic mechanisms. With continued shearing the rigid grains rotate and the fragments of each grain slide past each other along the fractures, allowing grains to extend in the direction of flow (Hanmer and Passchier, 1991). Two types of microfaults are distinguished: high angle fractures (50° - 130°) with antithetic offsets and low-angle fractures (0° - 20° and 160° - 180°) with synthetic offsets. The angles in between (20° - 50° and 130° - 160°) are ambiguous because rotation of the fractured grain may cause initial high angle fractures to change orientation (Simpson and Schmid, 1983).

- Other sense of shear indicators

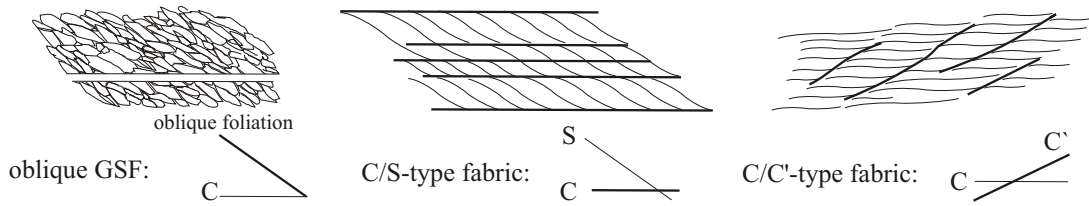
Other sense-of-shear indicators found in thin section include tiling of rigid minerals or mineral fragments and deformed quartz veins which could be used as displacement markers.

Hanmer and Passchier (1991) pointed out that tiling structures are not a reliable shear-sense indicator because the interpretation of the formation of the tiling structures is not unique. Therefore, the tiling structures are only reported as an additional shear sense indicator which may or may not agree with the other sense-of-shear criteria used in this study. Tiling structures are interpreted to form when rigid inclusions in a soft matrix are subjected to non-coaxial flow and interfere with each other and block each other's rotational behavior. In sinistral shear, the inclusions block at left-stepping overlaps forming structures resembling imbricated dominos or tipped books on a bookshelf.

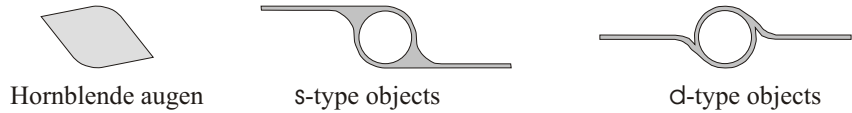
Several mylonites (appendix D) contain quartz veins which are less recrystallized than the quartz in the matrix. Quartz in the veins shows subgrains and undulatory extinction. Typically, the veins are less than 0.3 mm wide, they do not contain disseminated flakes of other minerals commonly found in the matrix, and the boundaries of the quartz veins are relatively sharp. These characteristics were used to trace the quartz veins under the microscope, and it was noted that some quartz veins are offset as they cut cloudy layers of fine-grained, fractured epidote and other Ca-Al-silicates. This was used to determine the sense of shear.



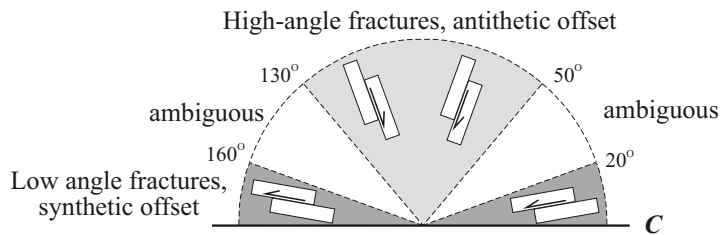
Foliation and shear bands:



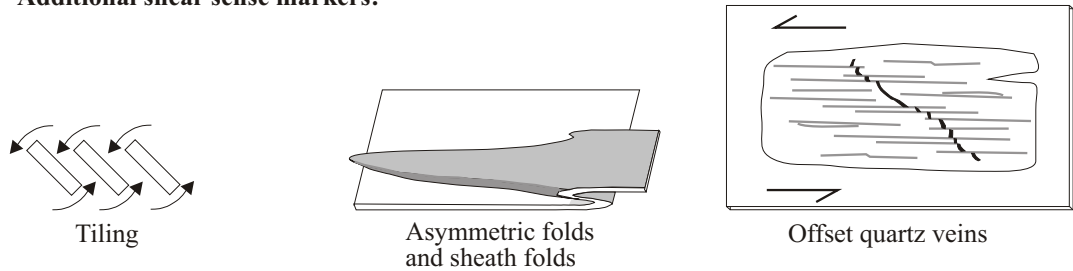
Porphyroclasts:



Microfaults in rigid inclusions:



Additional shear sense markers:



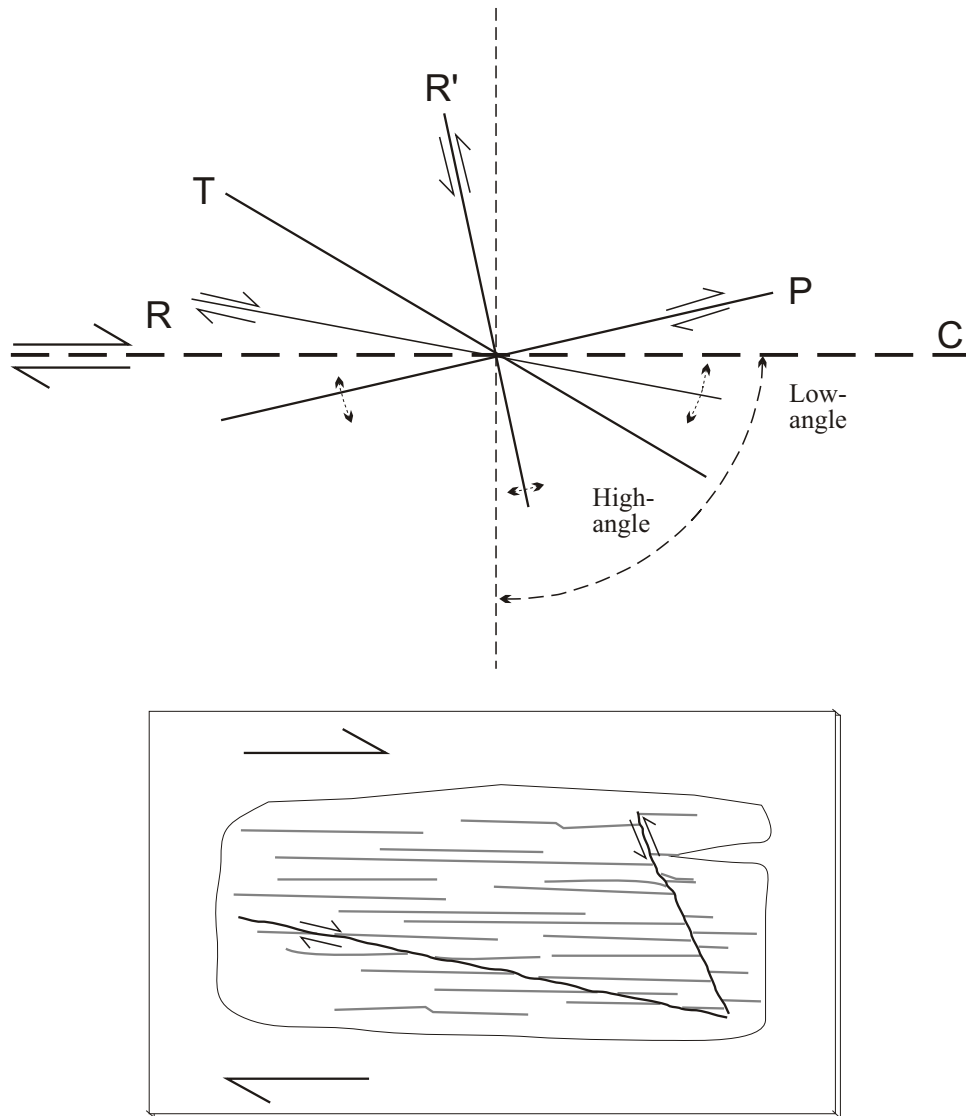


Figure 4.13b

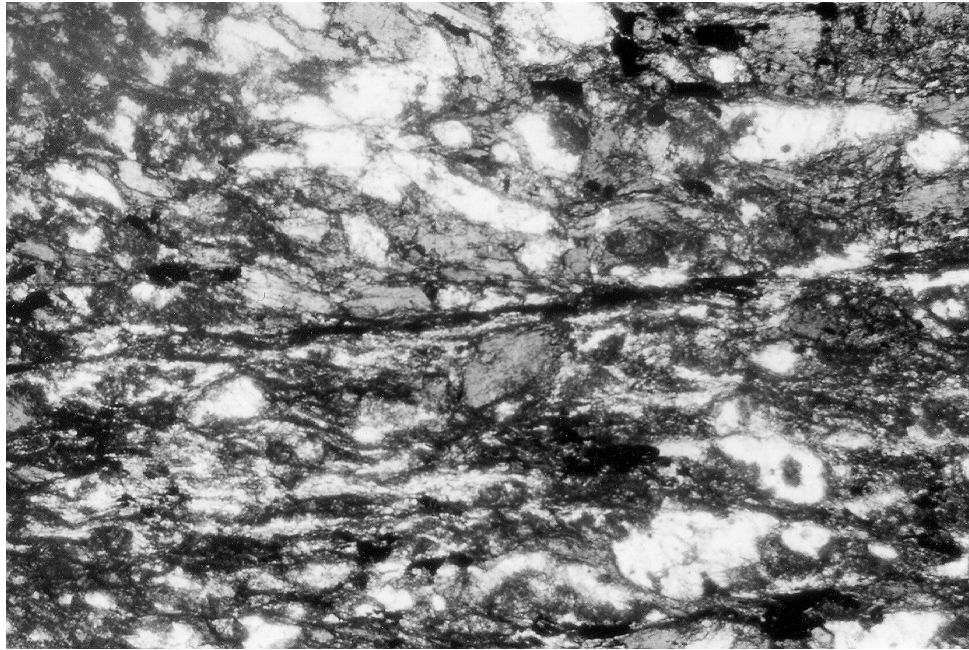
Riedel-type shears

In thin sections, cut parallel to stretching lineation and normal to foliation, microfaults occur at high and low angles with respect to the mylonitic foliation (next page), and the mylonitic foliation is occasionally offset along such microfaults (typically < 0.2 mm offset). The sense of shear on these microfaults is interpreted as that of secondary shear fractures similar to Riedel shears in brittle fault zones.

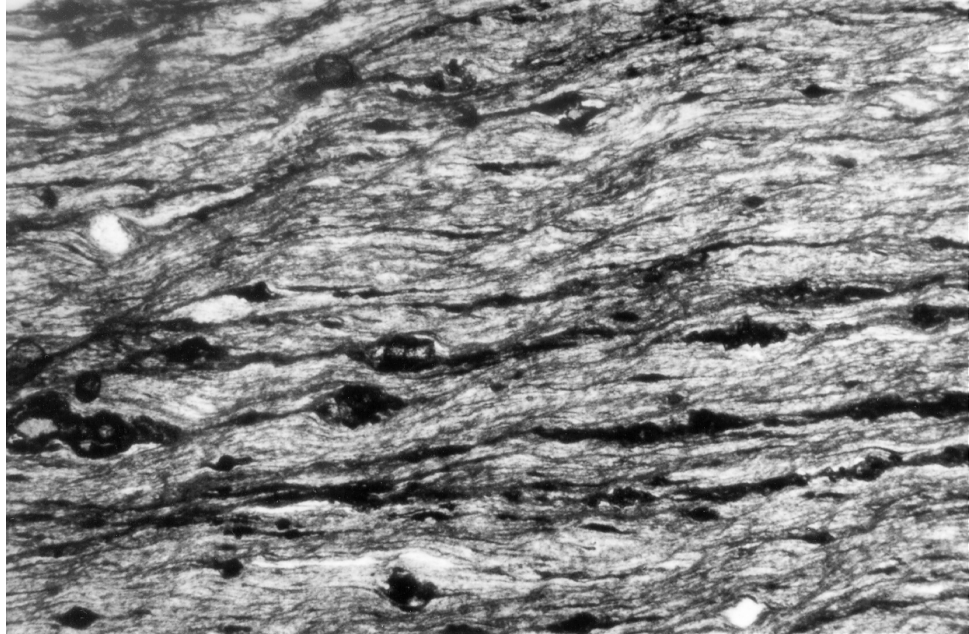
Figure 4.14

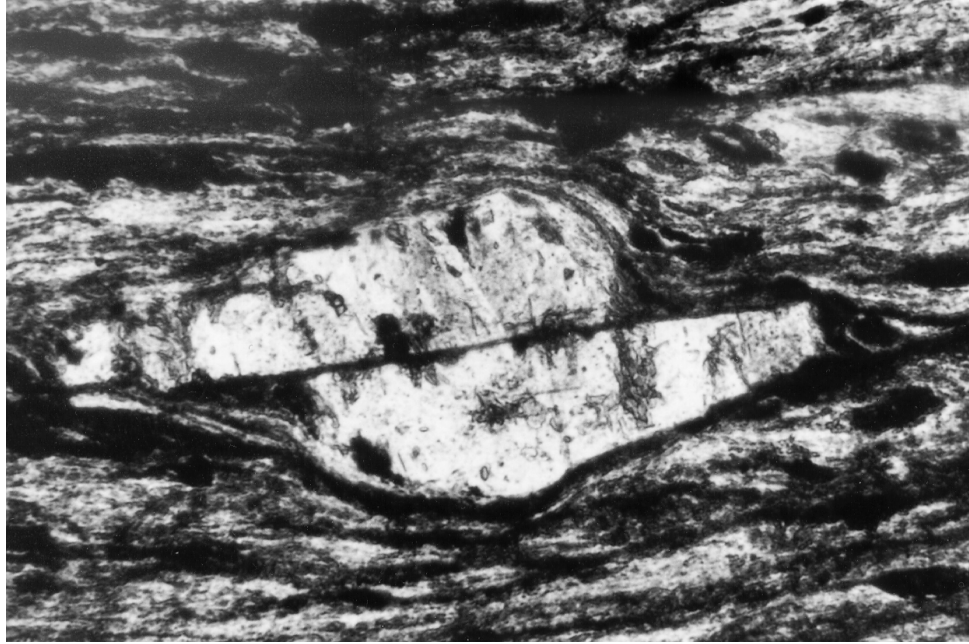
- A. Fabric in a mafic mylonite from the metagabbro unit (O/C-374b.4). This fabric has a similar geometry as S/C-type fabrics in quartzo-feldspathic rocks. The S-foliation (upper left to lower right) is defined by the alignment of elongate plagioclase and hornblende, whereas the transecting C-planes (horizontal) consist of extremely fine grained minerals (probably Ca-Al-silicates, chlorite, magnetite). The sense of shear is sinistral. The width of the photomicrograph is 2.12 mm (plane light).
- B. Example of a C/C'-type fabric in a chlorite-rich sample from the metatonalite unit (sample O/C-368e). The C'-planes trending from upper right to lower left are also termed "asymmetric extensional shear bands". The sense of shear is sinistral. Note the inclusions with tails indicating the same sense of shear. The width of the photomicrograph is 2.12mm (plane light).
- C. Fractured plagioclase porphyroclast with a low-angle, synthetic microfault (sample O/C-368e). The sense of shear is sinistral. The width of the photomicrograph is 0.54 mm (plane light).
- D. Fractured plagioclase porphyroclast with two high-angle, antithetic microfaults (sample O/C-368e). The sense of shear is sinistral. The width of the photomicrograph is 2.12 mm (crossed Nichols).
- E. Mylonite consisting of alternate layers of quartz and epidote \pm chlorite. Winged porphyroclasts of plagioclase and epidote can be used as sense of shear indicators, if porphyroclasts developed a monoclinic shape symmetry similar to σ - and δ -type objects (see figure 13). In this photomicrograph most porphyroclasts with monoclinic shape symmetry indicate sinistral shear (some σ -type inclusions seem to indicate dextral shear).

A



B





C



D

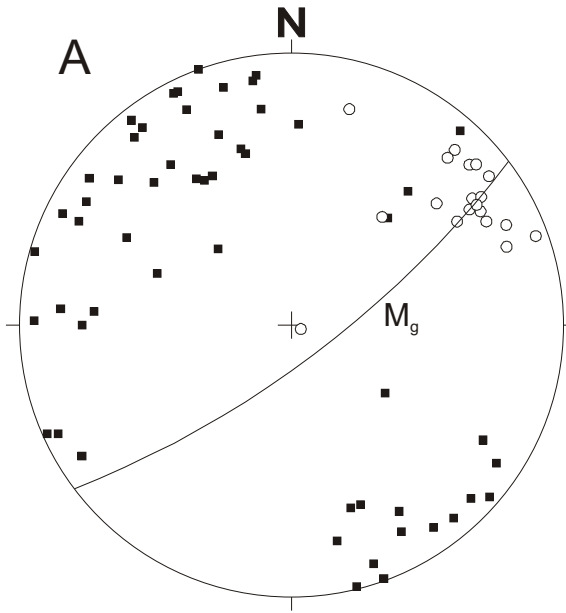
E



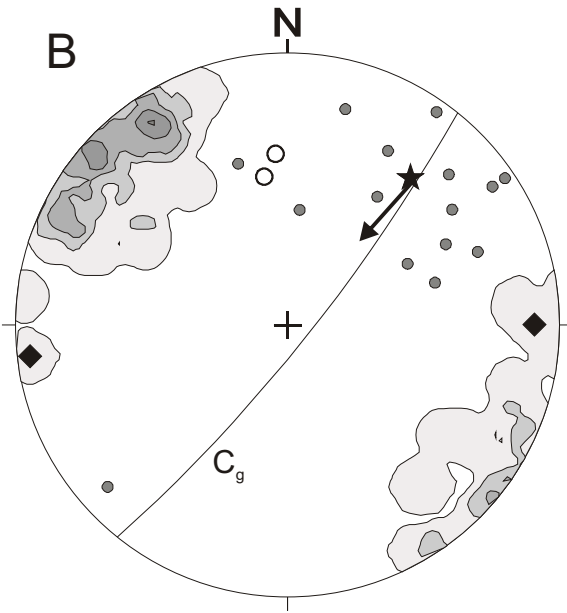
Figure 4.15

Lower hemisphere, equal area stereographic projections of foliations and lineations in the metagabbro unit, metatonalite unit and Blossom Bar shear zone.

- A. Poles to magmatic foliation in the metagabbro unit. The mean magmatic foliation M_g is shown as a great circle. The lineation is defined by the preferred orientation of subhedral hornblende and is interpreted as magmatic in origin (see text).
- B. Contoured poles to shear foliation in the metagabbro unit. The mean shear foliation C_g is shown as a great circle, which is subparallel to the magmatic foliation M_g . The stretching lineations scatter considerably, but the group mean of the stretching lineation plots close the great circle C_g . Sense of shear is dextral with a thrust-component.
- C. Contoured poles to shear foliation in the metatonalite unit. The mean shear foliation is plotted as a great circle (C_t). The mean shear foliation C_t is very similar in attitude to the mean shear foliation in the metagabbro unit. The stretching lineations are more clustered in the metatonalite unit than in the metagabbro unit. Shear sense is dextral with a thrust component.
- D. Contoured poles to shear foliation in the Blossom Bar shear zone. The strike of the mean shear foliation (C_{sz}) is subparallel to the shear foliation in the metagabbro unit and the metatonalite unit. However, the mean shear foliation dips steeply northwest. Also, most stretching lineations plunge steeply northwest. The sense of shear is normal.

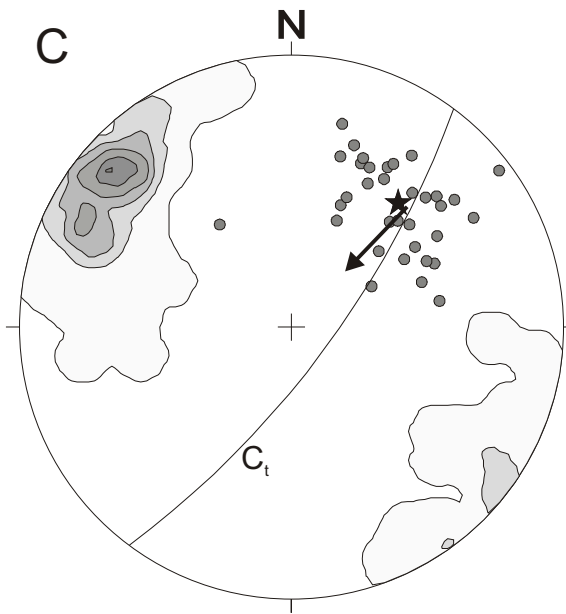


- pole to magmatic foliation (n=54)
- magmatic mineral lineation (n=19)

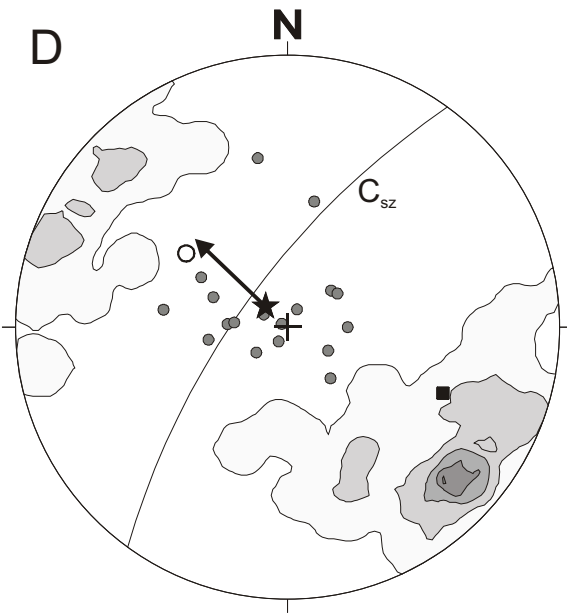


- Contours include shear foliation in metagabbro unit (n = 47)
 contour lines: 2.1, 6.4, 10.6, 14.9, 19.2% / 1% area
- stretching lineation (n = 17)
 - ★ mean stretching lineation

- pole to foliation
 - ◆ stretching lineation
- } O/C-372b, GH-97-6



- Contours include shear foliation in metatonalite unit (n = 115)
 contour lines: 0.9, 5.2, 10.4, 14.8, 20.0, 22.6% / 1% area
- stretching lineation (n = 34)
 - ★ mean stretching lineation



- Contours include foliation in Blossom Bar shear zone (n = 104)
 contour lines: 1.0, 4.8, 9.6, 14.4, 17.3% / 1% area
- stretching lineation (n = 19)
 - ★ mean stretching lineation
 - pole to foliation
 - stretching lineation
- } (O/C-17-S32)

Figure 4.16

Lower hemisphere, equal area stereographic projections of mean shear plane C_1 and stretching lineation in the metatonalite unit (a), of poles to cemented faults (b), and the results of the paleostress analysis (c, d) using data shown in (b).

- a. The contours of poles to shear foliation from figure 4.16a are shown as well as the mean shear plane C_1 and the mean stretching lineation. The arrow indicate the direction of transport (dextral-thrust). Additionally, the pole to C_1 with associated slip vector is shown (see figure 4.3).
- b. Poles to cemented faults and their associated slip vectors (Hoeppener, 1955). The arrows affixed to the poles to cemented faults indicate the direction of slip of the hanging wall block (see figure 4.3). Faults occurring at low angles with respect to the foliation (#1 and #5) have synthetic offsets (dextral-thrust), and faults occurring at high angles with respect to the foliation (# 2, #3 and #4) have antithetic offsets (sinistral-thrust) with respect to shear parallel C_1 in the direction of the mean stretching lineation.
- c. Solution of the analysis of cemented faults illustrated in figure 16b ($n = 19$) using ROMSA (Lisle, 1988). The contours (in %) express the most probable orientation of σ_1 ($062^\circ / 18^\circ$). The maximum compound likelihood is $P_{\text{Total}} = 77.1\%$ (contour interval = 10%). The corresponding σ_2 and σ_3 orientations are $154^\circ / 11^\circ$ and $273^\circ / 69^\circ$, respectively.
- d. Comparison of the results of the paleostress analysis using four different programs: solid symbol - ROMSA (Lisle, 1988); circle - TENSOR (Angelier, 1979); square - FAULTKIN (Allmendinger et al., 1994); triangle - STRESS (Reches, 1987). Significant differences exist between the principal stress axes computed by the four different programs for the data shown in figure 16b. Note that all programs computed almost identical σ_1 (T) directions whereas the programs returned various σ_2 - and σ_3 - directions which plot within the $\sigma_2\sigma_3$ plane normal to σ_1 .

Shear foliation and brittle faults, metatonalite unit

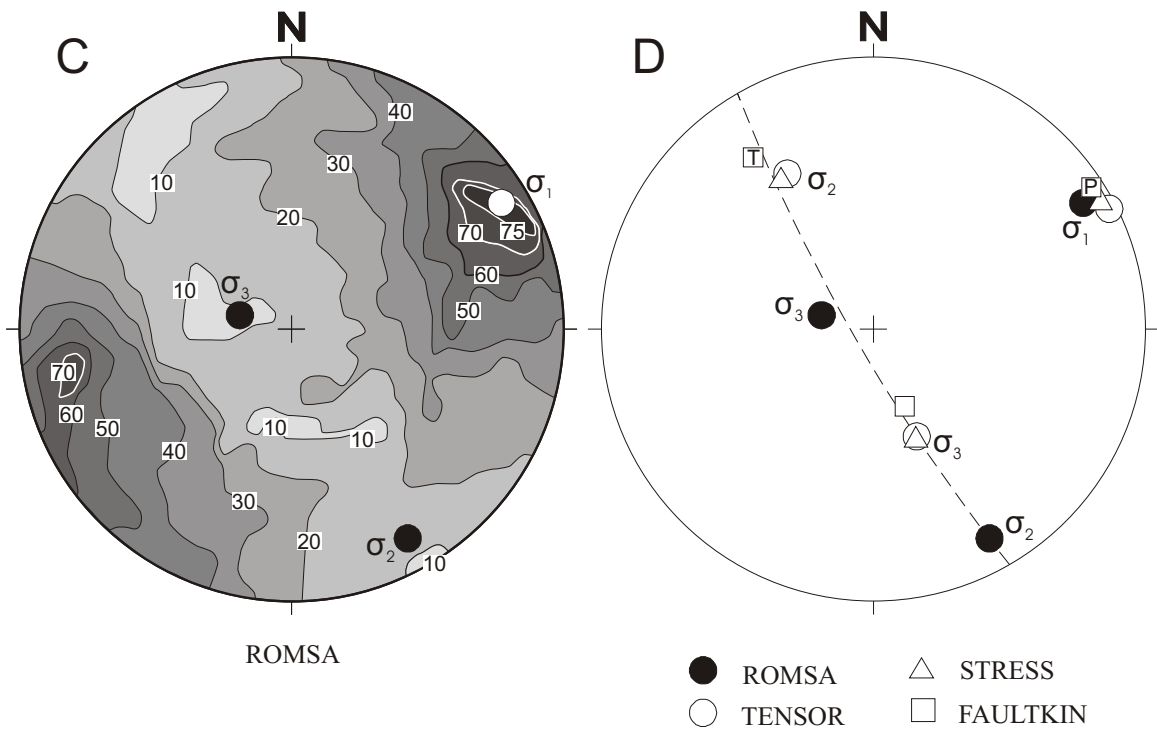
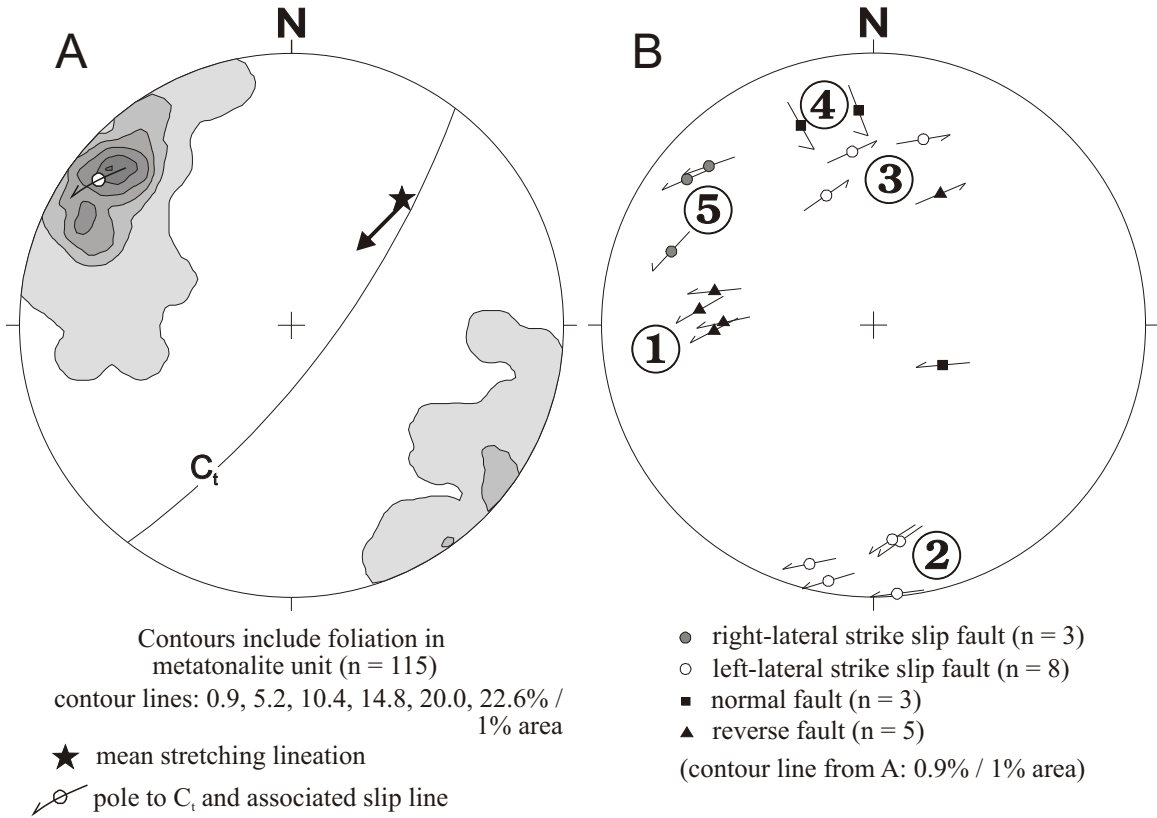
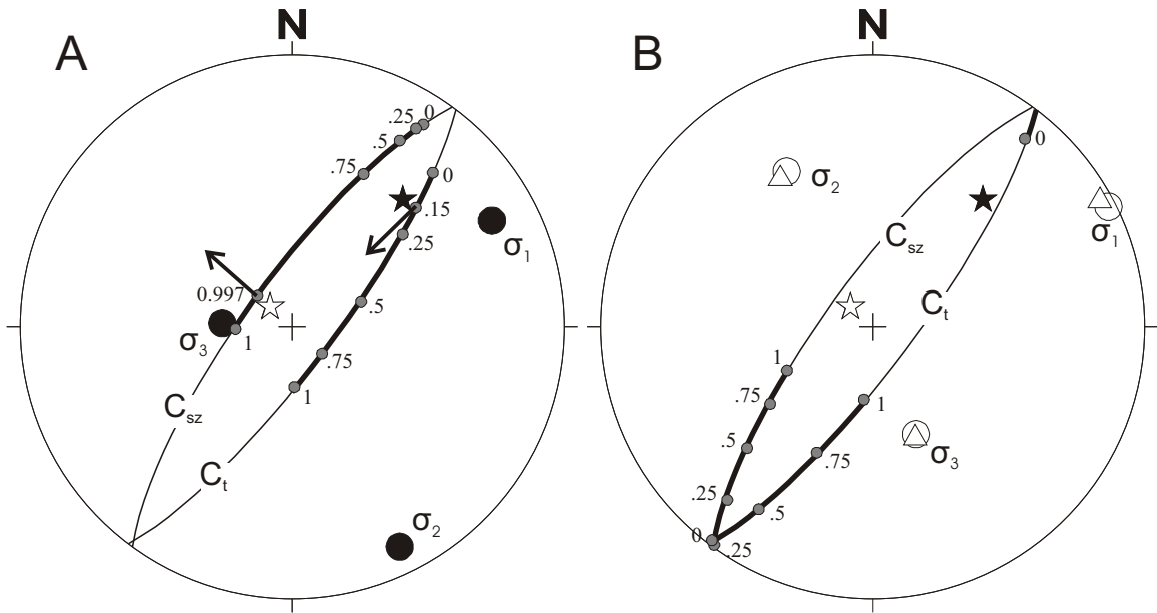


Figure 4.17

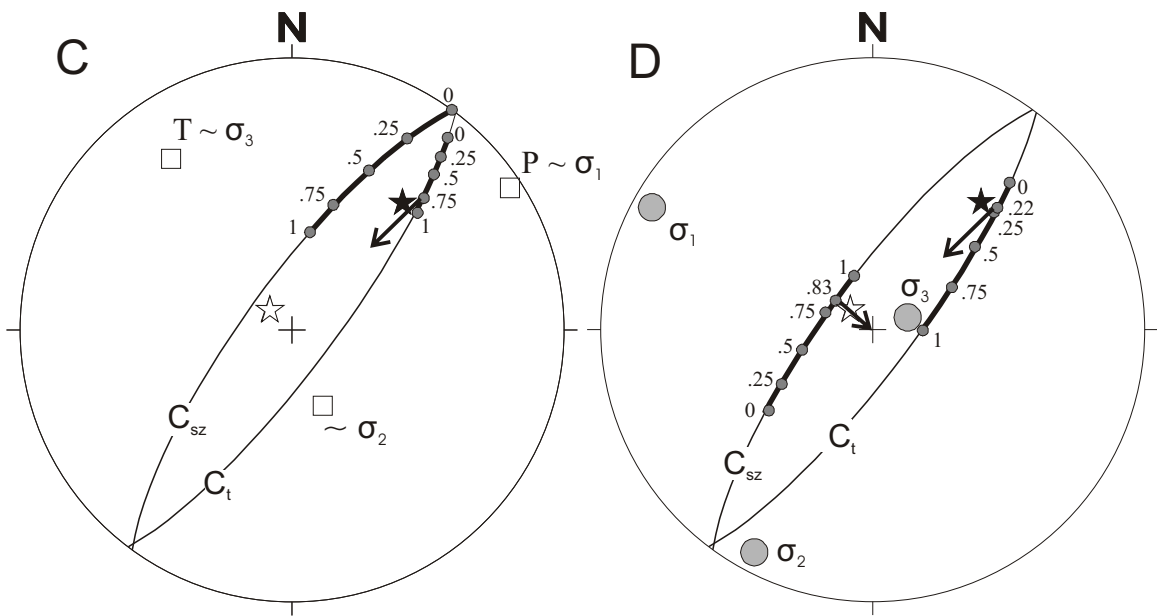
Lower hemisphere, equal area stereographic projections of the mean shear plane C_t and C_{sz} as well as corresponding mean stretching lineations L_t and L_{sz} in the metatonalite unit and Blossom Bar shear zone, respectively. The directions of the shear stress τ on C_t and C_{sz} for different stress fields are determined using the graphical method of Means (1989).

- a. The shear stress on C_t is parallel to the mean stretching lineation L_t if $\varphi = 0.15$, while the shear stress on C_{sz} is parallel to the mean stretching lineation L_{sz} if $\varphi = 0.997$.
- b. The shear stress on C_t and C_{sz} is not parallel to L_t and L_{sz} , respectively, for any value of φ .
- c. The shear stress on C_t is parallel to the mean stretching lineation L_t if $\varphi = 0.96$, whereas the shear stress on C_{sz} is not parallel to L_{sz} for any value of φ .
- d. The shear stress on C_t is parallel to the mean stretching lineation L_t if $\varphi = 0.22$, whereas the shear stress on C_{sz} is parallel to the mean stretching lineation L_{sz} if $\varphi = 0.83$. The direction of the shear stress is opposite to the sense of shear determined in mylonitic samples from the Blossom Bar shear zone.



● Stress axes determined by analysis of brittle faults in metatonalite unit using ROMSA

○ △ Stress axes determined by analysis of brittle faults in metatonalite unit using TENSOR and STRESS



□ P and T axes determined by analysis of brittle faults in metatonalite unit using FAULTKIN

● Mean of results from the paleostress analysis of brittle faults in the sheeted dike complex (domains A and B, figure 4.11d)

Explanation

- ☆ Mean stretching lineation (L_{sz}) in Blossom Bar shear zone
- ★ Mean stretching lineation (L_i) in metatonalite unit

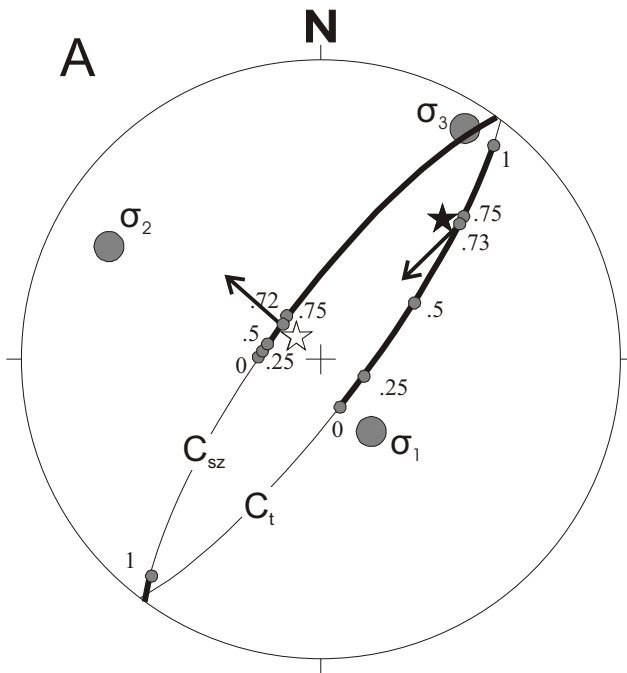
- C_t Mean foliation plane metatonalite unit
- C_{sz} Mean foliation plane Blossom Bar shear zone

- Shear stress τ on C_i for various values of ϕ $\phi = (\sigma_2 - \sigma_3) / (\sigma_1 - \sigma_3)$

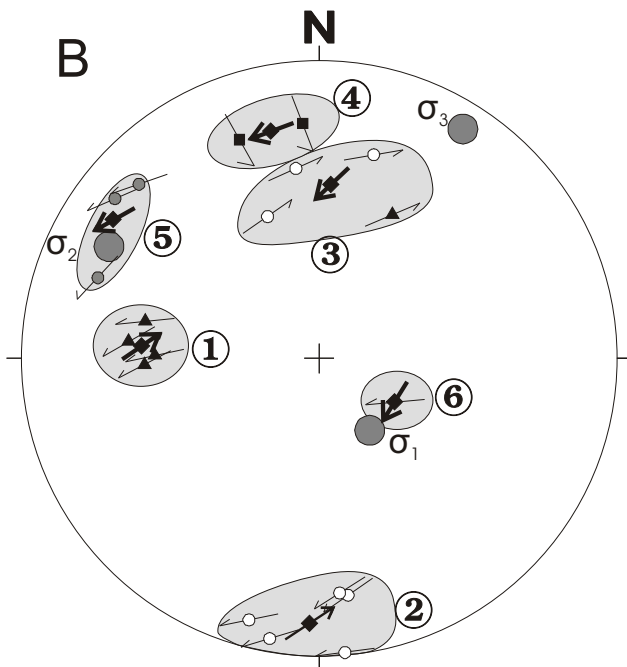
／ All possible directions of τ in the foliation plane C_i ($0 < \phi < 1$)

Figure 4.18

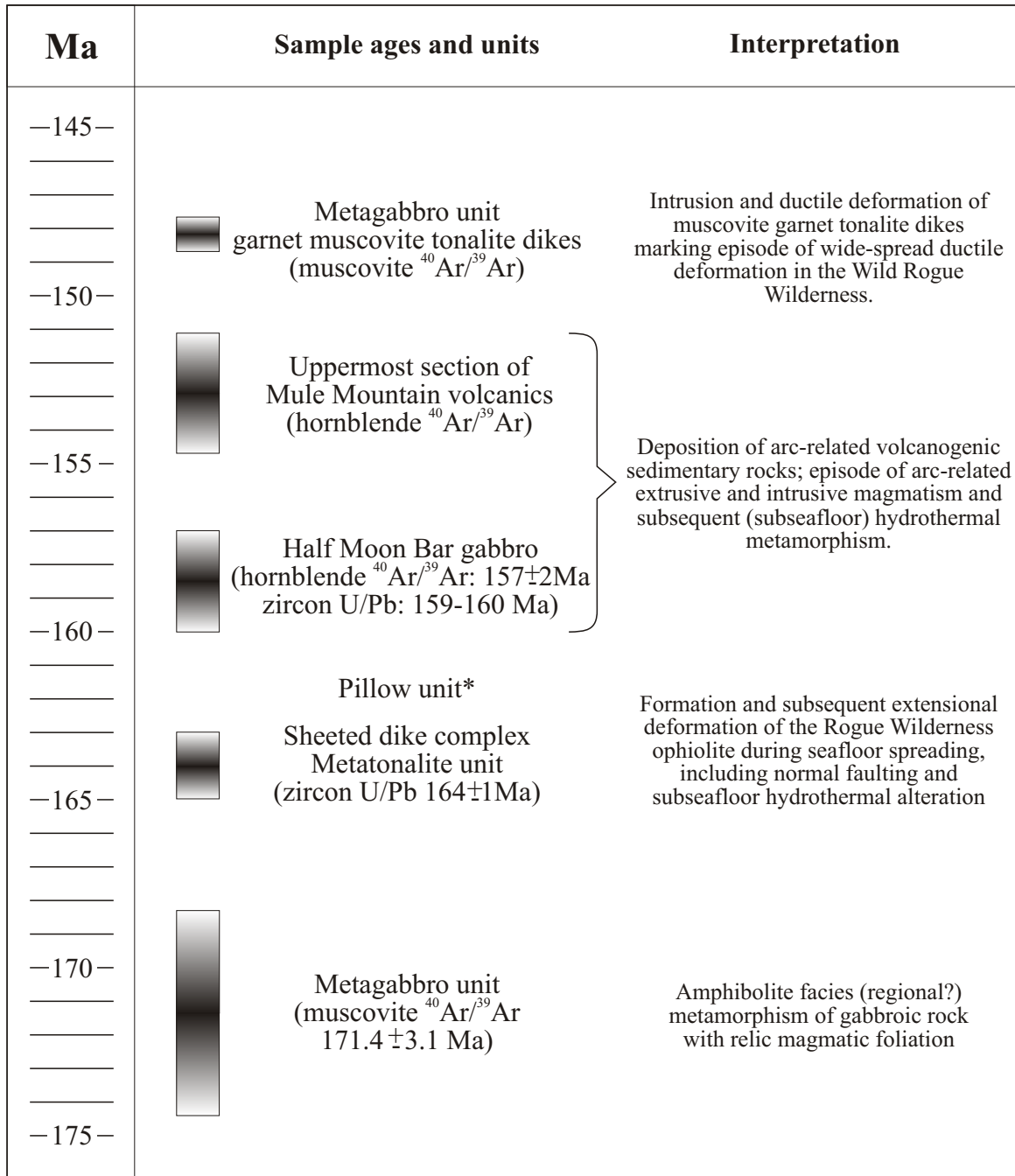
- a. Lower hemisphere, equal area stereographic projections of the mean shear plane C_t and C_{sz} and corresponding mean stretching lineations L_t and L_{sz} in the metatonalite unit and Blossom Bar shear zone, respectively. The directions of the principal stresses were obtained from the stress inversion using the mean shear planes C_t , C_g , and C_{sz} , the stretching lineations L_t , L_g , and L_{sz} and the sense of shear determined in thin section as “fault-slip data”. The results of the stress inversion and the predicted sense of shear on the shear planes C_t and C_{sz} are shown. It is demonstrated that the determined stress tensor is compatible with the sense and direction of ductile shearing in the Blossom Bar shear zone and metatonalite unit.
- b. The stress tensor of figure 18a is used to predict the sense of slip on faults cutting mylonitic foliation in the metatonalite unit. It is assumed that slip occurs in the direction of the maximum resolved shear stress on planes 1 through 6. The predicted sense of shear is opposite to observed sense of shear for faults #1, #2, and #3. The predicted sense of shear is consistent with fault #5, and the predicted sense of shear occurs at a high to intermediate angle with respect to observed sense of shear in faults #4 and #6.



- ☆ Mean stretching lineation Blossom Bar shear zone
- ★ Mean stretching lineation metatonalite unit
- Shear stress τ on C_i for various values of ϕ
 $\phi = (\sigma_2 - \sigma_3) / (\sigma_1 - \sigma_3)$
- M_t Mean foliation plane metatonalite unit
- M_{sz} Mean foliation plane Blossom Bar shear zone
- Section of foliation plane in which τ lies assuming $0 < f < 1$



- right-lateral strike slip fault (n = 3)
- left-lateral strike slip fault (n = 8)
- normal fault (n = 3)
- ▲ reverse fault (n = 5)
- ↙ Mean pole to fault clusters. The vector indicates the direction of shear stress τ (hangingwall block is assumed to slip in direction of τ)



* The minimum age of the pillow unit is constrained by the intrusion of the Half Moon Bar gabbro

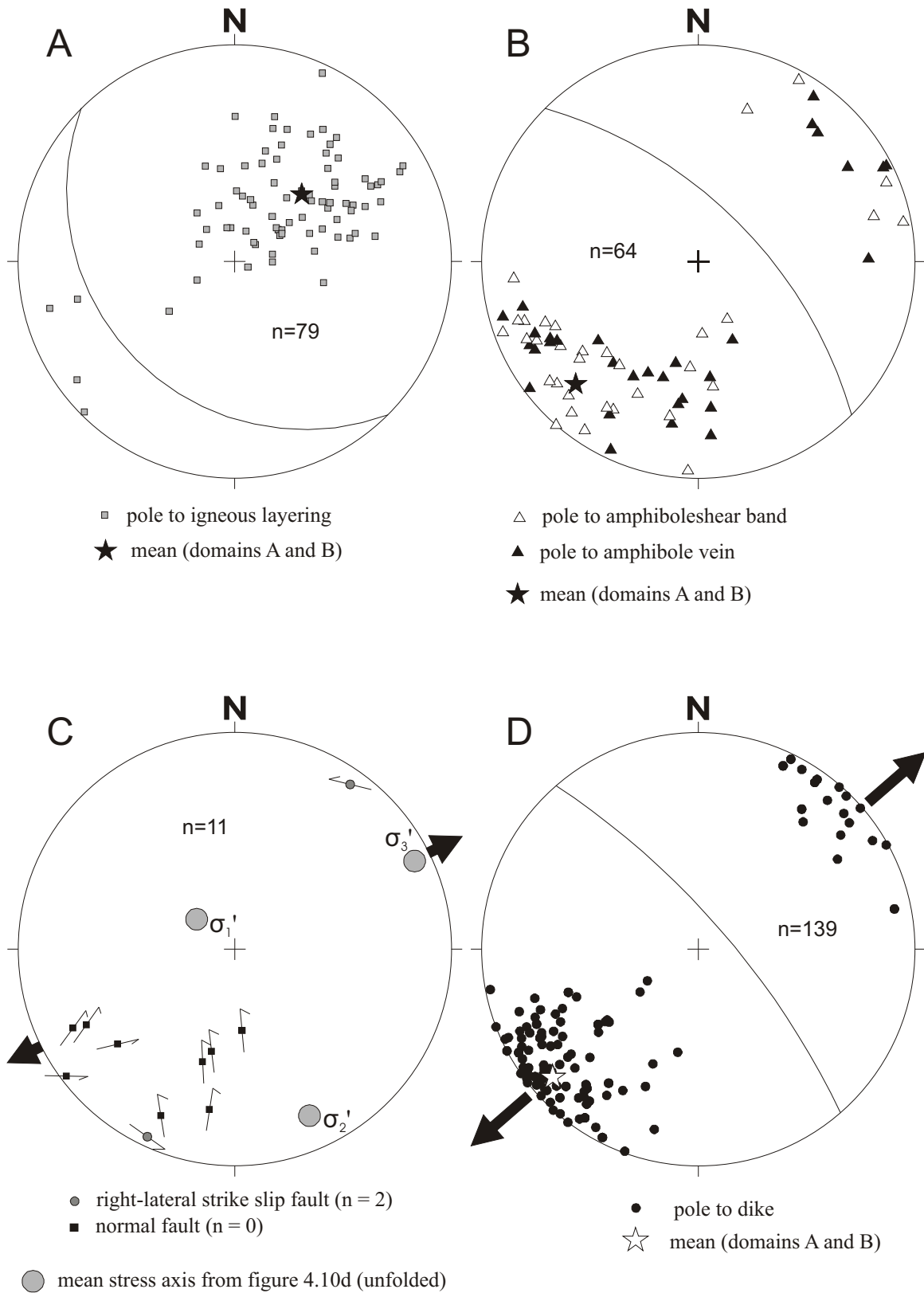
Figure 4.19: Summary and interpretation of isotopic ages in the Rogue Wilderness remnant of the CRO.

Figure 4.20

Lower hemisphere, equal area stereographic projections of structural data of domains A and B after correcting for Tertiary and Cretaceous folding.

- a. The mean igneous layering in the screens of cumulate gabbro dips 35° southwest and strikes north 045° west.
- b. The amphibole veins and shear bands remain subvertical after correcting for Tertiary and Cretaceous folding, are subparallel to the sheeted dikes (d) and occur at a high angle with respect to the igneous layering (a).
- c. The arrows affixed to the poles to cemented faults indicate the direction of slip of the hanging wall block (see figure 4.3). The solution of the paleostress analysis of the cemented faults (after correcting for Tertiary and Cretaceous folding) is consistent with extension by normal faulting.
- d. Most of the dikes are subvertical and subparallel to the amphibole veins and shear bands. Only few have relatively shallow dips. The average direction of extension for subvertical dike-injection is shown assuming dikes were injected perpendicular to the direction of the minimum principal stress.

Structural data from the sheeted dike complex corrected for Cretaceous and Tertiary folding



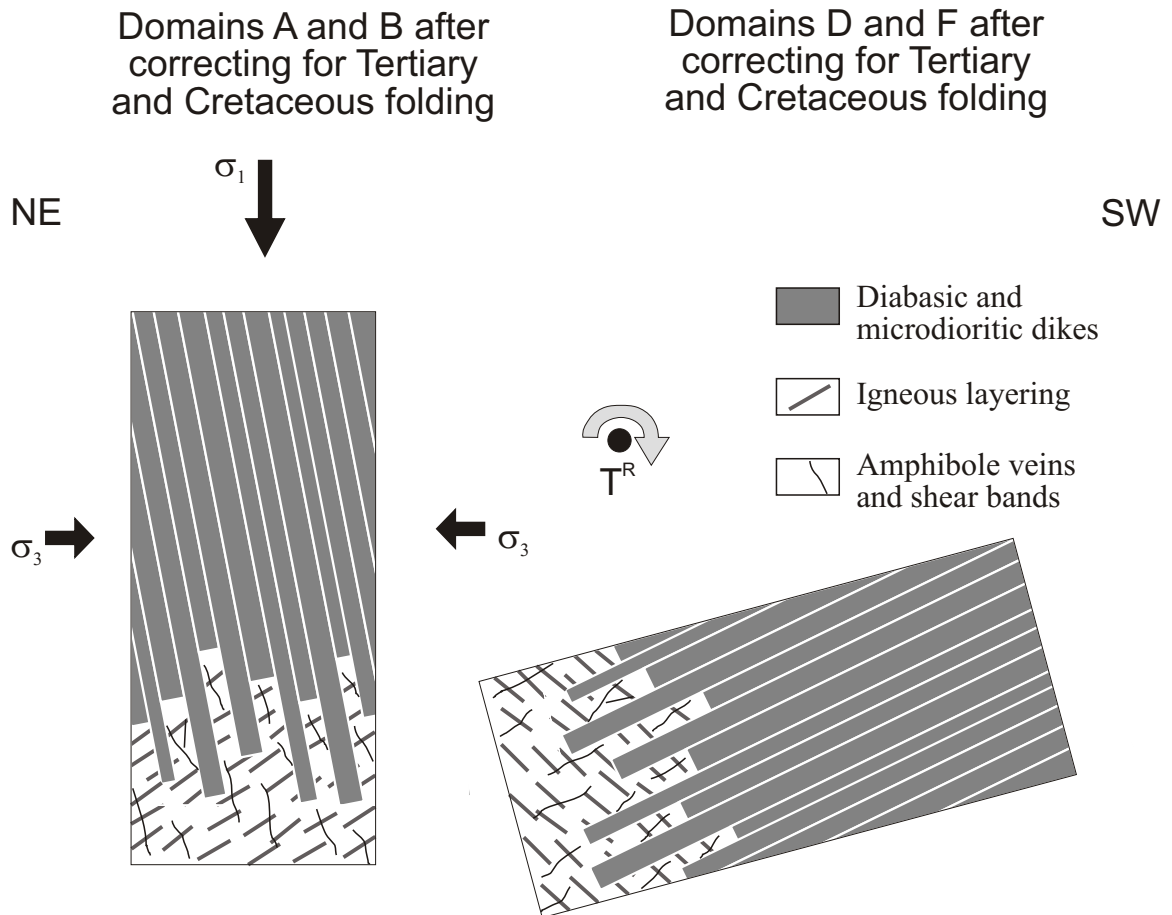


Figure 4.21

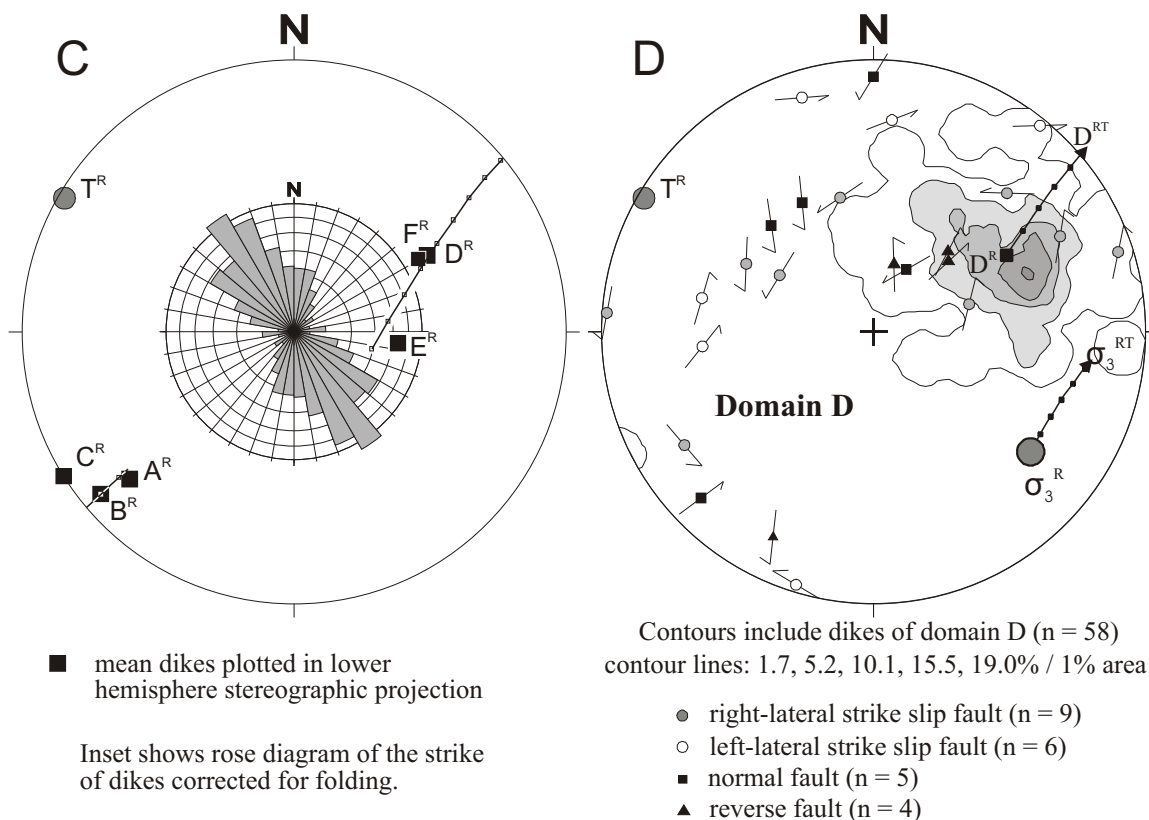
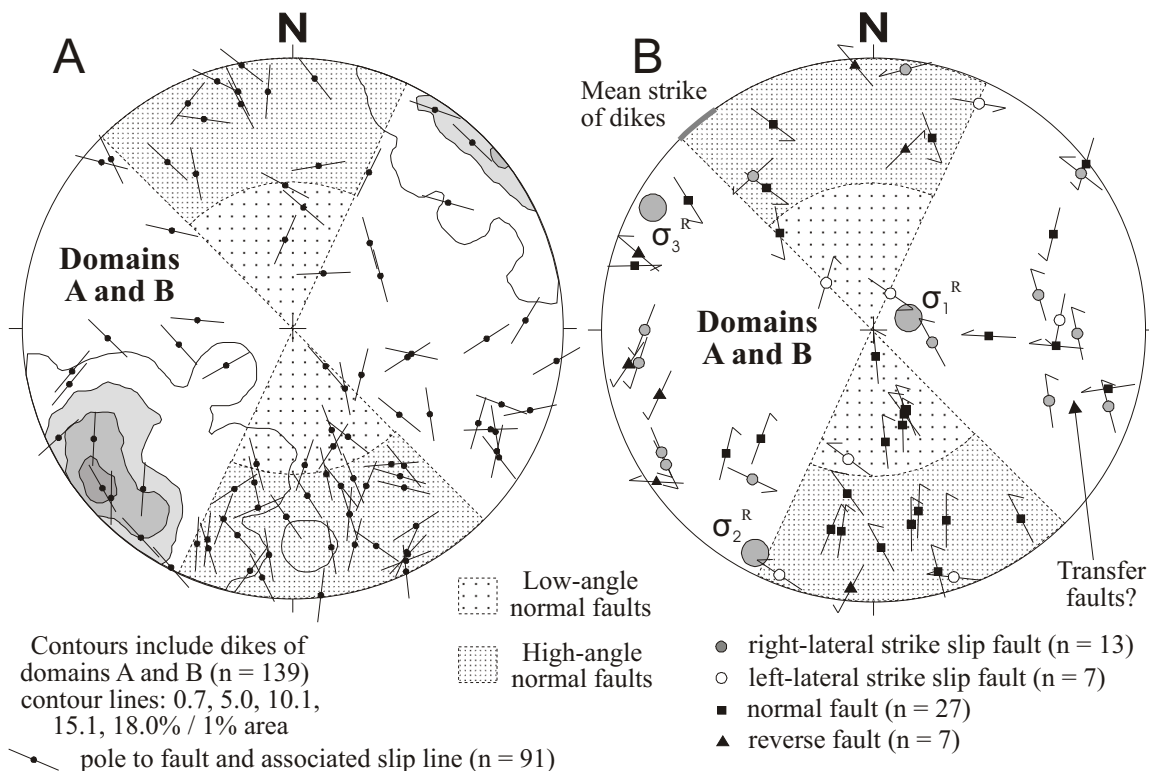
Geometric relationships of structures in domains A and B after correcting for Tertiary and Cretaceous folding. The intrusion and crystallization of the cumulate gabbro, containing moderately steep, southwest-dipping layers (figure 4.20a), is followed by the formation of steeply northeast-dipping amphibole veins and shear bands (figures 4.20b and 4.20c). Most of the shear bands indicate normal displacement, whereas amphibole veins are interpreted as mode 1 cracks. The formation of the amphibole veins and the shear bands is consistent with SW-NE directed extension by tensile parting and normal faulting, respectively. Then, SW-NE directed extension occurs by subvertical injection of diabasic and microdioritic dikes (figure 4.20d) into cumulate gabbro truncating older structures. Tilting of dikes determined in other domains is inferred around a horizontal axis (T^R) subparallel to the strike of the dikes (see figure 4.9).

Figure 4.22

Analysis of unfolded structural data of domains A, B and D: Lower hemisphere, equal area stereographic projections of contoured poles to dikes of domains A and B (a), of poles to cemented faults in domains A and B (a, b), poles to mean dike of domains A through F (c), and of contoured poles to dikes and poles to cemented faults in domain D (d).

- a. Poles to cemented faults (solid symbols) and associated slip line superimposed on the contours of poles to dikes of domains A and B after correcting for Tertiary and Cretaceous folding. The sense of slip on these faults was not determined. However, the direction of slip along the fault is indicated by the line affixed to the poles (figure 4.3). The sense of slip is probably the same as of similar faults in figure 4.22b (note the parallelism of faults and striae in figures 4.22a and 4.22b).
- b. Poles to cemented faults and their slip vectors (Hoepfner, 1955). The arrows affixed to the poles to cemented faults indicate the direction of slip of the hanging wall block (see figure 4.3). Most high- and low-angle normal faults (stippled field) occur at an angle with the sheeted dikes. Many faults parallel to the sheeted dikes are strike-slip faults. Other strike-slip faults occurring at a high angle to the strike of the dikes could be transfer faults. Note the similarity between normal faults in figure 4.22b and amphibole shear bands in figure 4.20c.
- c. Pole to mean dike of domains A through F and the best-fit Rotation axis T^R after correcting for Tertiary and Cretaceous folding (compare with figure 4.9). The unfolded rotation axis T^R is subhorizontal and occurs at a low angle to the strike of the subvertical dikes (A^R , B^R and C^R). For reference, the rose diagram indicating the strike of the dikes is shown.
- d. Pole to fault and associated slip vectors of domain D superimposed on the contoured poles to dike of domain D after correcting for Tertiary and Cretaceous folding. Faults of domain D are dissimilar to faults in domains A and B. Perhaps, many of the faults are tilted strike-slip or tilted normal faults that formed before or during the tilting of the dikes around T^R . Rotation of dikes and faults around T^R may restore the dikes in domain D to paleohorizontal. D^{RT} and σ_3^{RT} indicate rotation of D and σ_3 around R (unfolding), and rotation of D^R and σ_3^R around the rotation axis T^R (figure 4.21).

Structural data from the sheeted dike complex corrected for Cretaceous and Tertiary folding



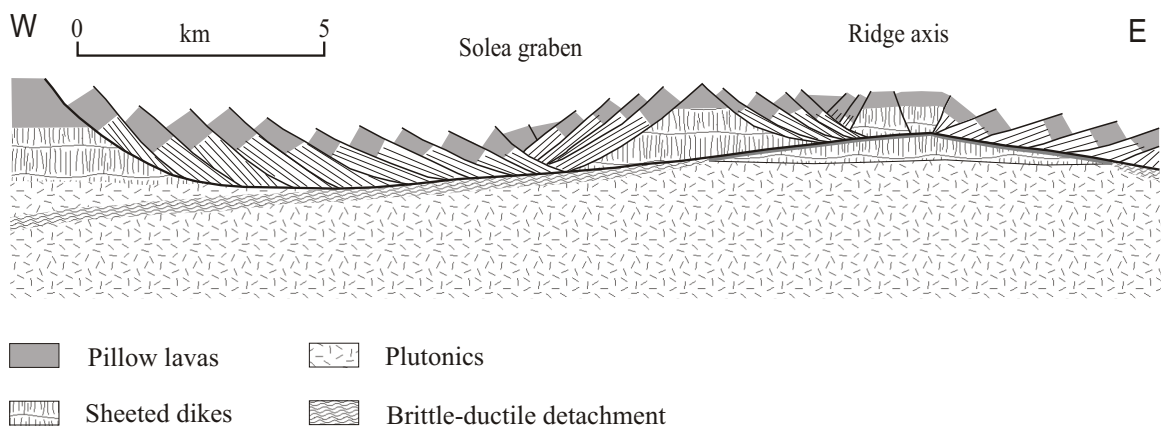


Figure 4.23

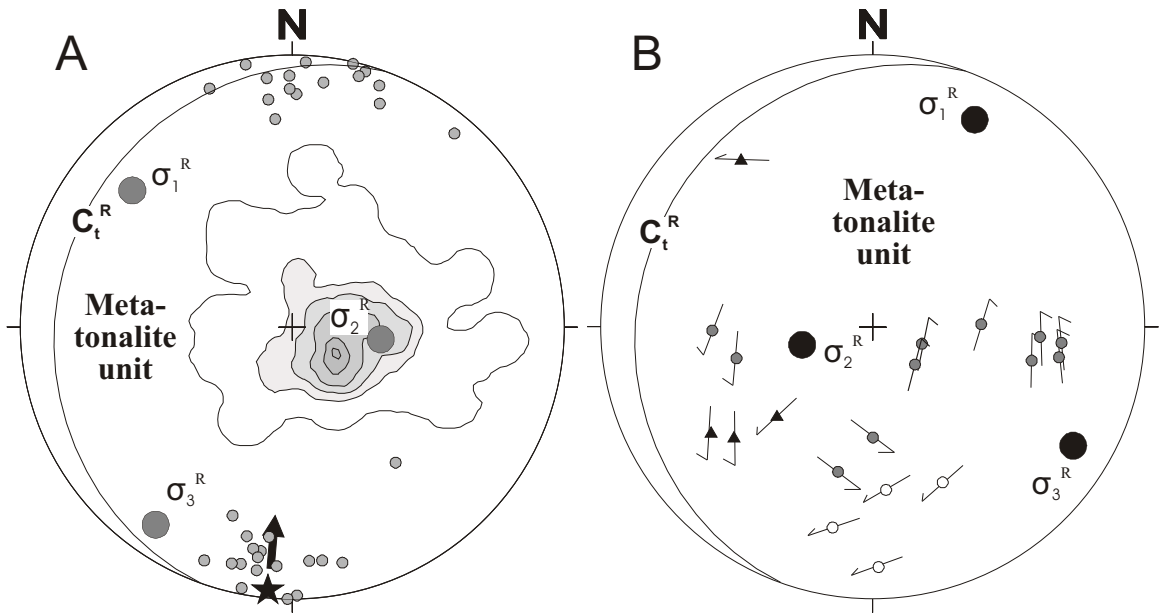
Model of the spreading and fault geometry of the Troodos ophiolite depicting the formation of the Solea graben (after Allerton and Vine; 1987). A detachment fault is inferred at depth bounding a fault mosaic comprised of listric and/or planar rotational faults. Tilting of blocks bound by rotational faults occurs in response to large-magnitude extension along the detachment during amagmatic cycles.

Figure 4.24

Structural data of the metatonalite unit (a, b), metagabbro unit (c), and Blossom Bar shear zone (d) after correcting for Tertiary and Cretaceous folding (lower hemisphere, equal area stereographic projections).

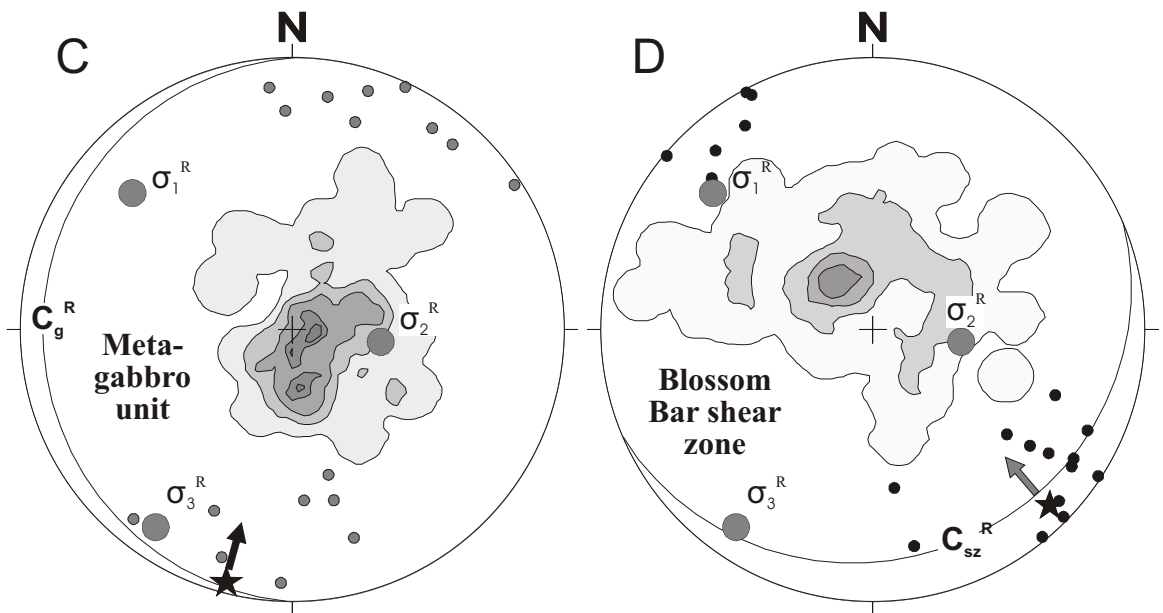
- a. The mean shear plane (C_t^R) dips shallowly west, and the mean stretching lineation trends south. The sense of shear indicators are consistent with top to the north transport (metagabbro unit is hangingwall block). The reoriented stress axes of figure 18a are shown.
- b. The poles to faults cutting mylonitic foliation in the metatonalite unit and associated slip vectors are shown. Cemented faults which occur at low angles with the subhorizontal foliation are sympathetic with the sense of shear in the mylonites. The reoriented stress axes of figure 4.16c are shown. The stress field that produced slip on the brittle faults in the metatonalite unit could not have produced slip on mean foliations (C_t^R , C_g^R , C_{sz}^R) in the directions of the mean stretching lineations.
- c. The mean shear plane (C_g^R) gently dips west, and the mean stretching lineation trends south. The sense of shear indicators are consistent with top to the north transport (Blossom Bar shear zone is hangingwall block). The reoriented stress axes of figure 4.18a are shown.
- d. The mean shear plane (C_{sz}^R) gently dips southeast, and the mean stretching lineation trends also southeast. The sense of shear indicators are consistent with top to the north thrusting (Mule Mountain volcanics is hangingwall block). The reoriented stress axes of figure 18a are shown.

Structural data corrected for folding



Contoured poles to shear foliation
 metatonalite unit (n = 115):
 contour lines: 0.9, 5.2, 9.6, 14.8, 20.0 and 22.6% / 1% area
 ● stretching lineation (n=34)
 ★ mean of stretching lineations (figs. a, c and d),
 arrows indicate motion of hangingwall block

▲ Thrust fault (n = 4)
 ● Right-lateral strike-slip fault (n = 11)
 ○ Left-lateral strike-slip fault (n = 4)
 ● ROMSA analysis of brittle faults cutting
 shear foliation in the metatonalite unit



Contoured poles to shear foliation
 metagabbro unit (n = 47)
 contour lines: 2.1, 6.4, 10.6, 14.9, 19.2% / 1% area
 ● stretching lineation (n = 17)

Contoured poles to shear foliation
 Blossom Bar shear zone (n = 104)
 contour lines: 1.0, 4.8, 9.6, 14.4, 17.3% / 1% area
 ● stretching lineation (n= 19)

● Stress axes compatible with slip on average shear plane parallel to mean stretching lineation (a, b, & d)

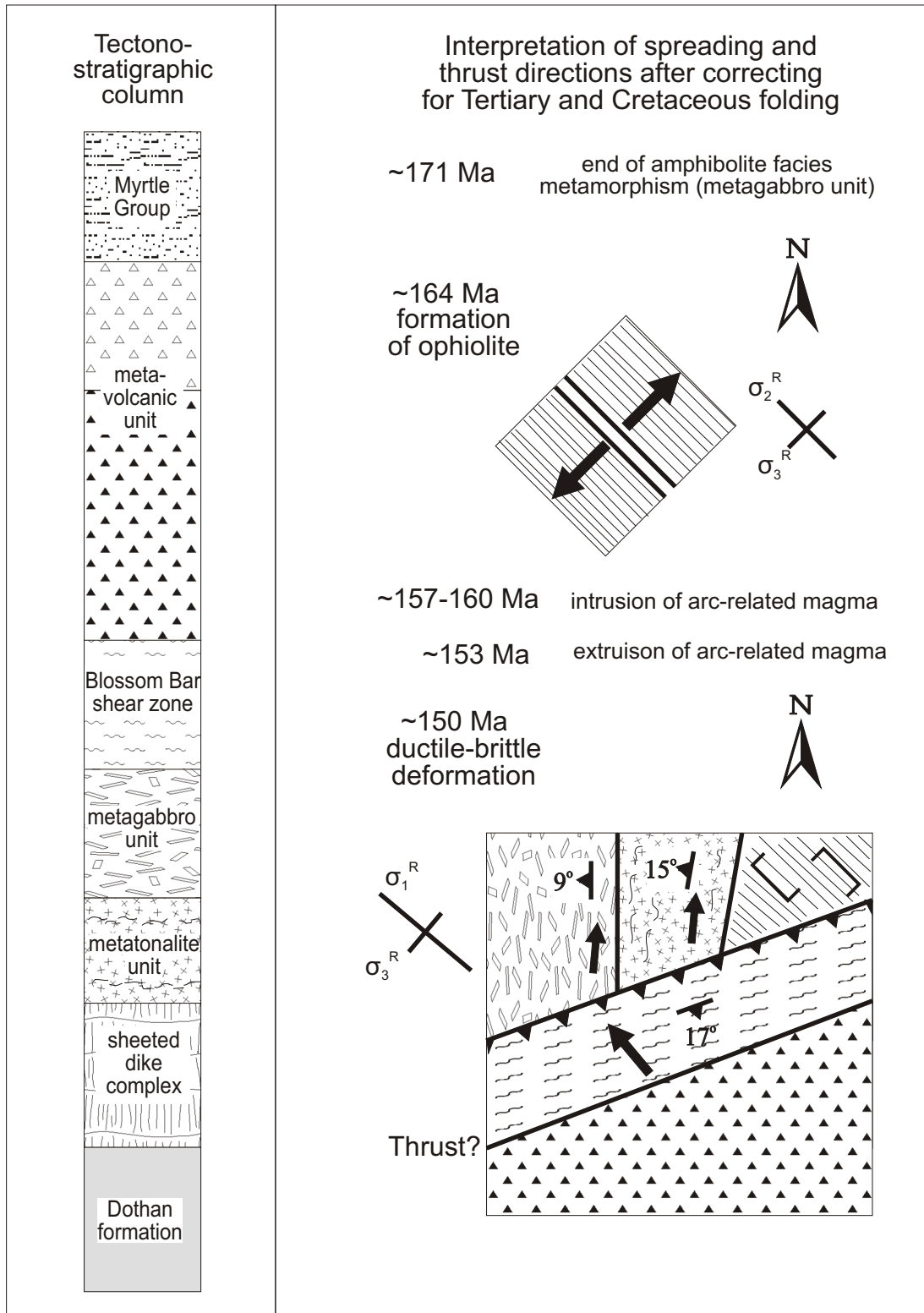


Figure 4.25: Cartoons depicting the directions of spreading at ~164 Ma, and directions of thrusting at ~150 Ma (not corrected for possible rotation around subvertical axis)

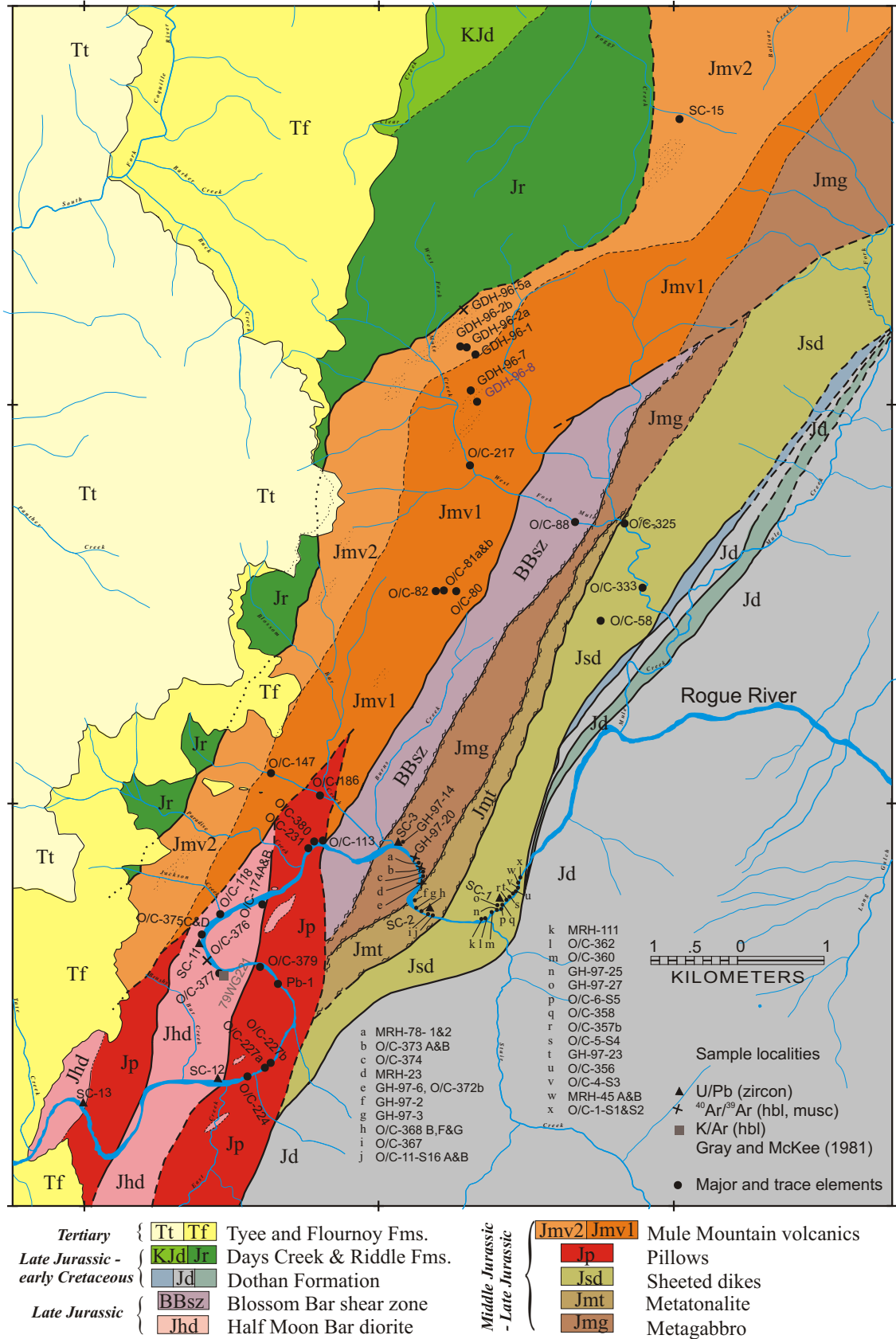


Figure 5.1: Simplified geologic map of the Wild Rogue Wilderness showing localities of analyzed samples.

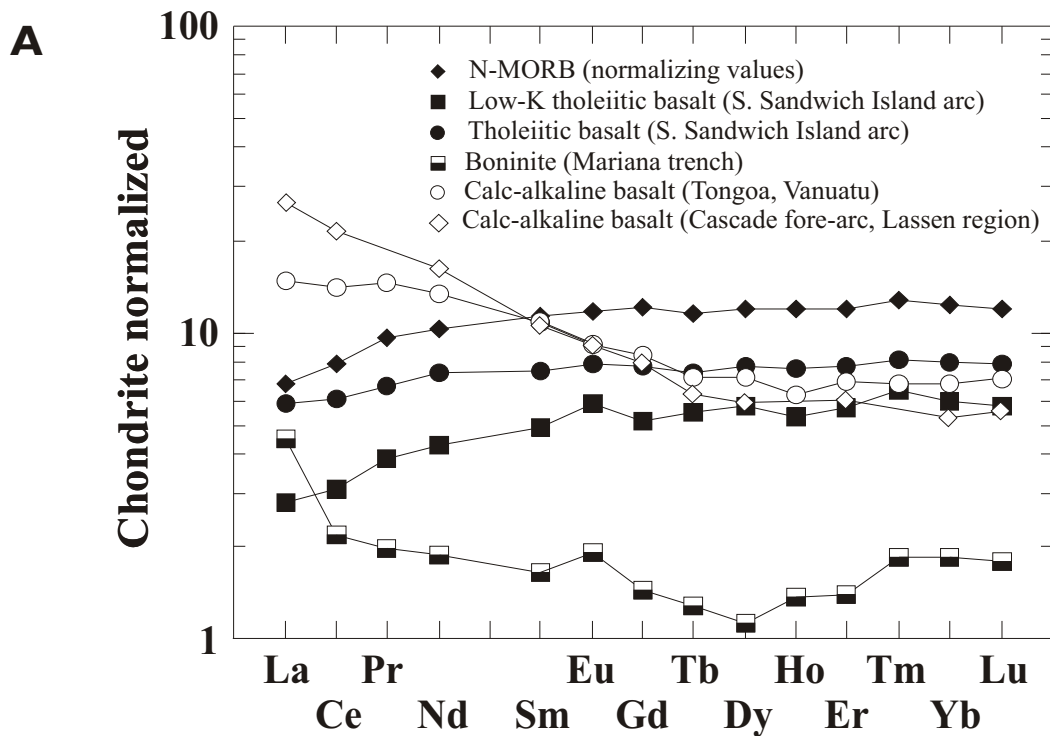


Figure 5.2

A. Chondrite normalized rare earth element distribution patterns of normal mid ocean ridge basalt

(MORB), island arc tholeiite (IAT), calc-alkaline basalt (CAB). Average N-MORB values are from Sun and McDonough (1989), the data for the IAT reference samples are from Pearce et al. (1995a), the BON reference sample is from Pearce and Parkinson (1993), and the CAB reference sample is from Pearce et al. (1995b) (Tonga) and Borg et al. (1997) (Cascade fore-arc). The chondrite normalizing values of Taylor and McLennan (1985) are used throughout this chapter.

B-D. (next page) Diagrams showing N-MORB normalized major and trace element distribution patterns of IAT, CAB and BON. Fractional crystallization and variations in the degree of partial melting (see text) change the level of the pattern, but have little effect on the shape (e.g., Pearce, 1983). Elements shown with open symbols are thought to be derived by significant subduction contribution whereas elements shown with solid symbols are thought to be derived almost entirely from the mantle wedge. The stippled lines in the diagrams for IAT, CAB and BON indicate the extrapolated compositions for elements in a hypothetical basalt derived by partial melting of the mantle prior to subduction contribution (after Pearce, 1983; Pearce and Parkinson, 1993).

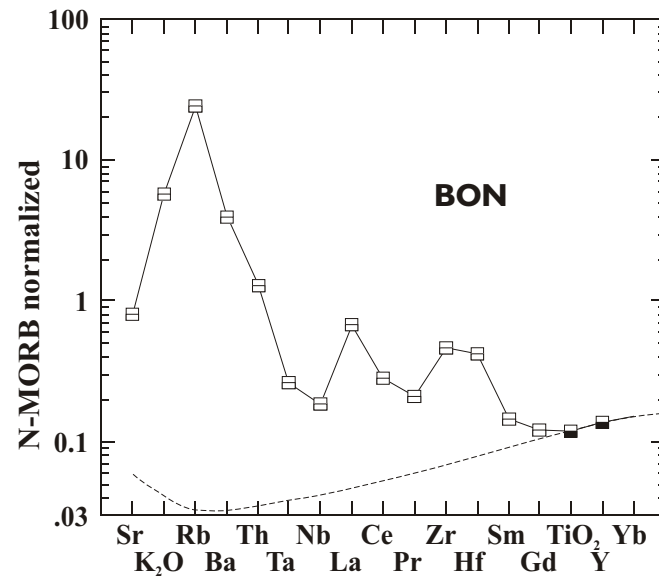
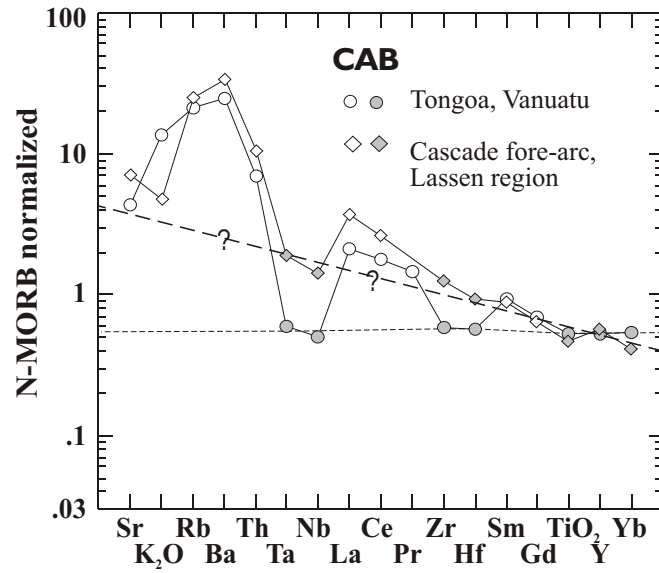
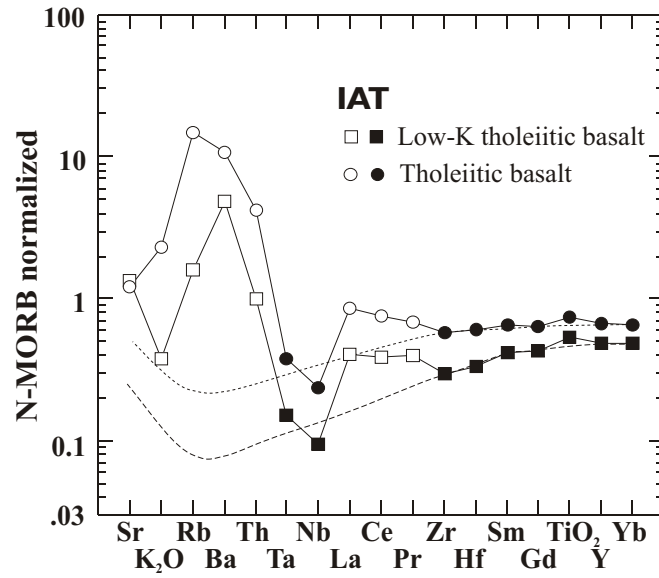


Figure 5.3

- A. Chondrite normalized REE distribution patterns of samples from the metagabbro unit. The patterns are parallel suggesting that the samples could be related by fractionation. The shape of the REE distribution pattern is very unusual: the LREE show a convex-up pattern centered on Nd. Such patterns are not observed in the continental crust and are very rare in mantle-derived liquids.
- B. N-MORB normalized major and trace element distribution patterns of samples from the metagabbro unit. The patterns show characteristics of arc-related rocks. Compared to N-MORB, the elements Ta, Nb, Hf, and Zr are strongly depleted, LILE are enriched, and REE are similar to N-MORB. This is enriched with respect to Ta and Nb, but depleted compared to N-MORB.

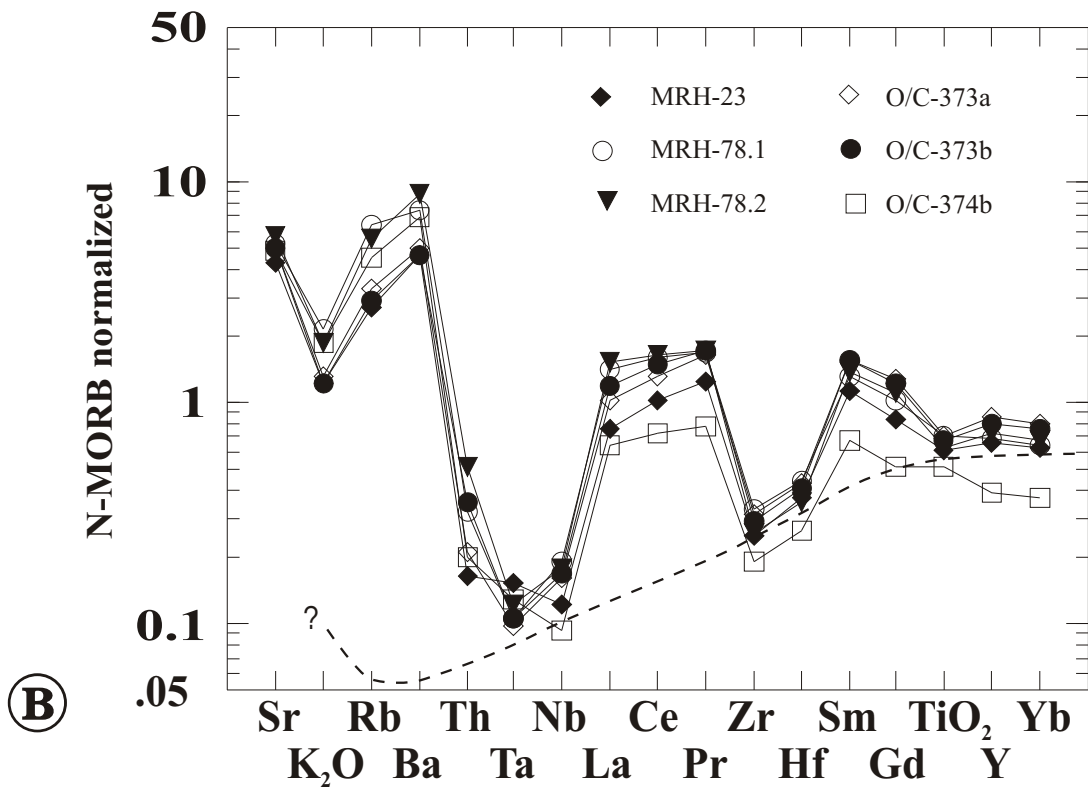
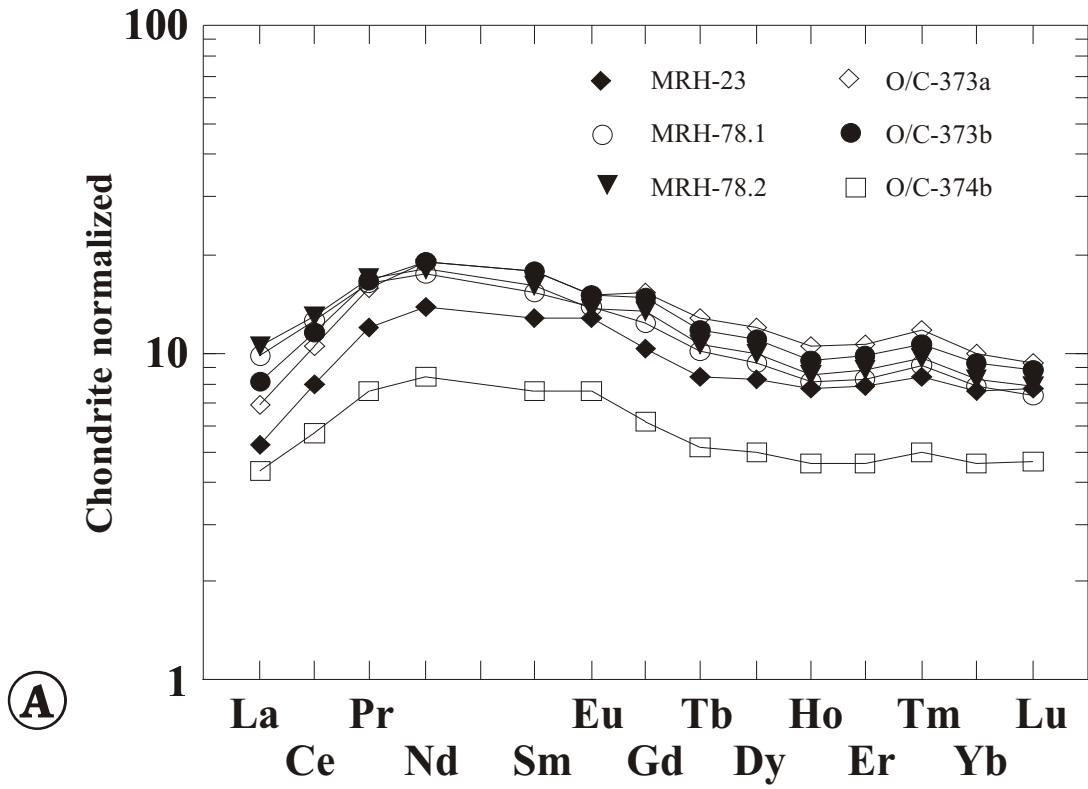
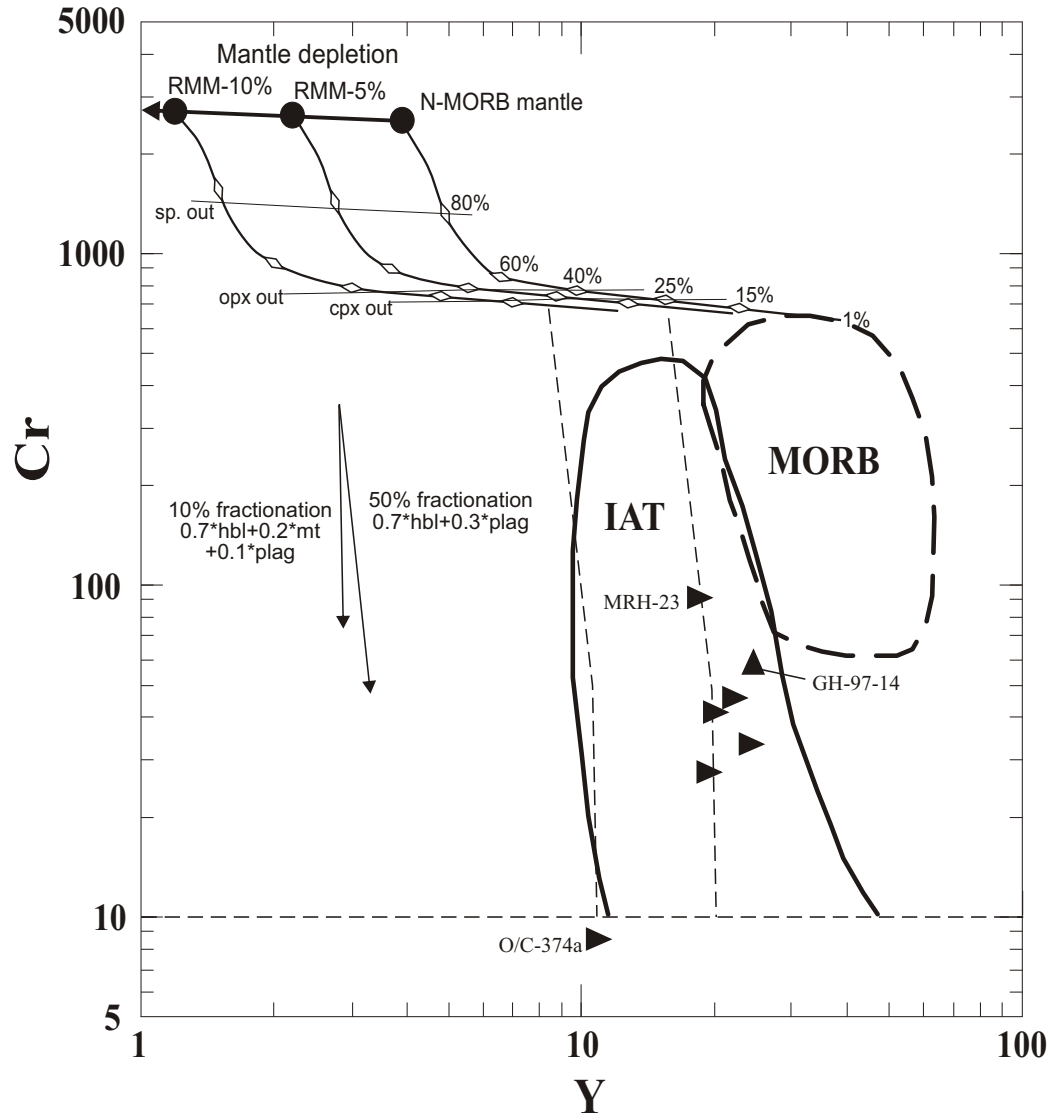


Figure 5.4

Cr vs. Y tectonic discrimination diagram of Pearce (1982) showing fields for mid-ocean ridge basalts (MORB) and island arc tholeiite (IAT) (the latter field also includes calc-alkaline and alkalic basalts from oceanic arcs). The samples from the metagabbro unit (sideways triangle) plot within the VAB field. Upright triangle is the hornblende quartz diorite in the metagabbro unit which may be much younger.

The curves indicate the degree of melting of variously depleted mantle sources are calculated using the equation for fractional melting modified and extended after Hertogen and Gubels (1976) to take into account non-modal melting as well as depletion of phases with progressive melting. RMM-5% and RMM-10% are the residual MORB mantle compositions after 5% and 10% melt extraction, respectively. The N-MORB mantle composition and the rate of phase disappearance are taken from Pearce and Parkinson (1993). The N-MORB mantle consists of 57.5% olivine, 2.0% spinel, 27.0% opx and 12.5% cpx and contains 2500 ppm Cr and 3.9 ppm Y. Cpx is depleted after 15%, opx after 40%, and spinel after 80% melting of the N-MORB mantle. The initial mantle composition and the initial rate of phase disappearance, given in Pearce and Parkinson (1993), were used to determine the mineral proportion for each melting step as well as the composition of RMM-5% and RMM-10%, and the rate of phase disappearance during melting of RMM-5% and RMM-10% (subvertical lines labeled cpx out, opx out, and sp out). The mineral/melt partition coefficients at 1300°C compiled in Pearce and Parkinson (1993) are used to calculate the melting curves. Following Pearce and Parkinson (1993), incomplete melt extraction is incorporated into the melting model by treating trapped melt as a phase with a partition coefficient of 1. The mass fraction of trapped melt is assumed to be 0.01 (see Pearce and Parkinson, 1993). The arrows indicating fractionation of hbl + plag and hbl + plag + mt are calculated using the equation for Rayleigh fractionation and mineral/melt partition coefficients for basaltic liquids compiled in Rollinson (1993). The dashed lines show possible petrogenetic pathways based on calculated fractionation vectors (fractionation of hbl + plag followed by hbl + plag + mt from two different parental magmas). O/C-374b has very low abundances of incompatible trace elements, including Y, suggesting that the parental magma of O/C-374b was generated by higher degrees of melting than the parental magma of the other samples. Alternatively, the mantle source of O/C-374b could have been more refractory than that of the other samples.



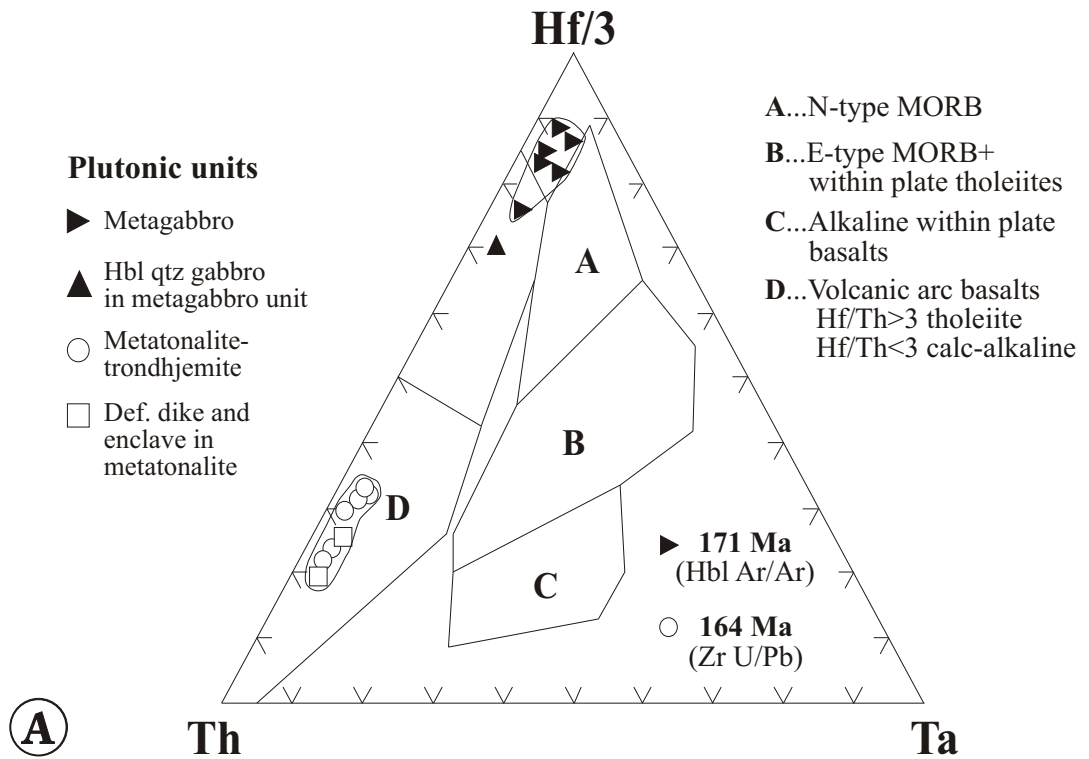
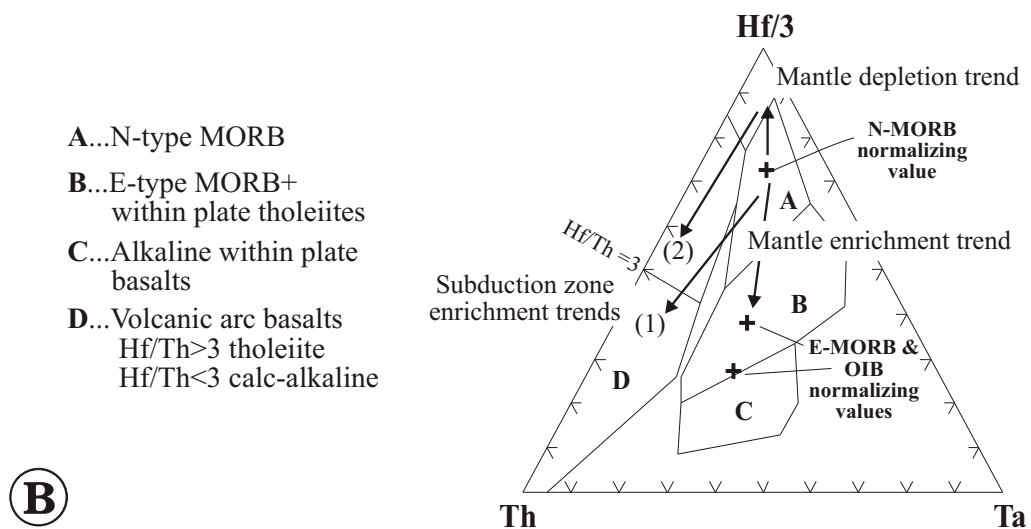


Figure 5.5A.

Hf/3-Th-Ta tectonic discrimination diagram of Wood et al. (1979). The samples from the metagabbro unit plot at depleted N-MORB compositions and overlap with the field of island arc tholeiite. The hbl-Qtz diorite (GH-97-14) which intrudes (?) the metagabbro and may be much younger (chapter 2) plots well within the IAT field. All samples from the metatonalite unit plot in the calc-alkaline field.

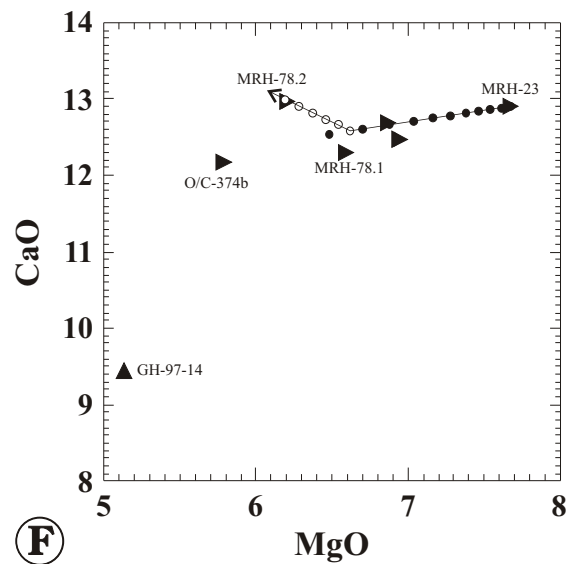
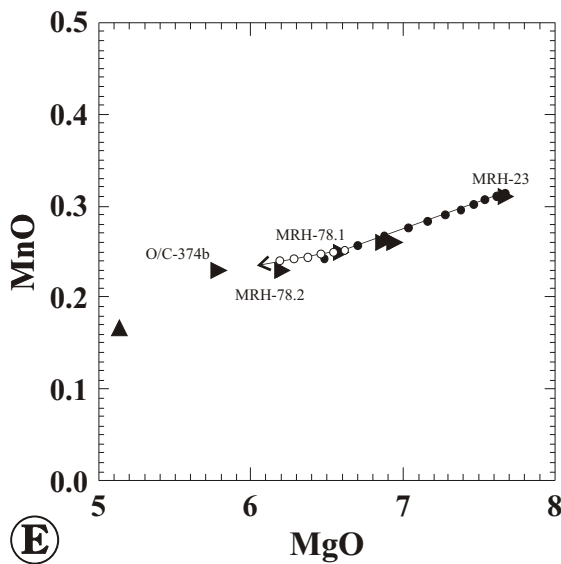
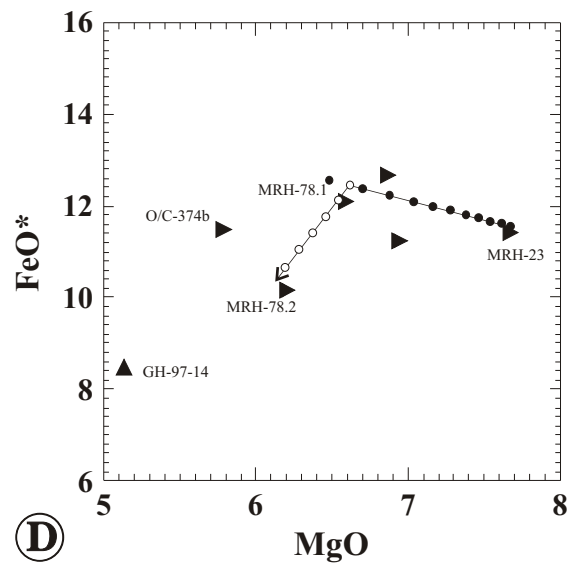
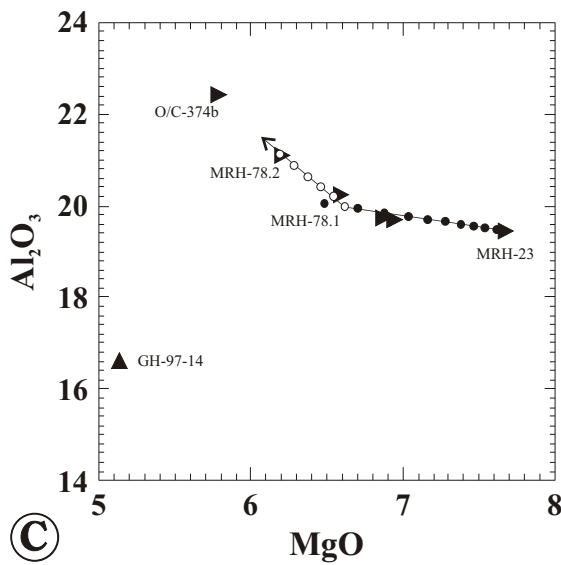
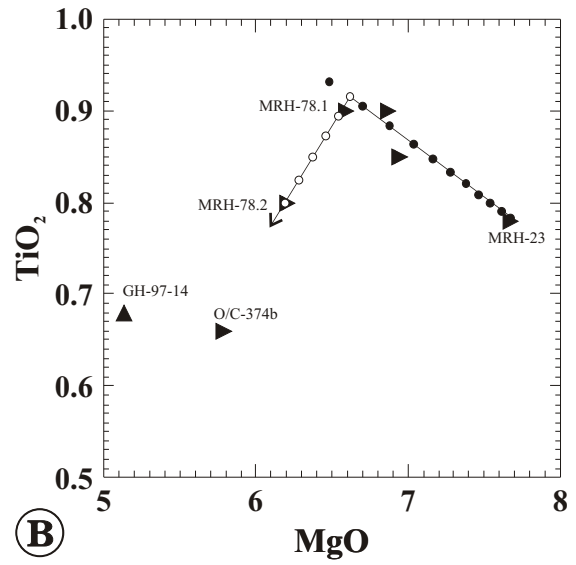
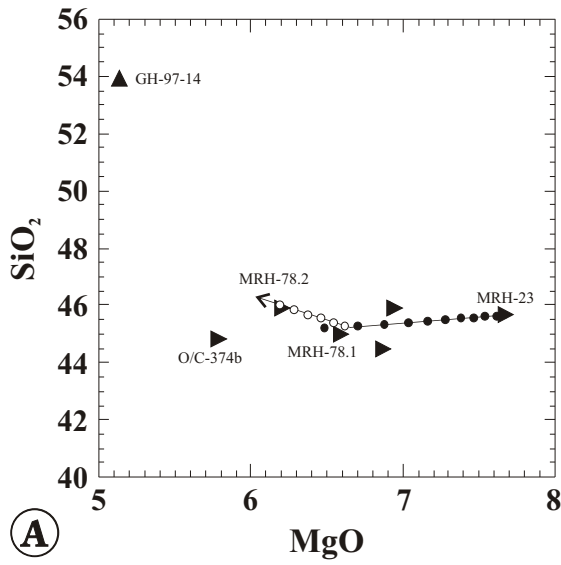


B. Petrogenetic pathways in the Hf/3-Th-Ta diagram of Wood et al. (1979). See text for explanation

Figure 5.6

A - J: MgO variation diagrams of samples from the metagabbro unit (sideways triangle) and the hornblende quartz diorite intrusion in the metagabbro unit (upright triangle, GH-97-14) which may or may not be related. MgO decreases with increasing fractionation. The trends are produced by subtraction of plagioclase (An_{85}) + hornblende (closed dots) followed by subtraction of plagioclase (An_{50}) + hornblende + magnetite (open dots) from the most primitive sample (MRH-23). SiO_2 decreases with increasing fractionation until the onset of fractionation of hornblende + magnetite + plagioclase.

K: The V vs. Ti diagram shows the fields for island arc tholeiite (IAT) and normal ocean floor basalt (OFB) after Shervais (1982). The samples from the metagabbro unit plot within the IAT field. The Ti/V ratio remains constant as Ti and V increase with fractionation of hornblende + plagioclase (closed dots). Then, the Ti/V ratio increases as Ti and V decrease with fractionation of hornblende + titanomagnetite + plagioclase (open dots).



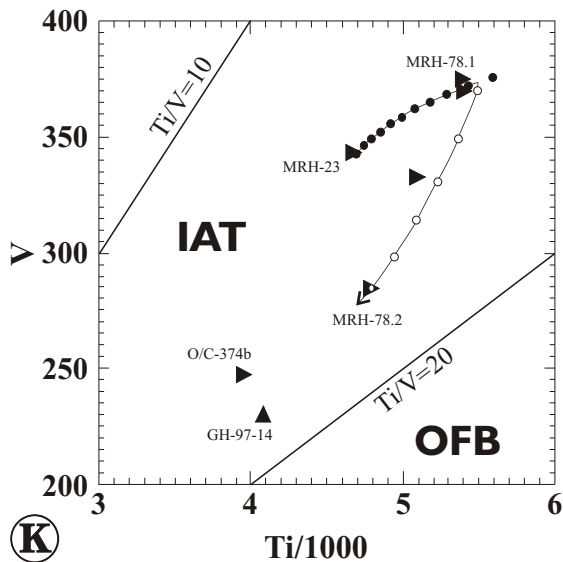
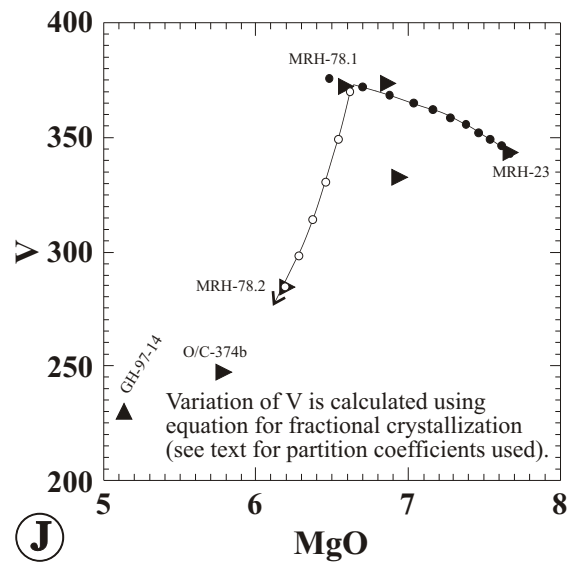
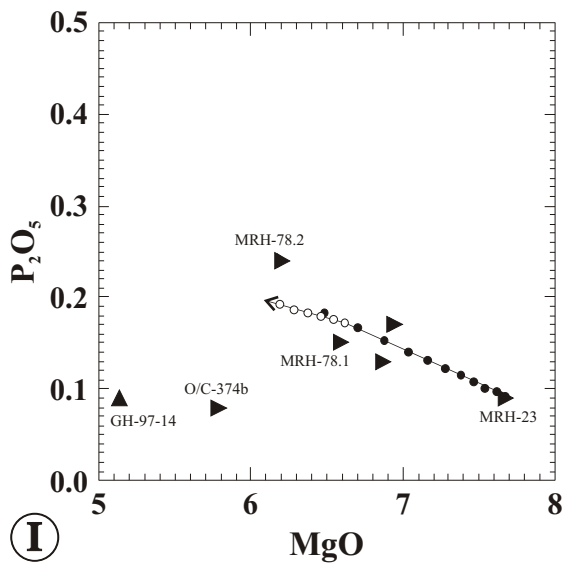
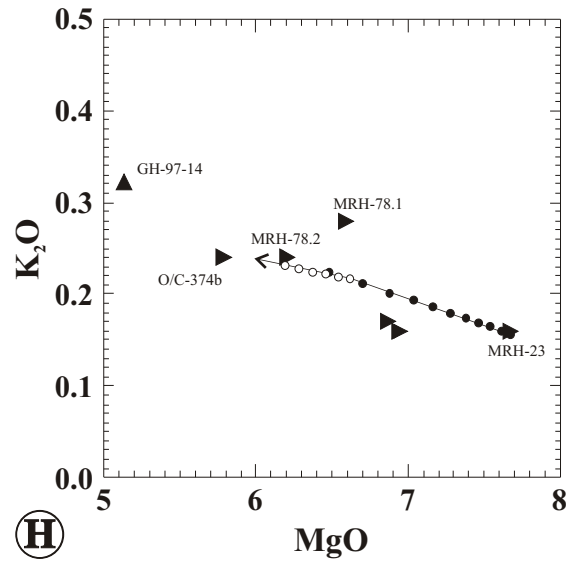
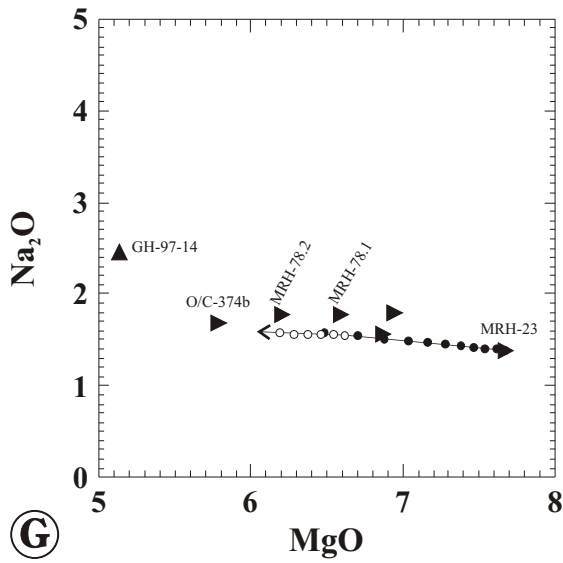


Figure 5.6 cont.

Subtraction of
 $0.692 \cdot \text{hornblende} + 0.308 \cdot \text{plagioclase (An}_{85})$
 (5% increments)

Subtraction of
 $0.723 \cdot \text{hornblende} + 0.089 \cdot \text{plagioclase (An}_{50})$
 $+ 0.189 \cdot \text{magnetite}$
 (2% increments)

Figure 5.7

- A. Chondrite normalized REE distribution pattern of the hornblende quartz diorite in the metagabbro unit.

The pattern of GH-97-4 differs from that of the samples from the metatonalite unit indicating it cannot be related by fractionation to the metatonalite unit. However, the shape of the REE distribution pattern is similar to that of the metagabbro unit in that it has a slightly convex-up shape centered on Nd.

- B. N-MORB normalized major and trace element distribution patterns of GH-97-14. The patterns show characteristics of arc-related rocks. Compared to N-MORB, the elements Ta, Nb, Hf, and Zr are strongly depleted, LILE are enriched, and REE are similar to N-MORB. Th is enriched with respect to Ta and Nb, and similar compared to N-MORB.

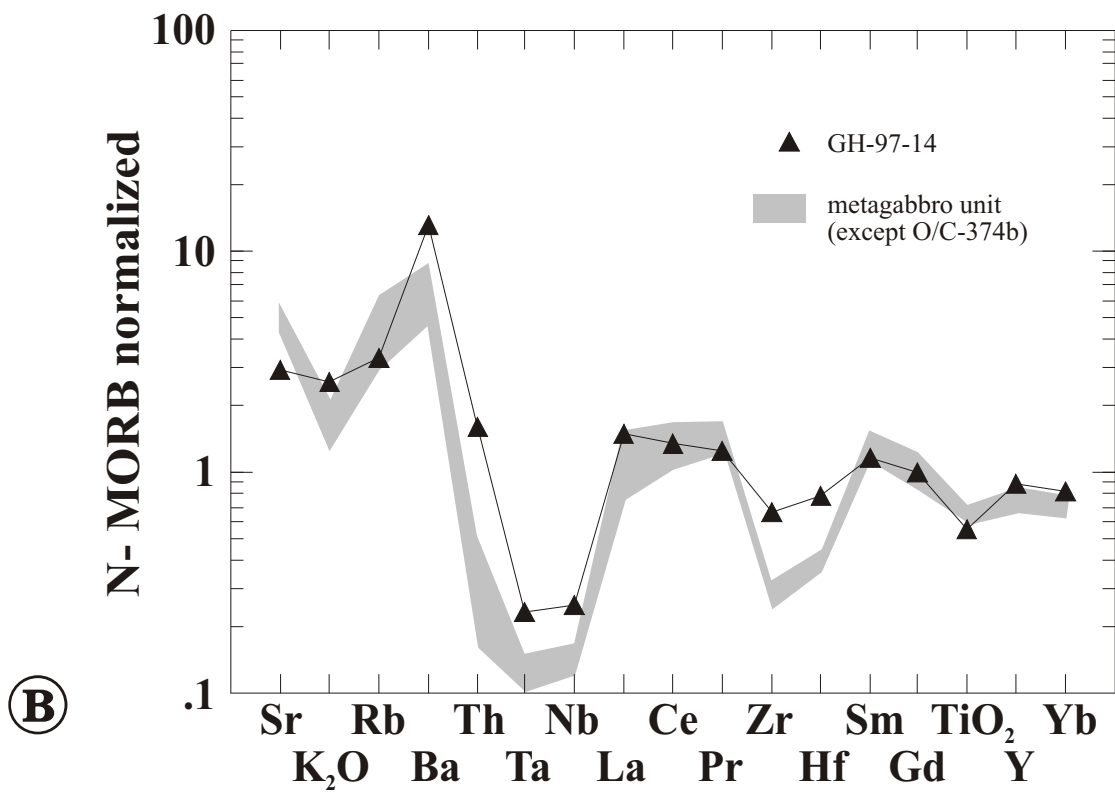
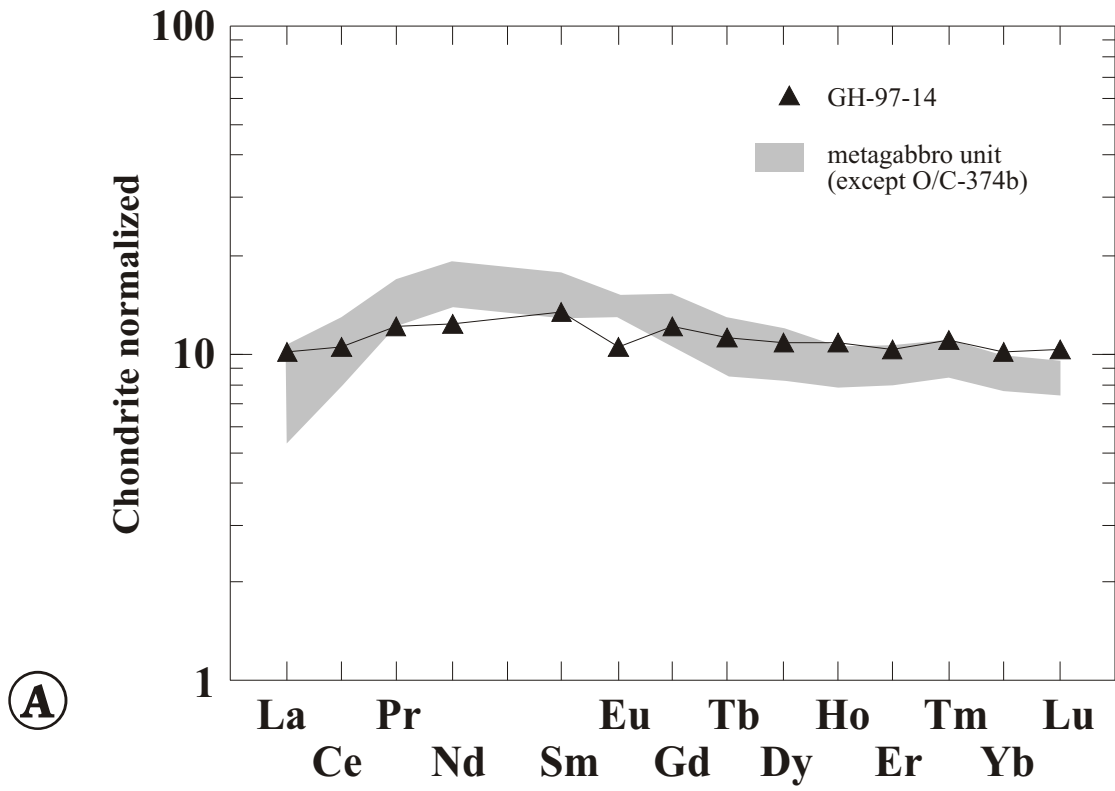
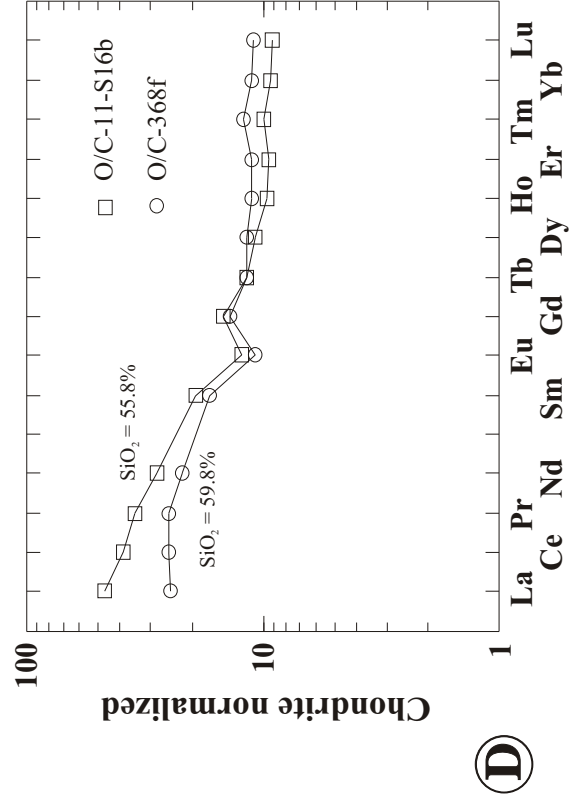
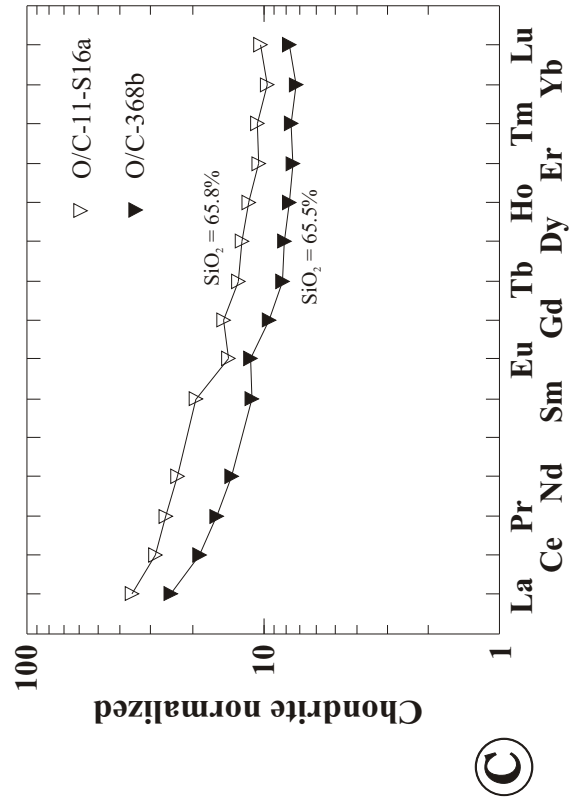
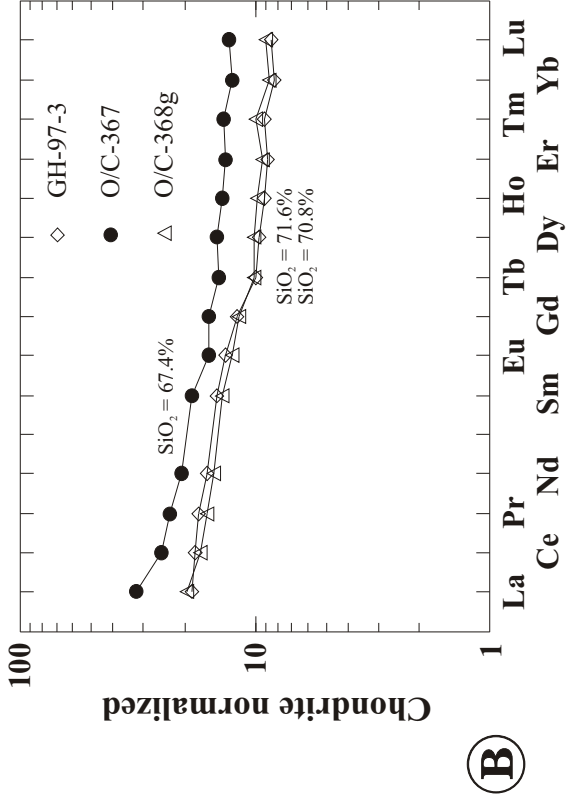
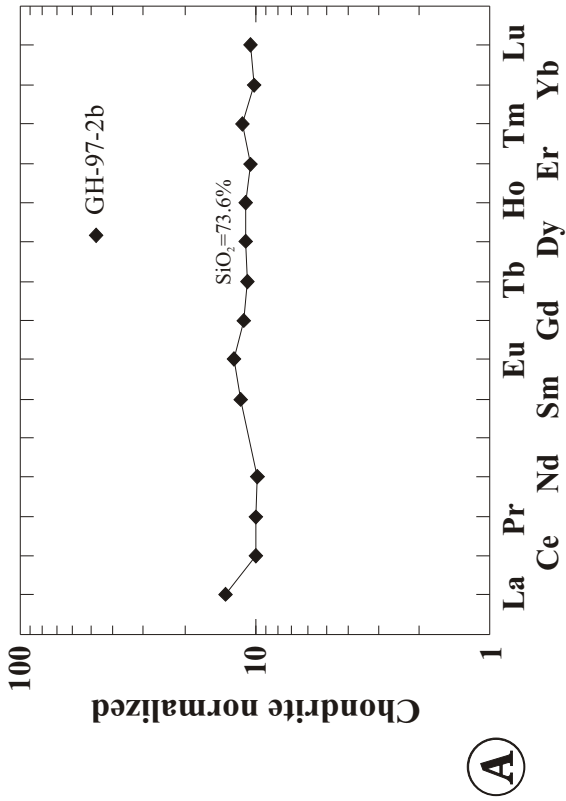
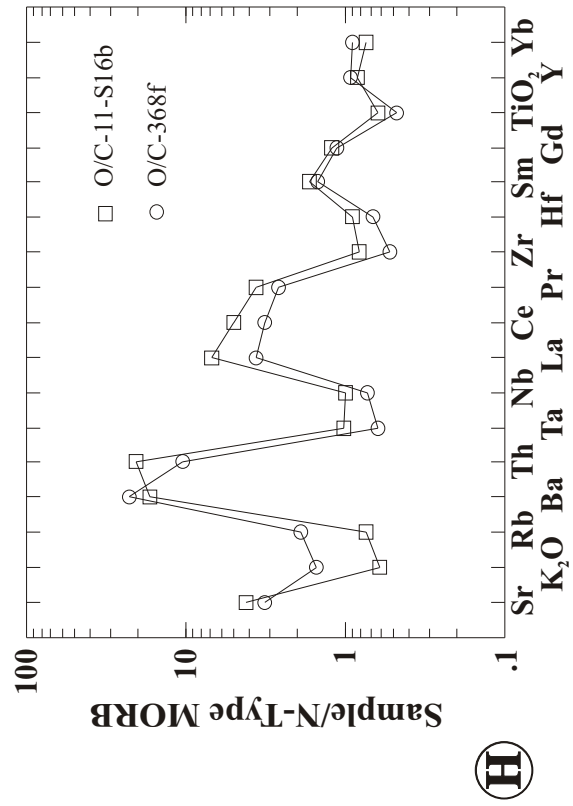
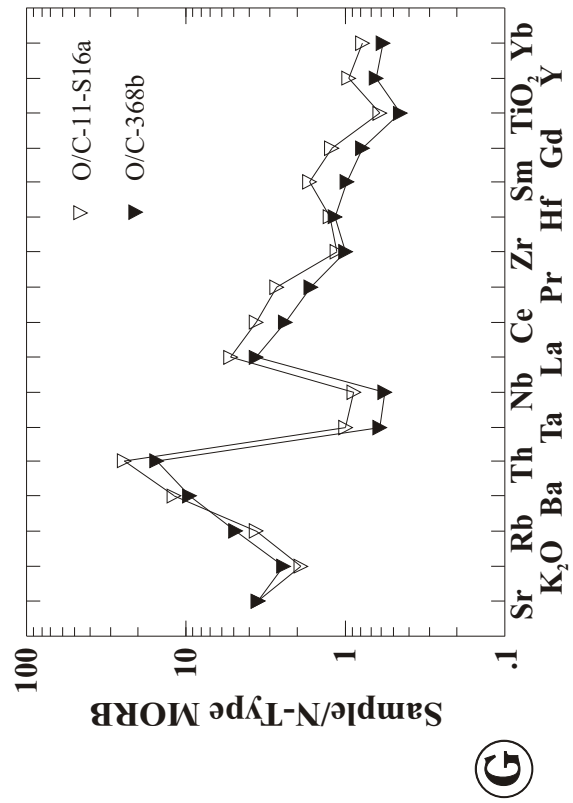
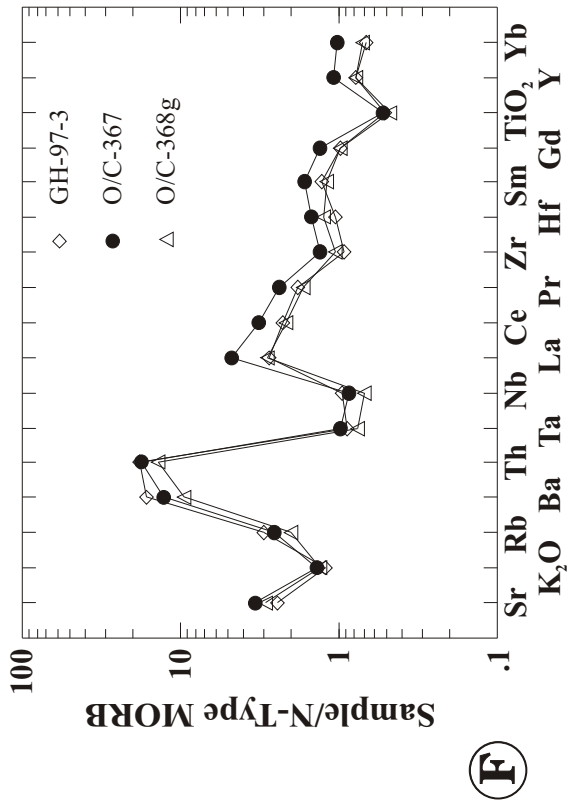
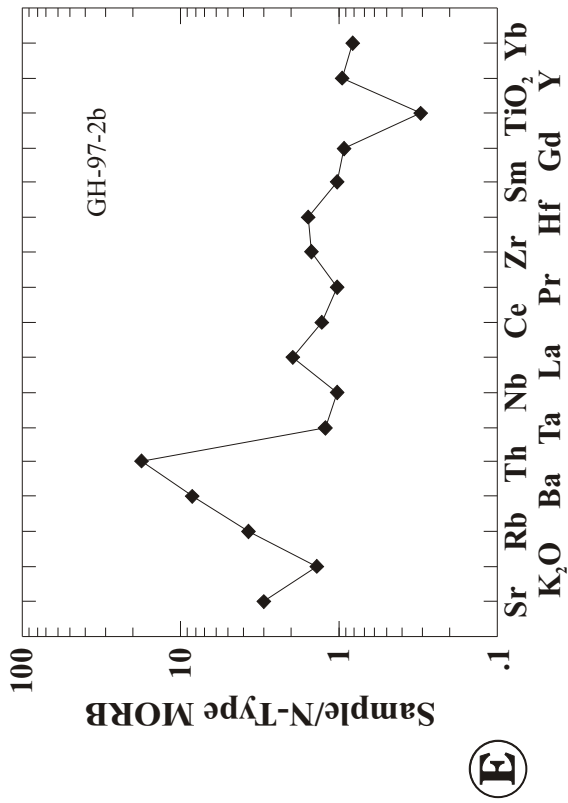


Figure 5.8

A - D: Chondrite normalized REE distribution diagrams of samples from the metatonalite unit. The patterns vary from flat to moderately LREE enriched. Sample GH-97-2b (figure 5.8a) has a $(La/Yb)_n$ ratio of 1.33. The ratios of samples GH-97-3, O/C-367 and O/C-368f ranges from 2.21 to 2.58 (figure 5.8b), and of samples O/C-11-S16a and O/C-368b from 3.42 to 3.77 (figure 5.8c). The deformed dike (O/C-11-S16b) in the metatonalite has the highest $(La/Yb)_n$ ratio of 5.04 (figure 5.8d), while the $(La/Yb)_n$ ratio of the enclave (O/C-368f) is similar to that of GH-97-3, O/C-367 and O/C-368f (figure 5.8b). In general, SiO_2 contents increase with decreasing $(La/Yb)_n$.

E - H: N-MORB normalized trace element distribution diagram of samples from the metatonalite unit. Ta, Nb, Zr and Hf are depleted while LILE, Th, and LREE are selectively enriched. These patterns are typical of calc-alkaline rocks, except LREE in the most silicic samples (GH-97-2b, GH-97-3, O/C-368g) are not very enriched (figure 5.8e and 5.8f).





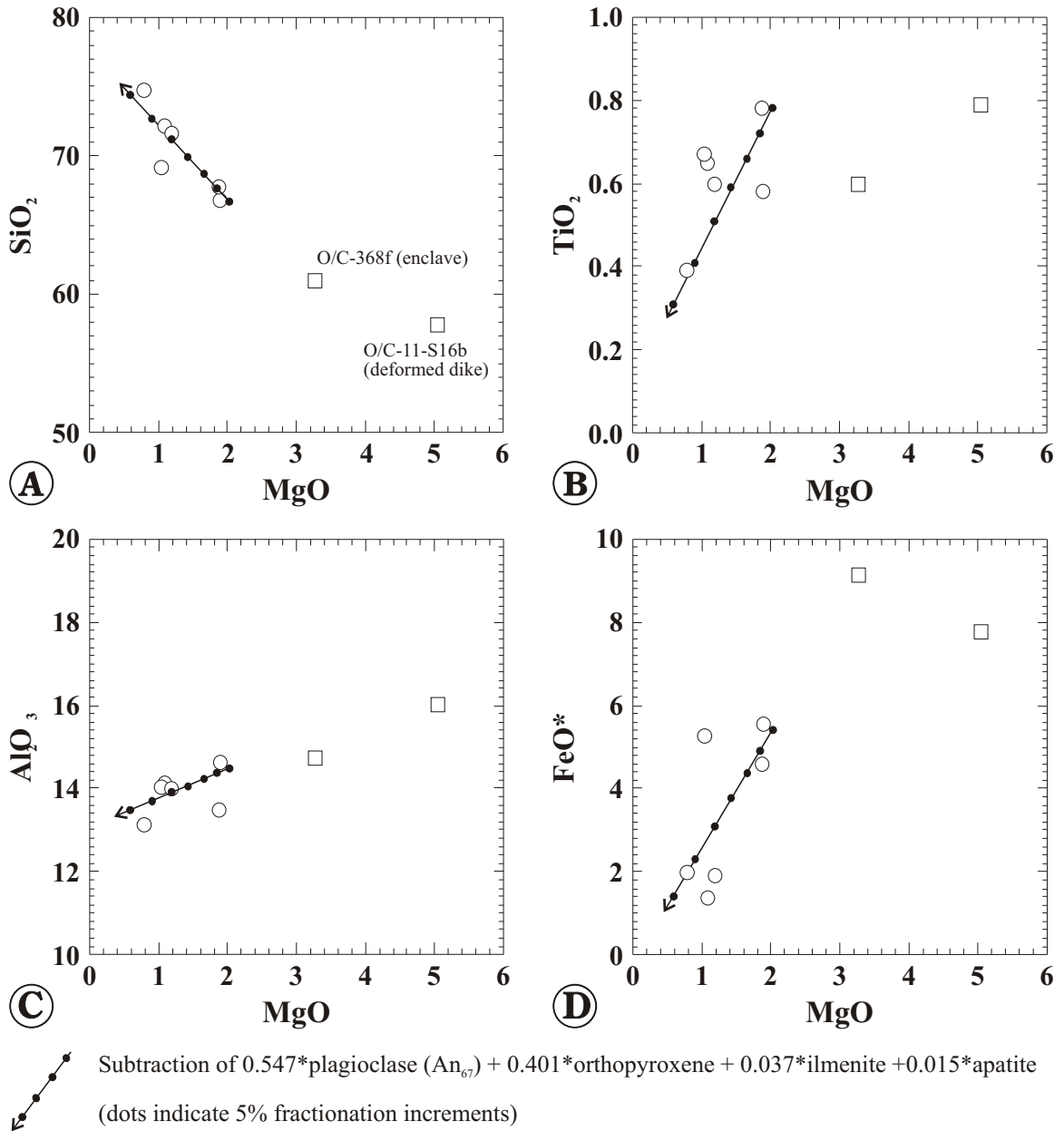


Figure 5.9

A-I: MgO variation diagrams of samples from the metatonalite unit. The trends are modeled by subtraction of plagioclase + orthopyroxene + ilmenite + apatite from a composition similar to O/C-11-S16a and O/C-368b. SiO_2 increases with increasing fractionation while MgO, TiO_2 , Al_2O_3 , FeO^* , MnO, CaO, and P_2O_5 decrease.

J: Al_2O_3 vs. SiO_2 bivariate plot showing the classification of trondhjemites after Barker (1979).

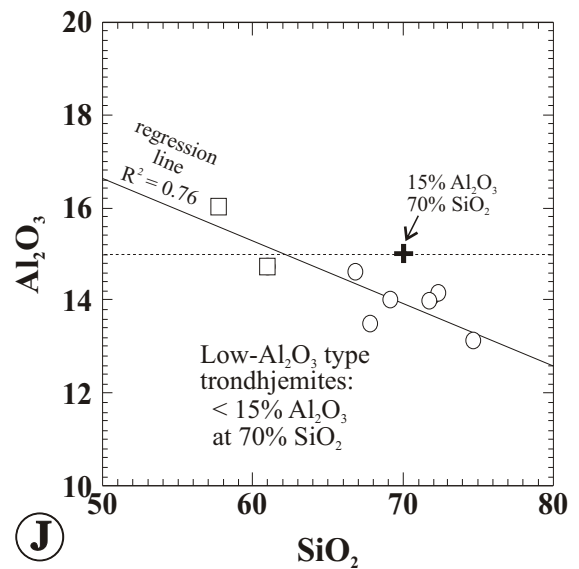
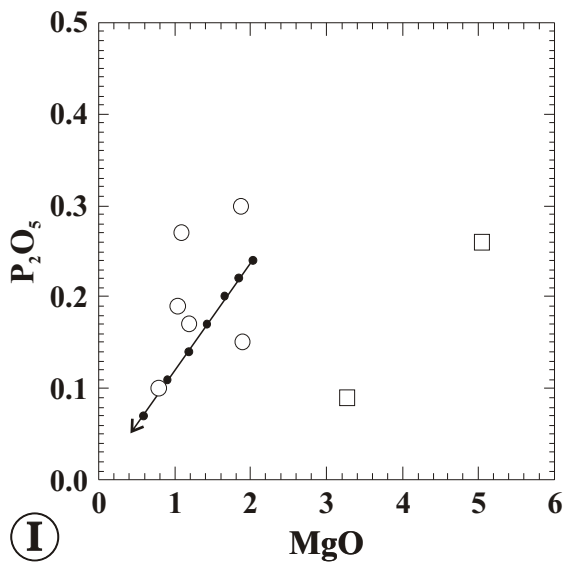
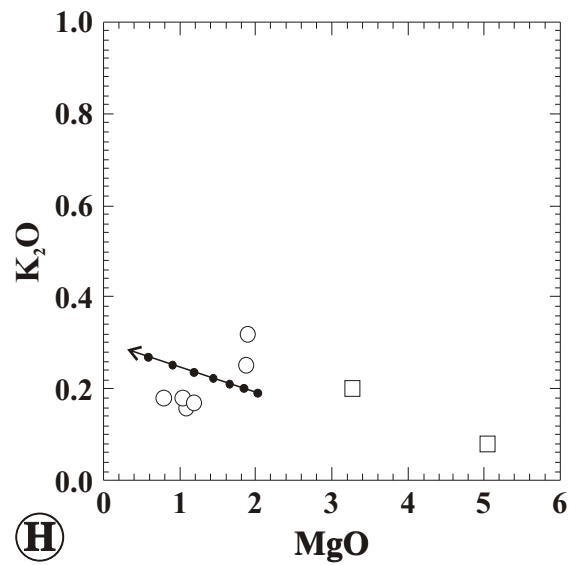
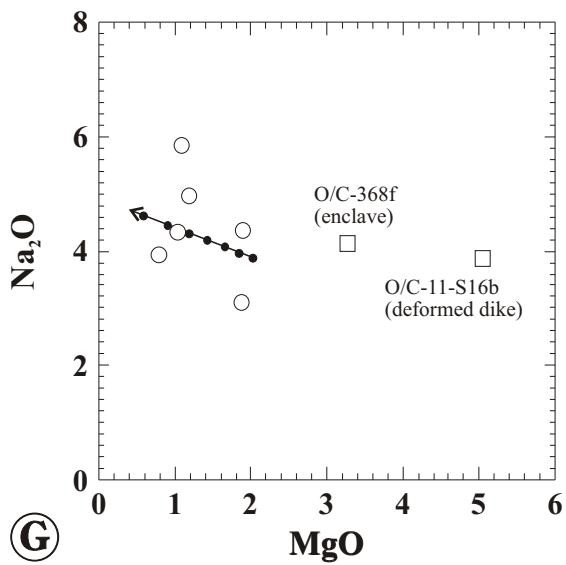
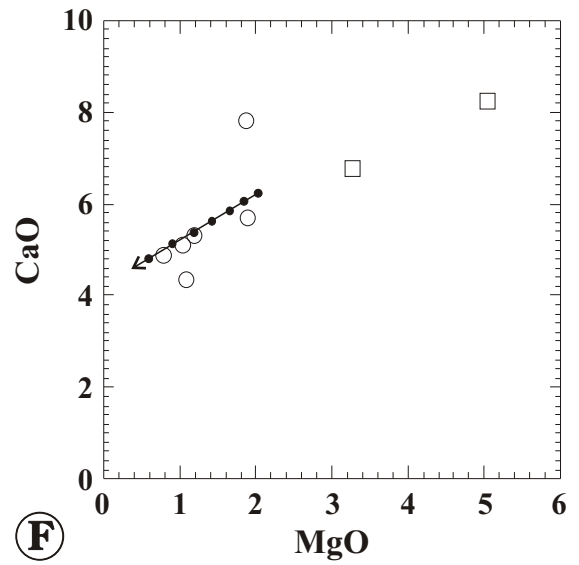
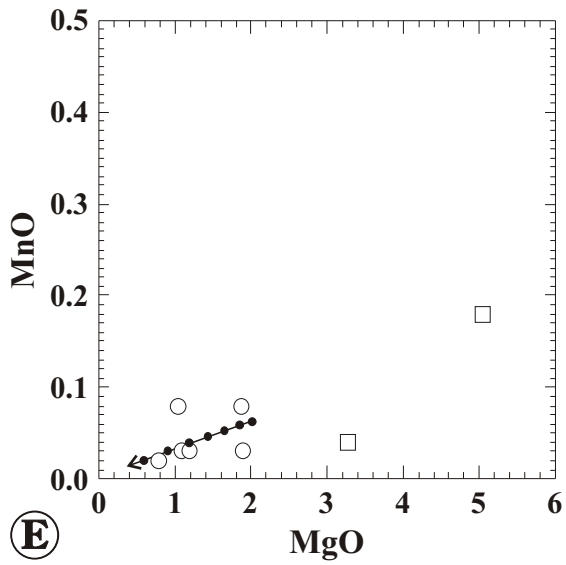
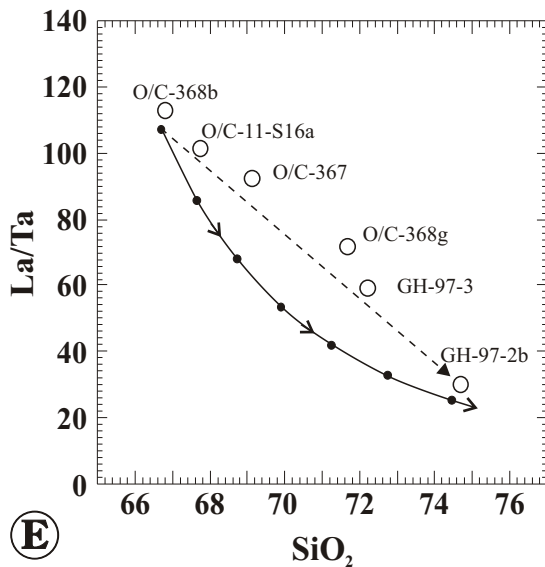
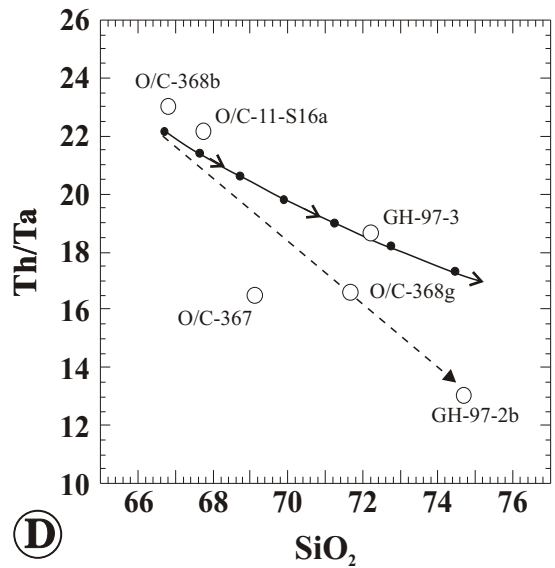
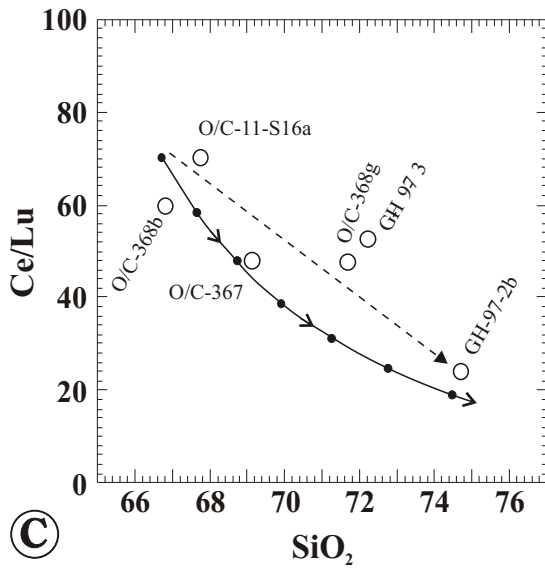
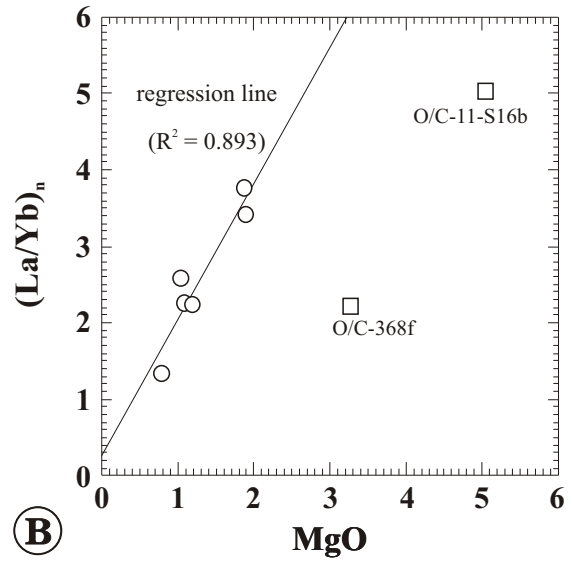
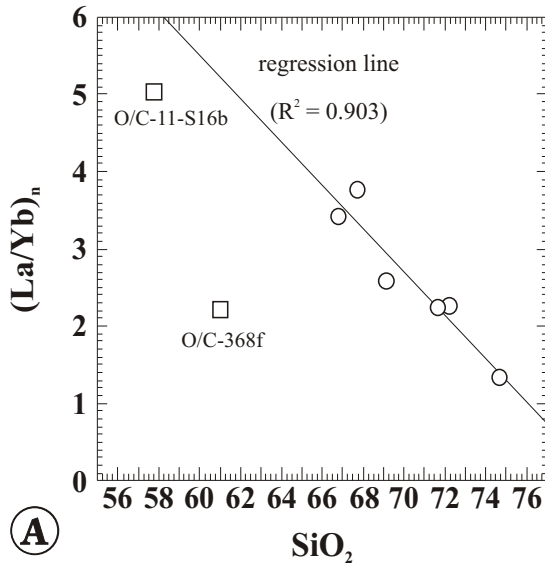


Figure 5.10

A - B: Chondrite normalized La/Yb ratios of samples from the metatonalite unit plotted against SiO₂ and MgO. The ratios decrease with increasing SiO₂ and decreasing MgO. The arrows indicate that fractionation of Mg-rich mafic phases (e.g., hornblende, pyroxene) + plagioclase + Fe-Ti oxides results in increase of SiO₂ and decrease of MgO but does not change the (La/Yb)_n ratios significantly. Fractionation involving allanite or magma mixing may explain the strong correlation between (La/Yb)_n and fractionation index (SiO₂ and MgO).

C - E: Trace element ratios in tonalite-trondhjemite samples plotted against SiO₂. Ce/Lu, Th/Ta and Ta/La decrease with increasing SiO₂ content. Fractionation of plagioclase + orthopyroxene + ilmenite + apatite + allanite (solid curve) can explain the decrease of these trace element ratios with increasing SiO₂. Alternatively, different magmas and magma mixing (dashed line) is also likely.

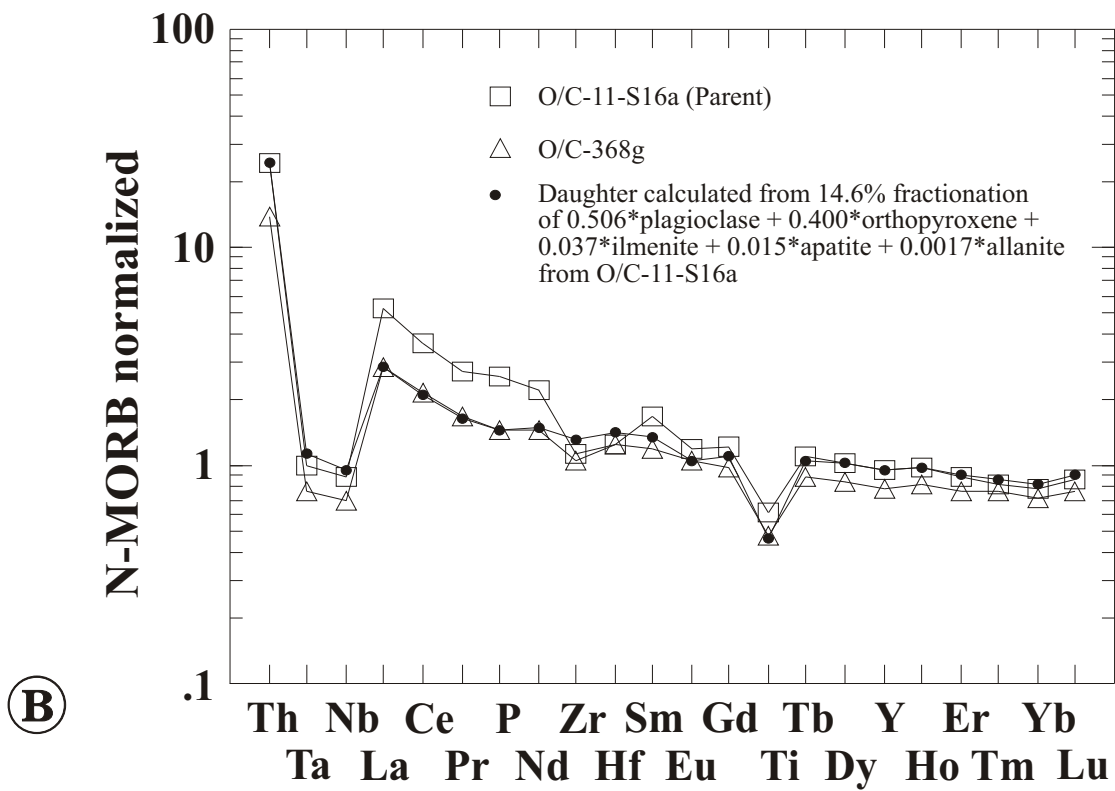
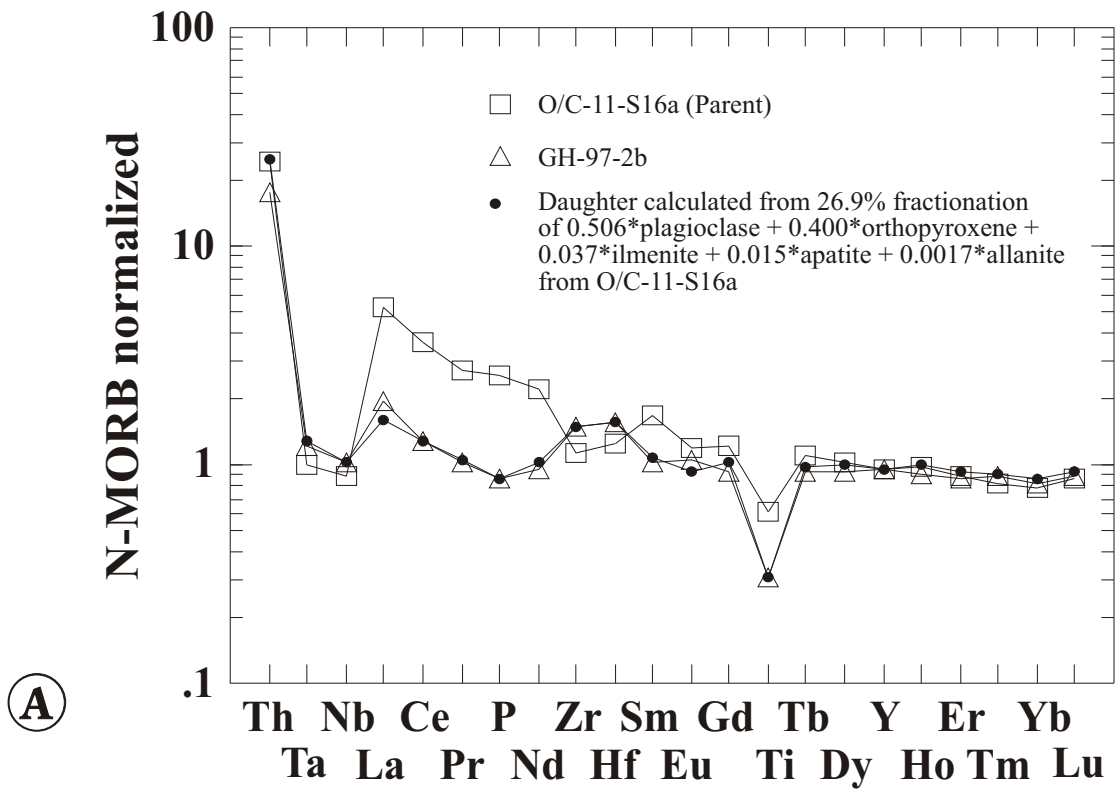


Fractionation trends (5% increments):
 $0.506 \cdot \text{plagioclase} + 0.400 \cdot \text{orthopyroxene} +$
 $0.037 \cdot \text{ilmenite} + 0.015 \cdot \text{apatite} +$
 $0.0017 \cdot \text{allanite}$

Magma mixing

Figure 5.11

N-MORB normalized REE and trace element variation patterns showing the effects of crystal fractionation in the metatonalite unit. (A) The REE and trace element composition of GH-97-2b is reproduced by 26.9% fractionation from O/C-11-S-16a. (B) The REE and trace element composition of O/C-368g is reproduced by 14.6% fractionation from O/C-11-S-16a. Fractionation involving allanite can explain the variations of REE, in the samples, however, it cannot explain the variations of Th, Ta, and Nb (figure 5.11a and 5.11b), and Th/Ta ratios with SiO₂ (figure 5.10).



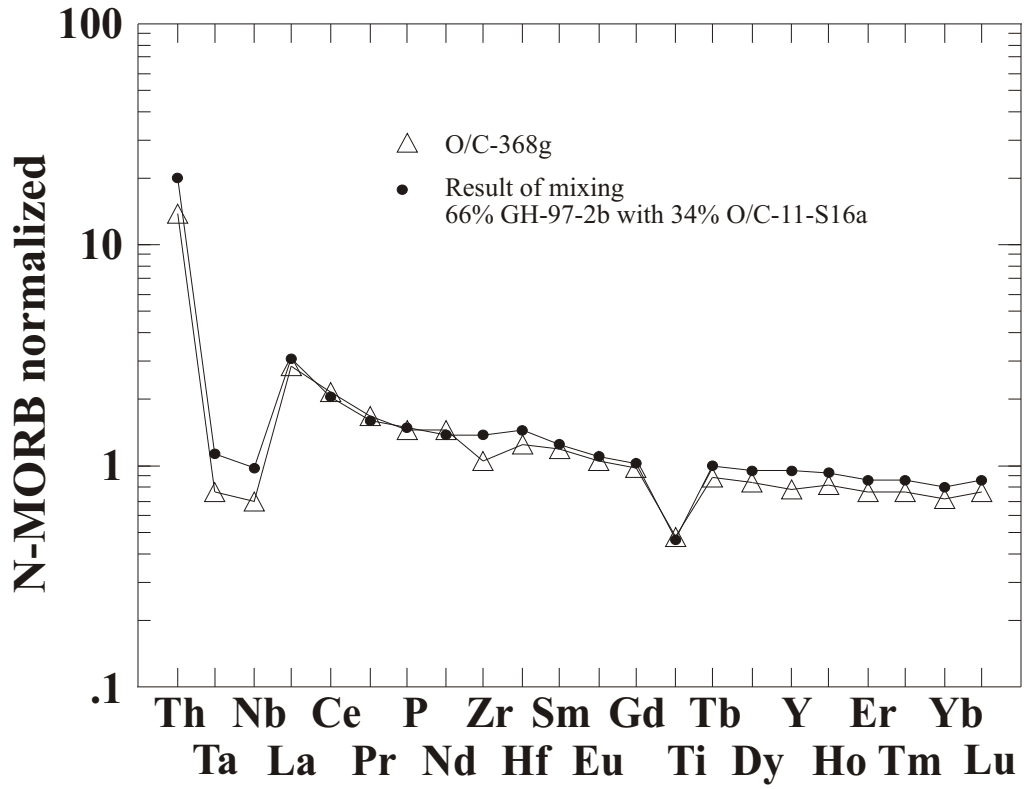


Figure 5.12

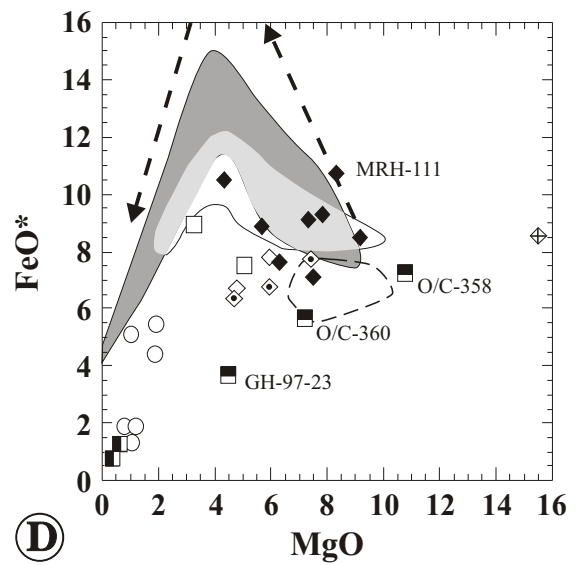
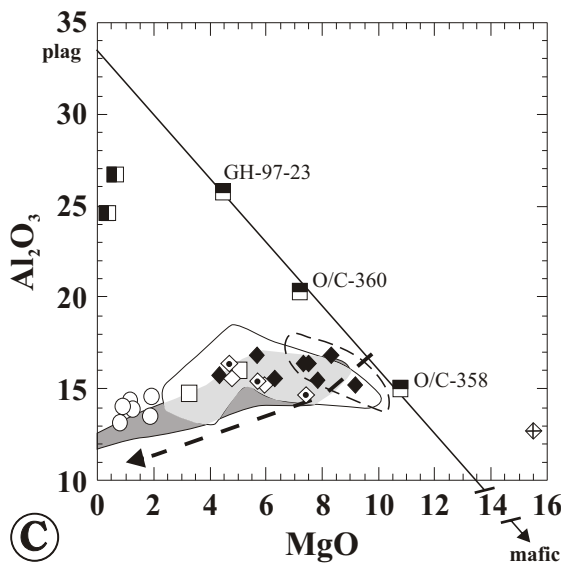
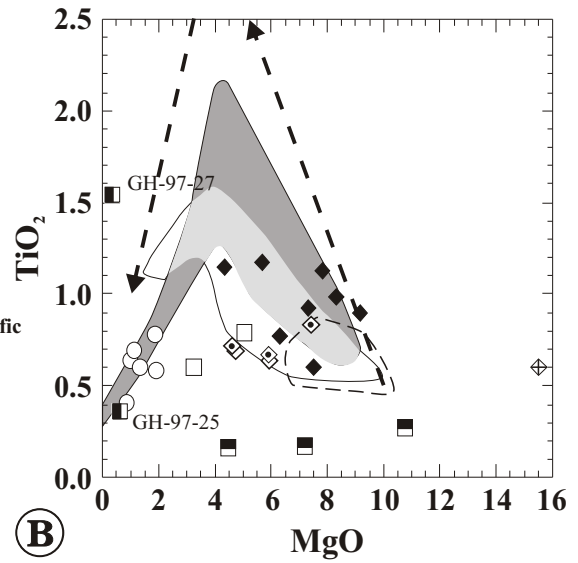
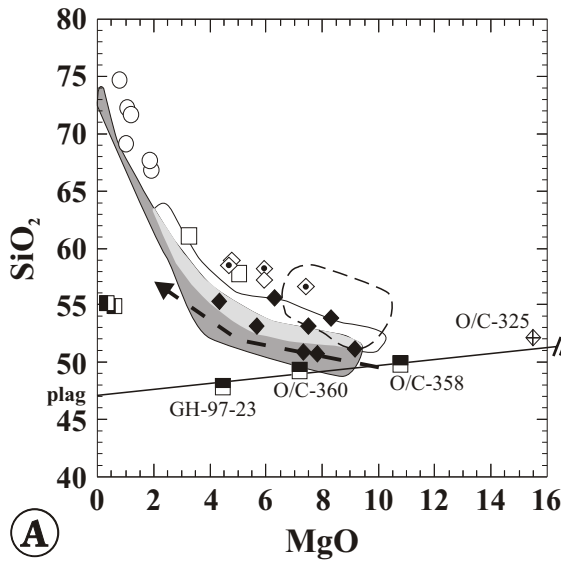
N-MORB normalized REE and trace element variation diagram showing the effects of mixing. GH-97-2b and O/C-11-S16a are mixed in proportions such that a composition most similar to O/C-368g is obtained. The composition of O/C-368g and the composition obtained by mixing GH-97-2b and O/C-11-S16a agree well suggesting that magma mixing is a likely process.

Figure 5.13

A - I: MgO variation diagrams of samples from the sheeted dike complex. Three samples from the cumulate gabbro screens lay on a straight line between plagioclase (plag) and a mafic mineral assemblage (mafic) suggesting different amounts of accumulation of plagioclase and mafic minerals. Figures 5.13 a, c, f, and g give the composition of plagioclase which is bytownite ($\sim\text{An}_{85}$). Based on CIPW norm calculations, the mafic mineral assemblage consists of 56.2% cpx, 40.5% opx, 0.1% olivine and 3.2% Fe-Ti oxides. The Fe/Mg ratio in cpx, opx and olivine is 0.28 (see text). In most MgO variation diagrams, the dikes of geochemical group 1 are distinct from dikes of geochemical group 2 (figures 5.13a, b, c, d, and f). The dikes of group 1 follow a tholeiitic fractionation trend similar to rift-related lavas recovered at ODP Leg 135 Site 839 in the Lau Basin, SW Pacific. Three dikes of group 1 have higher TiO_2 for a given MgO than Site 839 lavas (figure 5.13b) and appear to be similar to lavas dredged at the Eastern Lau Spreading center. In contrast the dikes of group 2 (and the samples from the metatonalite unit) follow a calc-alkaline fractionation trend. The analytical data of samples from the metatonalite unit are plotted for comparison. These data seem to form an extension of the trends defined by the microdioritic dikes.

J: FeO/MgO vs. SiO_2 discrimination diagram of Miyashiro (1974).

The field for ODP Leg 135 Site 839 (IAT) is defined by analyses published in Ewart et al. (1994a, 1994b), Hawkins and Allan (1994), Hawkins (1995), Hergt and Hawksworth (1994), and Pearce et al. (1995b). The field for the Eastern Lau Spreading Center (MORB-IAT) is defined by analyses published in Hawkins and Melchior (1985), Hawkins (1995), Frenzel et al. (1990), Davis et al. (1990), Boespflug et al. (1990), and Pearce et al. (1995b). The field for CAB from the Lassen region, California is defined by analyses published in Borg et al. (1997) and Conrey et al. (1997). The fractionation trend for N-MORB (dashed arrow) is from Hochstaedter et al. (1990a).



Metatonalite unit

- Tonalite-trondhjemite
- Dioritic dike and enclave

Sheeted dike complex

- ◆ diabasic dikes (geochemical group 1)
- diabasic and microdioritic dikes, (geochemical group 2)
- ◇ w/o ol-xenocrysts
- ◊ with 1-6% ol-xenocrysts
- ⊕ with ~25% olivine

- Gabbro screens
- cumulate gabbro
- plagioclasite

- Primitive calc-alkaline basalts with highest Sr/P ratios from the Lassen region, Cascade arc, California
- IAT: ODP Leg 135 Site 839, Lau Basin, SW Pacific
- Trans. IAT-MORB: Dredge samples, Eastern Lau Spreading Center
- ▲ Fractionation trend of N-MORB

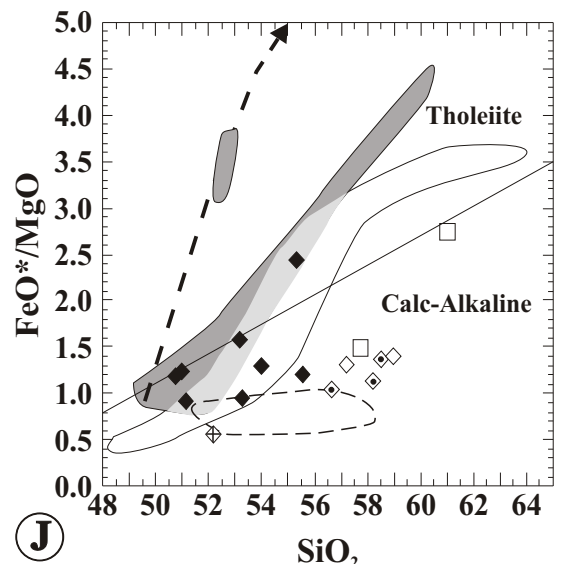
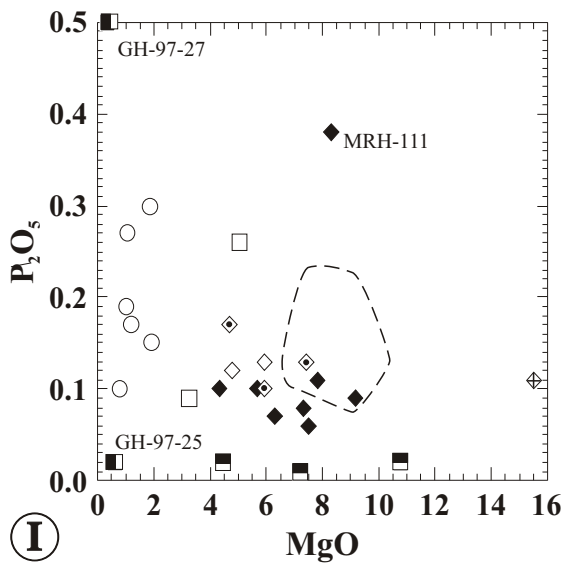
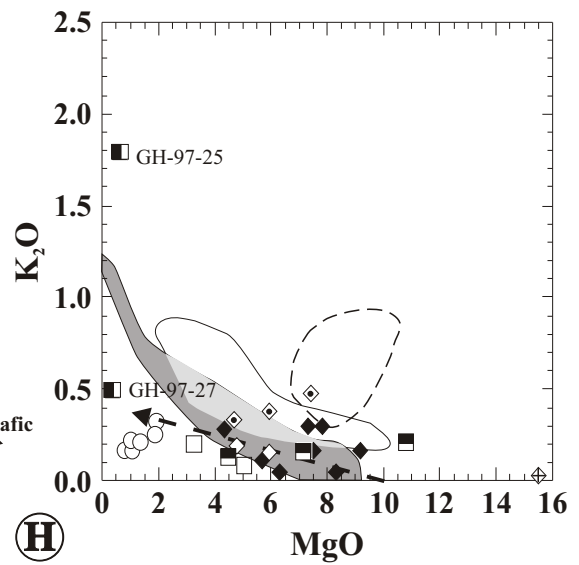
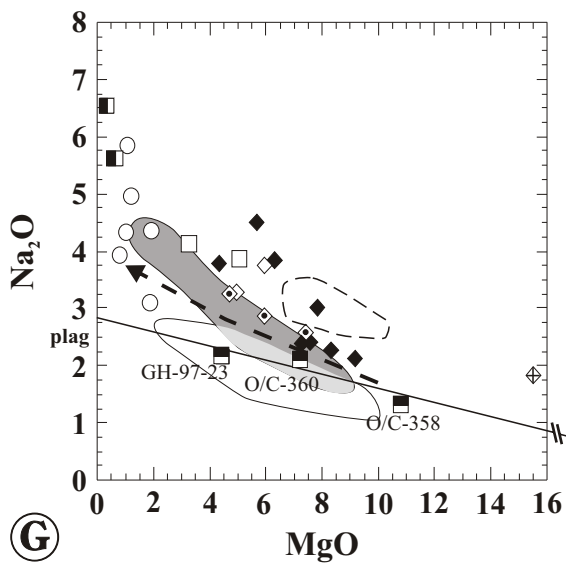
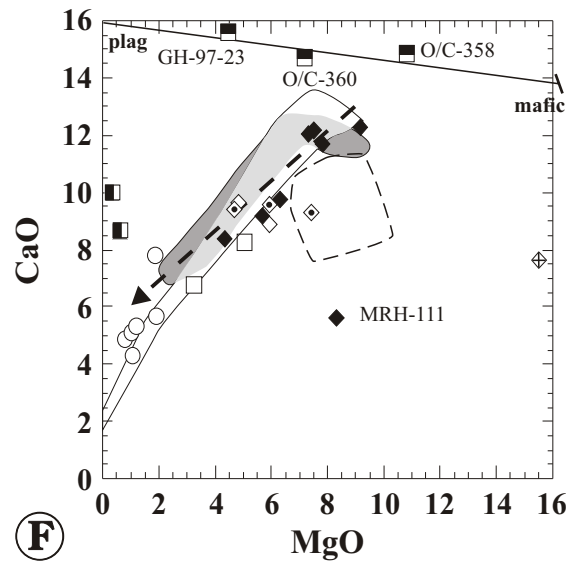
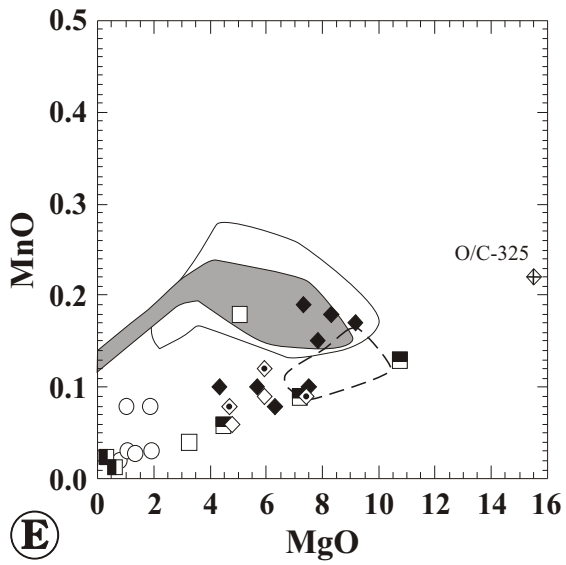
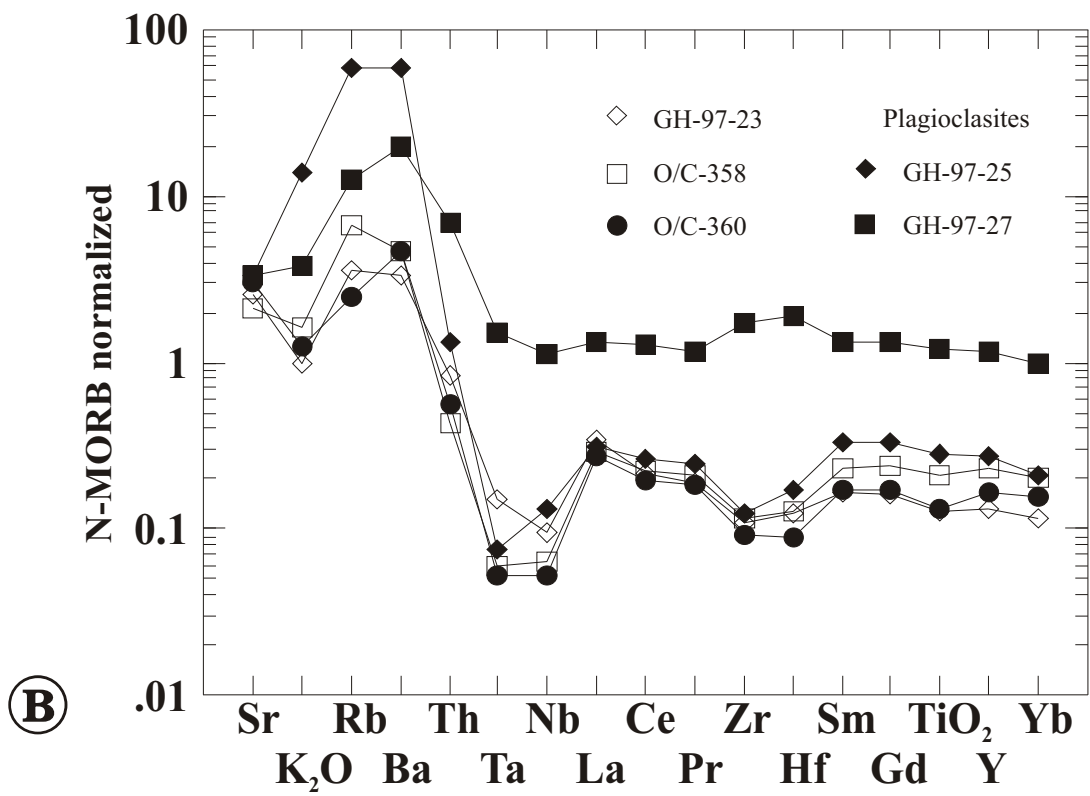
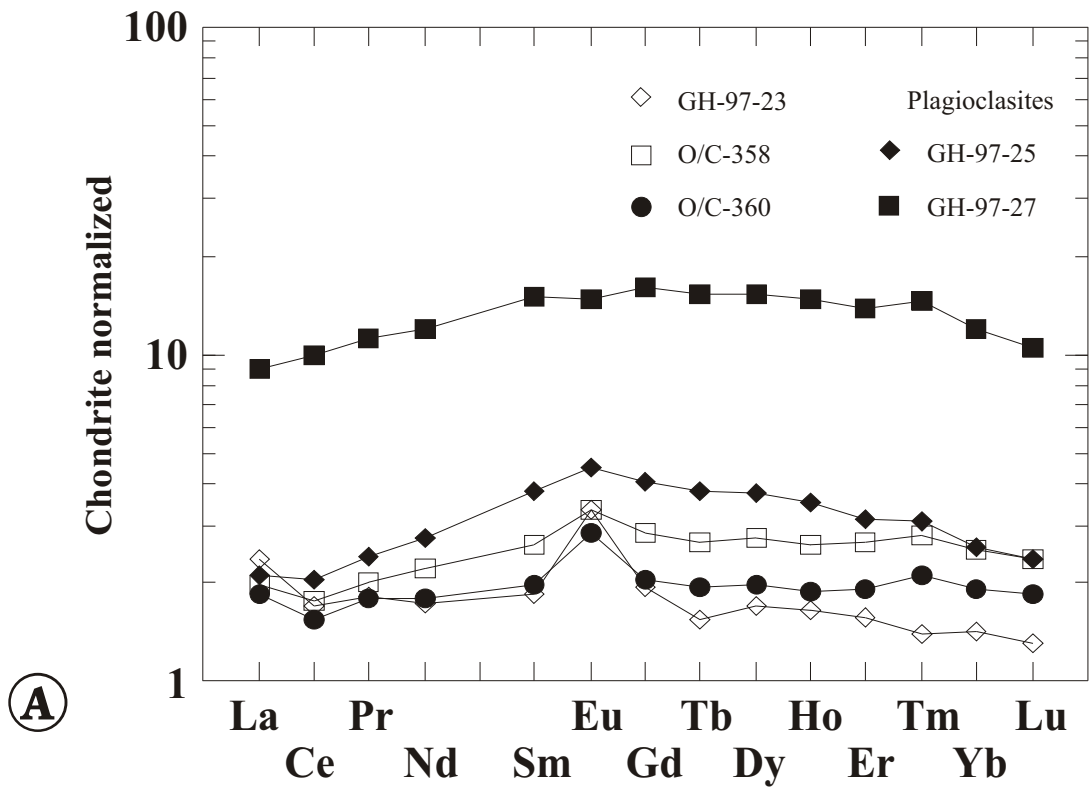


Figure 5.15

- A. Chondrite normalized REE distribution diagrams of samples from gabbroic screens in the sheeted dike complex. The patterns vary from flat to LREE depleted. The LREE depletion could reflect the composition of the parental magma. The positive Eu-anomaly increases with decreasing REE abundance suggesting accumulation of plagioclase.
- B. N-MORB normalized trace element distribution diagram of samples from the gabbroic screens in the sheeted dike complex. The patterns have a strong arc signature indicating selective enrichment of LILE and Th and relative depletion of Ta, Nb as well as Zr and Hf. Compared to island arc tholeiites (figure 5.2), the patterns of the cumulates are shifted down indicating very low abundance of incompatible elements. GH-97-27 is a sample consisting almost entirely of plagioclase similar to GH-97-25. However, the high concentrations of incompatible trace elements in GH-97-27 compared to the other cumulate samples suggest the presence of highly fractionated melt in between cumulate phases.



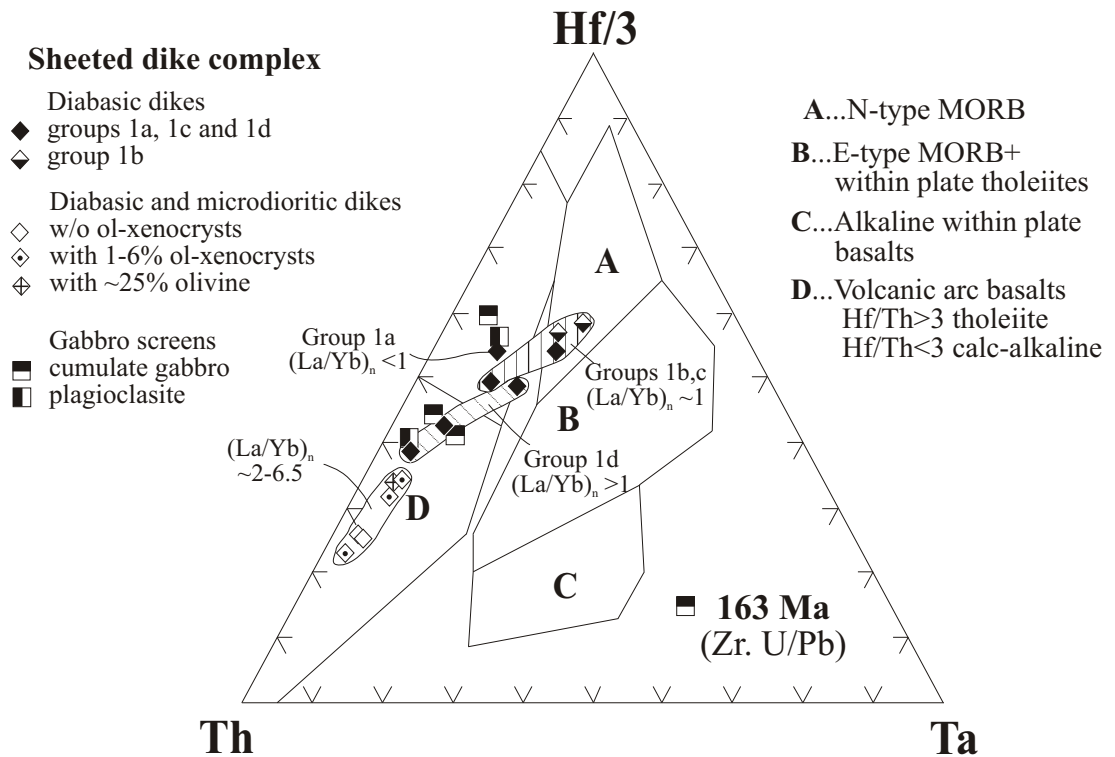


Figure 5.16

Hf/3-Th-Ta tectonic discrimination diagram with fields after Wood et al. (1979). The samples from the gabbro screens (cumulate gabbro and plagioclase) plot in the volcanic arc field. The dikes of geochemical group 1 plot in the field for N-MORB and IAT. The dikes of geochemical group 2 plot in the field for calc-alkaline rocks.

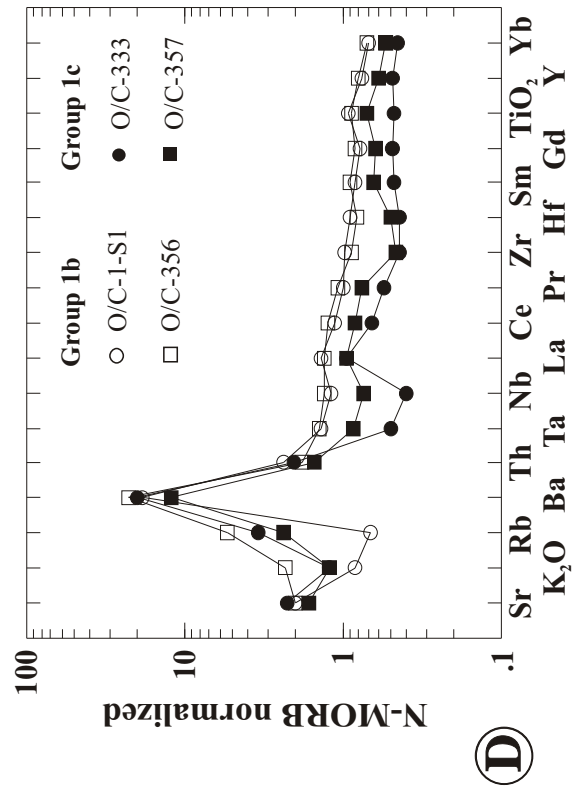
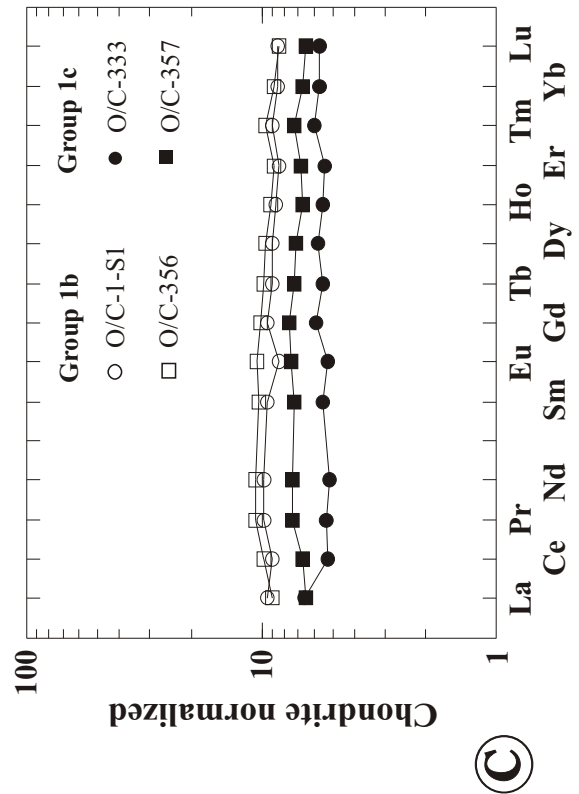
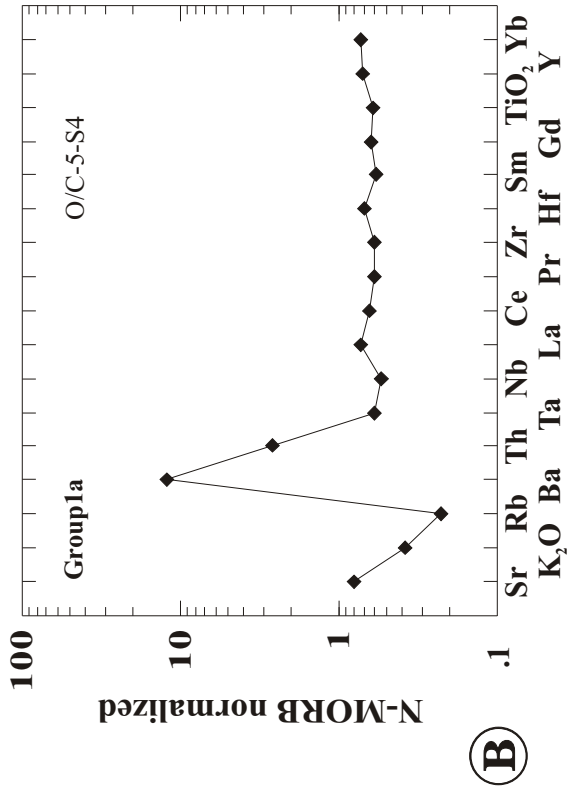
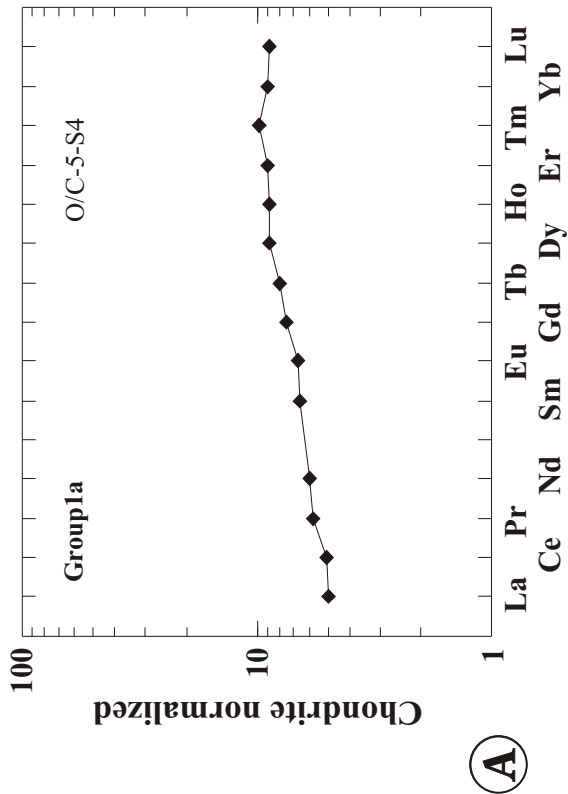
Figure 5.17

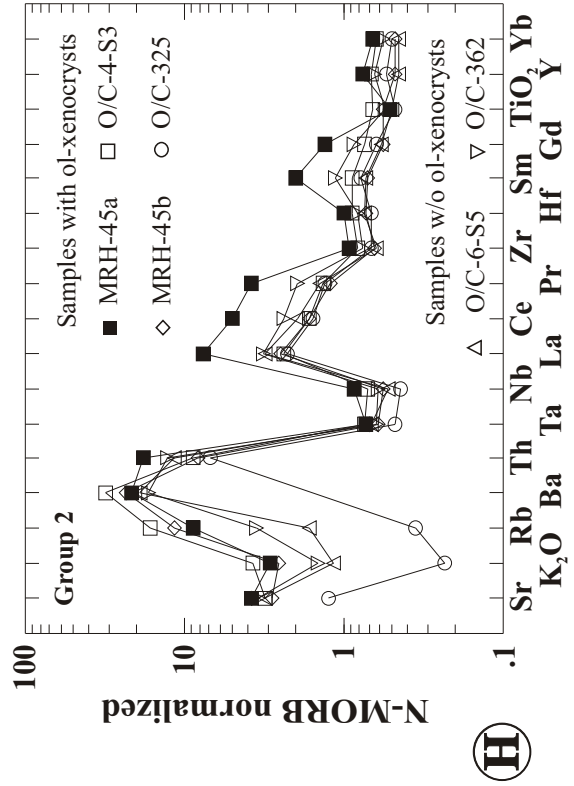
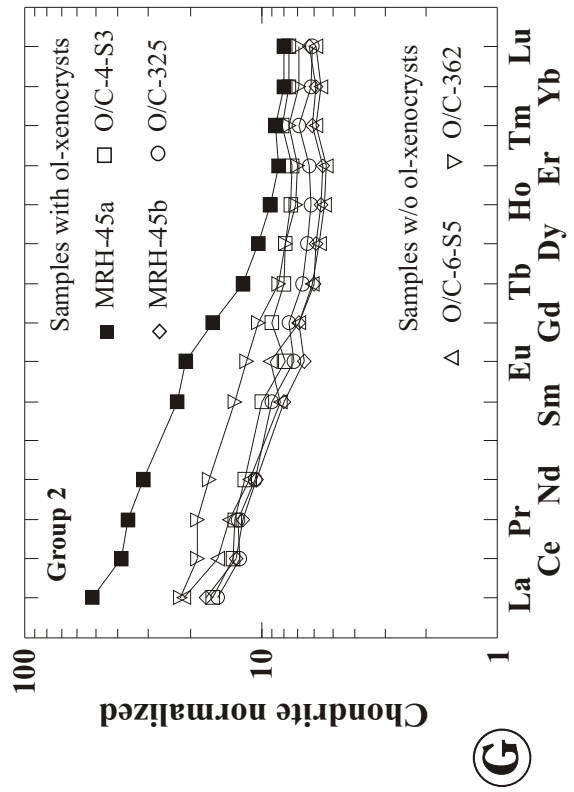
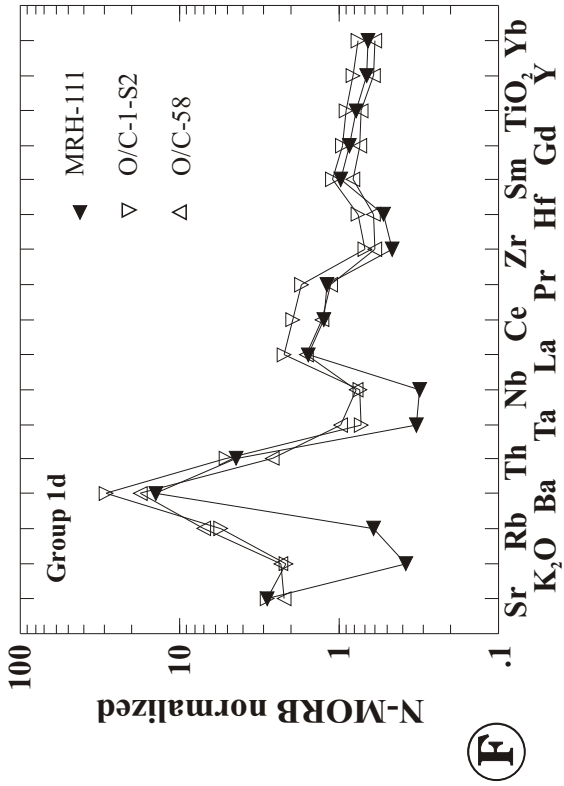
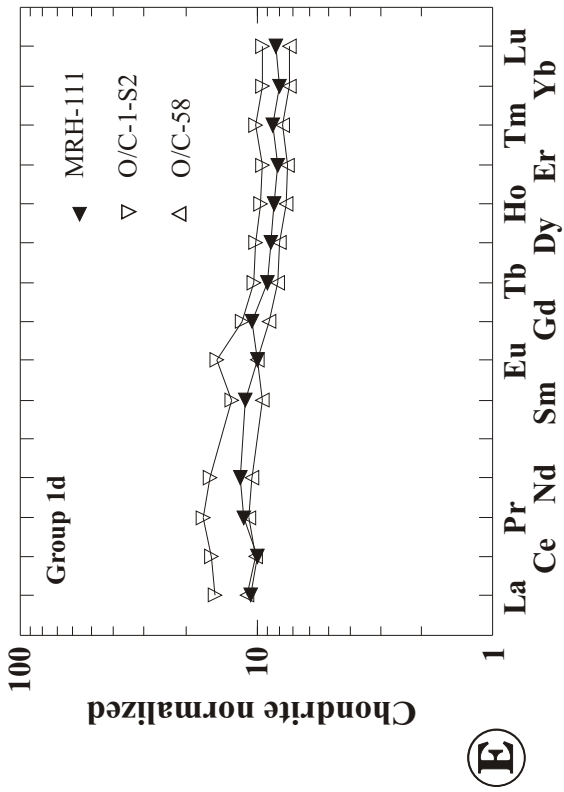
A - F: Chondrite and N-MORB normalized REE and trace element distribution diagrams of dikes of geochemical group 1. The REE patterns vary from LREE depleted (figure 5.17a) to flat (figure 5.17c) to slightly LREE enriched (figure 5.17e). Sample O/C-5-S4 has a $(La/Yb)_n$ ratio of 0.55. The ratios of samples O/C-1-S1, O/C-356, O/C-333 and O/C-357b range from 0.98 to 1.16, and of samples MRH-111, O/C-1-S2 and O/C-58 from 1.32 to 1.58.

Two distinct N-MORB normalized trace element variation diagrams are recognized. O/C-1-S1 and O/C-356 (subgroup 1b) are similar to N-MORB showing a pattern that gently slopes from Th to Yb. The patterns of the other dikes (subgroups 1a, 1c and 1d) are characterized by relative depletion of HFSE (e.g., negative Ta- and Nb- anomaly) and selective enrichment of LILE and Th, which is typical of IAT (see figure 5.2).

G - H: Chondrite and N-MORB normalized REE and trace element distribution diagrams of dikes of geochemical group 2. The dikes of group 2 are much more enriched in LREE ($(La/Yb)_n > 2$) than the dikes of group 1. However, similar to the dikes of group 1, $(La/Yb)_n$ ratios vary greatly ranging between 2.1 and 6.5.

The patterns in the N-MORB normalized diagram are characterized by very strong enrichment of LILE, Th and LREE, while Ta and Nb as well as Zr and Hf are depleted. The Ta/Yb ratios are similar to that of N-MORB whereas the levels of Ta and Nb are only 0.4 to $0.7 \times$ N-MORB. These are characteristics of CAB (see figure 5.2).





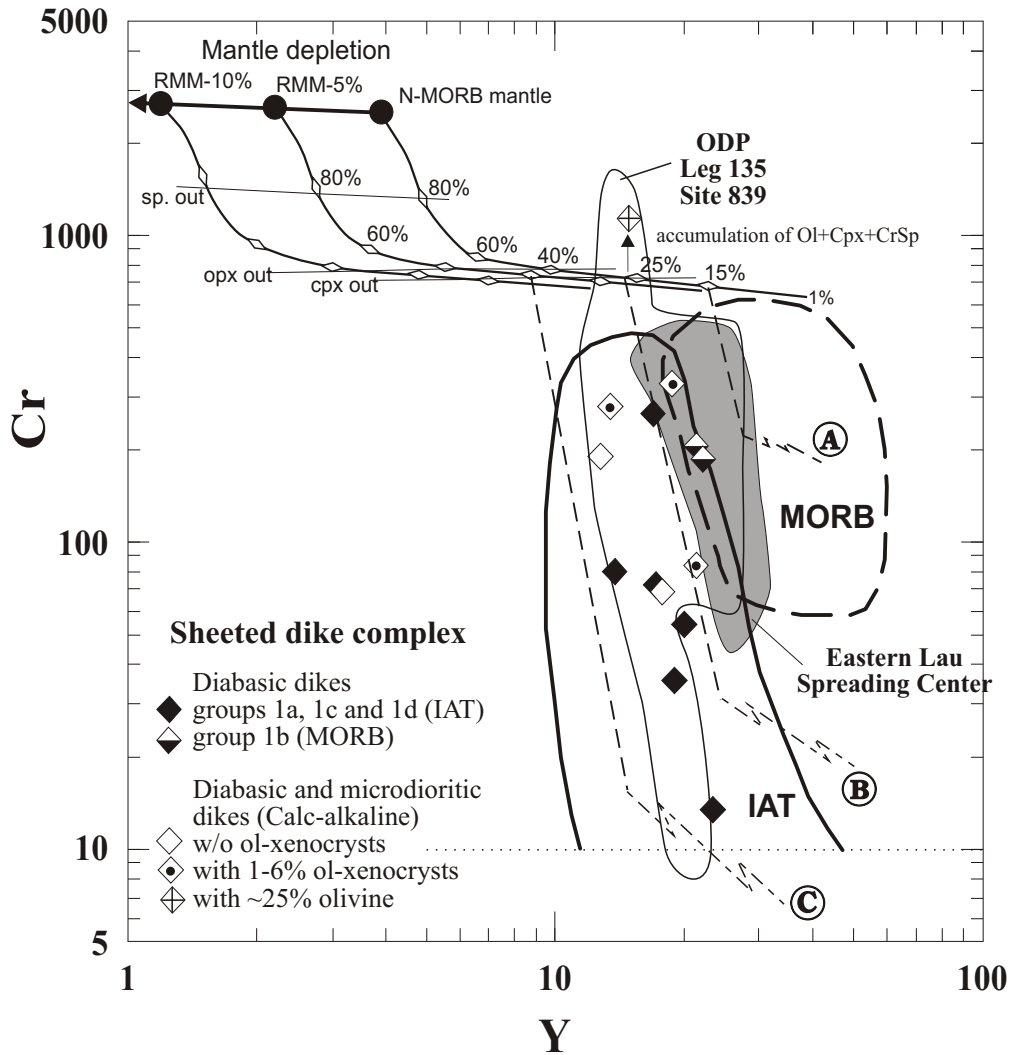


Figure 5.18

Cr vs. Y tectonic discrimination diagram of Pearce (1982) showing the fields for mid ocean ridge basalts (MORB) and island arc tholeiites (IAT) (the latter field also includes calc-alkaline and alkalic basalts from oceanic arcs). The modeled melting curves of the N-MORB mantle and the residual MORB mantle after 5% (RMM-5%) and 10% (RMM-10%) melt extraction are calculated as outlined in figure 5.4. The fractional crystallization trends for MORB (A), IAT (B) and boninite (C) are taken from Pearce et al. (1984a). The steep vector represents crystallization of olivine + Cr-spinel ± clinopyroxene, and the shallower vector represents crystallization of olivine + Cr-spinel + clinopyroxene + plagioclase. The dikes having trace element patterns similar to IAT and CAB have lower Y-contents than the dikes with N-MORB like patterns suggesting either higher degrees of partial melting or a more depleted mantle source.

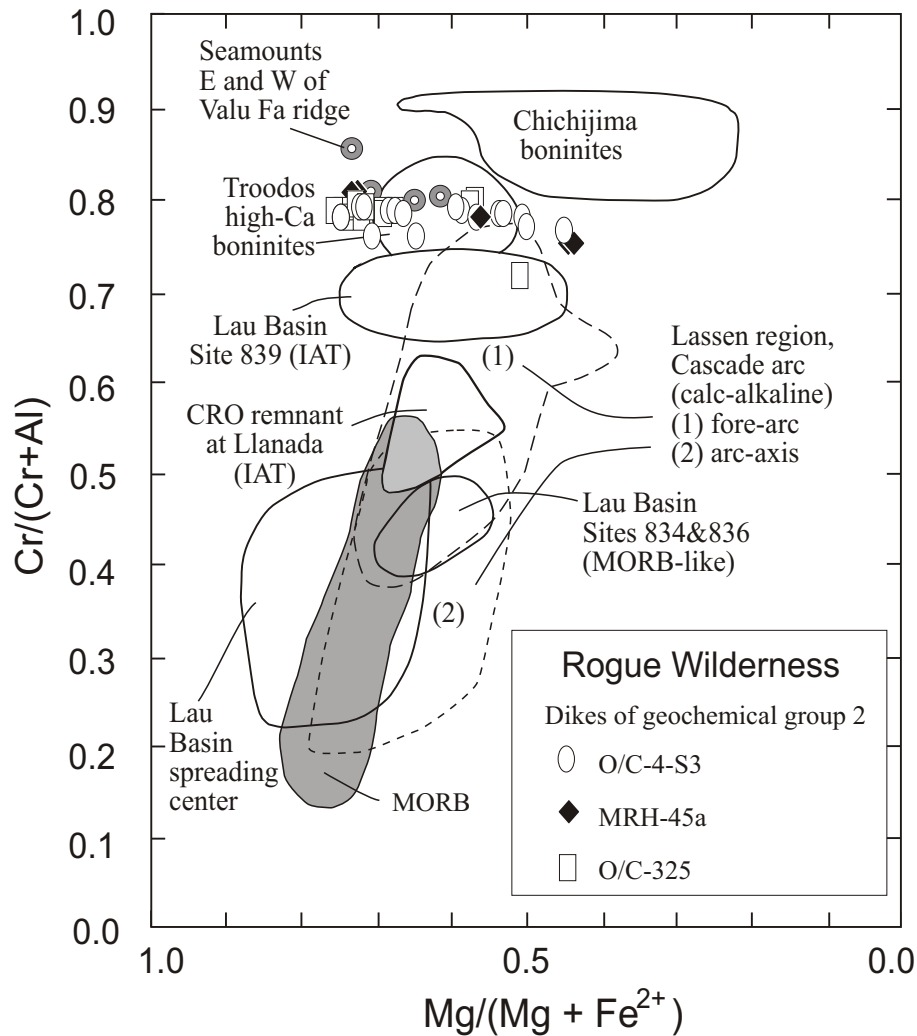
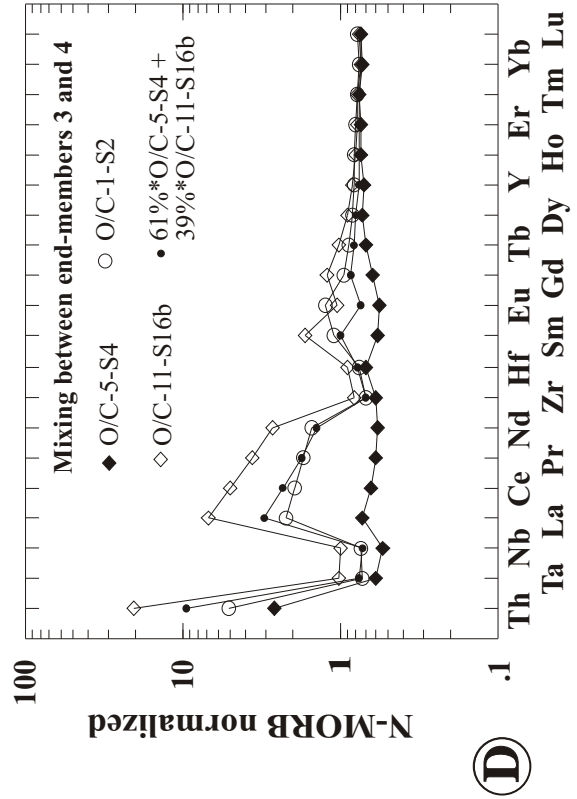
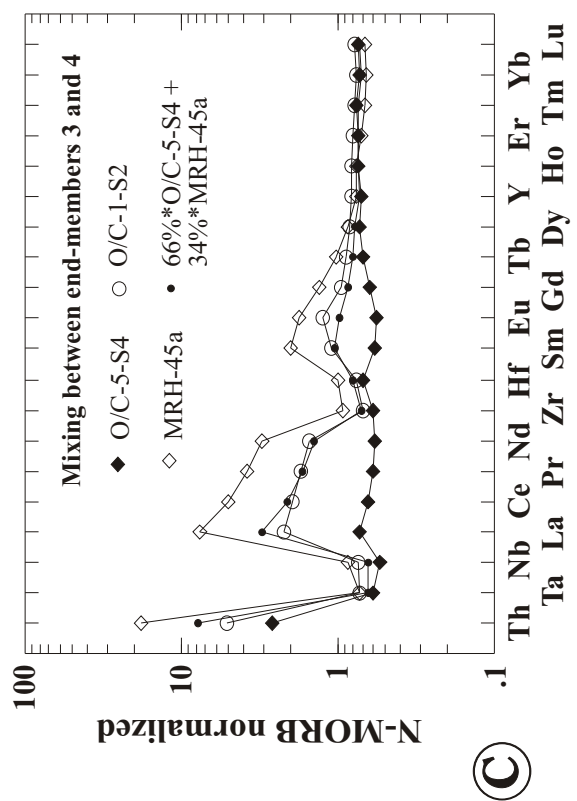
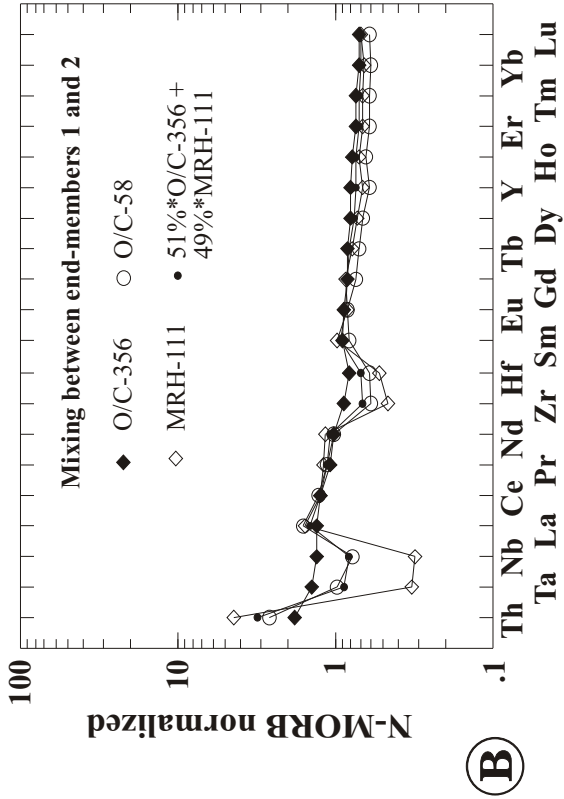
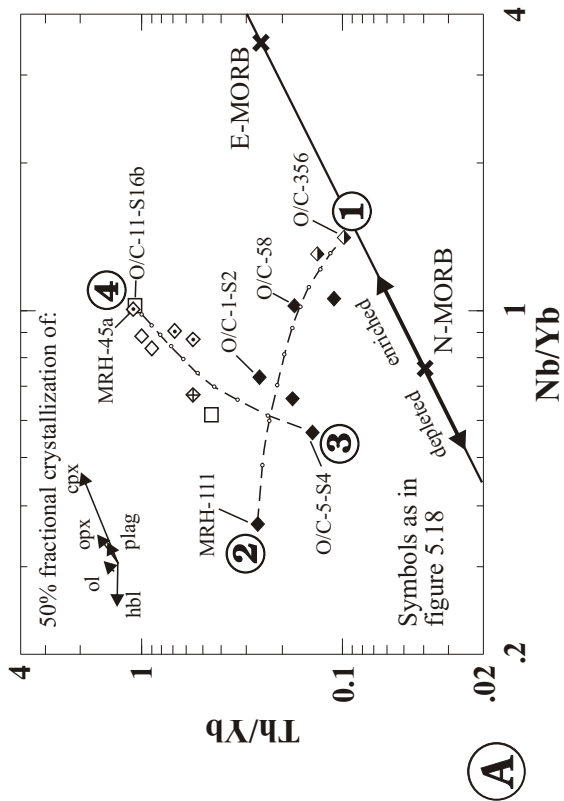


Figure 5.19

Comparison of the composition of Cr-spinel in dikes of geochemical group 2 (sheeted dike complex) with chromites from modern island arcs, the Troodos ophiolite, and the Coast Range ophiolite (CRO remnant at Llanada). The fields for Chichijima, Troodos, and the Lau Basin are from Meffre et al. (1996), for MORB from Dick and Bullen (1984), for the Coast Range ophiolite remnant at Llanada from Giaramita et al. (1998), and for the Cascade arc from Clynne and Borg (1997).

Figure 5.20

- A. Plot of Th/Yb vs. Nb/Yb for samples from the sheeted dike complex and metatonalite unit. The solid line indicates the variations of the Th/Yb and Nb/Yb ratios in MORB (from Pearce, 1982; Pearce and Peate, 1995; Pearce et al., 1995a, Pearce and Parkinson, 1993). The crosses on that line give the normalizing values for N-MORB and E-MORB. Also, the mantle depletion and enrichment trends relative to N-MORB are shown. Mixing of magmas derived by partial melting of four different mantle sources can explain the range of trace element compositions observed in dikes of geochemical group 1 (half-filled and solid diamonds) and dikes of geochemical group 2 (empty diamonds) from the sheeted dike complex as well as the deformed dike (O/C-11-S16b) and the enclave (O/C-368f) from the metatonalite unit (empty squares). The broken lines indicate the mixing curves between the different magmas.
- B. Mixing of O/C-356 (end member 1) and MRH-111 (end member 2) results in a composition similar to O/C-58.
- C. Mixing of O/C-5-S4 (end member 3) and MRH-45a (end member 4) results in a composition similar to O/C-1-S2.
- D. Mixing of O/C-5-S4 (end member 3) and O/C-11-S16b (end member 4) results in a composition similar to O/C-1-S2.



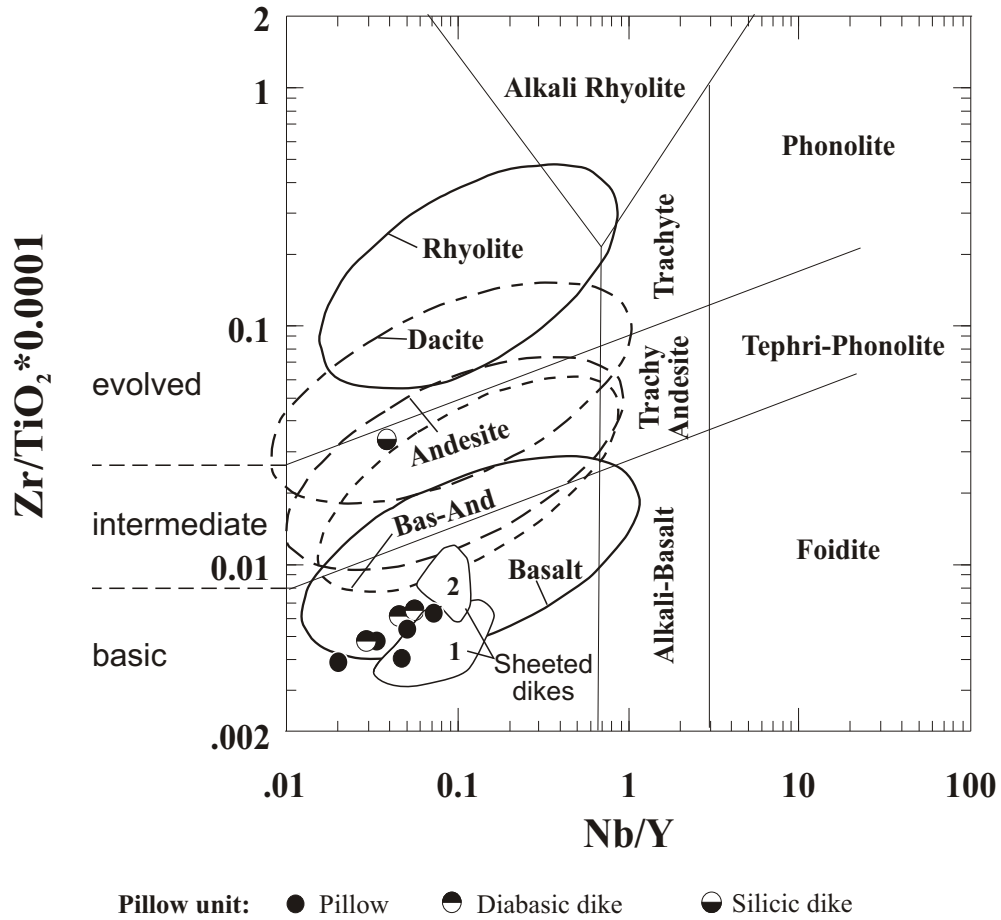


Figure 5.21

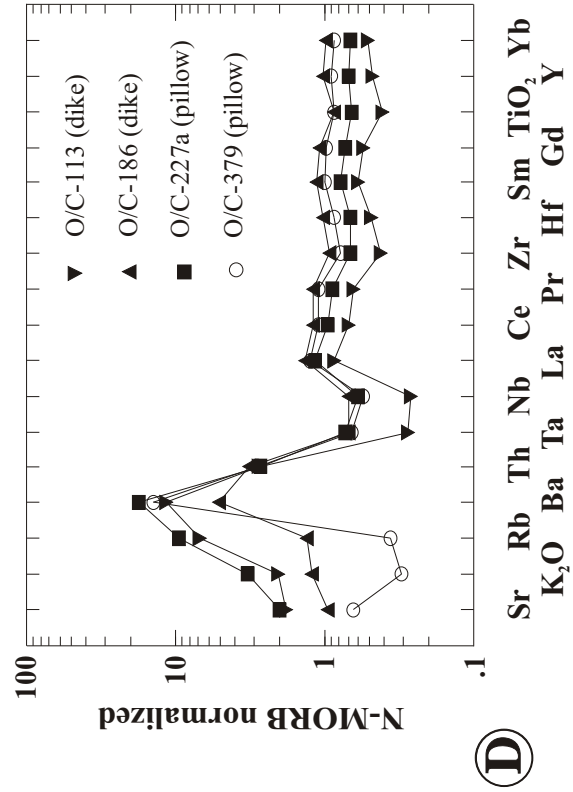
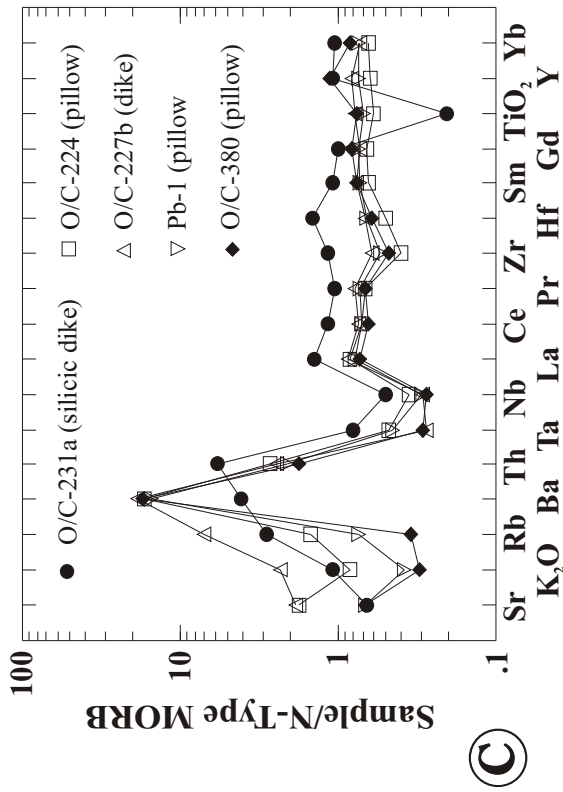
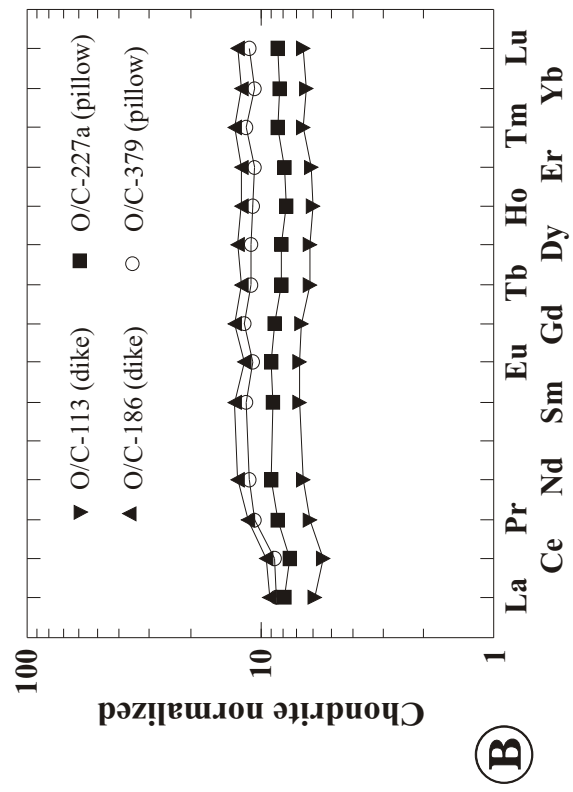
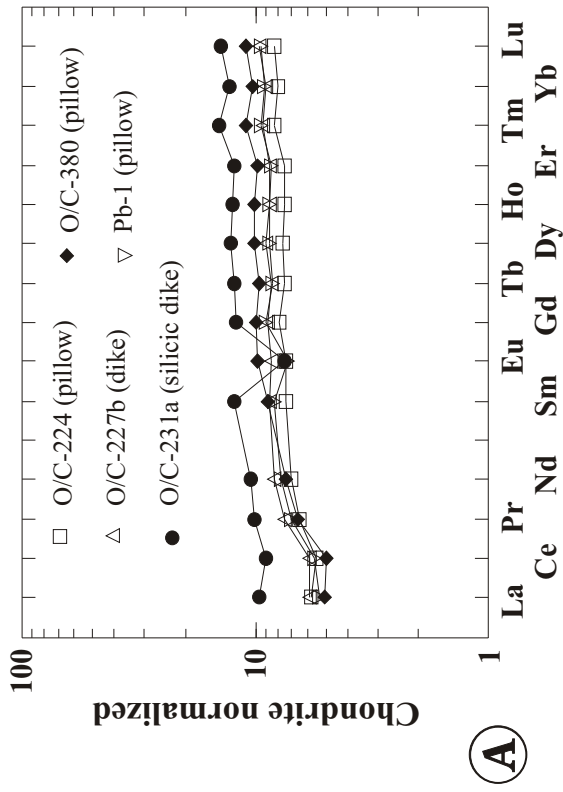
Zr/TiO_2 vs. Nb/Y diagram of Winchester and Floyd (1977) with fields revised by Pierce (1996).

Additionally, the 10% probability ellipses for TAS-defined rock types from subalkaline series are shown (after Pierce, 1996). The 10% probability ellipses overlap substantially. The samples from the pillow unit plot in the field for subalkaline basalts. For comparison, the fields for the dikes of geochemical groups 1 and 2 are shown. The basic samples from the pillow unit have higher Zr/TiO_2 ratios than dikes of geochemical group 1 from the sheeted dike complex.

Figure 5.22

A - B: Chondrite normalized REE distribution diagrams of samples from the pillow unit. The patterns range from LREE depleted to almost flat. All samples have a pattern with a strong negative Ce-anomaly. The $(La/Yb)_n$ ratios of the first group of samples (O/C-224, O/C-227b, O/C-231a, O/C-379 and PB-1) range from 0.51 to 0.79. The chondrite normalized values for Pr and Nd are smaller than the normalized values for Yb and Lu. Samples of the second group (O/C-113, O/C-186, O/C-227a and O/C-379) have almost flat REE patterns with $(La/Yb)_n$ ratios from 0.8 to 1.00. The chondrite normalized values for Pr and Nd are equal to the normalized values for Yb and Lu; only La and Ce are slightly depleted.

C - D: N-MORB normalized trace element distribution diagram of samples from the pillow unit. The HFSE Ta, Nb, Zr, and Hf are variably depleted and LILE, Th and LREE are selectively enriched. Highly mobile elements, such as Rb and K, may have been redistributed during hydrothermal alteration. The patterns of all samples are similar to IAT (figure 5.2).



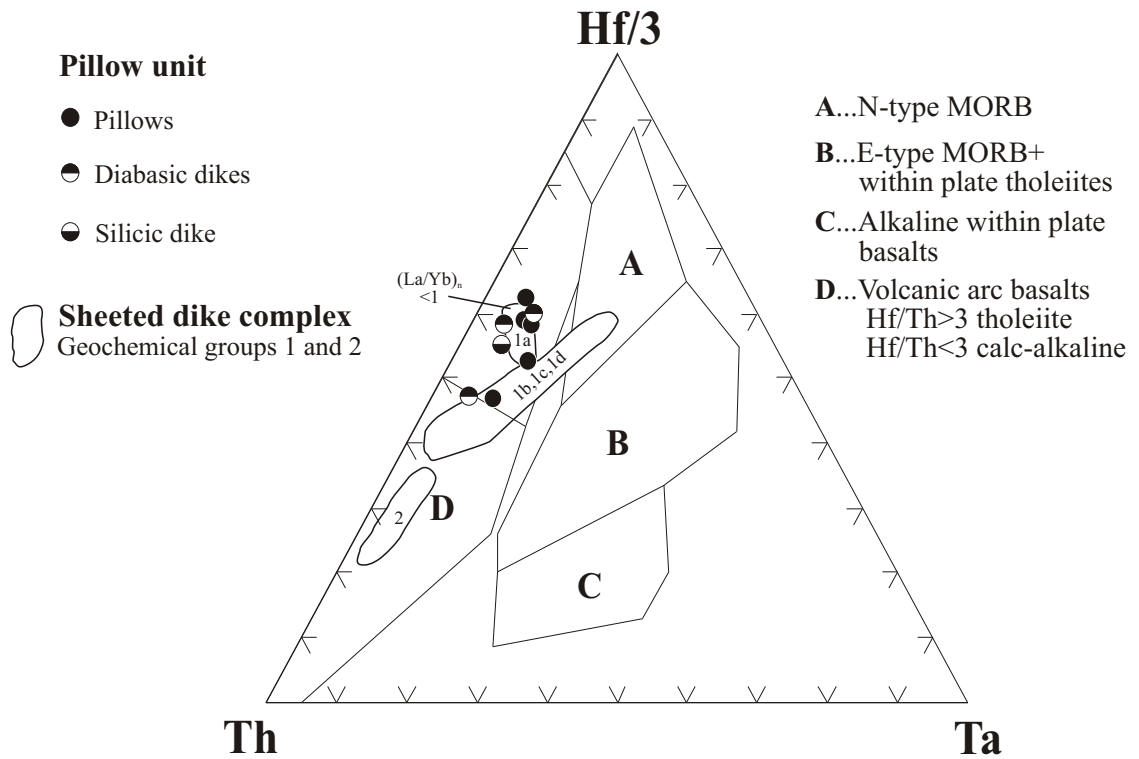


Figure 5.23

Hf/3-Th-Ta tectonic discrimination diagram with fields after Wood et al. (1979). The samples from the pillow unit plot in the field for island-arc tholeiite. For comparison the fields for dikes of geochemical group 1 (N-MORB and IAT) and dikes of geochemical group 2 (calc-alkaline) from the sheeted dike complex are shown.

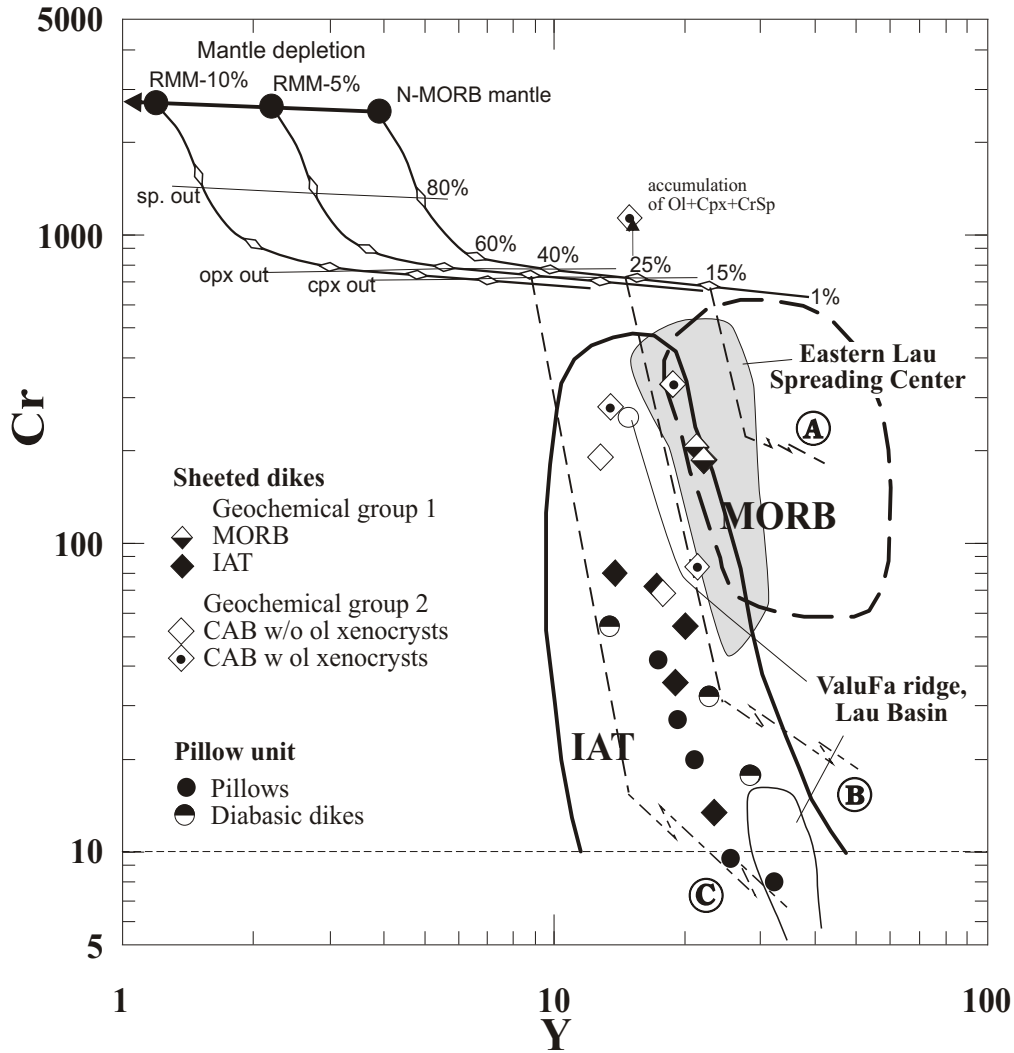


Figure 5.24

Cr vs. Y tectonic discrimination diagram of Pearce (1982) showing the fields for mid ocean ridge basalts (MORB) and island arc tholeiite (IAT) (the latter field also includes calc-alkaline and alkalic basalts from oceanic arcs). The modeled melting curves of the N-MORB mantle and the residual MORB mantle after 5% (RMM-5%) and 10% (RMM-10%) melt extraction are calculated as outlined in figure 5.4. The fractional crystallization trends for MORB (A), IAT (B) and boninite (C) are taken from Pearce et al. (1984a). The steep vector represents crystallization of olivine + Cr-spinel ± clinopyroxene, and the shallower vector represents crystallization of olivine + Cr-spinel + clinopyroxene + plagioclase. The samples from the pillow unit plot in the field for volcanic arc basalts.

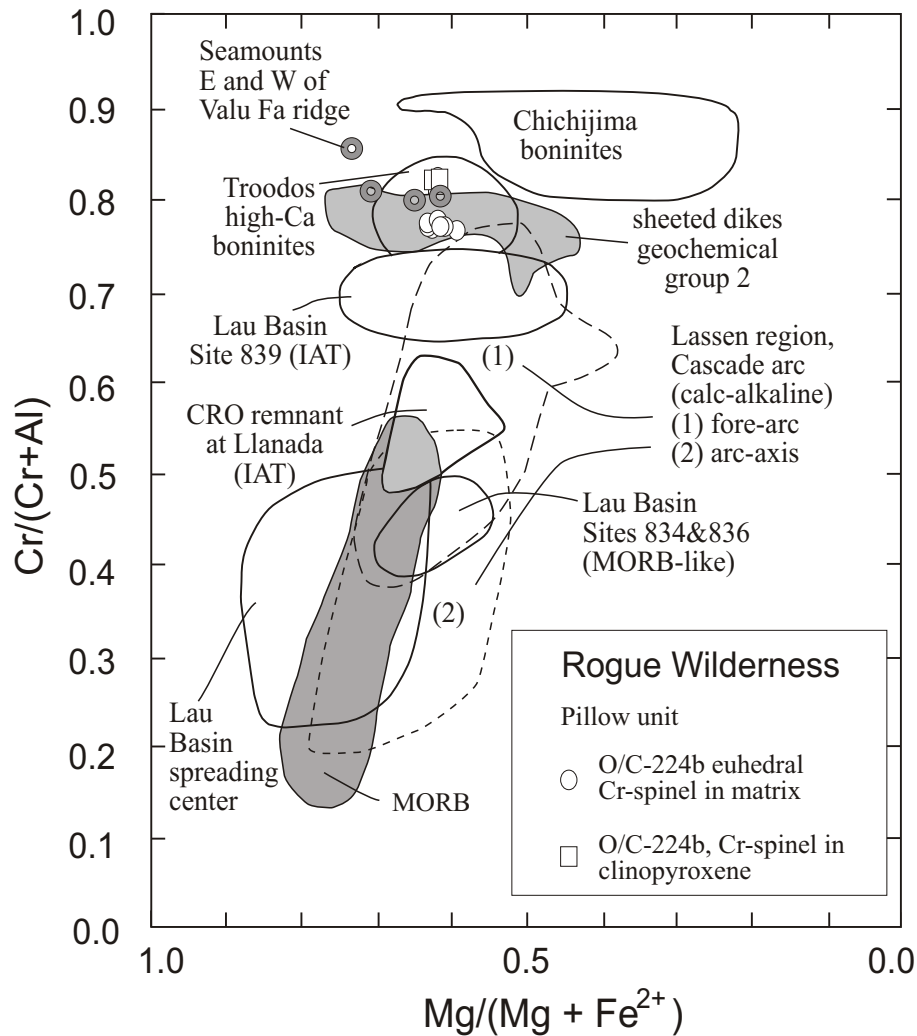


Figure 5.25

Comparison of the composition of Cr-spinel in a sample from the pillow unit (O/C-224b) with chromites from modern island arcs, the Troodos ophiolite, and the Coast Range ophiolite (CRO remnant at Llanada). The fields for Chichijima, Troodos, and the Lau Basin are from Meffre et al. (1996), for MORB from Dick and Bullen (1984), for the Coast Range ophiolite remnant at Llanada from Giaramita et al. (1998), and for the Cascade arc from Clynne and Borg (1997). The field for the dikes of geochemical group 2 from the sheeted dike complex is shown as well.

Figure 5.26

- A. Plot of Th/Yb vs. Nb/Yb for samples from the pillow unit. The solid line indicates the variations of the Th/Yb and Nb/Yb ratios in MORB (from Pearce, 1982; Pearce and Peate, 1995; Pearce et al., 1995a; Pearce and Parkinson, 1993). The crosses on that line give the normalizing values for N-MORB and E-MORB. Also, the mantle depletion and enrichment trends relative to N-MORB are shown. Dynamic melting of a mantle source M with selective tapping of the melting column produces a trend that runs parallel to the MORB array (Pearce et al., 1995a). Alternatively, mixing of magmas derived by partial melting of two different mantle sources can explain the range of trace element compositions observed in samples from the pillow unit. The broken lines indicate the mixing curves between the different magmas.
- B. Mixing of O/C-380 (end member 5) and O/C-227a (end member 6) results in a composition similar to Pb-1.

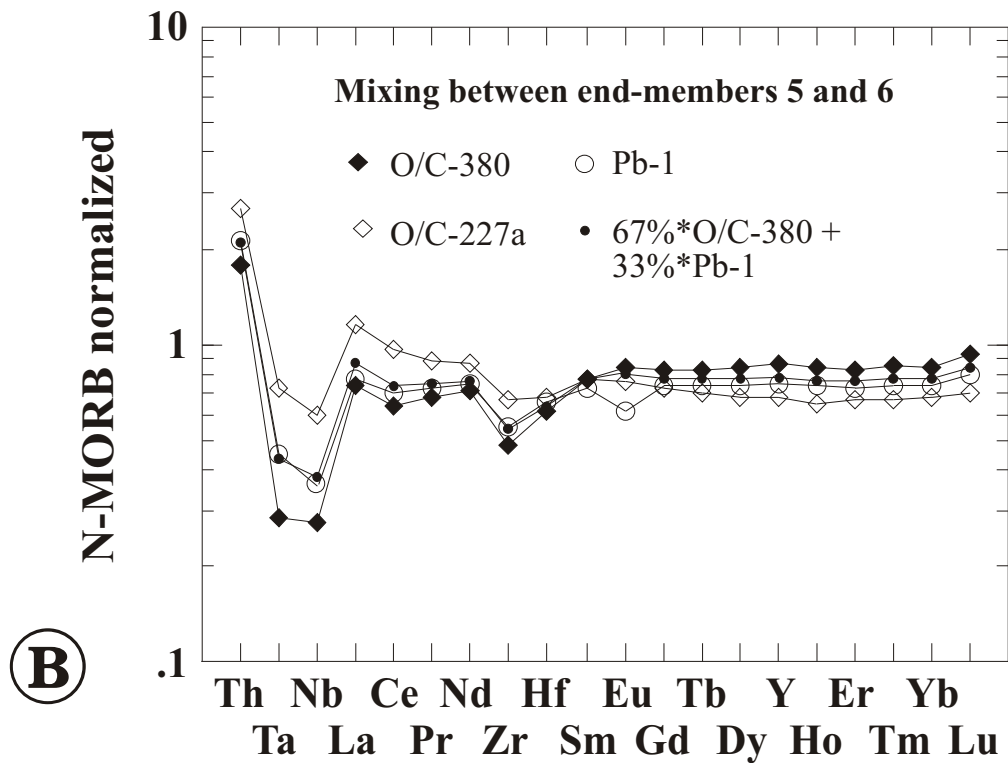
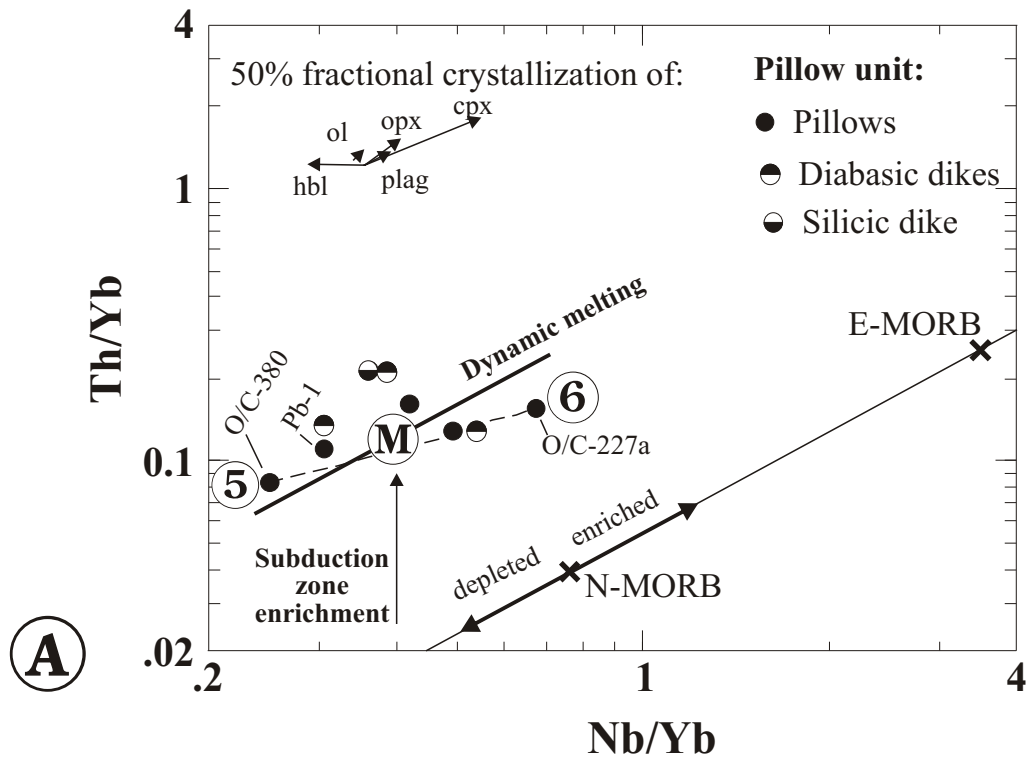
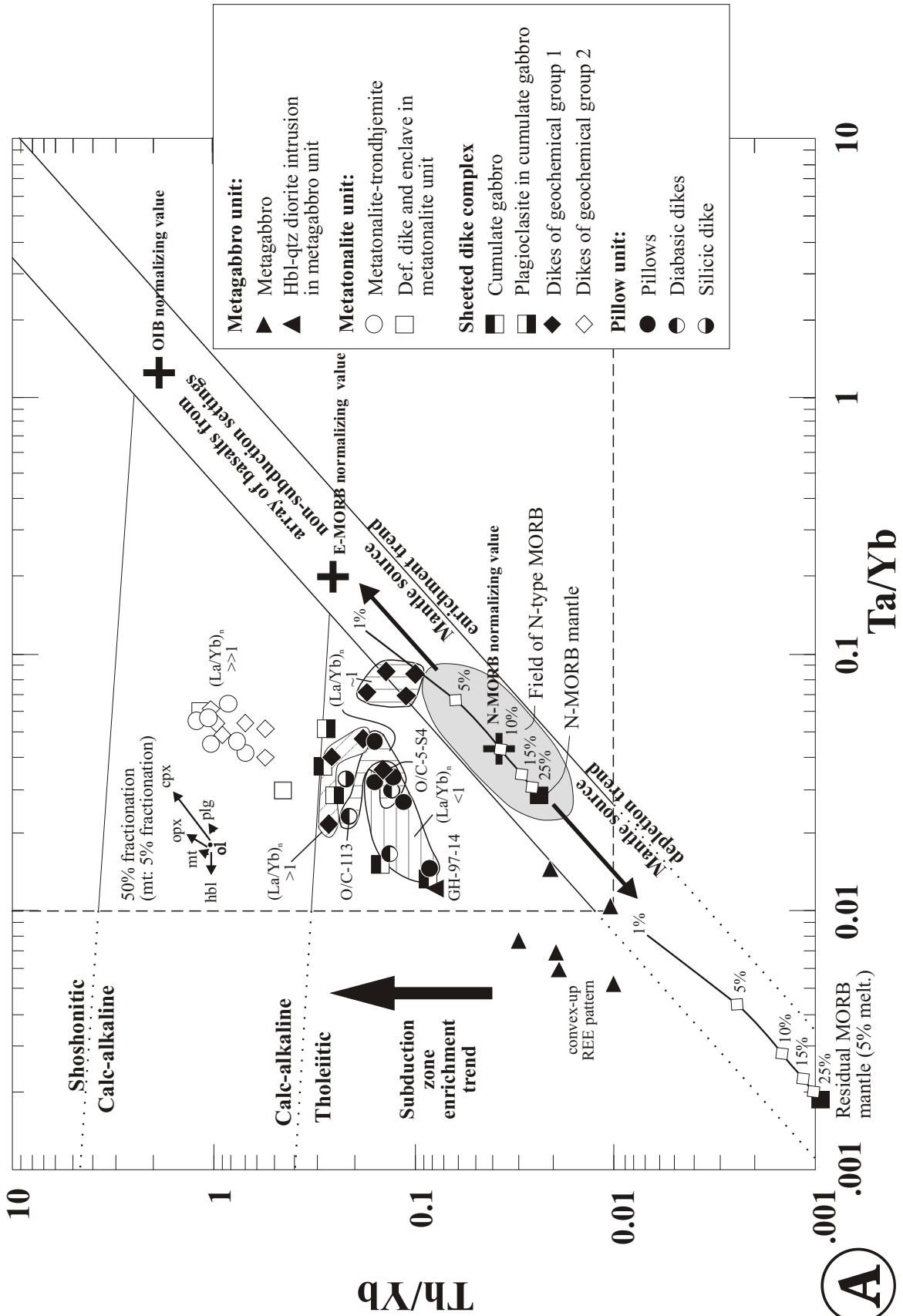
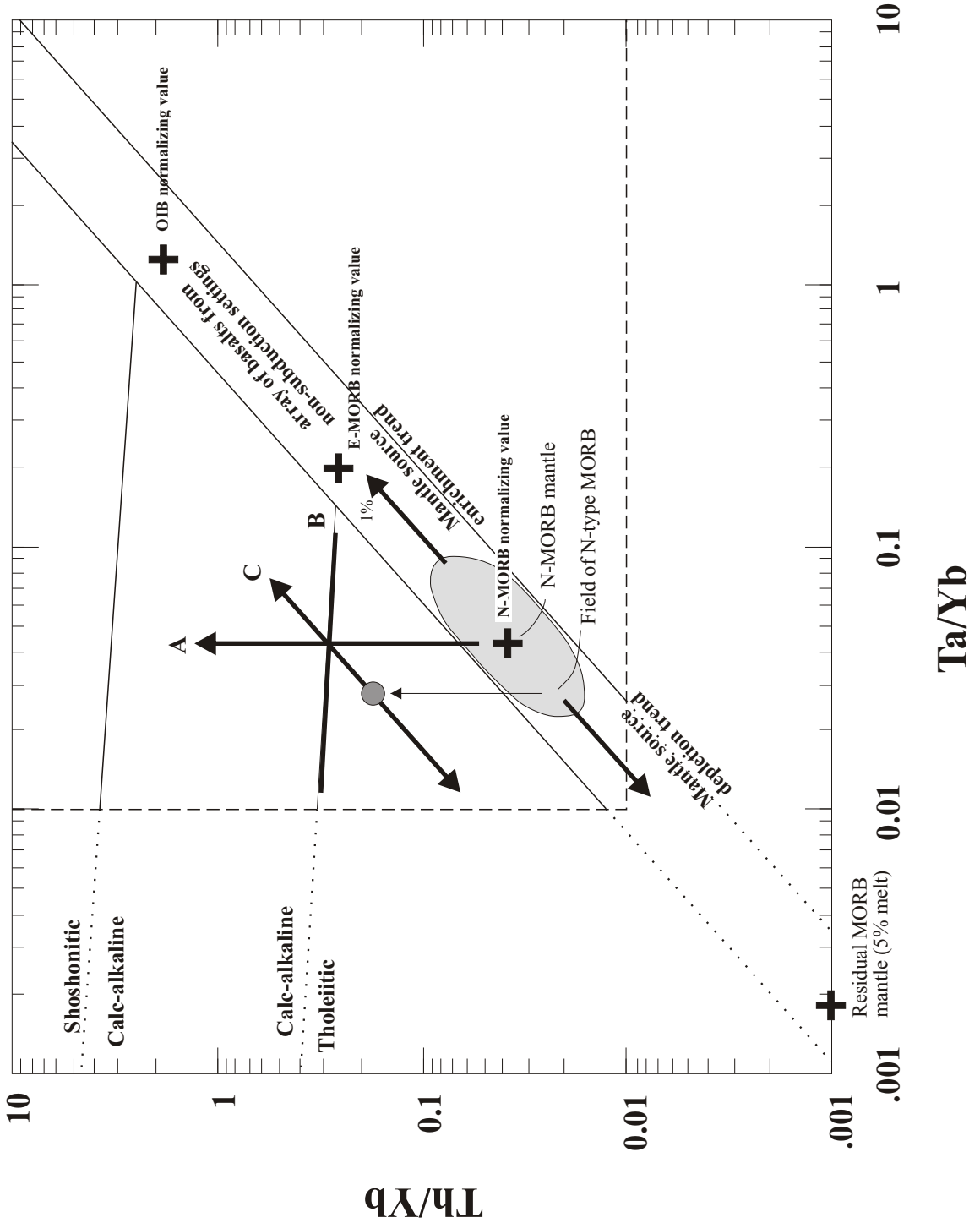


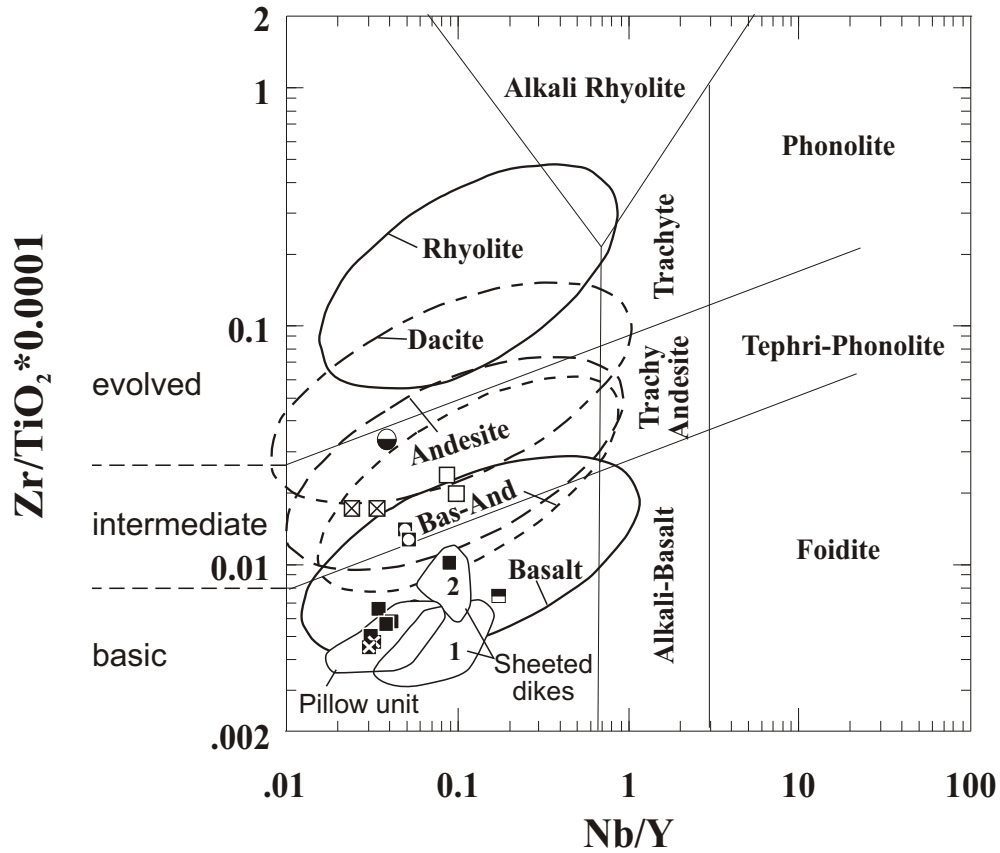
Figure 5.27

- A. Th/Yb vs. Ta/Yb tectonic discrimination diagram of Pearce (1982) showing samples from the Rogue Wilderness ophiolites. The melting curves for N-MORB mantle and residual MORB mantle (after 5% melt extraction) are calculated using the distribution coefficients in Pearce and Parkinson (1993), and the equations for fractional melting modified to take into account non-modal melting (see also figure 5.4). Variations due to partial melting are parallel to the MORB mantle array. N-MORB, E-MORB and OIB normalizing values are given as well as vectors showing mantle source depletion- and enrichment- trends. Elevated Th/Yb ratios compared to the mantle array indicate enrichment with a subduction component. Variations due to fractional crystallization are relatively small as shown by vectors indicating crystal fractionation.
- B. Possible petrogenetic pathways in the Th/Yb vs. Ta/Yb tectonic discrimination diagram. Pathway **A** indicates the trend produced by variable addition of a subduction component to a constant mantle composition. Pathway **B** shows the trend resulting from the addition of a constant subduction component to a variably depleted mantle (addition of Th to a mantle with high Th/Yb ratios does not affect the Th/Yb ratios significantly, but the addition of the same amount of Th to a mantle with very low Th/Yb ratios results in a large increase of the Th/Yb ratios; thus pathway B is not parallel to the array of basalts from non-subduction settings). Pathway **C** shows the trend produced by the addition of a constant subduction component to a constant mantle composition followed by dynamic melting. Dynamic or fractional melting of variable sources A and B results in a complex scatter across the diagram (after Pearce et al, 1995a).





B



- Mule Mountain volcanics:**
- Silicic dike in pillow unit (O/C-231a, plag+cpx+qtz phyric)
 - Basic volcanic rocks (plag+cpx phyric or aphyric)
 - ⊠ Accumulate volcanic rocks (ol+cpx+plag phyric)
 - GDH-2a and GDH-5a (hbl + plag phyric)
 - ⊠ GDH-1 and GDH-2b (plag+cpx+qtz phyric)
 - O/C-147 (aphyric) and O/C-217 (plag+cpx phyric)
 - SC-15

Figure 5.28

Zr/TiO₂ vs. Nb/Y diagram of Winchester and Floyd (1977) with fields revised by Pierce (1996).

Additionally, the 10% probability ellipses for TAS-defined rock types from subalkaline series are shown (after Pierce, 1996). The 10% probability ellipses overlap substantially. The samples from the Mule Mountain volcanics plot in the field for subalkaline basalts and andesites. For comparison, the fields for the dikes of geochemical groups 1 and 2 from the sheeted dike complex and the field for samples from the pillow unit are shown.

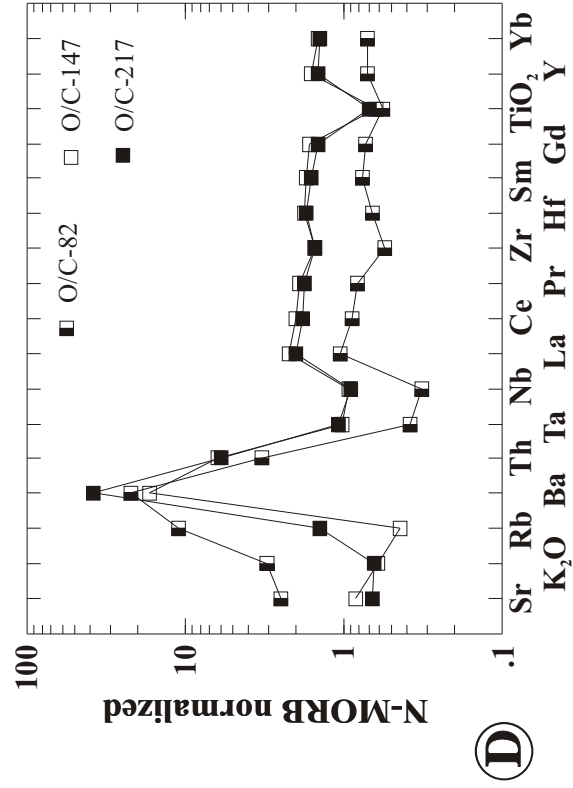
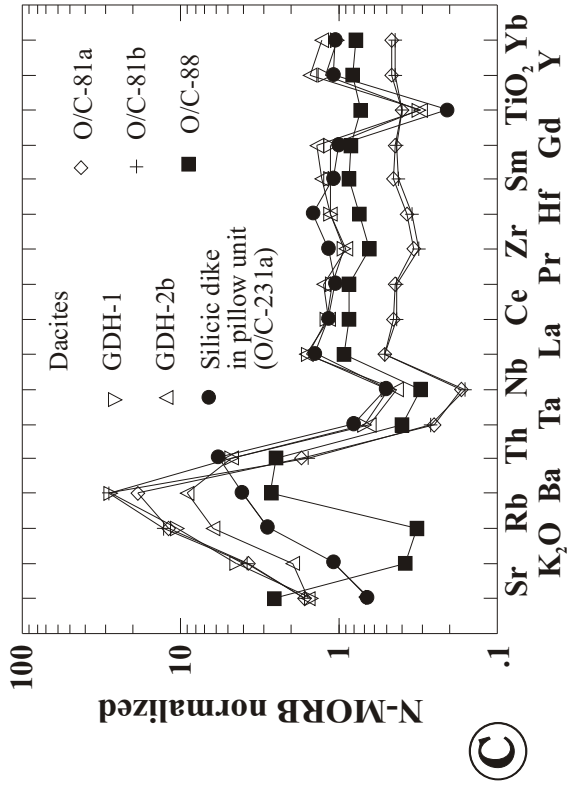
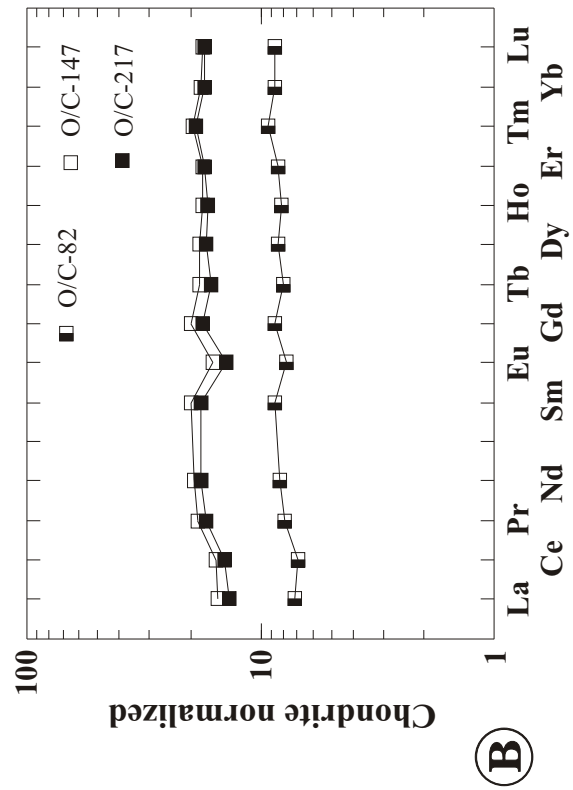
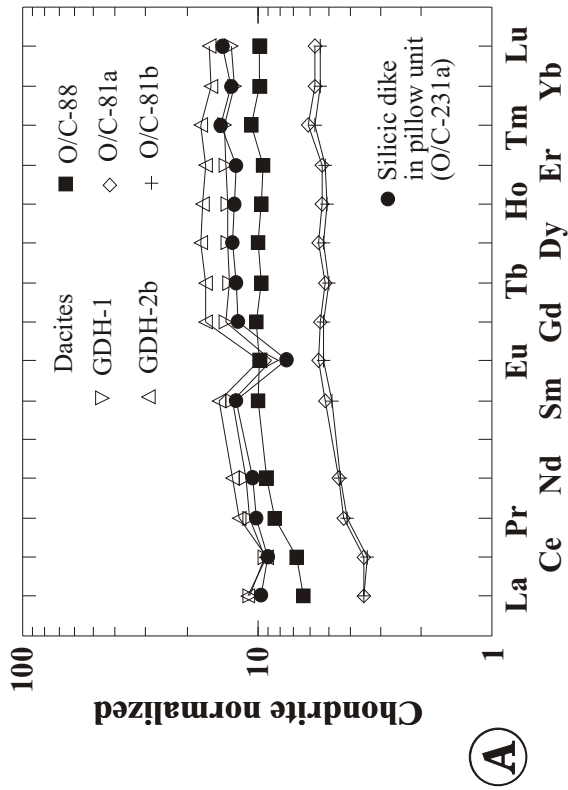
Figure 5.29

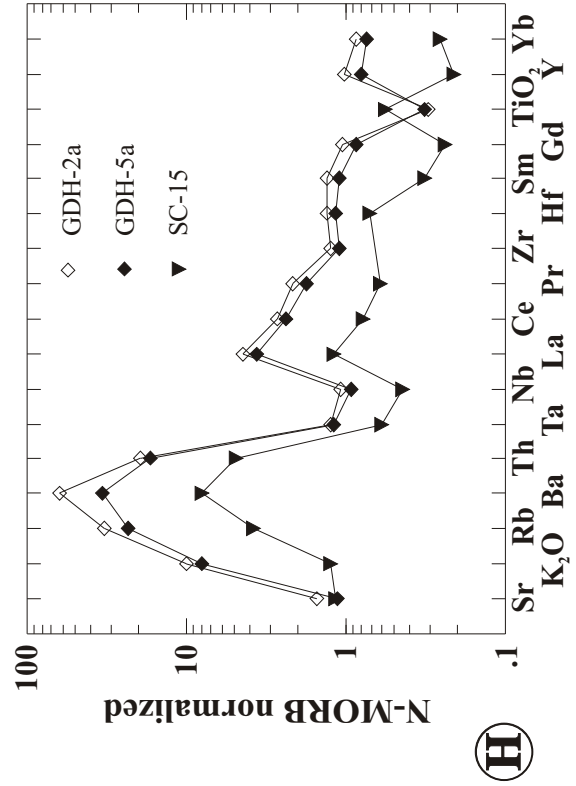
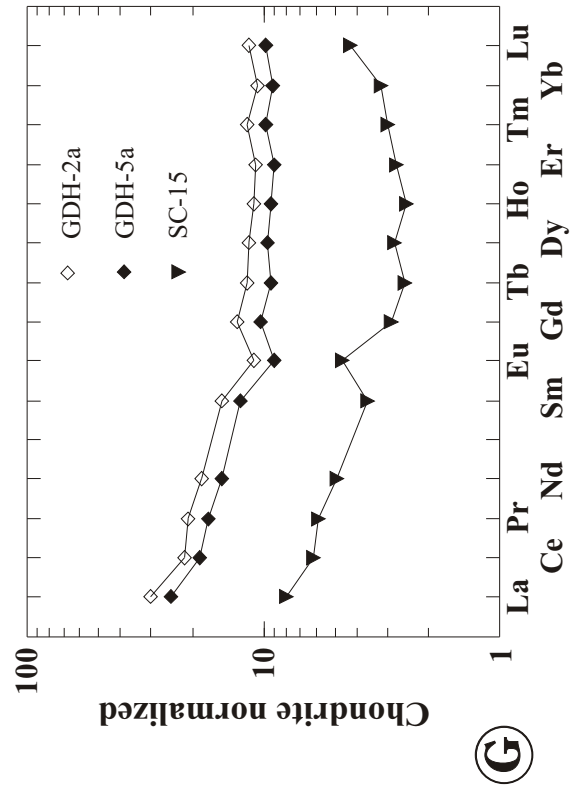
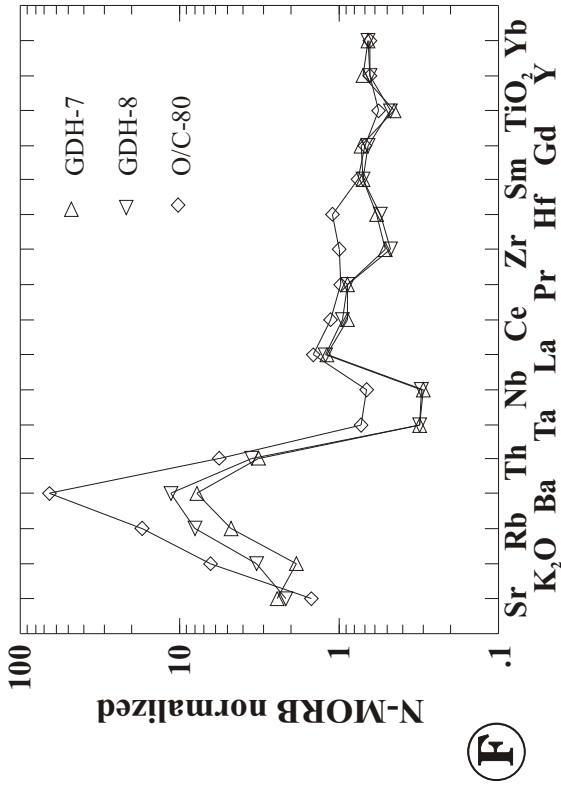
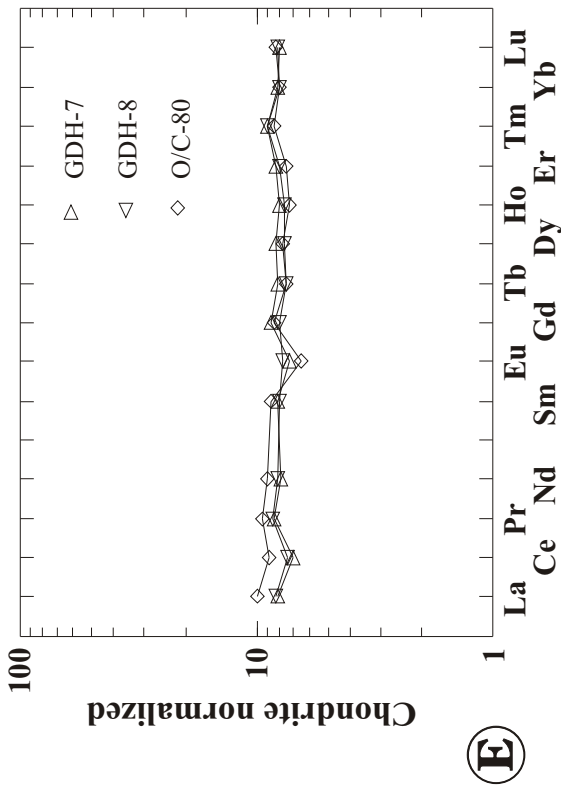
A - F: Chondrite and N-MORB normalized REE and trace element distribution diagrams of samples from the Mule Mountain volcanics having LREE depleted to flat REE patterns. Samples GDH-1, GDH-2b, O/C-81a, O/C-81b and O/C-88 have LREE depleted patterns and $(La/Yb)_n$ ratios between 0.66 and 0.74 (figure 5.29a). The $(La/Yb)_n$ ratios of samples O/C-82, O/C-147, and O/C-217 range from 0.82 to 0.9 (figure 5.29c), and of samples GDH-7, GDH-8, and O/C-80 from 1.05 to 1.33 (figure 5.29e).

The N-MORB normalized patterns of these samples are characterized by relative depletion of HFSE (e.g., negative Ta- and Nb- anomaly) and selective enrichment of LILE and Th, which is typical of IAT (see figure 5.2). In contrast to the other samples in figures 5.29a through 5.29f, O/C-80 has a slightly positive Hf- and Zr-anomaly which is often observed in boninites (see figure 5.2).

G - H: Chondrite and N-MORB normalized REE and trace element distribution diagrams of samples having LREE enriched patterns. Two distinct REE patterns are recognized (figure 5.29g). The REE patterns of GDH-2a and GDH-5a indicate a $(La/Yb)_n$ ratio of ~ 3 and are flat from Gd to Lu. In contrast, the REE pattern of SC-15 is U-shaped similar to boninites (see figure 5.2).

The N-MORB normalized patterns of GDH-2a and 5a are typical of calc-alkaline rocks. LILE, Th and LREE are highly enriched and Ta and Nb as well as Zr and Hf are depleted. Depletion of TiO_2 is most likely related to fractionation of Fe-Ti oxides. The N-MORB normalized pattern of SC-15 is very similar to that of boninites. LILE Th, LREE and Hf (Zr not analyzed) are enriched compared to HREE, MREE and Ta and Nb (see figure 5.2).





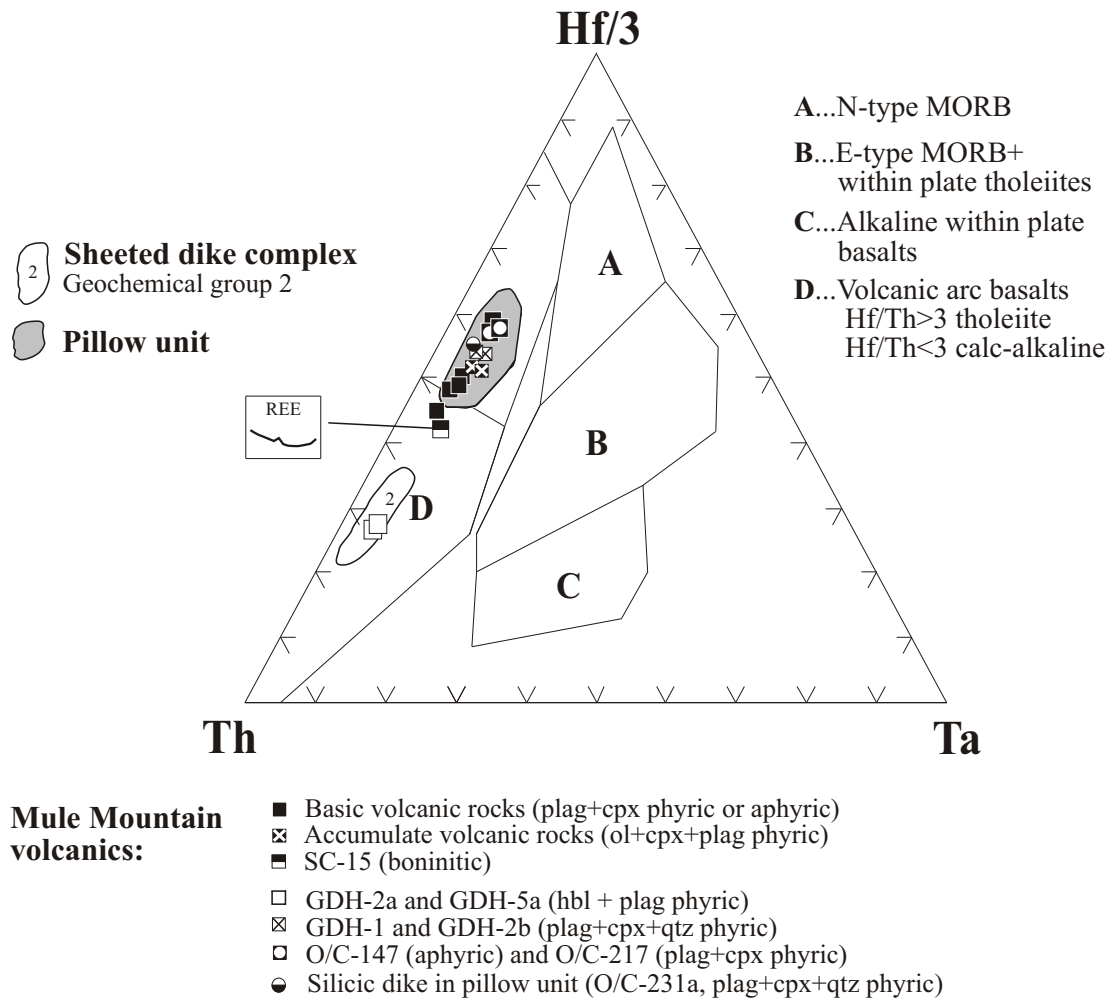


Figure 5.30

Hf/3-Th-Ta tectonic discrimination diagram with fields after Wood et al. (1979). The samples from the Mule Mountain volcanics plot in the field for island-arc tholeiite and calc-alkaline rocks. For comparison the fields for the pillow unit and the dikes of geochemical group 2 (calc-alkaline) from the sheeted dike complex are shown.

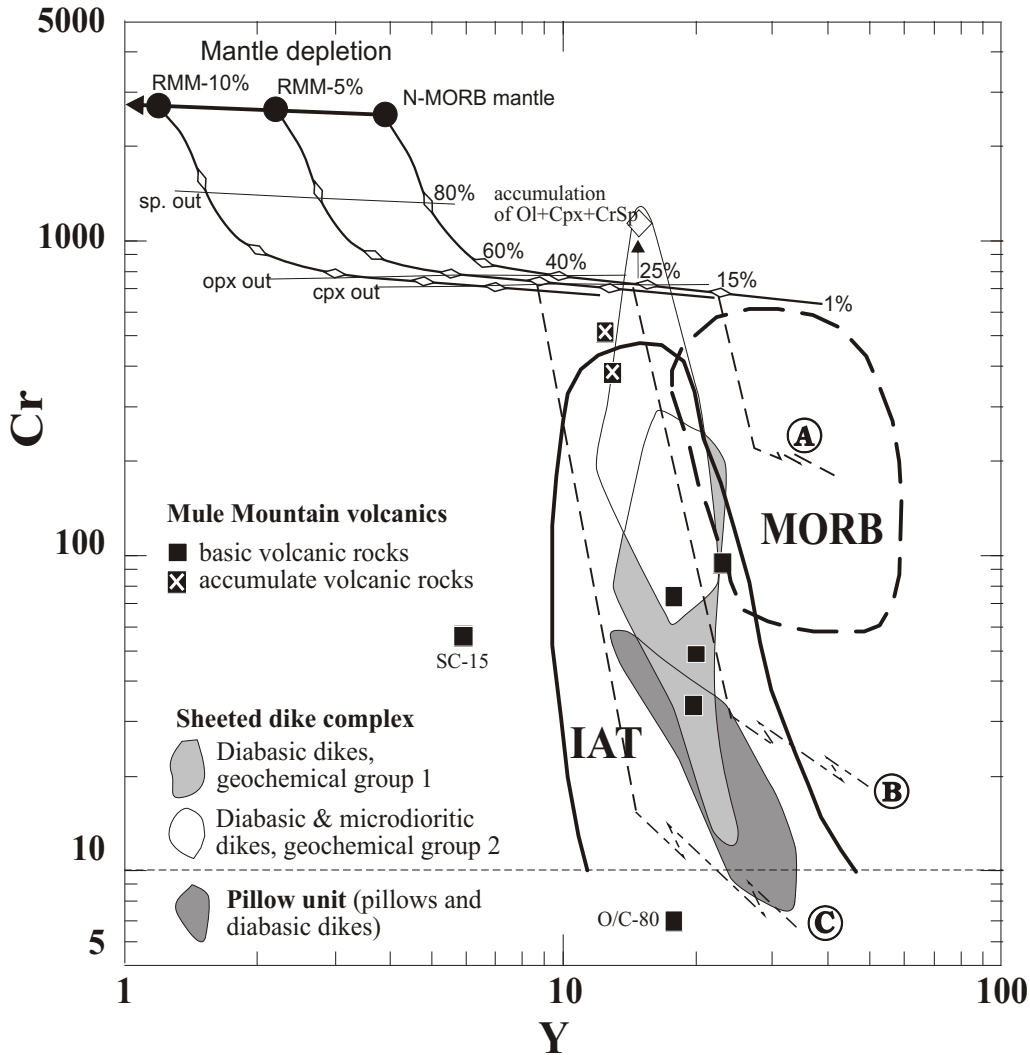
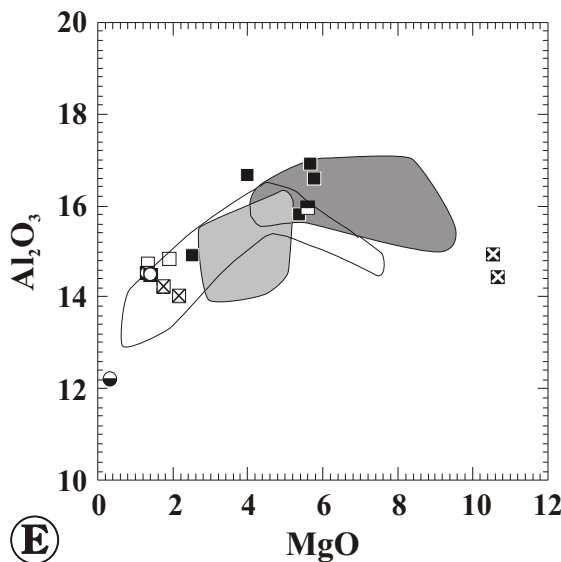
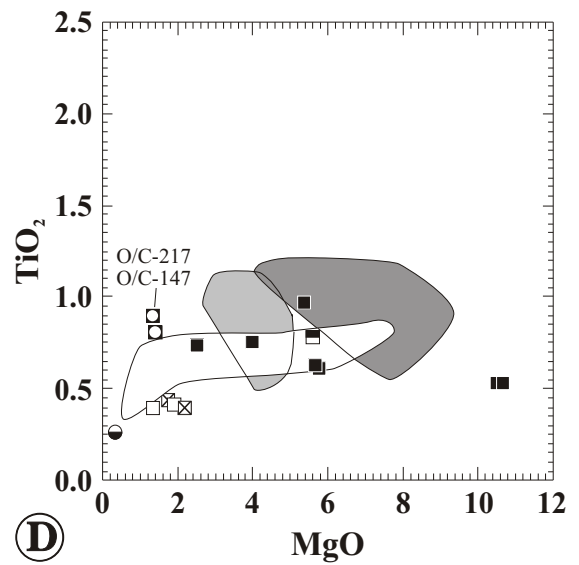
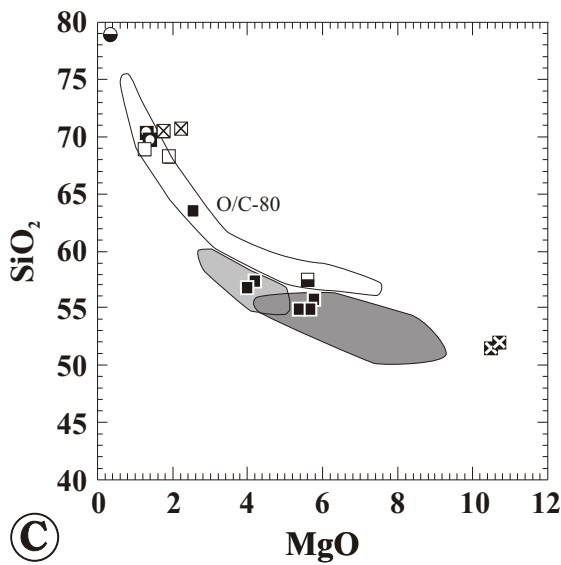
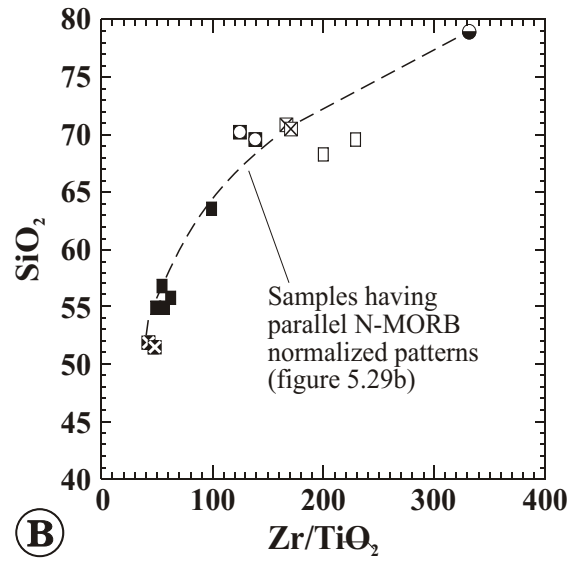
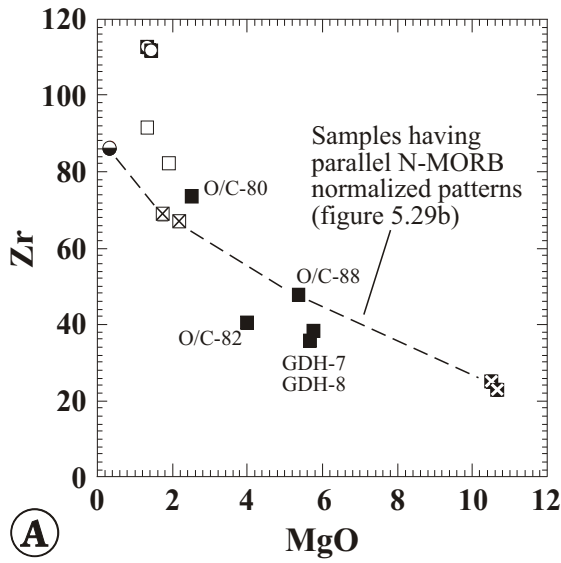


Figure 5.31

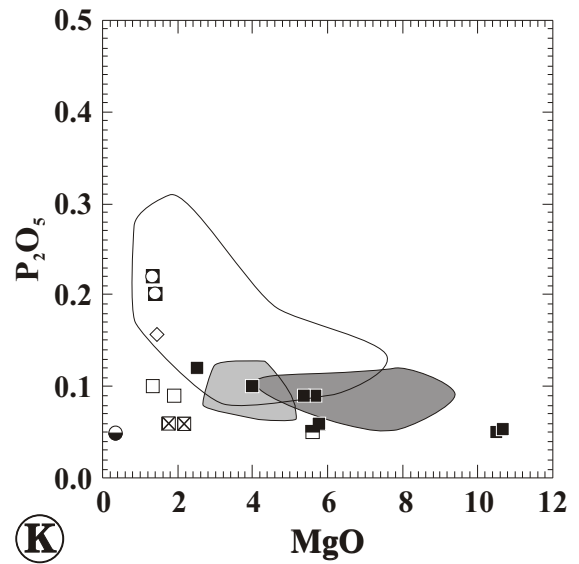
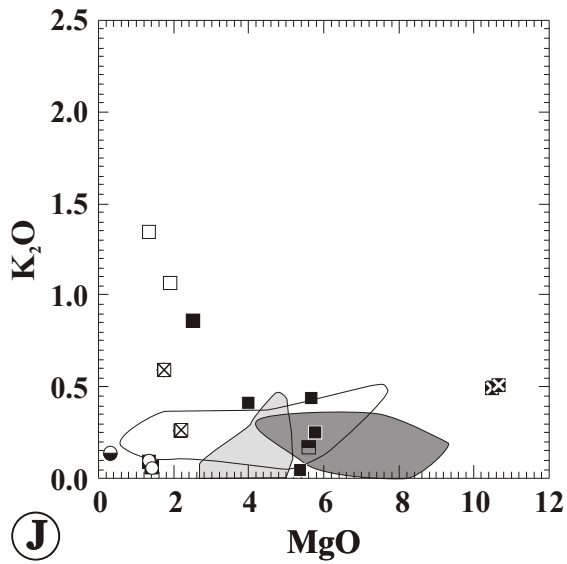
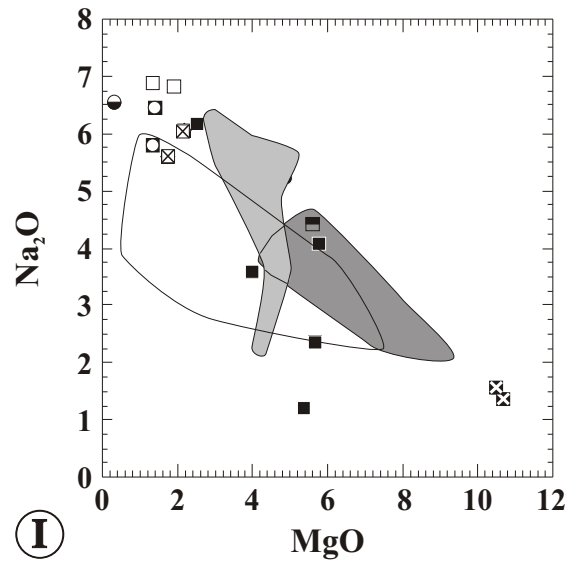
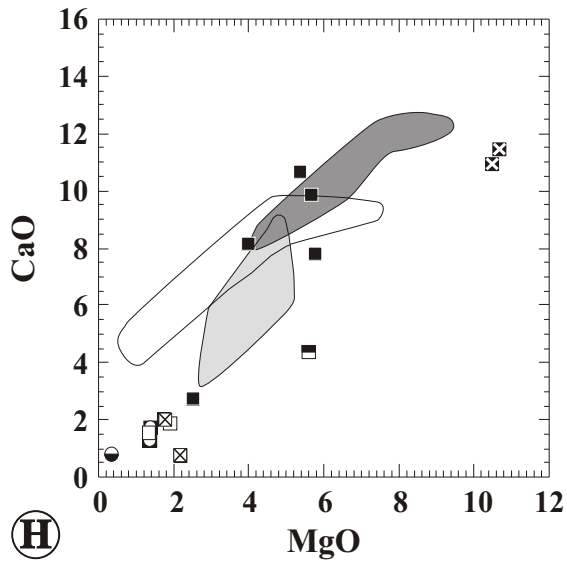
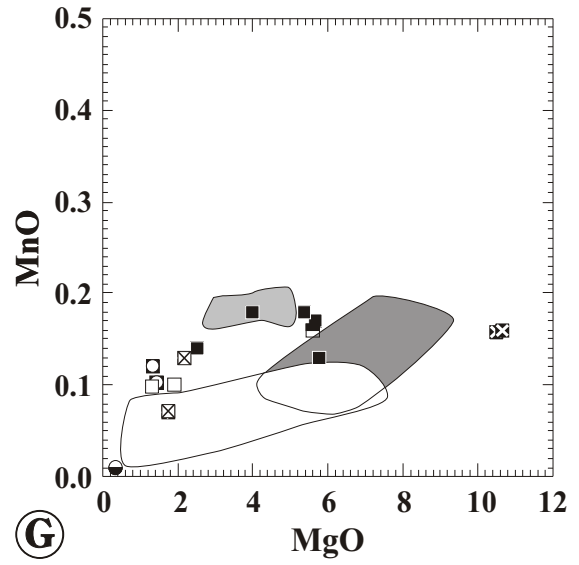
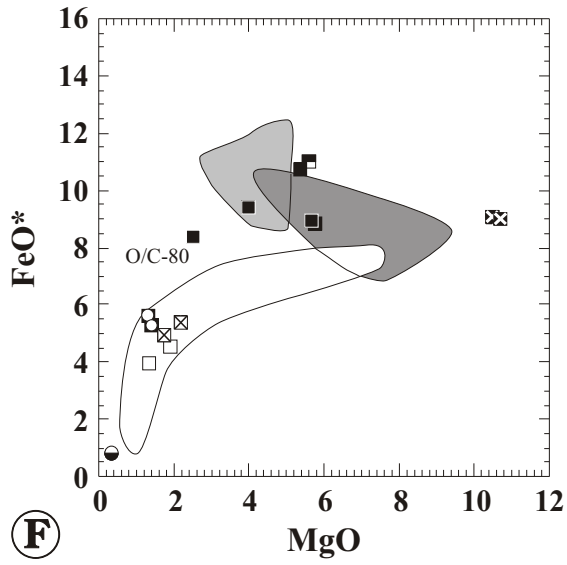
Cr vs. Y tectonic discrimination diagram of Pearce (1982) showing the fields for mid ocean ridge basalts (MORB) and island arc tholeiite (IAT) (the latter field also includes calc-alkaline and alkalic basalts from oceanic arcs). The modeled melting curves of the N-MORB mantle and the residual MORB mantle after 5% (RMM-5%) and 10% (RMM-10%) melt extraction are calculated as outlined in figure 5.4. The fractional crystallization trends for MORB (A), IAT (B) and boninite (C) are taken from Pearce et al. (1984a). The steep vector represents crystallization of olivine + Cr-spinel ± clinopyroxene, and the shallower vector represents crystallization of olivine + Cr-spinel + clinopyroxene + plagioclase. The samples from the Mule Mountain volcanics plot in the field for island arc basalts, except SC-15 and O/C-80. For comparison, the fields for the sheeted dike complex and the pillow unit are plotted.

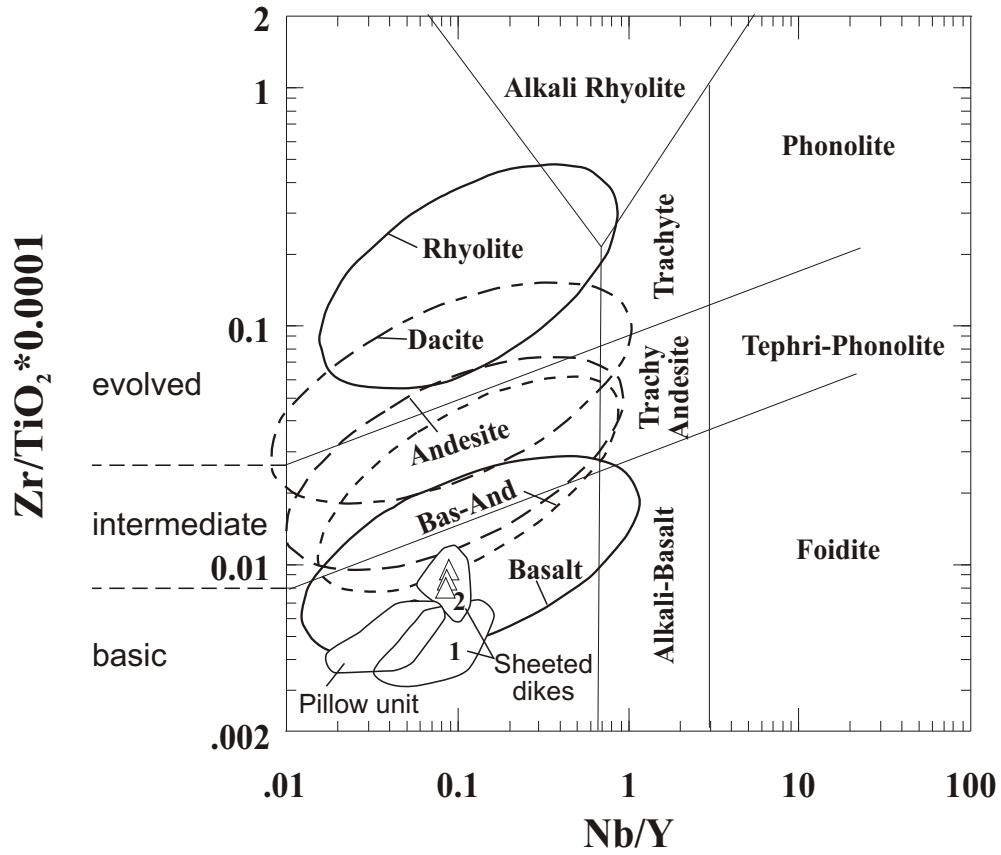
Figure 5.33

- A:** Zr vs. MgO variation diagram of samples from the Mule Mountain volcanics. The samples having parallel MORB normalized patterns lay on a straight suggesting MgO was immobile.
- B:** SiO₂ vs. Zr/TiO₂ diagram of samples from the Mule Mountain volcanics. The strong correlation between Zr/TiO₂, a fractionation index (figure 5.28), and SiO₂ suggests SiO₂ was not mobile.
- C - K:** MgO variation diagrams of samples from the Mule Mountain volcanics. For comparison, the fields for the metatonalite unit + dikes of geochemical group 2, the dikes of geochemical group 1 and the pillow unit are shown. In most MgO variation diagrams, the samples having similar trace element compositions form curvilinear trends (figures 5.33c, d, e, f, g, h, and k). These samples follow a tholeiitic fractionation trend (see text). Silicic samples derived from tholeiitic parental magmas (GDH-1, GDH-2b) cannot be distinguished from silicic samples derived from calc-alkaline parental magmas (GDH-2a, GDH-5a) based on the major elements.



- Basic samples (plag+cpx phyric or aphyric)
- ⊠ Accumulate samples (ol+cpx+plag phyric)
- SC-15 (highly altered boninitic sample)
- GDH-2a and GDH-5a (hbl + plag phyric)
- ⊠ GDH-1 and GDH-2b (plag+cpx+qtz phyric)
- O/C-147 (aphyric) and O/C-217 (plag+cpx phyric)
- Silicic dike in pillow unit, O/C-231a (plag+cpx+qtz phyric)
- Dikes of geochemical group 1, sheeted dike complex
- Dikes of geochemical group 2, sheeted dike complex; samples from the metatonalite unit
- Pillows and diabasic dikes, pillow unit





△ Dikes in the Half Moon Bar diorite

Figure 5.34

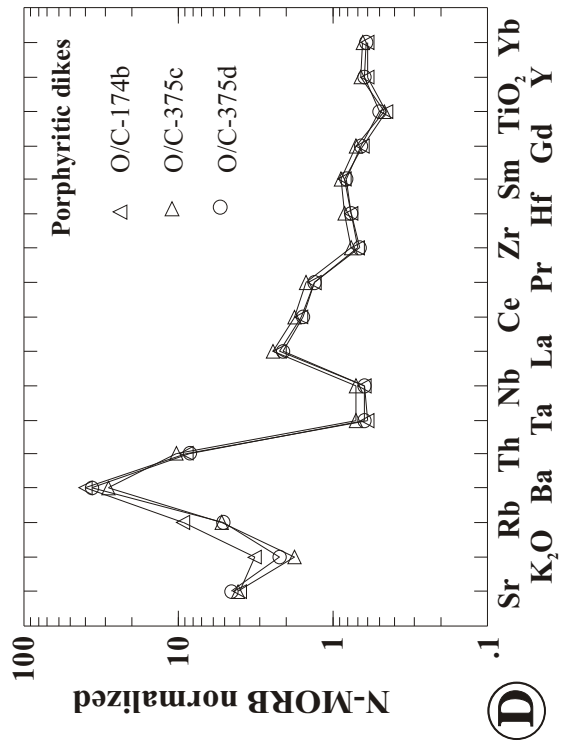
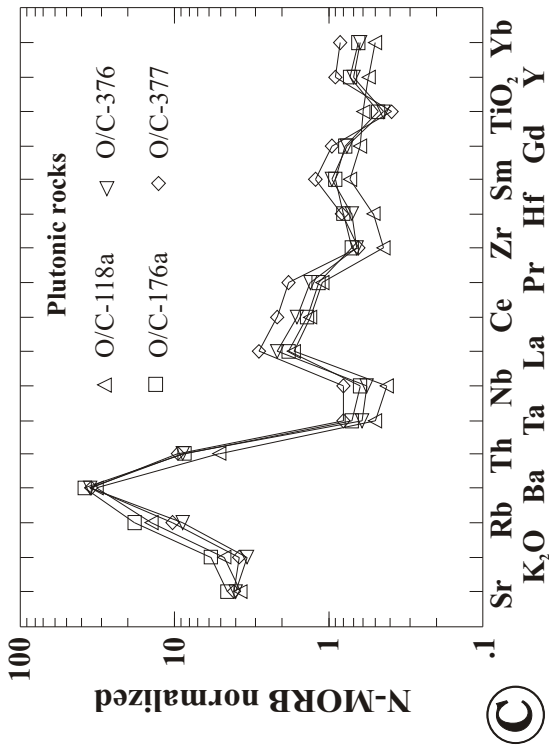
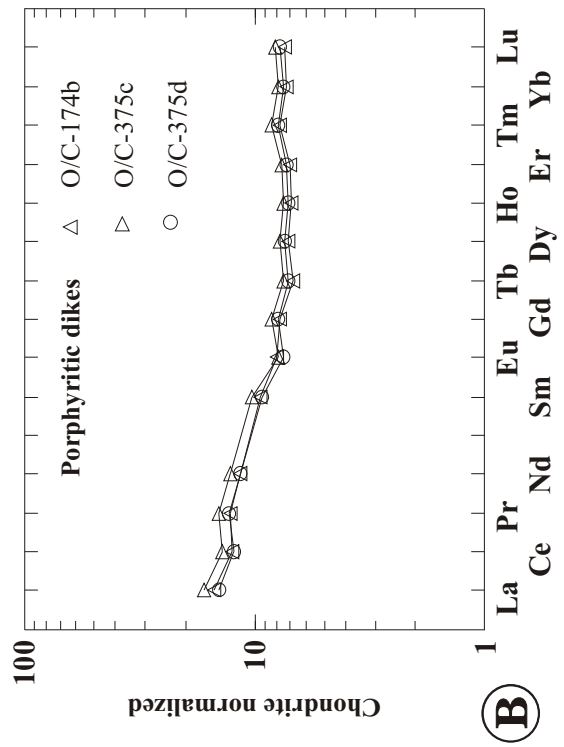
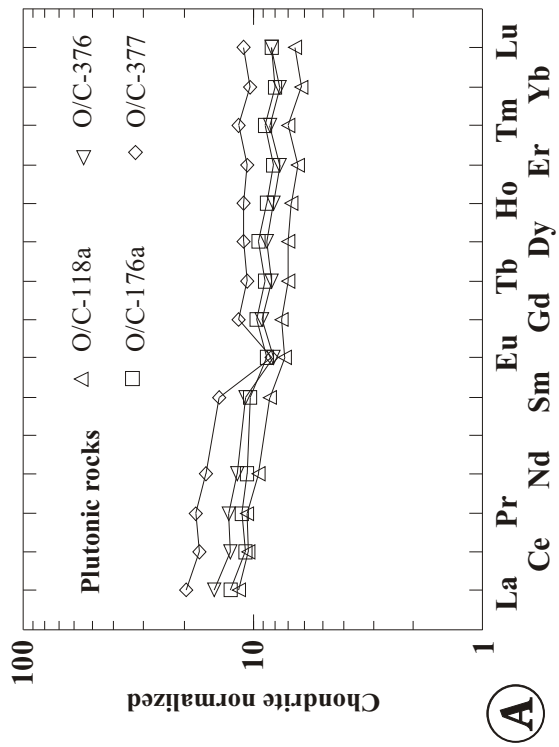
Zr/TiO₂ vs. Nb/Y diagram of Winchester and Floyd (1977) with fields revised by Pierce (1996).

Additionally, the 10% probability ellipses for TAS-defined rock types from subalkaline series are shown (after Pierce, 1996). The 10% probability ellipses overlap substantially. The dikes in the Half Moon Bar diorite have similar Zr/TiO₂ and Nb/Y ratios as dikes of geochemical group 2 from the sheeted dike complex.

Figure 5.35

A - B.: Chondrite normalized REE distribution patterns of samples from the Half Moon Bar diorite and porphyritic dikes intruding diorite. The patterns are LREE enriched, and the range of the chondrite normalized La/Yb ratios is very limited (1.66-2.22). All samples have a negative Ce-anomaly.

C - D: N-MORB normalized trace element distribution diagram of samples from the Half Moon Bar diorite and porphyritic dikes intruding diorite. The HFSE are depleted and LILE, Th and LREE are strongly enriched. The negative TiO₂ anomaly increases with increasing incompatible trace element abundance suggesting fractionation of Fe-Ti oxides. The patterns are parallel suggesting the samples are related by fractionation. The patterns are typical of rocks of calc-alkaline affinity (compare with figure 5.2).



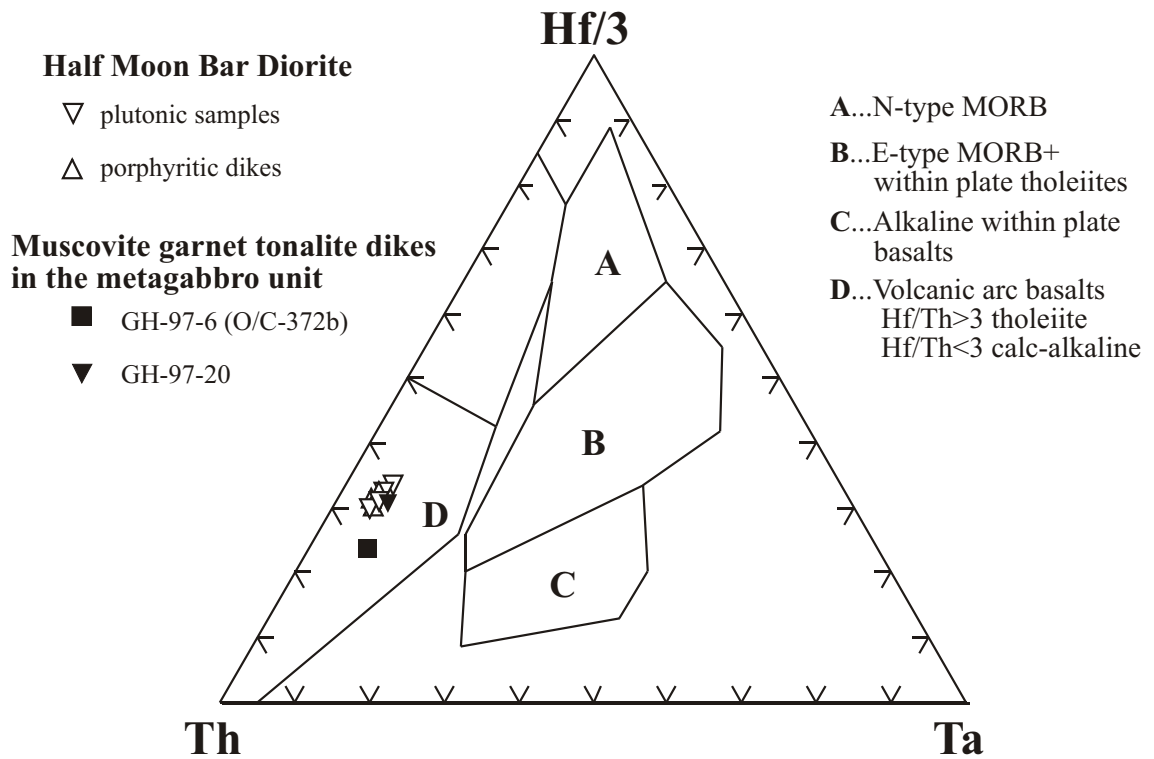


Figure 5.36

Hf/3-Th-Ta tectonic discrimination diagram with fields after Wood et al. (1979). The samples from the Half Moon Bar diorite plot in the field for calc-alkaline rocks.

Figure 5.37

- A. Chondrite normalized REE distribution patterns of two muscovite garnet tonalite dikes in the metagabbro unit. The REE patterns are flat in the HREE and increase steeply from Sm to La which is characteristic of garnet fractionation or garnet as residual phase in the source. The patterns differ in level and shape which can be explained with fractionation (GH-97-6) or accumulation (GH-97-20) of garnet.
- B. N-MORB normalized trace element distribution diagram of two muscovite garnet tonalite dikes in the metagabbro unit. The patterns resemble that of rocks of calc-alkaline affinity. However, there are important differences such as strong depletion of Ti, Y, and Yb.

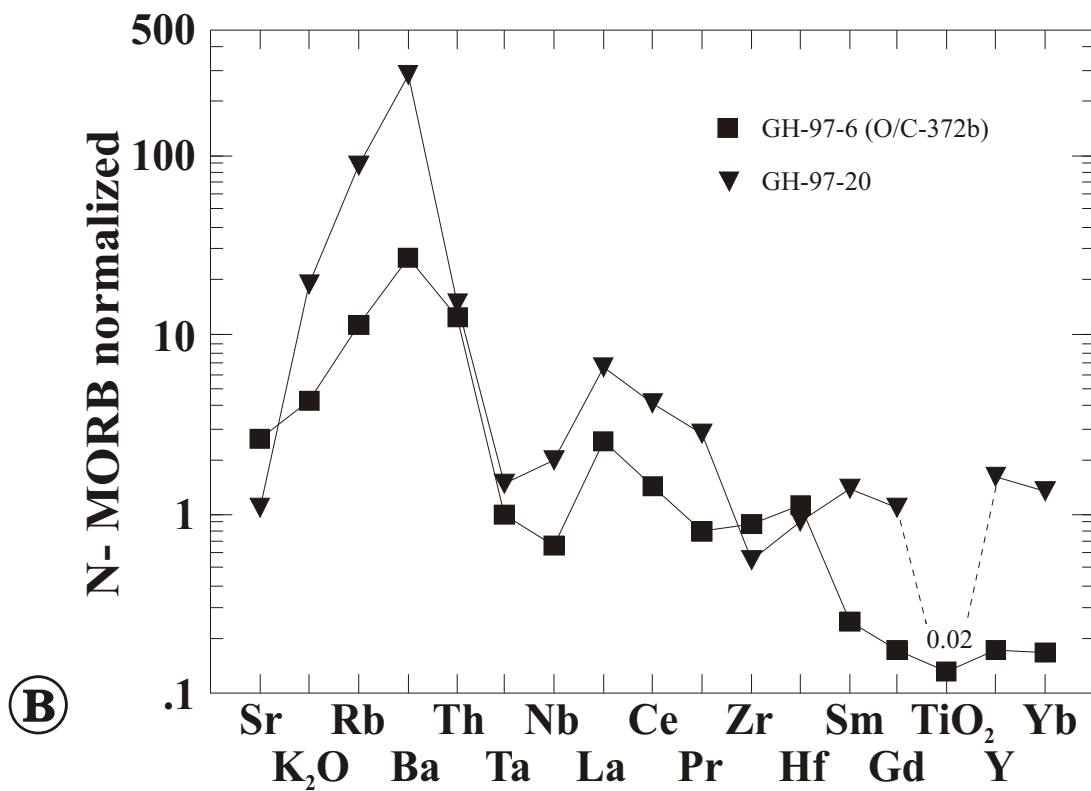
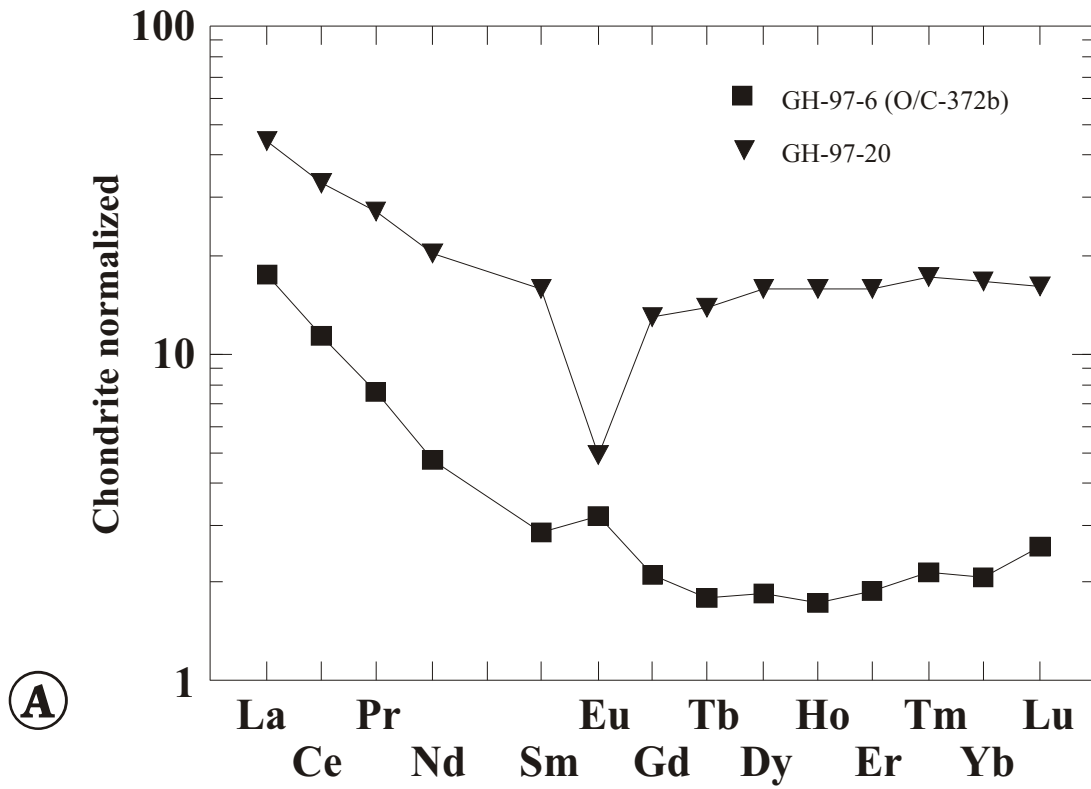


Figure 5.38

- A. Zr/Y vs. Zr tectonic discrimination diagram of Pearce and Norry (1979) to distinguish island arc basalts, MORB and within plate basalts. Note large overlap field between MORB and IAT.
- B. Zr/Y vs. Zr tectonic discrimination diagram of Pearce (1983). Once it is established that the basalts erupted in an arc setting, the Zr/Y ratio can be used to distinguish oceanic and continental arc settings. The dikes of geochemical group 2 from the sheeted dike complex plot in the continental arc field while the IAT dikes, all samples from the pillow unit and most samples from the upper volcanic unit plot in the island arc field.

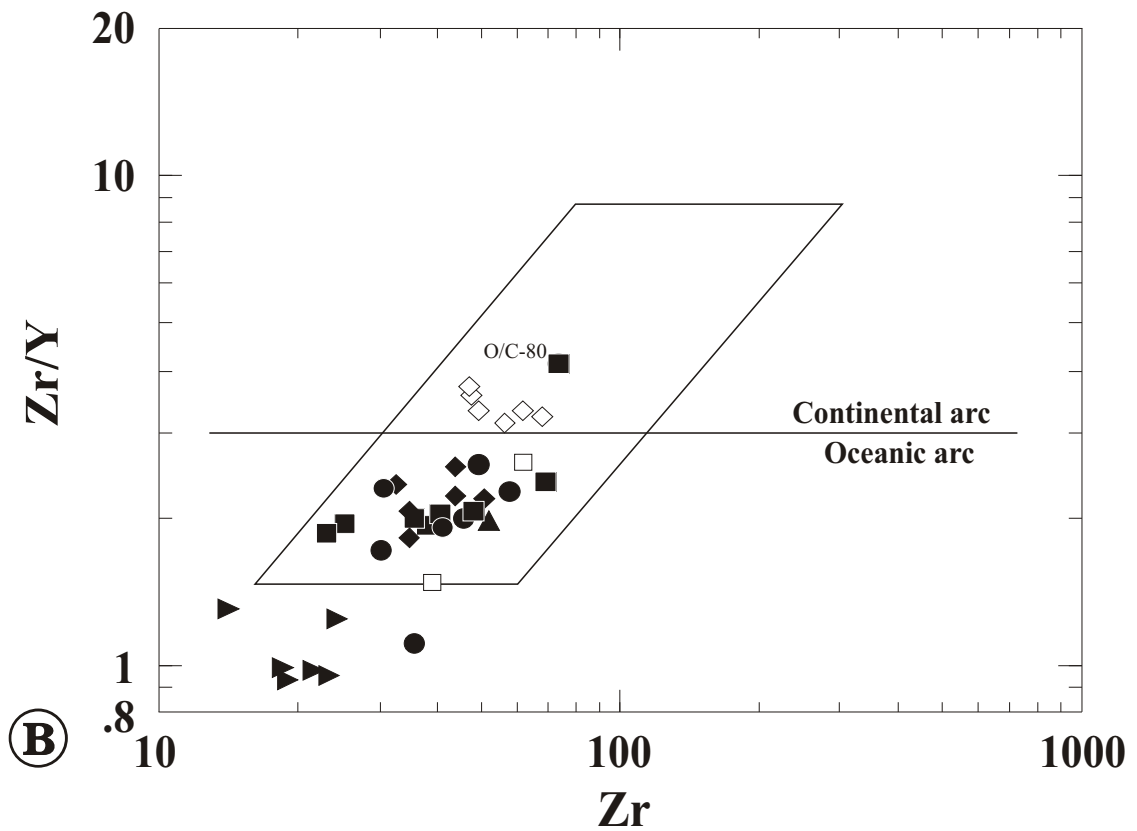
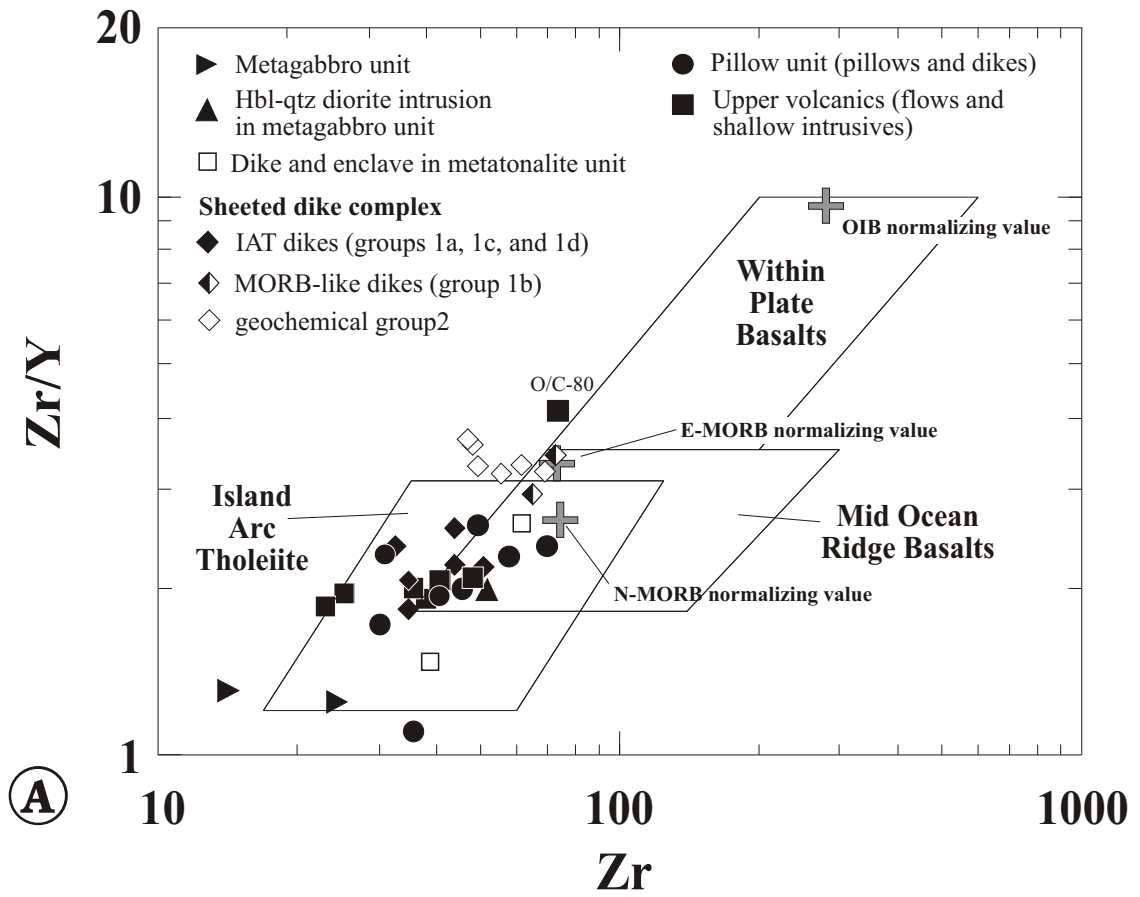


Figure 6.1

Generalized map showing major accretionary terranes but also mid- to late Jurassic ophiolitic and related rocks of California and SW Oregon. Map modified from Harper et al. (1985). Two belts of mid- to late Jurassic ophiolites include the Coast Range ophiolite (western belt), and the Josephine - Smartville ophiolites (eastern belt). Numbers refer to the localities listed below.

1. Wild Rogue Wilderness: 164 Ma (Saleeby, 1984)
2. Snow Camp Mountain: 169 Ma (Saleeby et al., 1984).
3. Josephine ophiolite: 162 Ma (Harper et al., 1994)
4. Preston Peak 'ophiolite' (Saleeby and Harper, 1993)
5. Devils Elbow remnant of the JO: 164 Ma (Wyld and Wright, 1988)
6. Smartville ophiolite: 160-164 Ma (Edelman et al, 1989; Saleeby et al, 1989).
7. Northern Coast Range ophiolite remnants (e.g., Elder Creek, Paskenta, Stonyford)
8. Black Mountain
9. Del Puerto: 155-157 Ma (Hopson et al., 1981; Evarts et al., 1992)
10. Llanada: 164 Ma (Hopson et al., 1981)

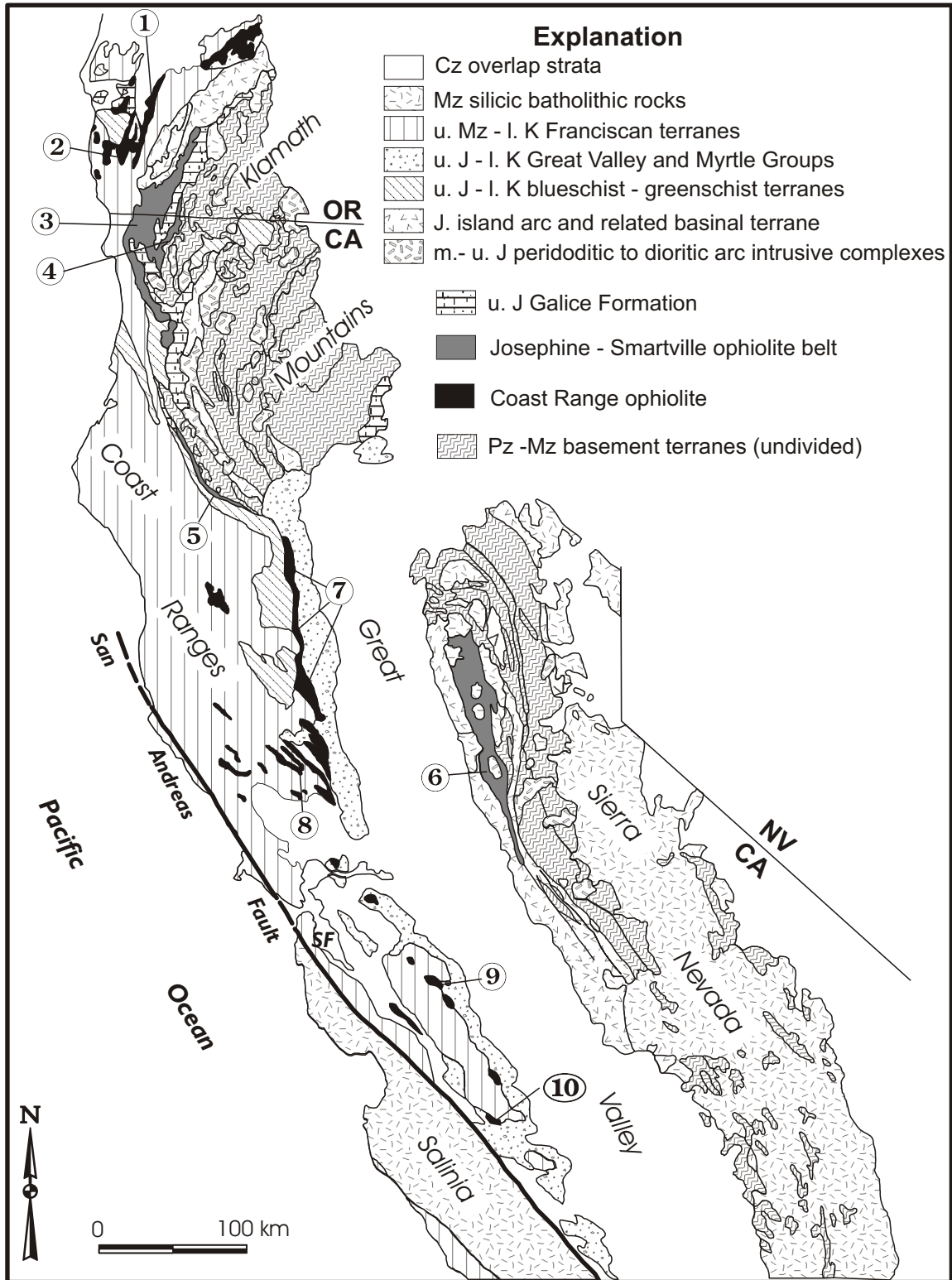


Figure 6.2

Tectonostratigraphic diagram comparing Coast Range ophiolite (CRO) - basal Great Valley Group (volcanopelagic sequence) succession with the Josephine ophiolite -Galice succession. The age range for the northern Coast Range ophiolite remnants is based on the compilation of isotopic ages in Robertson (1990) as well as on ages of interlava radiolarian cherts (Oxfordian-Kimmeridgian). Dated northern CRO remnants include Harbin Springs (164 ± 2 Ma zircon U/Pb, and 169 ± 2 Ma titanite U/Pb), Elder Creek (155 ± 5 Ma and 163 ± 5 Ma hornblende K/Ar), Paskenta (166 ± 3 Ma and 162 ± 3 Ma hornblende K/Ar). Minimum and maximum possible ages of the Coast Range ophiolite remnant at Cuesta Ridge, Point Sal and Llanada are based on U/Pb and Pb/Pb isotopic ages, respectively (Hopson et al. in Dickinson et al., 1996). The age for the CRO remnant at Del Puerto are from Evarts et al. (1992). Terrigenous sedimentation on Coast Range ophiolite - volcanopelagic sequence began with basal strata of the Great Valley Group in the latest Jurassic. Ages for the Josephine ophiolite are from Harper et al. (1994) and Harper et al. 1996), for the Rogue Chetco island arc complex from Yule (1996). The zircon U/Pb age for a gabbro in the Snow Camp Mountain area is from Saleeby et al. (1984) and radiolarian ages from E. Pessagno (samples collected by G.D. Harper, unpublished field mapping, 1997). The age data for the Rogue Wilderness are summarized in chapter 2 (Saleeby; 1984; Saleeby personal communication, 1999; Heizler, personal communication 1998).

Figure 6.3

Comparison of geochemical data from the Wild Rogue Wilderness ophiolite with that from the Coast Range ophiolite remnants at Llanada, Black Mountain, Point Sal and Snow Camp Mountain in the Cr-Y discrimination diagram of Pearce (1982).

Figure 6.4

Comparison of geochemical data from the Wild Rogue Wilderness ophiolite with that from the Coast Range ophiolite remnants at Llanada, Black Mountain, Point Sal, Stonyford and Snow Camp Mountain in the Hf/3-Th-Ta discrimination diagram of Wood (1979).

Figure 6.5

Comparison of geochemical data from the Wild Rogue Wilderness ophiolite with that from the Coast Range ophiolite remnants at Llanada, Black Mountain, Point Sal and Snow Camp Mountain in the Th/Yb and Ta/Yb discrimination diagram of Pearce (1982).

Figures 6.3 through 6.5 (references for compilation of analytical data)

- Llanada: Lagabrielle et al. (1986), Shervais (1990), Giaramita et al. (1998), and ICP-MS data obtained at Union College (appendix F).
- Black Mountain: Blake and Jones (1981), Lagabrielle et al. (1986), Giaramita et al. (1998), and ICP-MS data obtained at Union College (appendix F).
- Point Sal: Menzies et al. (1977a, 1977b) and Shervais (1990).
- Stonyford: the analytical data are from Shervais (unpublished data)
- Snow Camp Mountain: ICP-MS data obtained at Union College (appendix F)

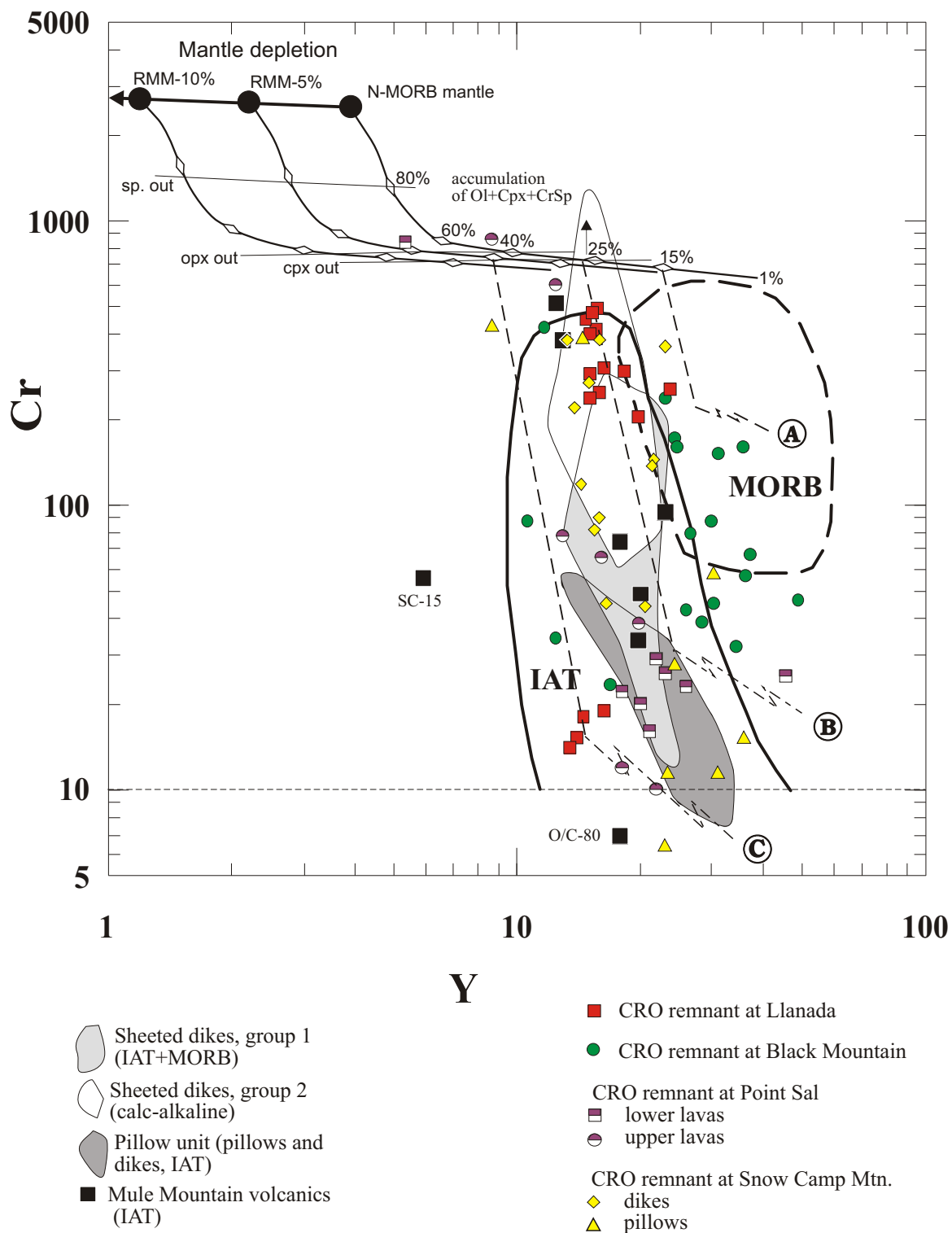


Figure 6.3: Comparison in the Cr vs. Y diagram of Pearce (1982). The fractionation paths for N-MORB (A), IAT (B) and Boninites (C) are shown (after Pearce et al.; 1984a). See figure 5.4 (chapter 5) for calculation of melting curves for N-MORB mantle and Residual MORB mantle (RMM).

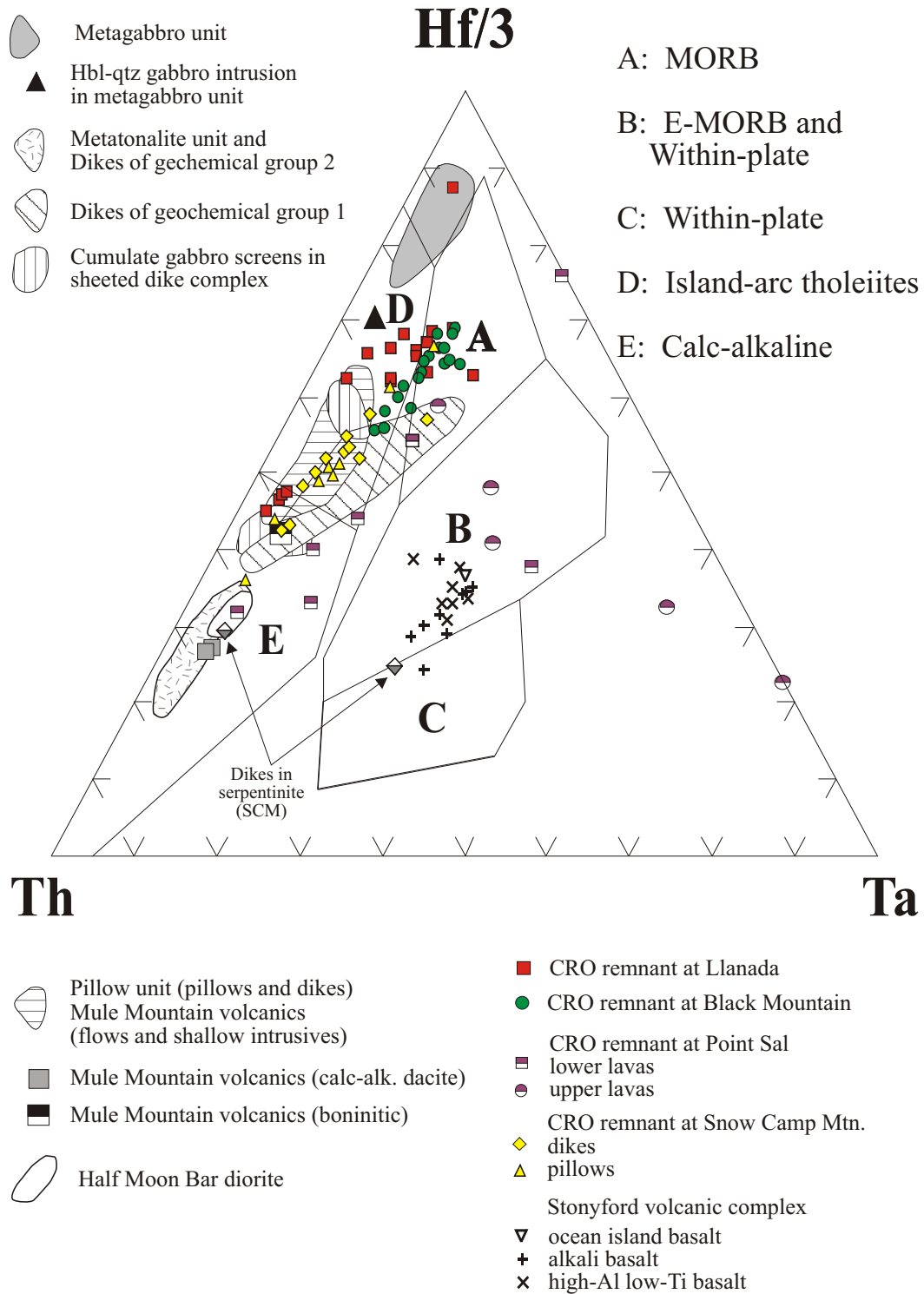


Figure 6.4: Comparison in the Hf/3-Th-Ta diagram of Wood (1979).

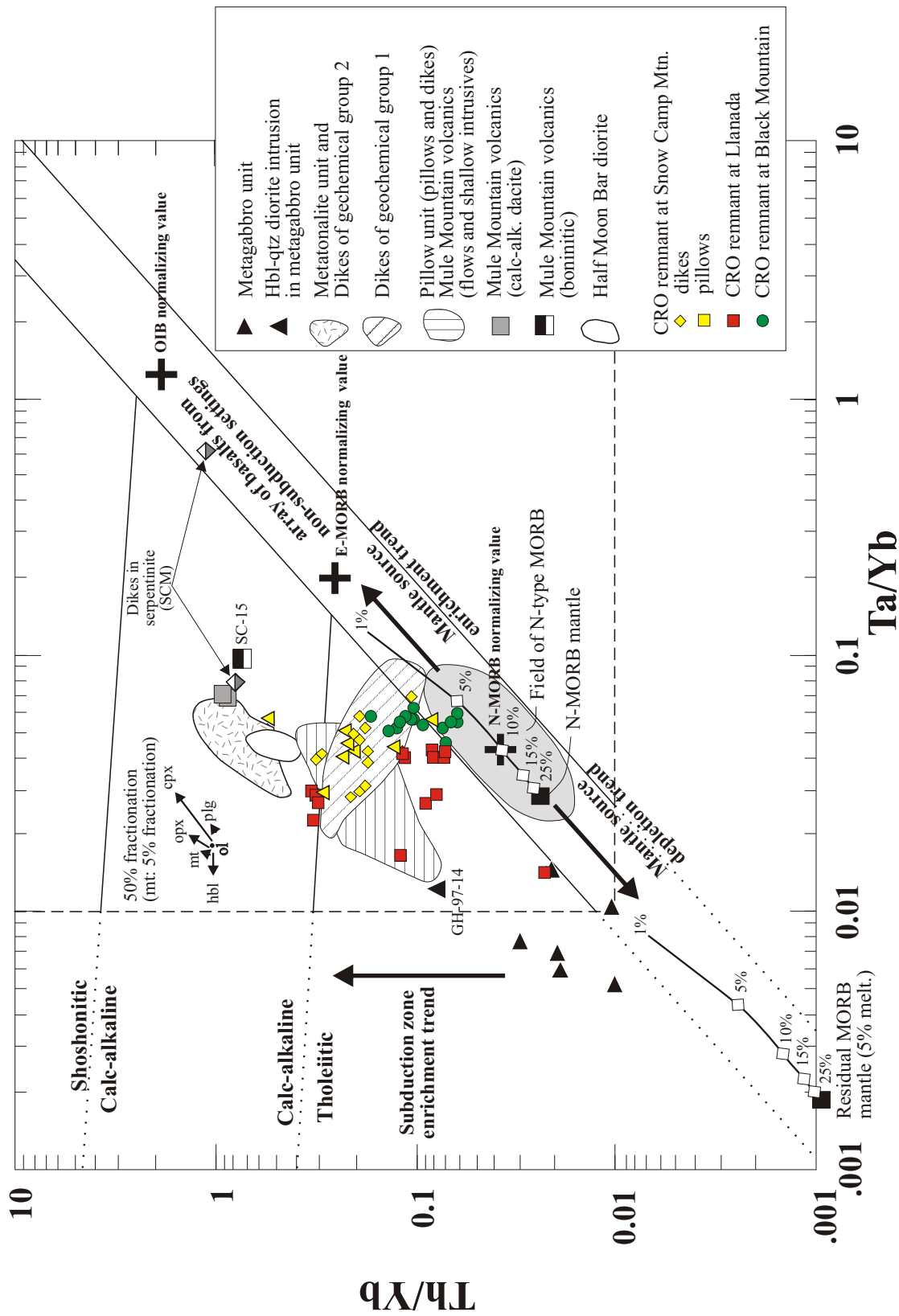


Figure 6.5: Comparison in the Th/Yb vs. Ta/Yb diagram of Pearce (1982). See chapter 5 for calculation of melting curves.

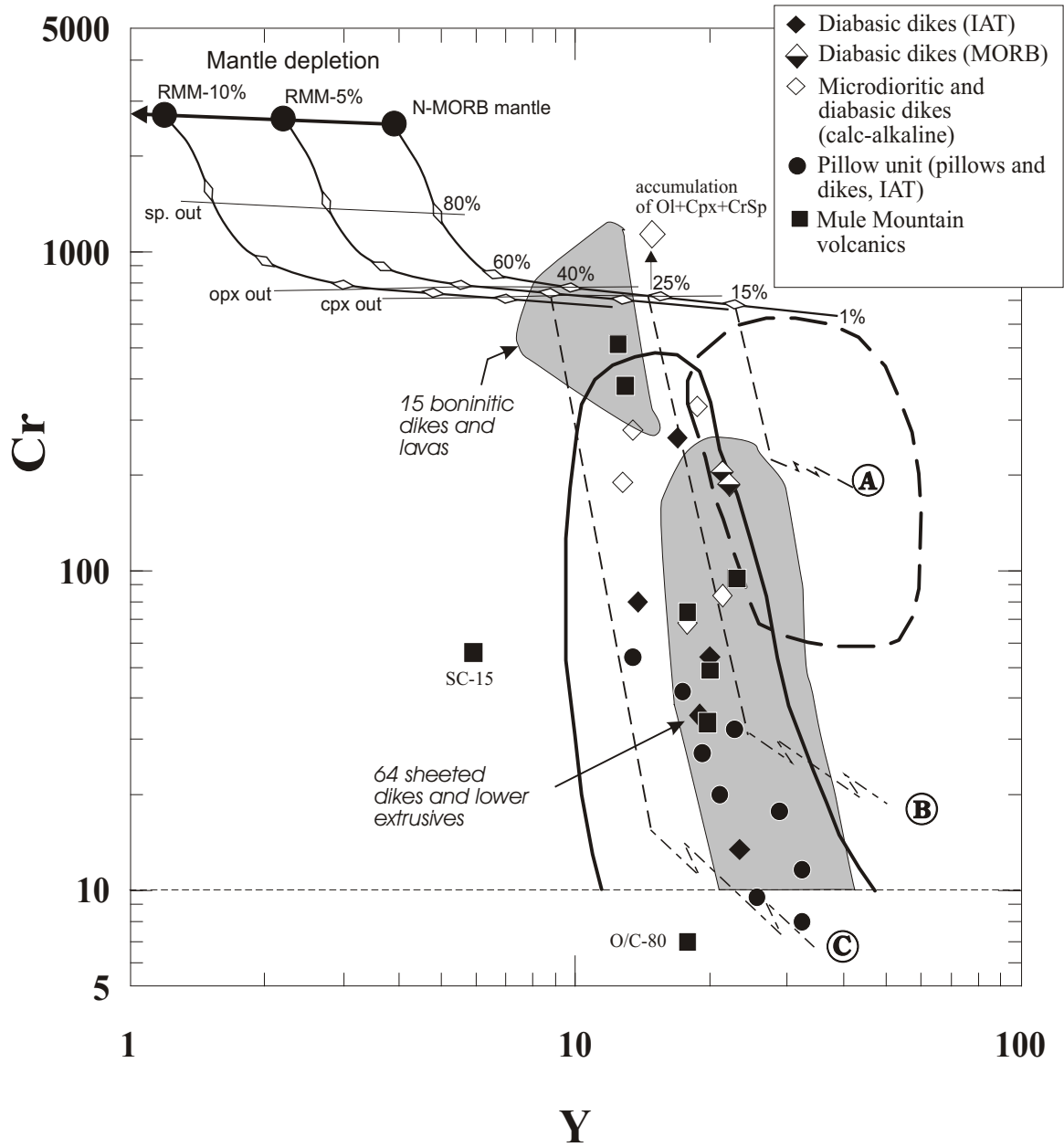
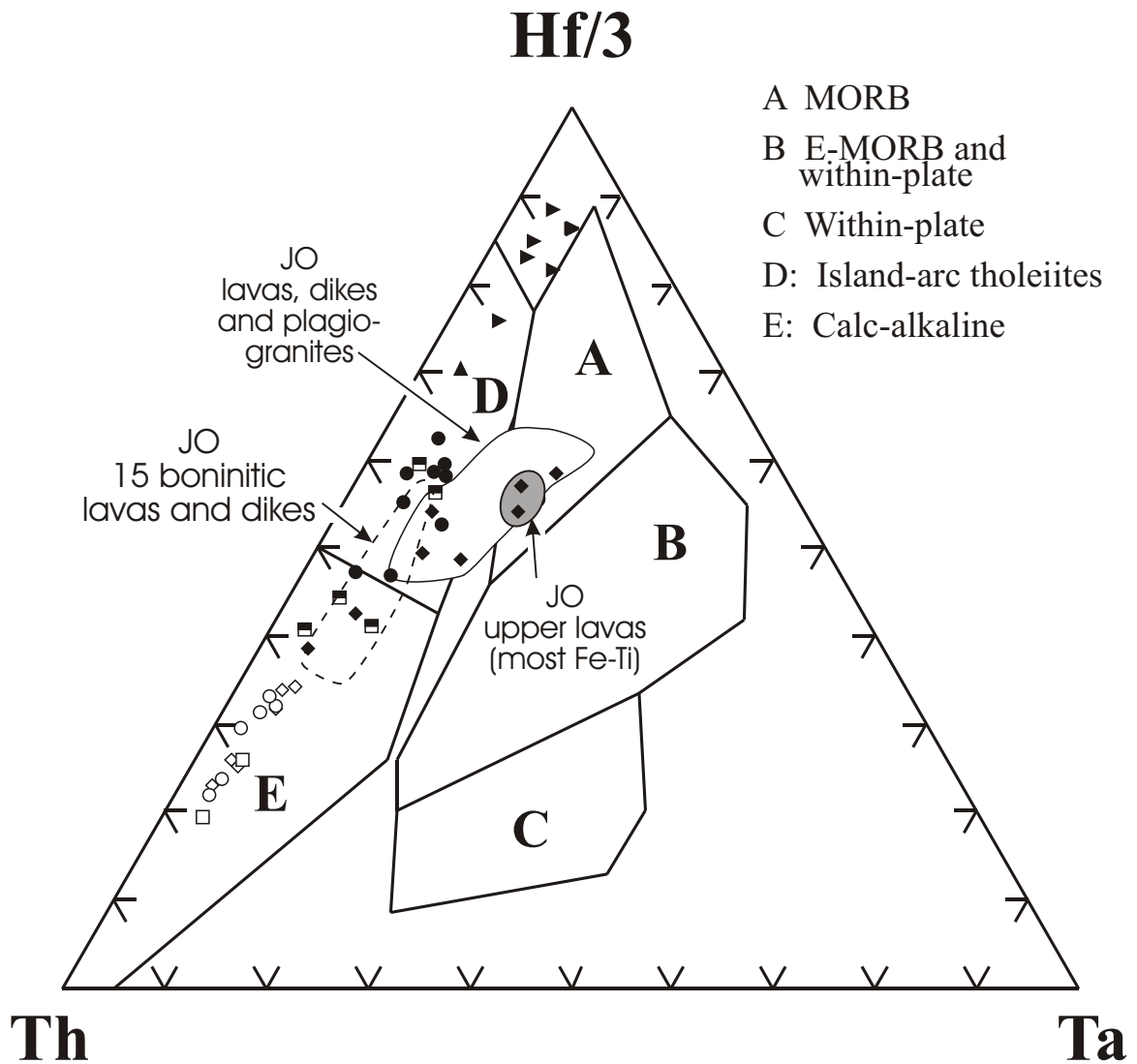


Figure 6.6

Comparison between the Josephine ophiolite and Wild Rogue Wilderness ophiolite in the Cr vs. Y tectonic discrimination diagram of Pearce (1982) showing fields for mid-ocean ridge basalts (MORB) and island arc tholeiite (IAT) (the latter field also includes calc-alkaline and alkalic basalts from oceanic arcs). The fields for the Josephine ophiolite are taken from Harper (in review). The fractionation paths for MORB (A), IAT (B) and boninite (C) are shown (after Pearce et al., 1984). See figure 5.4 (chapter 5) for calculation of the melting curves for MORB-mantle and residual MORB-mantle.



Wild Rogue Wilderness ophiolite

Plutonic units

- ▶ Metagabbro
- ▲ Hbl-qtz diorite in metagabbro
- Metatonalite-trondhjemite
- Def. dike and enclave in metatonalite

Sheeted dike complex

- ◆ Dikes of group 1
- ◇ Dikes of group 2
- Cumulate gabbro screens

Pillow unit

- Pillows and dikes

Figure 6.7

Comparison between the Josephine ophiolite and Wild Rogue Wilderness ophiolite in the Hf/3-Th-Ta tectonic discrimination diagram of Wood (1979). The fields for the Josephine ophiolite are taken from Harper (in review).

Figure 6.8

Hf/3-Th-Ta tectonic discrimination diagram showing samples from the Rogue Wilderness ophiolites.

- A. The samples from the metagabbro unit plot at depleted N-MORB compositions and overlap with the field for island-arc tholeiites. All samples from the metatonalite unit plot in the calc-alkaline field.
- B. The samples from the sheeted dike complex plot in the N-MORB field, island-arc tholeiite field and calc-alkaline field. Dikes of petrographic group 1 (diabasic dikes) range from N-MORB to island-arc tholeiite in composition whereas dikes of petrographic group 2 (diabasic and microdioritic dikes) are calc-alkaline. The screens of cumulate gabbro have IAT and transitional IAT-CA magmatic affinities. This diagram also shows that the $(La/Yb)_n$ ratios increase with increasing Th/Hf ratios.
- C. All samples from the pillow unit plot within the island-arc tholeiite field. One dike from the sheeted dike complex and two cumulate gabbro samples overlap with the field of the pillow unit and also have $(La/Yb)_n < 1$.
- D. Most samples from the Mule Mountain volcanics plot in the island-arc tholeiite field, and two dacitic samples plot well within the calc-alkaline field. The field containing samples with $(La/Yb)_n < 1$ overlaps completely with the field of the pillow unit suggesting that the pillow unit and part of the Mule Mountain volcanics are related. SC-15 appears to be a boninite having an U-shaped REE pattern and low concentrations of HFS elements. Similar to the samples from the sheeted dike complex, the $(La/Yb)_n$ ratios increase slightly with increasing Th/Hf ratios.
- E. The samples from the Half Moon Bar diorite plot in a very small cluster in the calc-alkaline field. Small variations in incompatible trace element ratios indicate the samples are related by fractionation of a common parental liquid. Also, the muscovite garnet tonalite dikes in the metagabbro unit plot in the calc-alkaline field.
- F. Petrogenetic pathways in the Hf/3-Th-Ta diagram of Wood et al. (1979) after Pearce et al. (1984). The vectors show mantle depletion due to previous partial melting and mantle enrichment from a “within-plate” component. Vectors (1) and (2) indicate enrichment of normal and depleted mantle with Th derived from a subducted slab.

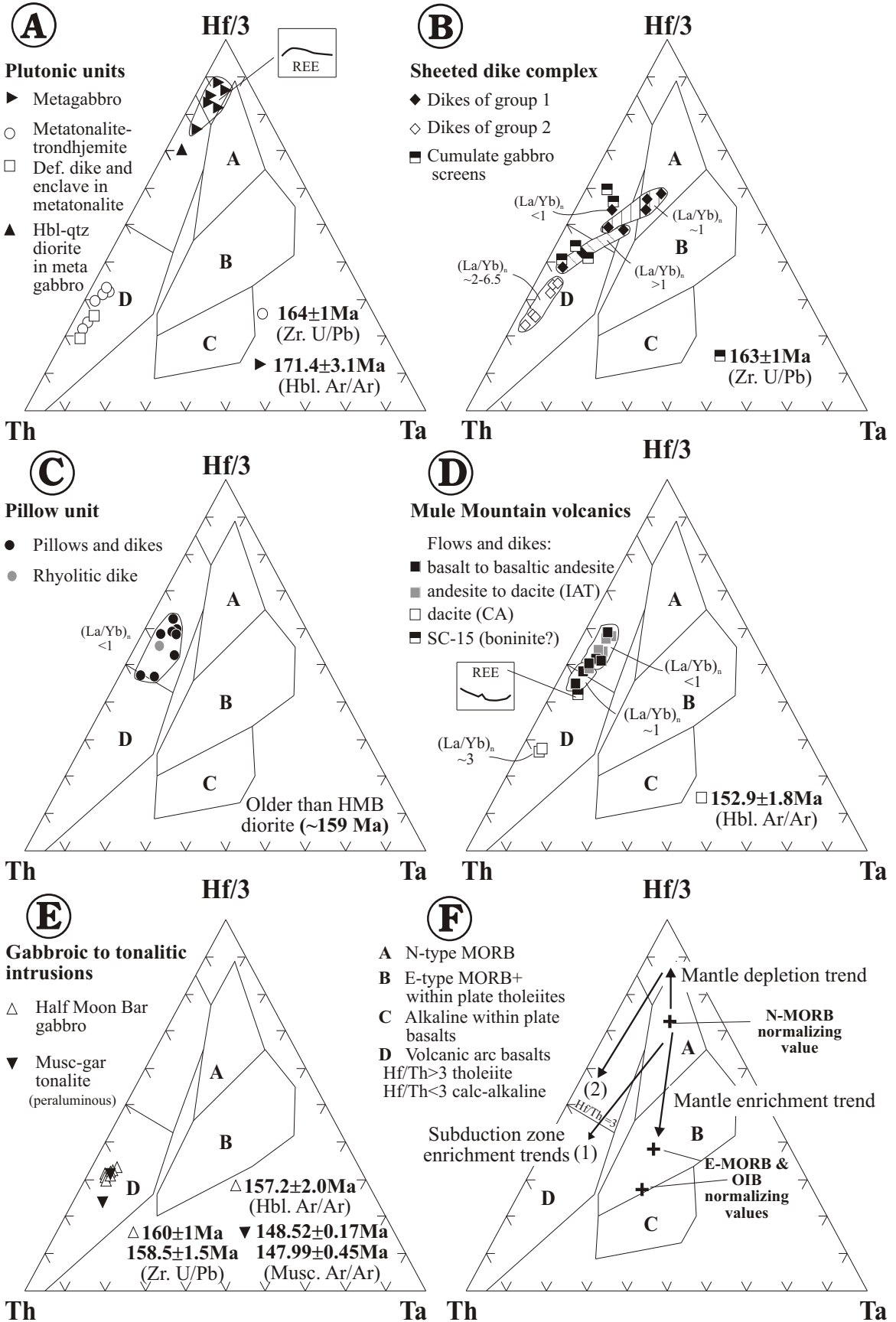


Figure 6.9

Location map of the Lau Basin after Hergt and Farley (1994) showing bathymetry, location of Lau and Tonga ridges, and drill-hole sites (Leg 135 and DSDP Site 203). CLSC, ILSC and ELSC are the Central Intermediate and Eastern Lau Spreading centers, respectively. The three spreading segments between the islands of Niuafu'ou and Tafahi form the King's triple junction. Also shown (dashed lines extending from the Peggy Ridge to the Valu Fa ridge) is the approximate boundary between the older western and eastern Lau Basin crustal Provinces. The western Lau Basin has horst-and-graben topography as a result of tectonic extension of arc crust while the eastern Lau basin crust formed by true seafloor spreading (Parson and Hawkins, 1994).

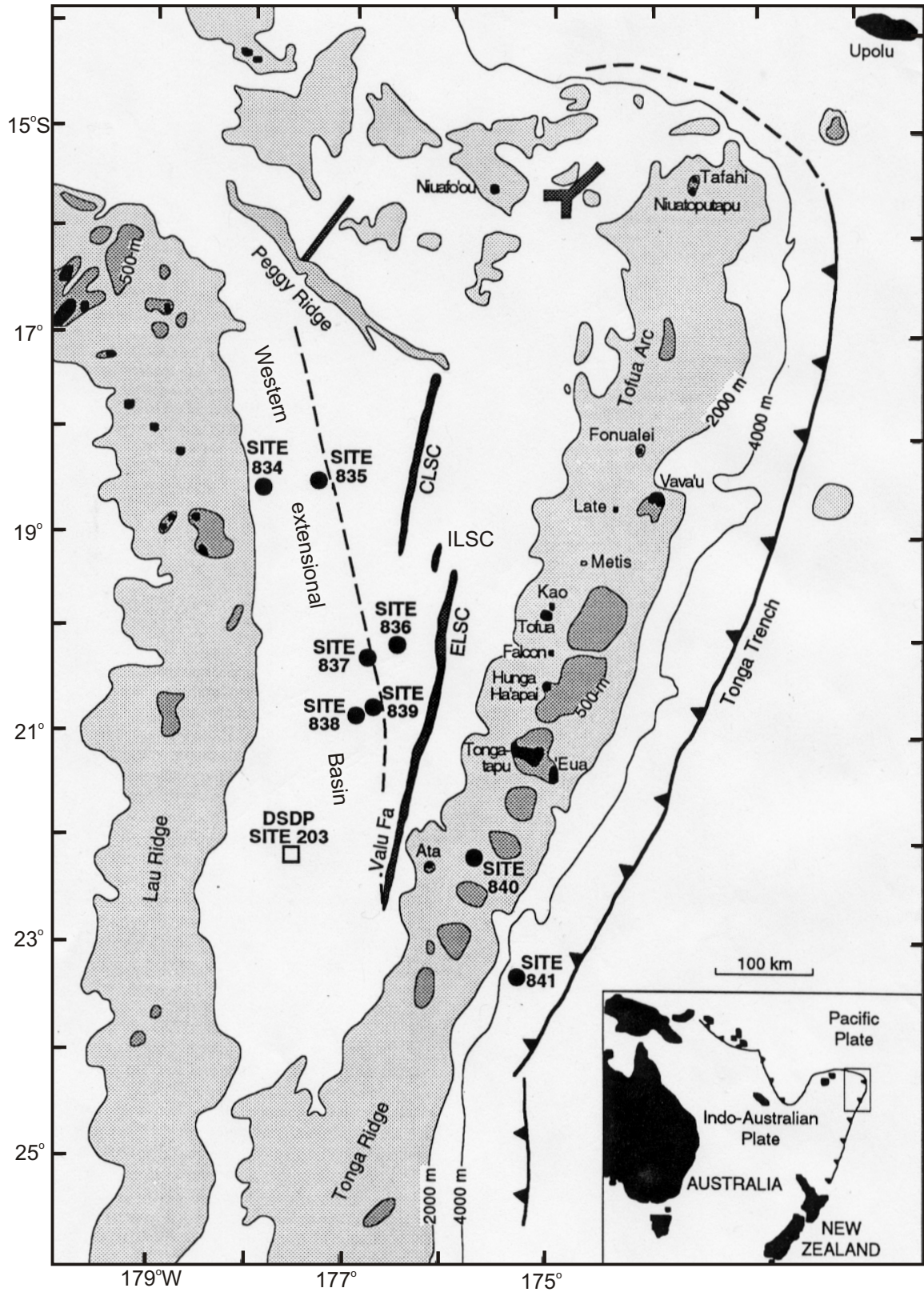


Figure 6.9: Location map of the Lau Basin

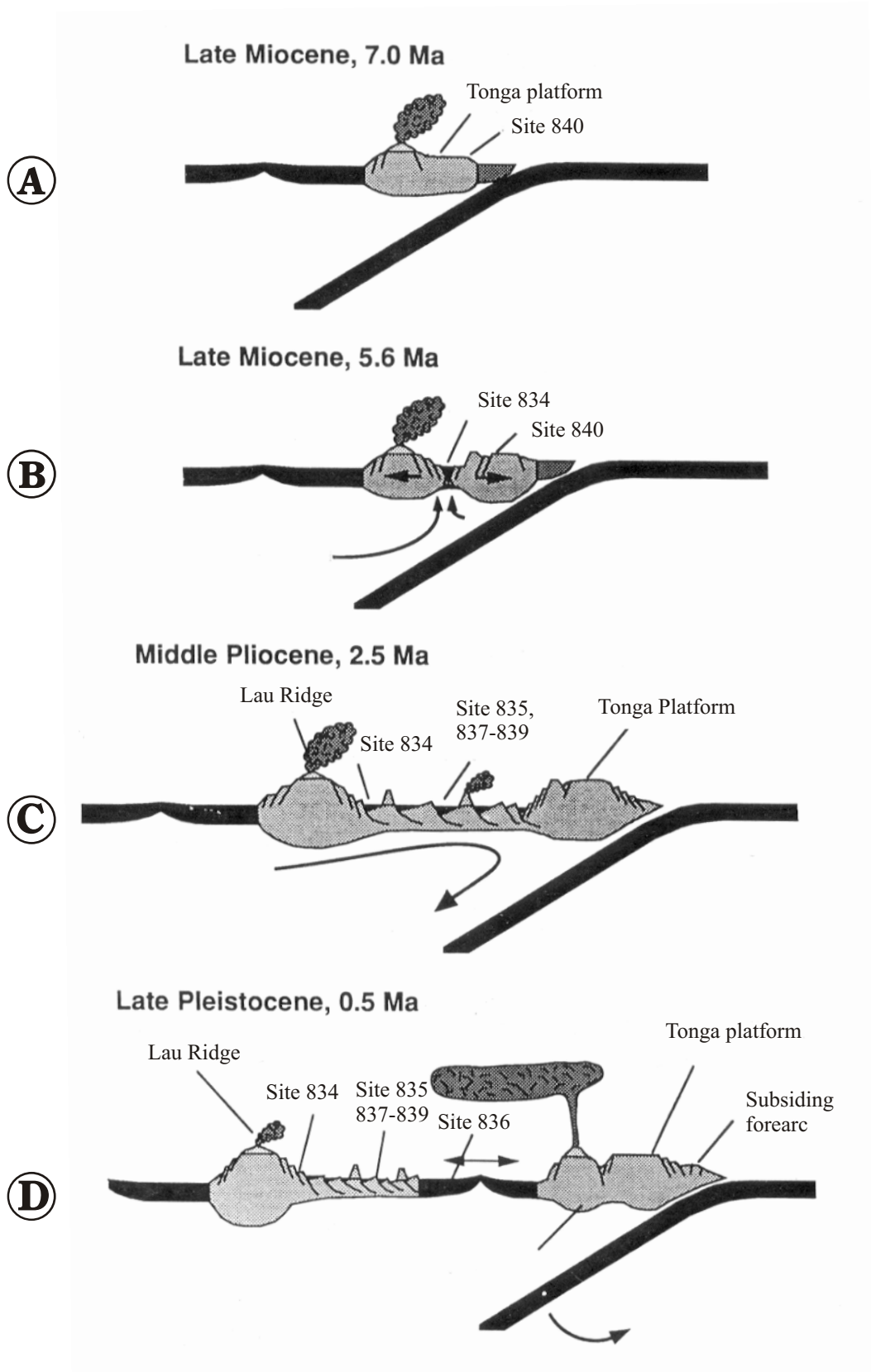


Figure 6.10: Diagram showing the tectonic evolution of the Lau Basin (after Clift and Dixon, 1994)

See text for details.

Figure 6.11

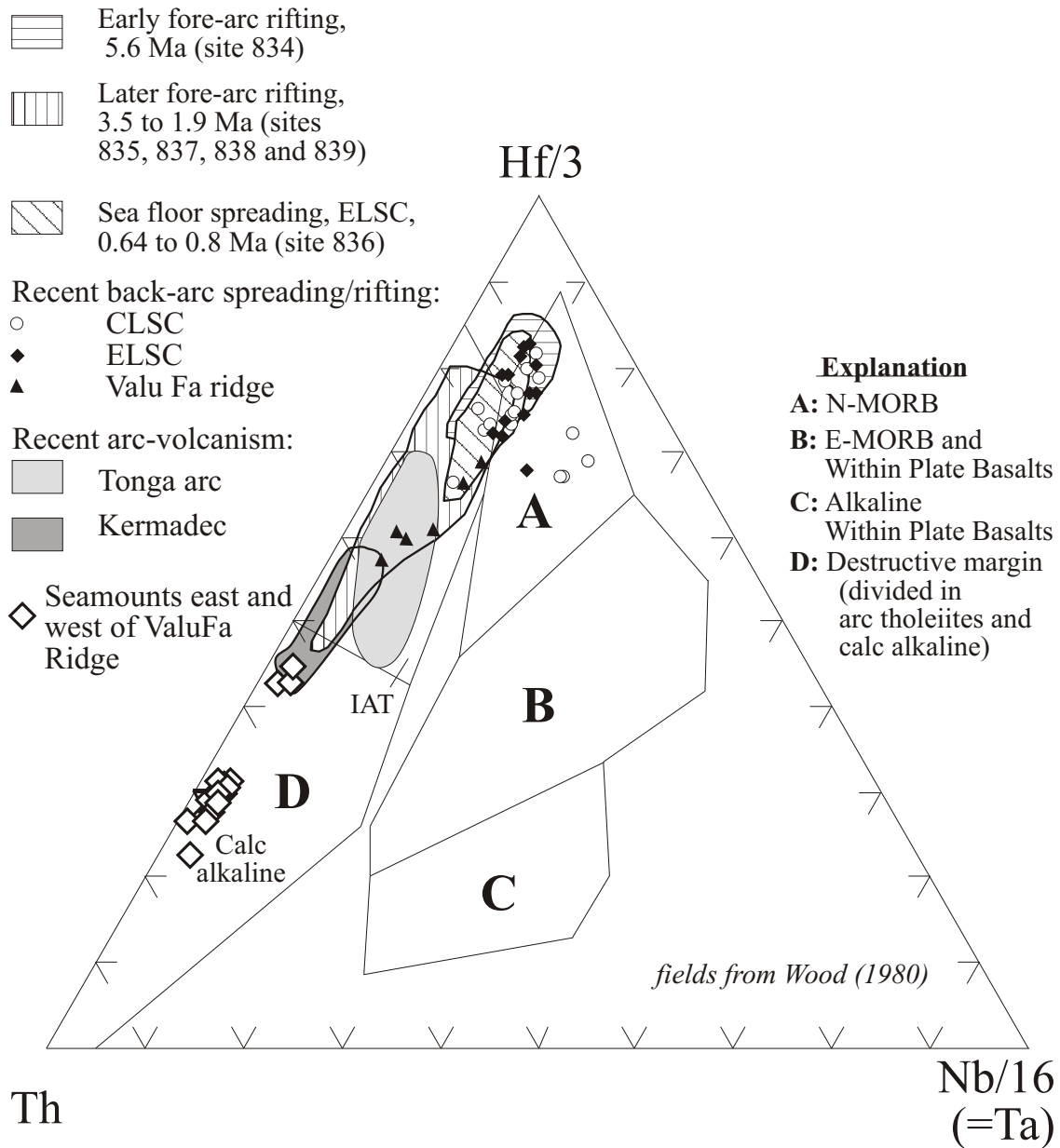
Published geochemical data from the Lau Basin, SW Pacific plotted in the Hf/3-Th-Ta discrimination diagram of Wood (1979).

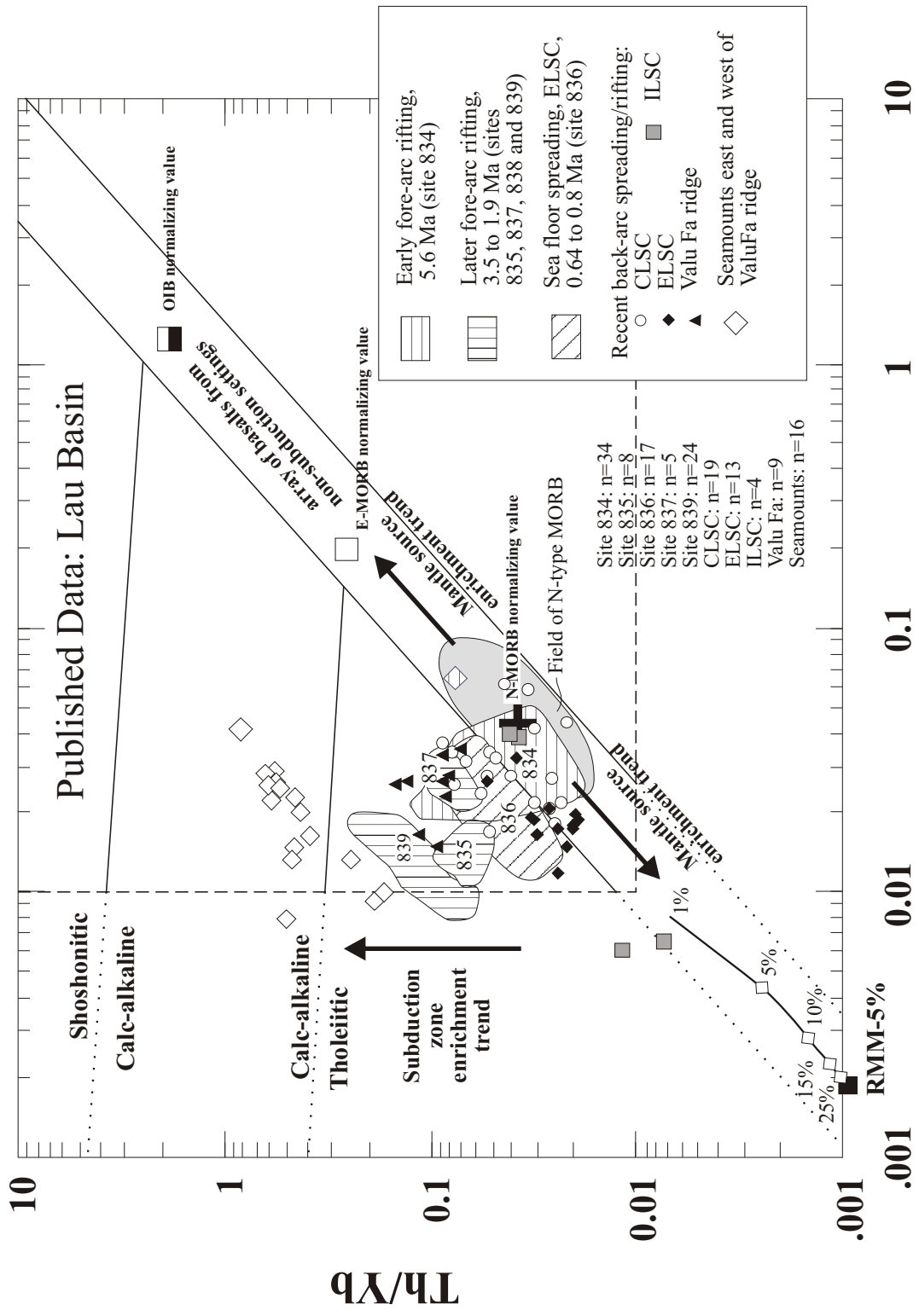
Figure 6.12

Published geochemical data from the Lau Basin, SW Pacific plotted in the Th/Yb vs. Ta/Yb discrimination diagram of Pearce (1982).

The analytical data shown in figures 6.11 and 6.12 are compiled mainly from ODP volume 135 and include the data reported in Ewart et al. (1994a), Ewart et al. (1994b), Hergt and Farley (1994), Allan (1994), Hawkins and Allan (1994), and Hergt and Hawkesworth (1994). Other data include those of Pearce et al. (1995b), Hawkins (1995), Hawkins and Melchior (1985), Kamenetsky et al. (1997), Jenner et al. (1987), Frenzel et al. (1990), and Boespflug et al. (1990).

Published Data: Lau Basin





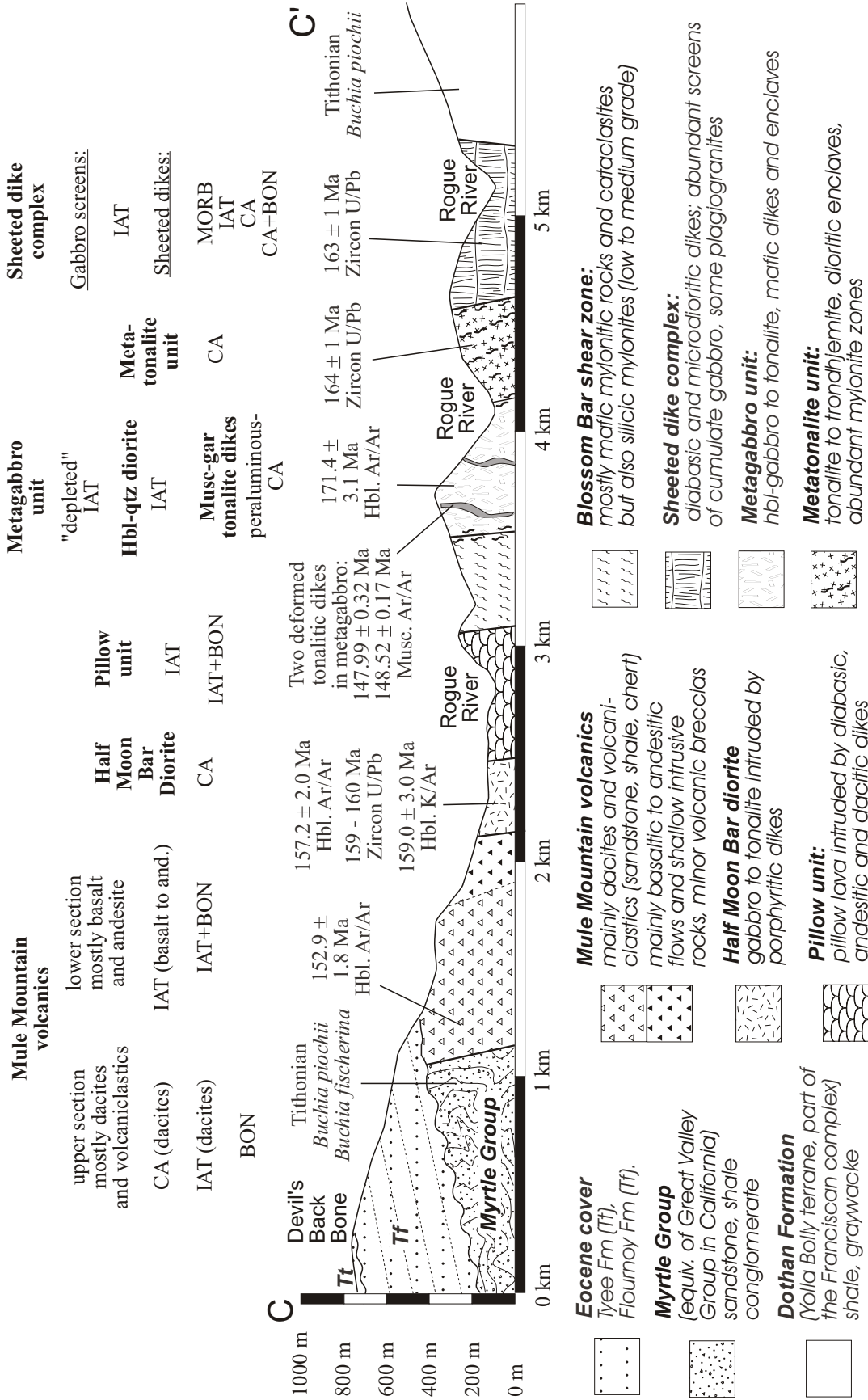


Figure 7.2: Cross section showing the units of the Wild Rogue Wilderness, sample ages and magmatic affinities.